

Heat transfer, fluid flow analysis and energy management of micro-channel heat sinks using vortex generators and nanofluids

By

Mushtaq Talib Khazaal Al-Asadi

Submitted in accordance with the requirements for the degree of Doctor of
Philosophy

The University of Leeds
School Mechanical engineering
Institute of ThermoFluids (iTF)



April, 2018

The candidate confirms that the work submitted is his own, except where work formed jointly-authored publication has been included.

The contribution of the candidate and other authors to this work has been explicitly indicated overleaf. The candidate confirms that appropriate credit has been given within the thesis where reference has been made to the work of others.

This copy has been supplied on the understanding that it is copyright material and that no quotation from the thesis may be published without proper acknowledgement.

© 2018 The University of Leeds and Mushtaq T. K. Al-Asadi.

This work is dedicated to:

My beloved parents

Talib and Suad

My beloved wife, son and daughters

Anfal Al-Rubei

Abdullah, Fatima and Retal

Work appearing in Jointly Authored Publications

- **Published papers:**

1- Part of chapter 2, section 2.4 nanofluids overview:

Al-Asadi, M.T., et al., Heat Transfer Enhancements Using Traditional Fluids and Nanofluids in Pipes with Different Orientations: A Review. *Journal of Nanofluids*, 2017. 6(6): p. 987-1007.

2- Chapter 3 and section 4.2 of chapter 4:

Al-Asadi, M.T., A. Al-damook, and M.C.T. Wilson, Assessment of vortex generator shapes and pin fin perforations for enhancing water-based heat sink performance. *International Communications in Heat and Mass Transfer*, 2018. 91: p. 1-10.

3- Chapter 4, section 4.3:

Al-Asadi, M.T., F. S. Alkasmoul, and M. C. T. Wilson, "Heat transfer enhancement in a micro-channel cooling system using cylindrical vortex generators," *International Communications in Heat and Mass Transfer*, vol. 74, pp. 40-47, 5// 2016.

4- Chapter 5 and section 7.3 of chapter 7:

Al-Asadi, M.T., F.S. Alkasmoul, and M.C.T. Wilson, Benefits of spanwise gaps in cylindrical vortex generators for conjugate heat transfer enhancement in micro-channels. *Applied Thermal Engineering*, 2018.

5- Chapter 5

Al-Asadi, M.T., and M. C. T. Wilson, Evaluation of nanofluids performance with vortex generators for enhanced micro-channel heat transfer, *Thermal Engineering: Theory and Application*, February 25-28, 2018 Doha, Qatar, Paper ID 81.

Abstract

High heat fluxes generated by modern electronic chips continue to motivate efforts to improve the efficiency of associated cooling systems. This thesis seeks to enhance heat transfer in liquid-based micro-channel heat sinks, while keeping power consumption low, using geometrical modifications and the replacement of water coolant by nanofluids.

Preliminary investigation of a perforated pinned heat sink shows that geometrical enhancement strategies proven for air-cooled systems do not necessarily work well with liquid coolant. However, simple solid cylindrical or prismatic vortex generators (VGs) positioned at intervals along the base of a micro-channel are found to offer heat transfer benefits for liquid coolants flowing under laminar conditions. The performance of various VGs with different cross-sectional shapes (including semi-circular, triangular, elliptical and rectangular) is examined using detailed finite element analysis validated against published experimental data. Results show that the half-circle VGs offer the best heat transfer improvement among the considered shapes, but with a substantial increase in pressure drop along the micro-channel. To reduce the pressure penalty, various gaps are introduced along the span of the VGs and shown to reduce the pressure while further improving the heat transfer performance. A performance evaluation criteria (PEC) index is used to assess the VG benefits versus pressure penalty.

A critical evaluation of various ($\text{Al}_2\text{O}_3/\text{SiO}_2$ -water) nanofluids in terms of energy management is conducted, highlighting that performance comparisons at equal Reynolds numbers are misleading because of kinematic viscosity differences. Enhancement of heat transfer can appear much more significant than when comparing at equal flow rate. However, it is also shown that a novel combination of elliptical VGs with nanofluids can offer genuine benefits.

Finally, an optimisation study illustrates that CFD-validated surrogate modelling provides an accurate representation of the system performance over a range of design parameters, enabling optimal heat transfer and pressure drop to be determined.

Acknowledgements

All the praises be to Allah, the Most Beneficent, the Most Merciful.

I express my extreme gratitude to my supervisor, Dr Mark Wilson for all his worth guidance, continuous support and encouragement during this research. His stimulating comments and suggestions have been of immense benefit to me.

Also, I thank Dr Zinedine Khatir for coding the optimisation data in chapter 7. Furthermore, I thank Basra Oil Company (BOC) for financial support of this work, as well as Iraqi Ministry of oil.

Above all else, I thank my family, my parents, brothers and sister so much for their support and prayers during all periods of my life.

Table of Contents

Work appearing in Jointly Authored Publications.....	iv
Abstract.....	v
Acknowledgements.....	vi
Chapter 1: Introduction.....	1
1.1 Introduction	1
1.2 Heat sink and micro-channel	1
1.3 Heat transfer enhancement classification	3
1.4 Vortex generators	4
1.5 Air cooling and liquid cooling	6
1.6 Nanofluid principles	6
1.7 The aim and objectives of this research	7
Chapter 2: Literature Review.....	9
2.1 Introduction	9
2.2 Uniform micro-channels.....	11
2.2.1 Single phase flow	12
2.2.2 Two-phase flow	17
2.2.3 Curved and tapered rectangular micro channels.....	21
2.3 Non-uniform channels and vortex generators.....	22
2.3.1 Non-uniform channels	22
2.3.2 Cylindrical vortex generators.....	28
2.4 Nanofluids overview.....	29
2.4.1 Nanofluids preparation	30
2.4.2 Thermo-physical Properties of Nanofluids.....	31
2.5 Nanofluid equations	39
2.5.1 Thermal conductivity:	39

2.5.2 Viscosity equation	39
2.5.3 The density equation:.....	40
2.5.4 The effective heat capacity equation:.....	40
2.5.5 The effective thermal expansion equation:.....	40
2.6 Drawbacks of nanofluids.....	41
2.7 Evaluation of heat transfer improvement	42
2.8 Validation of numerical methods versus experimental investigations	42
2.9 Conclusions from the literature	45
Chapter 3: Numerical method	47
3.1 Introduction.....	47
3.2 Background of CFD	47
3.3 Governing equations.....	51
3.4 COMSOL Multiphysics®.....	53
3.5 Nanofluid equations.....	53
3.6 Geometry description and boundary conditions.....	53
3.7 Heat transfer performance characterisation.....	57
3.8 Mesh sensitivity and code validation.....	58
3.9 Experimental and numerical validation of nanofluids	62
3.10 Preliminary Investigation of perforated pinned heat sink	64
3.10.1 Geometry description	64
3.10.2 Perforated PHS using water	66
3.11 Summary	68
Chapter 4: Heat and Flow Analysis of Circular Vortex Generators Design	69
.....	
4.1 Introduction.....	69
4.2 Influence of VGs shape in the micro-channel	71
4.2.1 Triangular shapes	73
4.2.2 Rectangular shapes	75

4.2.3 Circular shapes	78
4.2.4 Comparison of the VGs shapes	80
4.2.5 Hydraulic thermal performance	82
4.3 Further exploration of half-circle VGs	83
4.3.1 Thermal-hydraulic performance	85
4.4 Summary	87
Chapter 5: Benefits of spanwise gaps in cylindrical vortex generators	89
5.1 Introduction	89
5.2 The gap performance	90
5.2.1 End gaps (E-type vortex generators)	91
5.2.2 The effect of end-gap width on conjugate heat transfer	91
5.2.3 Performance evaluation criteria index	92
5.2.4 Vortical flow structure and solid temperature distribution	94
5.2.5 The effect of VG position and number.....	96
5.2.6 The effect of VG radius	98
5.2.7 The effect of solid thermal conductivity	99
5.3 Vortex generators with a single central gap (C-type VGs)	102
5.4 The effect of combining central and end gaps	105
5.5 Comparison of the 'best' of each vortex generator type.....	107
5.5.1 Thermal resistance and pressure drop.....	107
5.5.2 Thermal-hydraulic performance index.....	108
5.5.3 Solid and fluid temperature distributions	109
5.6 Summary	113
Chapter 6: Evaluation of nanofluid performance	115
6.1 Introduction	115
6.2 Evaluating nanofluid performance in a uniform channel	117
6.2.1 Thermal resistance.....	117

6.2.2 Pressure drop.....	121
6.3 Nanofluid performance with half-circle (C-model) VGs.....	128
6.3.1 Thermal resistance.....	128
6.3.2 Pressure drop.....	130
6.4 Combining nanofluids and elliptical (EL-model) VGs.....	133
6.4.1 Thermal resistance.....	133
6.4.2 Pressure drop.....	135
6.5 Summary	137
Chapter 7: Energy Management considerations	139
7.1 Introduction.....	139
7.2 Full-span VGs with water coolant	140
7.3 Effect of gaps on energy management.....	143
7.4 Performance of nanofluids.....	146
7.4.1 Effect of VGs shape	146
7.4.2 Effect of gaps	148
7.5 Optimisation of the uniform micro-channel	155
7.5.1 Multi-objective design optimisation.....	158
7.6 Summary	163
Chapter 8: Conclusion and recommendation for future work.....	165
8.1 Achievements – general discussion.....	165
8.2 Vortex generators	165
8.3 Nanofluid performance	167
8.4 Limitations of this study	168
8.5 Future Work.....	169
REFERENCES.....	171

List of Tables

Table 1.1: Channel classification [8],[9].....	2
Table 1.2: Heat transfer enhancement classification.....	4
Table 2.1: Heat transfer enhancement using different fluids.	32
Table 3.1: Dimensions of the micro-channel and VGs models.....	55
Table 3.2: The boundary conditions of the conjugate heat transfer model. .	56
Table 3.3: Code validation with Abdollahi and Shams [259].....	61
Table 3.4: Comparison of predicted nanofluid equations with experimental work at 20° C [262].	63
Table 3.5: Thermo-physical properties of nanofluids used in this study at the inlet temperature (293.15K).....	64
Table 4.1: Micro-channel and VGs dimensions in μm	70
Table 5.1: Dimensions of the micro-channel and VG configurations.....	89
Table 6.1: VGs dimensions in μm	117
Table 7.1: Dimensions with temperature and pressure drop at fixed Reynolds number.....	157
Table 7.2: Microchannel design performance at five operating conditions points located on the Pareto front together with CFD validation.....	161

List of figures

Figure 1.1: Micro-channel heat sink (L=10 mm and the corresponding width of each channel W= 0.3 mm) [13].	3
Figure 1.2: Vortex generator types which are suitable for air flows [39].	5
Figure 2.1: (a) Plate-fin heat exchanger and its surface geometries: (b) plain rectangular fins, (c) plain triangular fins, (d) wavy fins, (e) offset strip fins, (f) perforated fins, (g) louvered fins; after Webb [71].	10
Figure 2.2: Micro-channel omega shape in mm [82].	13
Figure 2.3: Different inlet and outlet positions and header shapes of micro-channel heat sinks [84].	15
Figure 2.4: Magnetic fields distribution to enhance the heat transfer [85].	15
Figure 2.5: Growth in number of publications of micro-channels [98].	20
Figure 2.6: Curved duct with square cross sectional area [99].	21
Figure 2.7: Rectangular micro-channel [103]; (a) Geometry description, (b) various cylindrical grooves (cases A0-A3) and square ribs (case b).	24
Figure 2.8: Square channel having different ribs and cavities [105].	25
Figure 2.9: Irregular channel [106].	25
Figure 2.10: Various types of fins (a) LRFA, (b) LTFA, (c) ARFA, and (d) ATFA [110].	27
Figure 2.11: Growth of publications in nanofluids [98].	29
Figure 2.12: The influence of nanoparticle concentrations on thermal conductivity [204].	36
Figure 2.13: The influence of nanoparticle concentrations on thermal conductivity [205].	37
Figure 2.14: Validations between numerical and experiments, (a) friction coefficient, (b) inlet thermal resistance, and (c) outlet thermal resistance.	44
Figure 3.1: Mesh of a geometry having elements and nodes.	48

Figure 3.2: Types of quadratic one, two and three-dimensional elements [253].	49
Figure 3.3: FEM process	50
Figure 3.4: The connection between the three stages [254]......	51
Figure 3.5: Geometry description: (a) rectangular micro-channel containing vortex generators; (b) 3-D view a heat sink comprised of a series of micro- channels [258]; (c) view along the channel showing the definition of parameters governing the dimensions of the geometry.....	55
Figure 3.6: The boundary conditions of the geometry.	56
Figure 3.7: Grid independence test for a smooth channel, showing the maximum temperature calculated using increasingly refined meshes, with $q =$ 100 W/cm^2 and $Re = 600$	59
Figure 3.8: Grid independence test for micro-channel with VGs; $q = 100$ W/cm^2 , $Re = 100$	59
Figure 3.9: Code validation by comparison of calculated temperature distribution along a graphene micro-channel with heat flux 181 W/cm^2 and flow rate $8.6 \text{ cm}^3/\text{s}$ [78].	60
Figure 3.10: Code validation by comparison of calculated temperature distribution along a graphene micro-channel with heat flux 277 W/cm^2 and flow rate $8.6 \text{ cm}^3/\text{s}$ [78].	60
Figure 3.11: Validation of the present model against experimental data of Kawano et al. [260] and alternative numerical results of Qu and Mudawar [261].	62
Figure 3.12: Pinned fin heat sink.....	65
Figure 3.13: Boundary condition of perforated pinned heat sink.	65
Figure 3.14: The pin fin model description, all dimensions in mm [263].	65
Figure 3.15: Comparisons between solid and perforated PHS (3 holes) with water as a coolant: (a) Pressure drop; (b) Base plate temperature.	67

Figure 4.1: Geometry description: (a) rectangular micro-channel containing vortex generators; (b) view along the channel showing the definition of parameters governing the dimensions of the geometry..... 70

Figure 4.2: Side view of different shapes of VGs: (a) Forward triangular (FT); (b) Backward triangular (BT); (c) Symmetry triangular (ST); (d) Vertical rectangular (VR); (e) Horizontal rectangular (HR); (f) Square (S); (g) Half-circle (C). 71

Figure 4.3: Different range of heat flux with the full range of Re using uniform channel: (a) thermal resistance; (b) pressure drop..... 72

Figure 4.4: Different configurations of triangular VGs forward triangular (FT), backward triangular (BT) and Symmetric triangular (ST): (a) thermal resistance; (b) pressure drop. 74

Figure 4.5: X-Z planes of various triangular VGs models with flow direction from the left to the right at Re 800: (a) temperature contour (K) at the wall of the channel; (b) contours of x velocity component (m/s) at the centre of the channel..... 75

Figure 4.6: Different VGs of rectangular model (Vertical rectangular (VR), Horizontal rectangular (HR) and Square (S)): (a) thermal resistance; (b) pressure drop. 77

Figure 4.7: X-Z planes of various triangular VGs models (Vertical rectangular (VR), Horizontal rectangular (HR) and Square (S)) with flow direction from the left to the right at Re 800: (a) temperature contour (K) at the wall of the channel; (b) contours of x velocity component (m/s) at the centre of the channel..... 77

Figure 4.8: Circular VGs compared to uniform channel using Re from 300 to 2000: (a) thermal resistance; (b) pressure drop. 79

Figure 4.9: X-Z plane of uniform channel and circular VGs at Re =800: (a) temperature contour; (b) contours of x velocity component (m/s) at the centre of the channel..... 79

Figure 4.10: Comparison of the lowest thermal resistance configurations (ST, S and C models); (a) thermal resistance; (b) pressure drop..... 81

Figure 4.11: X-Z plane comparing the uniform channel to ST, S and C VGs models at $Re = 800$: (a) temperature contour; (b) velocity contour.	81
Figure 4.12: PEC of the lowest thermal resistance models with the full range of Re	82
Figure 4.13: Thermal resistance and pressure drop as a function of VG radius for full-span half-circle VGs: (a) $Re = 100$ to 900 ; (b) $Re = 1100$ to 1500	84
Figure 4.14: Comparison of the thermal resistance and pressure drop characteristics of the uniform channel and the half-circle VG considered, with radius equal to $200 \mu\text{m}$	85
Figure 4.15: Variation of PEC index with Reynolds number for centred half-circle VGs of various radii.....	86
Figure 5.1: Geometry description: (a) uniform rectangular micro-channel with governing the dimensions of the geometry; (b) front-view cross-section of a 'central' ('C') gap VG; (c) front-view cross-section of an 'end' ('E') gap VG; (d) front-view cross-section of a 'CE' VG, with central and end gaps; (e) boundary conditions applied; (f) 3D view of the uniform channel.	90
Figure 5.2: PEC index values for various end-gap widths.	93
Figure 5.3: Thermal resistance and pressure drop versus Re for E-type VGs of radius $400 \mu\text{m}$ having various gaps of combined width indicated in the legend. The $r = 0 \mu\text{m}$ line refers to the uniform channel with no VG present.	93
Figure 5.4: Paths of passive tracer particles in the flow, illustrating the effect of (a) a full-span cylindrical VG and (b) an E-type VG on transverse and longitudinal vortex generation. The VGs have radius $400 \mu\text{m}$. The flow is from right to left with Reynolds number 500 and the gap at each end of the VG is $75 \mu\text{m}$. Plot (c) is an enlarged view of (b).	95
Figure 5.5: Temperature contours (in K) along channels containing five E2 or full-span (F) VGs. The planes shown are within the solid and located $2 \mu\text{m}$ away from the water: (a) the base of the channel, (b) the side wall of the channel.....	95

Figure 5.6: Effect of the number of E2 VGs on thermal resistance and pressure drop.....	96
Figure 5.7: Effect of single E2 VG position on thermal resistance and pressure drop.....	97
Figure 5.8: PEC versus Re for series of equally-spaced E2 VGs of radius 400 μm	98
Figure 5.9: Effect of VG radius on thermal resistance and pressure drop for E2 VGs.....	99
Figure 5.10: Temperature contours (in K) along copper and aluminium channels containing five E2 VGs of radius 400 μm with flow at $Re=300$. The planes in (a) and (b) are within the solid, 2 μm away from the water: (a) the side wall of the channel, (b) the base of the channel. The (y,z) cross-sections in (c) are at the outflow.....	101
Figure 5.11: Performance of copper versus aluminium in terms of thermal resistance and pressure drop.....	102
Figure 5.12: Thermal resistance and pressure drop calculated for C-type cylindrical VGs as a function of Reynolds number.	103
Figure 5.13: PEC values as a function of Reynolds number for the C-type VGs considered.....	104
Figure 5.14: Temperature contours (in K) on a y-z plane located 100 μm downstream of the trailing edge of the first VG in the channel: (a) full-span VGs without gap, (b) C-type VGs with a central gap of 100 μm . The arrows indicate y,z velocity components at $Re=300$	105
Figure 5.15: Calculated thermal resistance for CE-type VGs with a gap of 100 μm at each end and a variable width central gap. The width in the legend refers to the combined width of all three gaps.....	106
Figure 5.16: Comparison of the thermal resistances and pressure drops for the 'best' of each VG type.	107
Figure 5.17: Performance Evaluation Criteria (PEC) index, equation (3.14), versus Reynolds number for the VGs of each type offering the lowest thermal resistance.....	109

Figure 5.18: Temperature contours on (a) a plane parallel to the side wall located 100 μm from the wall, and (b) a plane parallel to the solid base located at 2 μm below the fluid flow, for different VG types operating at $Re = 300$. The flow is from the left to the right.	111
Figure 5.19: (a) Contours of the x component of fluid velocity (in m/s) and y,z velocity vectors on a spanwise cross-sectional plane located 100 μm downstream of the first VG; (b) temperature contours and y,z velocity vectors on a cross-section located 2000 μm downstream of the centre of the last VG in the channel. The Reynolds number is 500, and the VGs are (from left to right) CE1, C2, full-span, and E2 (see Table 5.1).....	112
Figure 6.1: Side view of VGs: (a) half-circle (C); and (b) half-elliptic (EL). ..	117
Figure 6.2: Thermal resistance of different working fluids with various concentrations in the uniform channel; (a) SiO_2 -water at different concentrations up to 4% with water, (b) Al_2O_3 - water nanofluids (4%) and water, (c) a comparison of Al_2O_3 and SiO_2 nanoparticles in the water (0 and 4) %.....	119
Figure 6.3: Kinematic viscosity of different nanoparticles concentration. ...	120
Figure 6.4: Thermal resistance for uniform channel model with nanofluid and pure water.	121
Figure 6.5: Pressure drop of pure water compared to different nanofluids in the uniform channel at given Re ; (a) SiO_2 -water at different concentrations up to 4% with water, (b) Al_2O_3 - water nanofluids (4%) and water, (c) a comparison of Al_2O_3 and SiO_2 nanoparticles concentration of 4% in the water with pure water.	123
Figure 6.6: Pressure drop for the uniform channel model with water and Al_2O_3 nanofluid at different concentrations.....	124
Figure 6.7: X-component of fluid velocity for water and Al_2O_3 nanofluid at different concentrations in the uniform channel.....	124
Figure 6.8: Kinematic viscosity of Al_2O_3 nanofluid at various concentrations; (a) at the inlet of the micro-channel (at the inlet temperature), (b) at the outlet of the micro-channel (temperature dependent).	125

Figure 6.9: Kinematic viscosity of SiO ₂ nanofluid at various concentrations; (a) at the inlet of the micro-channel (at the inlet temperature), (b) at the outlet of the micro-channel (temperature dependent).	126
Figure 6.10: Comparison of Kinematic viscosity of Al ₂ O ₃ and SiO ₂ nanofluids at 4% of nanoparticles concentration; (a) at the inlet of the micro-channel (at the inlet temperature), (b) at the outlet of the micro-channel (temperature dependent).	127
Figure 6.11: Thermal resistance comparison of the uniform channel and C-model with water and Al ₂ O ₃ nanofluid at the concentration of 4%; (a) C-model with nanofluid and water, (b) comparison of the uniform channel and C-model with water and nanofluid.	129
Figure 6.12: Thermal resistance Vs MFR for geometries and fluids, C-model and uniform channel with water and Al ₂ O ₃ nanofluids at the concentration of 4%.	130
Figure 6.13: pressure drop with Reynolds number for C-model and uniform channel using water and Al ₂ O ₃ nanofluid at 4% of concentration.	131
Figure 6.14: Pressure drop comparison of the uniform channel and C-model using water and nanofluid.	131
Figure 6.15: Velocity comparison of different fluids in the uniform channel with respect to: (a) Reynolds number; (b) MFR.	132
Figure 6.16: Thermal resistance of various shapes and fluids with different Reynolds number.	134
Figure 6.17: Thermal resistance for EL, C and uniform channel models. ...	135
Figure 6.18: Pressure drop comparison of elliptical VGs with (0-1) % nanofluids and half-circle VGs using pure water.	136
Figure 6.19: Pressure drop for C-model and uniform channel with water and EL-model with Al ₂ O ₃ nanoparticles concentration in water (0-4) %.	136
Figure 7.1: Average and maximum temperatures of the solid base achieved with various vortex generators at Reynolds number 1000 using water.	141
Figure 7.2: actual temperature distribution along the centre line of the microchannel.	142

Figure 7.3: Maximum fluid temperature at the outlet for C, R and T models at Re=1000.	142
Figure 7.4: Average and maximum water velocities at the outlet of the uniform channel and various VGs at Reynolds number of 1000.	143
Figure 7.5: Average and maximum temperatures on the solid base achieved with various half-circle VGs with gaps and without gaps and Reynolds number 1500. See Table 5.1 for a description of the VG types.	145
Figure 7.6: Maximum temperatures for different half-circle VGs compared to the uniform channel at different pumping power using water as a coolant.	146
Figure 7.7: X-Z plane comparing the uniform channel to C-model, EL-model and the uniform channel at Re =800: (a) temperature contour; (b) velocity contour.	147
Figure 7.8: Maximum temperature with pumping power for various VG models compared to the uniform channel.	148
Figure 7.9: Pressure drop for different VGs shapes; (a) water for wide range of Re, (b) using SiO ₂ -water nanofluids at the concentration of 2%.	150
Figure 7.10: Different VG shapes with Al ₂ O ₃ nanoparticles at the concentration of 0.5% in water; (a) Maximum temperature Vs pumping power; (b) thermal resistance using average temperature Vs Re.	151
Figure 7.11: Thermal resistance with different pumping power of various VG shapes using SiO ₂ of 0.5% in water.	152
Figure 7.12: Pumping power for different VG shapes compared to triangular VGs having gap of 100 μm (50 μm each side near the walls) using SiO ₂ -water at the concentration of 0.5%; (a) maximum temperature (K); (b) thermal resistance using average temperature.	153
Figure 7.13: Average and maximum temperatures on the solid base achieved with various vortex generators at Reynolds number 1000 using SiO ₂ -water at the concentration of 0.5%.	154
Figure 7.14: X-Z plane comparing the T-model having Gap of 100 μm to full-span T-model, R-model and the C-model at Re =1000 with SiO ₂ -water at the concentration of 0.5%: (a) Velocity contour; (b) Temperature contour.	154

Figure 7.15: Distribution of design points for the design variables in: (a) Design variable space and (b) Corresponding microchannel dimensions.	156
Figure 7.16: Response surface of function T from the surrogate model together with the DOE points.	159
Figure 7.17: Response surface of function ΔP from the surrogate model together with the DOE points.	159
Figure 7.18: Pareto front for; (a) the design given in Table 7.1, (b) predicted points adopted from the Pareto front.	160
Figure 7.19: Validation between predicted data and CFD results; (a) maximum temperature, (b) maximum pressure drop.	162

Nomenclature

A_s	surface area of the whole heat sink (μm^2)
CFD	Computational Fluid Dynamics
C_p	Specific heat, J/Kg.K
C_{p_f}	Specific heat of fluid, J/Kg.K
C_{p_s}	Specific heat of solid particles, J/Kg.K
D	Diameter, μm
FEM	Finite Element Method
FVM	Finite Element Method
K	Thermal conductivity, W/m.K
L	Channel length, μm
MFR	Mass flow rate, kg/s
VGs	Vortex generators
P	Pressure, N/m^2
P_p	Pumping power. W
q	Uniform heat flux, W/cm^2
r	Radius of VGs, μm
Re	Reynolds number
T	Temperature, K
X	Axial distance, μm
X_{in}	Distance from the inlet to the first VG, μm

Greek Symbols

β	Empirical functions of nanoparticles
ϕ	Nanoparticles concentration, %
ρ_f	Density of fluid, kg/m^3
ρ_s	Density of solid particles, kg/m^3
μ	Viscosity, Kg/ms
Θ	Thermal resistance, K/W

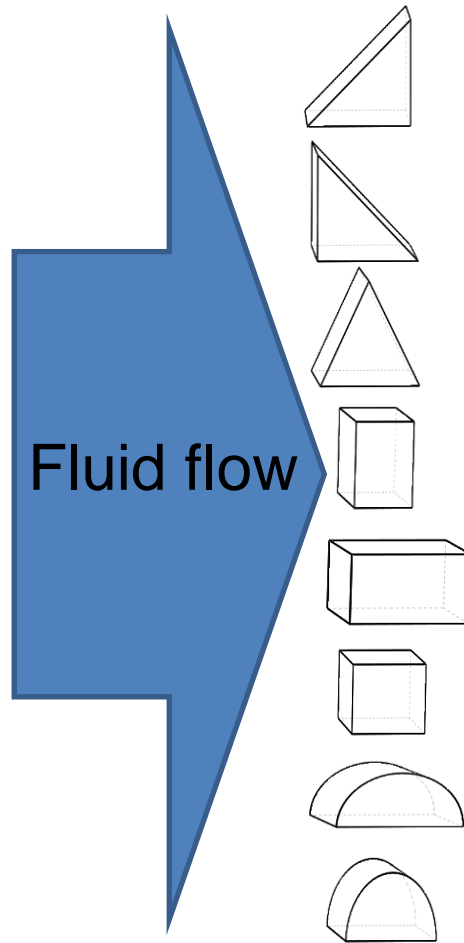
Subscripts

- ave* Average
- In* Inlet
- Max* Maximum
- Out* Outlet
- S* Surface
- L* Liquid

Vortex generators abbreviations

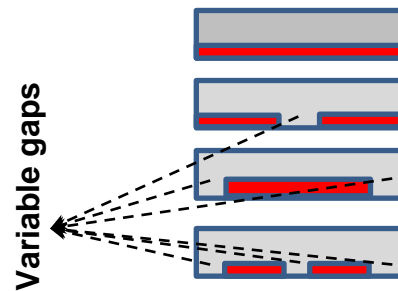
Side view

- FT* Forward triangular
- BT* Backward triangular
- ST* Symmetry triangular
- VR* Vertical rectangular
- HR* Horizontal rectangular
- S* Square
- EL* Elliptical
- C* Half circle



Front View of Half-circle models (C)

- F* Full span (no gap)
- C* Central gap
- E* End gap
- CE* Central and End gaps



Chapter 1: Introduction

1.1 Introduction

In 1941, the computer first appeared in the United States for military purposes and had a size and weight of 1800 square feet (167 m²) and 30 tons (2.75x10⁴ kg) respectively [1]. It was developed with time, focusing on reduction of size and weight while increasing the efficiency, resulting in a challenge point for heat transfer. This challenge was how to reject the heat from the computer with a limitation of space, and it was solved using forced convection instead of natural convection. That forced convection requires an energy input like a pressure gradient to drive the flow, so developing energy efficient cooling methods requires a consideration of this cost.

Recently, cooling has become even more challenging due to rapid development of electronic applications which focus on size and weight reduction while increasing the efficiency simultaneously [2, 3]. These applications have recently arisen in various industries such as biomedical, environmental, aerospace, nuclear reactors, and other electronic cooling device applications [4].

Therefore, the recent motivation is to investigate the behaviour of conjugate heat transfer of cooling systems to reach high thermal and low-pressure drop performance especially for the small systems. One of these systems is a micro-channel heat sink (MCHS), which has the ability to reject the heat and enhance the thermal performance, and forms the primary focus of this study.

1.2 Heat sink and micro-channel

To reject the generated heat from the electronic components or devices, a heat sink can be used to remove the heat either passively using natural convection (no fan is required) or actively using forced convection (fan is required).

There is a need to develop cooling systems by decreasing their size and weight to micro- and mini-scale systems, such as micro-channel heat exchangers and heat sinks [5], while simultaneously increasing the efficiency to meet this development [6].

Mini- and micro-channels have shown high heat transfer performance, they are different in size from the traditional channels and can be classified according to their associated hydraulic diameters, D_h , [7-9] as presented in Table 1.1.

Table 1.1: Channel classification [8],[9].

Mehendale et al. [8].		Kandlikar and Grande [9].	
Conventional channels	$D_h > 6 \text{ mm}$	Conventional channels	$D_h > 3 \text{ mm}$
Compact Passages	$1 \text{ mm} < D_h \leq 6 \text{ mm}$	Minichannels	$1 \mu\text{m} < D_h \leq 3 \text{ mm}$
Meso-channels	$100 \mu\text{m} < D_h \leq 1 \text{ mm}$	Micro-channels	$10 \mu\text{m} < D_h \leq 200 \mu\text{m}$
Micro-channels	$1 \mu\text{m} < D_h \leq 100 \mu\text{m}$	Transitional channels	$0.1 \mu\text{m} < D_h \leq 10 \mu\text{m}$
		Molecular nanochannels	$D_h \leq 0.1 \mu\text{m}$

The term ‘micro-channel’ first appeared in 1981 [10], and a heat sink based on micro-channels is presented in Fig. 1.1. The concept had a great influence in thermal science as it decreased the hydraulic diameter and enhanced the heat transfer. From an analysis perspective, a key feature of micro-channels is that the hydraulic diameter becomes comparable with the channel wall thicknesses, and consequently in transverse cross-sections of micro-channel heat sinks, the area of the solid material is commensurate with the fluid area [11]. This means that conjugate heat transfer phenomena such as axial conduction in the solid must be accounted for, and boundary conditions

applied at channel walls based on Nusselt number correlations from larger channels can lead to inaccurate results [12]. Therefore the motivation of this study is to improve the heat transfer in a limited area which generates heat flux.

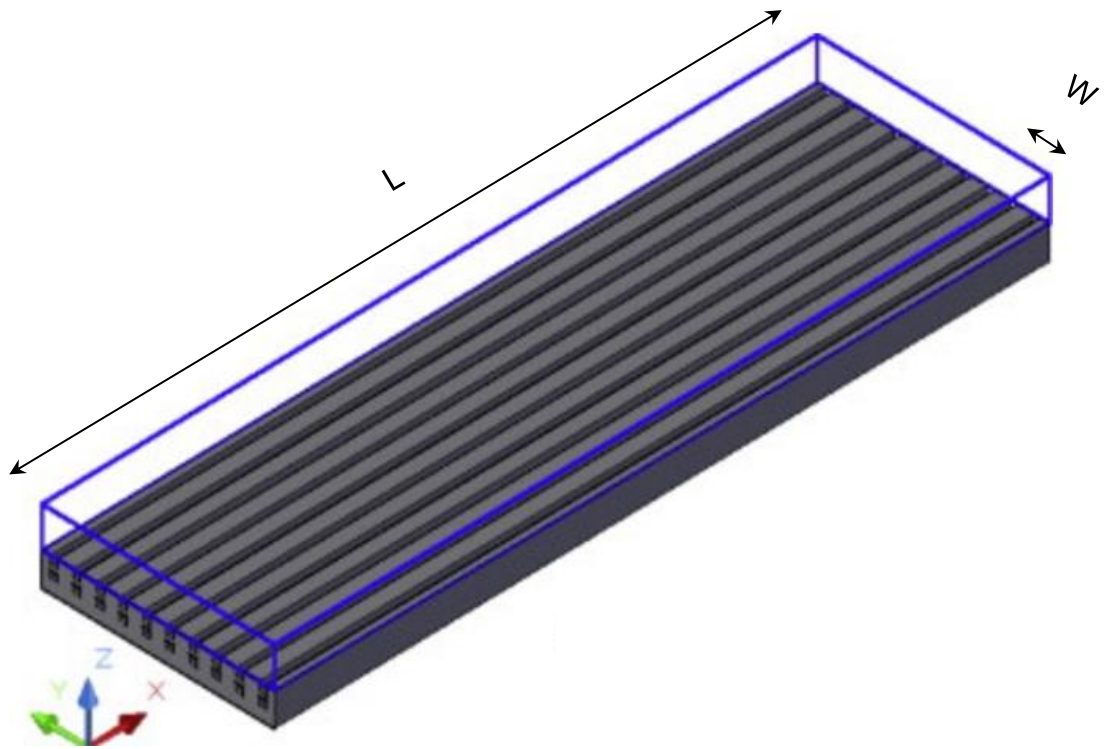


Figure 1.1: Micro-channel heat sink ($L=10$ mm and the corresponding width of each channel $W= 0.3$ mm) [13].

1.3 Heat transfer enhancement classification

Sixteen different enhancement techniques have been identified as passive or active techniques. A list of the various methods or devices under each of these two categories is given in Table 1.2 [14]. The primary distinguishing feature is that unlike active methods, passive techniques do not require direct input of external power, though they may incur indirect energy cost, for instance through increase of pressure drop, as will be seen later in this thesis.

Table 1.2: Heat transfer enhancement classification

Passive Techniques	Active Techniques
Treated surfaces	Mechanical aids
Rough surfaces	Surface vibration
Extended surfaces	Fluid vibration
Displaced enhancement devices	Electrostatic fields
Swirl flow devices	Injection
Coiled tubes	Suction
Surface tension devices	Jet impingement
Additives for liquids	
Additives for gases	

This thesis discusses two passive techniques to enhance the heat transfer performance of a micro-channel heat sink, namely, vortex generators which present the extended surface area and swirl flow devices, and nanofluids that fall under the additives for liquids category in Table 1.1.

1.4 Vortex generators

In the revolution of advanced manufacturing processes, many experimental and numerical studies investigated ways in which heat transfer can be enhanced by modifying the conventional heat sinks. The modification can be achieved by adding various geometrical features which extend the cooling surface area of the heat sink and disturb the flow to promote the formation of vortices in the flow [15]; such features are known as ‘vortex generators’ (VGs). Most of the modern thermal systems offer a high heat transfer performance when using VGs [16-19].

There are two types of vortex generators; they are called transverse vortex generators (TVGs) when the axis of vortices is perpendicular to the fluid flow, however, they are known as longitudinal vortex generators (LVGs) when the

axis of the vortices is parallel to the fluid flow [20]. Both types can be applied within channels to extend the surface area and generate vortices to enhance the heat transfer. Studies have reported that better heat transfer enhancement is achieved using LVGs compared to TVGs [20, 21].

Vortex generators can take various forms such as grooves and ribs [22-25]. Also, they can be protrusions, wings, inclined blocks, winglets and fins [26, 27] as shown in Fig. 1.2. They have been used to enhance heat transfer in different geometries such as circular and non-circular ducts under turbulent flow [28-30]. They have also been used in laminar flow [31], with flat plate-fins in rectangular channels [32-34], tube heat exchangers [35], heat sinks [31, 36] and rectangular narrow channels [37, 38].

Though vortex generators can decrease the thermal resistance of a micro-channel heat sink, a key problem is that the pressure drop through the heat sink increases. This can lead to an increase in the cost of driving the forced convection, or increased bypass of the heat sink. One of the aims of this investigation is to develop VGs that offer benefits in heat transfer improvement while minimising the impact of pressure drop.

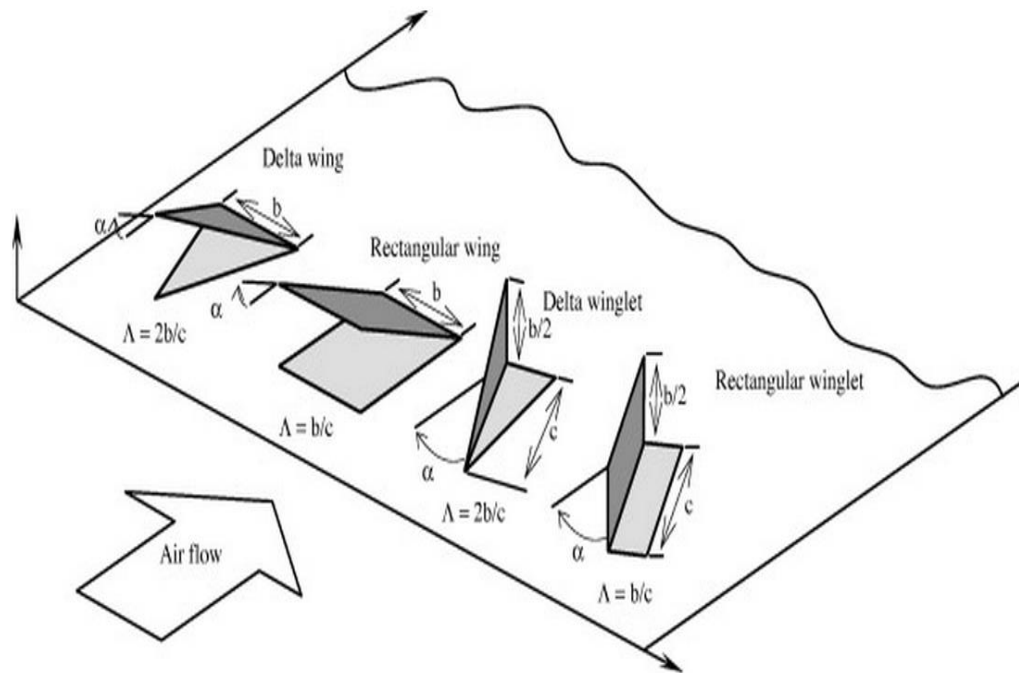


Figure 1.2: Vortex generator types which are suitable for air flows [39].

1.5 Air cooling and liquid cooling

Cooling systems can be classified as direct and indirect [40, 41] based on whether or not the working fluid has direct contact with the electronic chip or component being cooled. As the terms suggest, in direct cooling systems the fluid is in contact with the electronic chip in the cooling process, while indirect cooling system means that there is no direct contact between the fluid and the electronic chip (e.g. when a heat sink is used between the chip and the fluid). Both direct and indirect cooling systems might use a natural or a forced convection method as a way to reject the generated heat from the electronic component, and they are both widely used in cooling systems and can be used with either air or liquid as a working fluid [42]. Rapid developments of electronic chips led researchers of heat transfer and fluid flow to enhance cooling systems. One of the ways to enhance cooling systems might be using liquid instead of air; since much lower flow rates are needed. Nowadays, micro cooling systems using liquid cooling with vortex generators are becoming the focus of research to enhance the heat transfer performance [43]. Thus, liquid is used in this study due to the better thermal properties compared to air, whilst the focus will be on the reduction of the pressure penalty by suggesting new geometries to get the benefit from heat transfer enhancement.

1.6 Nanofluid principles

Another method for potentially improving heat transfer is to modify the working liquid. Recently, rejecting generated heat from microchips has become very critical, therefore suggesting the use of an advanced fluid with better thermal properties compared to conventional fluid such as water, oil and ethylene glycol. Such advanced fluids are called nanofluids [44]. Nanofluids consists of a base fluid and nano-sized particles, and were proposed by Choi [45] in 1995. "Nanofluids" is an eye-catching term in the heat transfer community nowadays [46]. Many review papers and books have illustrated the thermal properties of nanofluids [47, 48]. Different cases have illustrated that the heat transfer can be enhanced by using nanofluids [49], while others have shown that nanofluids are not beneficial [50]. Furthermore, adding small particles of nano-

size (i.e. less than 100 nm) to the traditional fluid leads to improvement of the thermal properties while maintaining the nanofluid stability [51],[52]. However, they have drawbacks like issues of erosion, pressure drop penalty, sedimentation and clogging although this less than for earlier solid-liquid mixtures with larger particles [53].

Improvements to make heat transfer equipment more energy efficient would need to focus on miniaturization on the one hand and an astronomical increase in heat flux on the other hand. Heat transfer fluids such as water, mineral oil and ethylene glycol play a vital role in many industrial processes, including power generation, chemical processes, heating or cooling processes, and microelectronics [54, 55]. Moreover, nanofluids are being developed to achieve ultrahigh-performance cooling and have potential to be next-generation coolants, representing a very significant and far reaching cooling technology for cross cutting application [55, 56].

The benefit of nanofluids in the context of VGs and micro channel will be also explored in this thesis.

1.7 The aim and objectives of this research

The aim of this study is to enhance the heat transfer rate with minimum pressure penalty in a micro-channel heat sink. This can be achieved by using vortex generators (VGs) within the micro-channel to provide an efficient heat transfer system. Furthermore, management of the power consumption caused by the VGs needs to be considered. This can be by suggesting different shapes of VGs. Thus, the objectives of this study are broken down into five objectives:

- To examine the influence of geometry design on heat transfer and fluid flow characteristics using laminar flow with Reynolds number ranging from 100 to 2300 and different shapes of VGs.
- To investigate the impact of the fluid type such as traditional fluid such as water and advanced fluid like nanofluid on the conjugate heat transfer.

- To design a model using traditional fluid to enhance the heat transfer and reduce the pressure penalty.
- To investigate the optimal fluid type for the designed model to provide lower thermal resistance and pressure drop.
- To investigate the energy consumption of the optimal design and fluid type in terms of pumping power and heat transfer enhancement.

Having now given an introduction to micro-channel heat sinks, defined the problem and stated the objectives, the next chapter (chapter 2) provides a wide overview of the relevant literature, while the methodology is illustrated in chapter 3. Following that the results chapters are chapters 4 to 6, with chapter 7 focusing on the energy management aspects of the system explored in the preceding chapter. Finally chapter 9 presents the conclusions and future work suggestions.

Chapter 2: Literature Review

2.1 Introduction

Since 1931, researchers have explored ways of managing the heat flux generated from electrical devices and offering better heat transfer rates using different approaches to enhance the heat transfer in mini and micro cooling systems.

Nowadays, the impact of heat transfer and fluid flow have become more interesting and challenging simultaneously due to rapid developments in electronic and electrical devices and systems which become increasingly small in size, light in weight but high in heat transfer dissipation demands. Therefore, enhancing the heat transfer in such systems has been a strong motivation for this current research [27].

One of the possible and effective approaches to enhance the heat transfer is a design of a heat sink and the most popular heat sinks used in air-cooled systems is a plate-fin heat sink (PFHS) because of its simplicity to manufacture. Many investigations of PFHSs have studied and optimized the fins' height, thickness and separation, yielding predictions of heat transfer and entropy [57-60]. Other designs such as pinned heat sinks (PHSs) have also been considered in both inline and staggered arrangements to enhance the heat transfer rate [61]. They can take several shapes such as rectangular, square [62], circular [63], elliptical, NACA and drop form [64-66]. The key components in the cooling of computer systems, and many other applications such as air conditioning, are heat exchangers and heat sinks [5, 67-69]. Based on the working fluid, heat exchangers are generally classified as gas, liquid, or a combination. Some examples of heat exchangers are shown in Fig. 2.1. Many studies have shown that the liquid heat exchangers and heat sinks systems had great potential for enhancing the heat transfer compared to gas systems based on their thermal conductivity, which is higher in the liquid than in the gas [21, 70].

Continuing developments in electronic and electrical devices, and the increased heat density associated with miniaturisation, mean that the thermal management of high heat fluxes remains an active area of research [3].

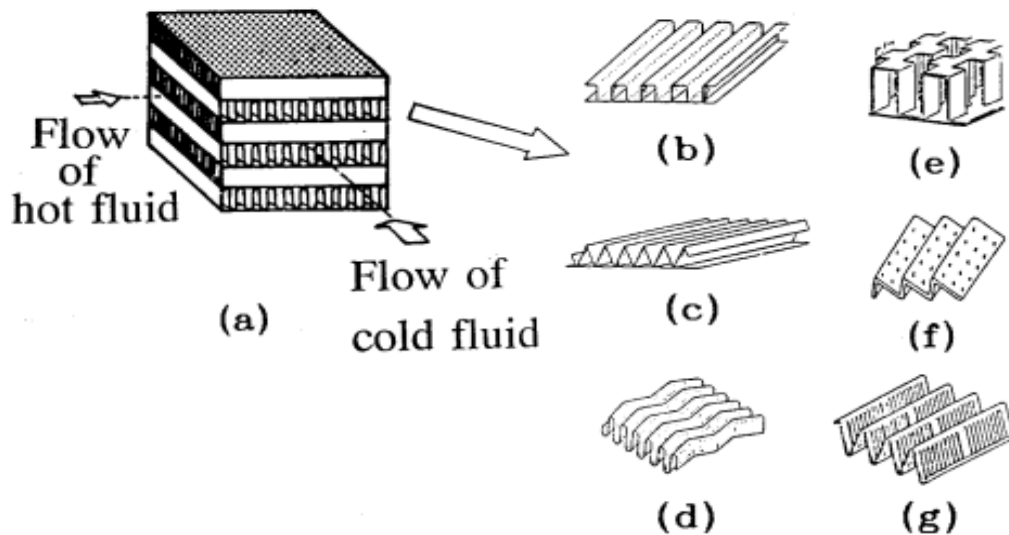


Figure 2.1: (a) Plate-fin heat exchanger and its surface geometries: (b) plain rectangular fins, (c) plain triangular fins, (d) wavy fins, (e) offset strip fins, (f) perforated fins, (g) louvered fins; after Webb [71].

However, another approach to improve the heat performance of the cooling systems is to improve the thermo-physical properties of the coolants, for example by developing nanofluids [55, 68]. Alternatively, the geometry of the heat sinks can be adapted to improve heat transfer, for example by modifying the pins in PHSs or the channels in PFHSs. One very successful approach for air applications is the use of micro-channels. Note that the micro-channels first appeared in 1981 [10].

Many ways by which the heat transfer might be enhanced such as suggestions of new designs of the geometry and/ or advanced fluids can be used. Various geometries were designed to achieve high performance of heat transfer using an extended surface area [72].

Many experimental and numerical studies investigated the heat transfer and fluid flow performance of various modified geometries such as micro-channels

with grooves and ribs [22-25]. The effect of vortex generators (VGs) on heat transfer and fluid flow characteristics were investigated experimentally in 1969 [73].

In addition to the surface area enhancement, vortex generators can be considered as a geometry improvement which creates secondary flows that can enhance the heat transfer [28, 43].

In the revolution of advanced manufacturing processes, VGs can take up various forms such as protrusions, wings, inclined blocks, winglets, fins, and ribs [26, 27], and have been used to enhance heat transfer in different geometries such as circular and non-circular ducts under turbulent flow [28-30]. They have also been used in laminar flow [31], with flat plate-fins in rectangular channels [32-34], tube heat exchangers [35], heat sinks [31, 36] and rectangular narrow channels [37, 38] as shown in Fig. 2.1.

One of the promising systems by which high performance heat rejection can be achieved is micro and mini-scale systems, such as micro-channel heat exchangers and heat sinks [5, 6, 69, 74, 75]. They are different from traditional channels, and can be classified according to their associated hydraulic diameters, D_h , [7-9], as mentioned in chapter 1 (see 1-1).

On the other hand, utilizing advanced fluids instead of traditional fluids (e.g. air and water) has become common and effective. It can be a combination of two fluids like mixing water and glycerine [76] or it can be a suspension of particles in a liquid which is well known as a nanofluid [77].

This chapter is divided into three main sections that consider straight micro-channels, vortex generators, and nanofluids.

2.2 Uniform micro-channels

This section provides an idea of the investigations that have been carried out on a uniform channel. It is divided into two sections namely, single phase flow and two phase flow.

2.2.1 Single phase flow

A numerical investigation of various shapes of rectangular micro-channels with the range of width 44-56 μm , height 287-320 μm and length 10 mm was conducted by Shkarah et al. [78]. The materials used were aluminium, silicon, and graphene. Different values of volumetric flow rate and heat flux with fully developed laminar flow of water were utilized. The results showed that the thermal resistance was reduced by using graphene in the micro-channel. However, the findings have not yet been confirmed experimentally and the numerical method considered the thermo-physical properties of the materials as non-temperature dependent which may affect the results when compared to the experimental setup.

Laminar flow of deionized water in a copper rectangular micro-channel with hydraulic diameter ranged from 200 to 364 μm and length of 120 mm was numerically studied by Lee et al. [79]. The finite volume method was implemented to determine Nusselt number at various aspect ratios. The study presented the distribution of local and average Nusselt numbers as a function of non-dimensional axial distance. The researchers proposed correlations which helped to enhance the heat transfer. The proposed correlations considered the entrance length effect on heat transfer rate, and were in very good agreement with previous experimental studies. It was found that the new correlation was applicable for thermally developed flow for local and average Nusselt number under laminar flow.

Mansoor et al. [80] performed three-dimensional simulations of a rectangular micro-channel using single-phase laminar flow (Re ranged from 500-2000) of deionized water as a working fluid. A heat flux of $130 W/cm^2$ was considered to investigate the thermal characteristics in a copper micro-channel. The study used FLUENT commercial software, and the results were compared with previous numerical and experimental works and showed a good agreement. It was found that the heat transfer coefficient was decreased as heat flux increased. In addition, high Reynolds number and heat flux led to transition from single to two-phase flow, while there was no transition when heat flux was less than $100 W/cm^2$.

An experimental study of a copper rectangular micro-channel with hydraulic diameter in the range of 318-903 μm and length of 24.5 mm was conducted by Lee et al. [81], using deionized water as a working fluid. The study used laminar and turbulent flows, with Reynolds number ranged from 300 to 3500 to investigate the heat transfer and fluid flow regimes using single-phase flow. The results showed that heat transfer was increased as the channel size decreased. However, decreasing the dimensions of the rectangular channel requires more pumping power resulting from increase in the associated pressure drop.

Deng et al. [82] compared a traditional rectangular cross-section copper micro-channel with an omega shape micro-channel heat sinks of the same hydraulic diameter with ethanol and deionized water as two-phase boiling flow as shown in Fig. 2.2. The results showed that water is better than ethanol in both micro-channel types. Moreover, using omega micro-channel decreased the pressure drop compared to the conventional rectangular micro-channel.

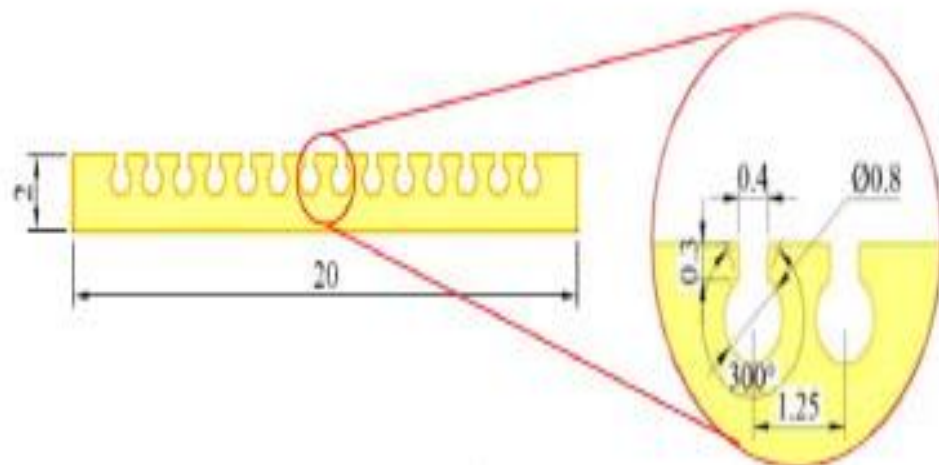
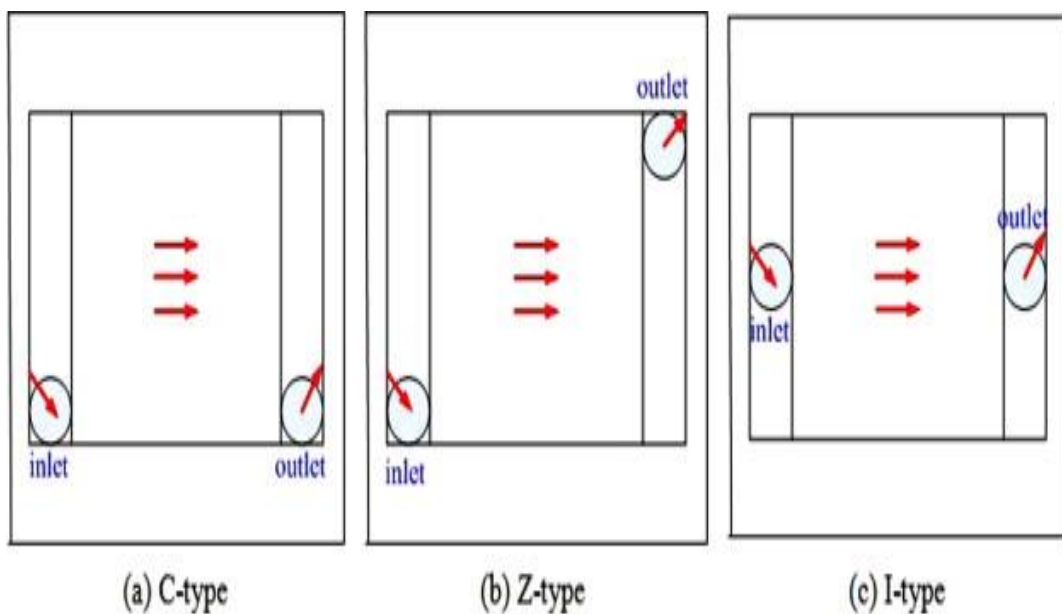


Figure 2.2: Micro-channel omega shape in mm [82].

Micro-channels can be used not only with liquid, but also with gas as a working fluid and Balaj et al. [83] studied the influence of shear stress in micro and nano-channels using constant wall heat flux. The simulation model used the direct simulation Monte Carlo method. It was found that there is a sensible

effect of the magnitude of viscous dissipation on heat and flow performance, therefore, it should be considered in heat transfer predictions. The study has also shown that the heat transfer is significantly enhanced when the heating condition is applied while the heat transfer is decreased while utilizing the cooling condition.

Xia et al. [84] studied numerically heat transfer and fluid flow characteristics of a liquid-cooled heat sink with three different inlet and outlet locations named c, l, and z and different header shapes that feed the micro-channels as shown in Fig. 2.3. The traditional shape of a rectangular micro-channel was compared with a triangular shape. The results showed that the best geometry is the rectangular and the best location of the inflow regime was l, then c, then z. Also, the results shown that better heat transfer characteristics were achieved with the rectangular header shape. However, the results showed that using the position shown in Fig. 2.3 c was the best design when using a volume flow rate of 150 *ml/min*. This is can be attributed to the velocity uniformity compared to the trapezoidal and triangular shapes.



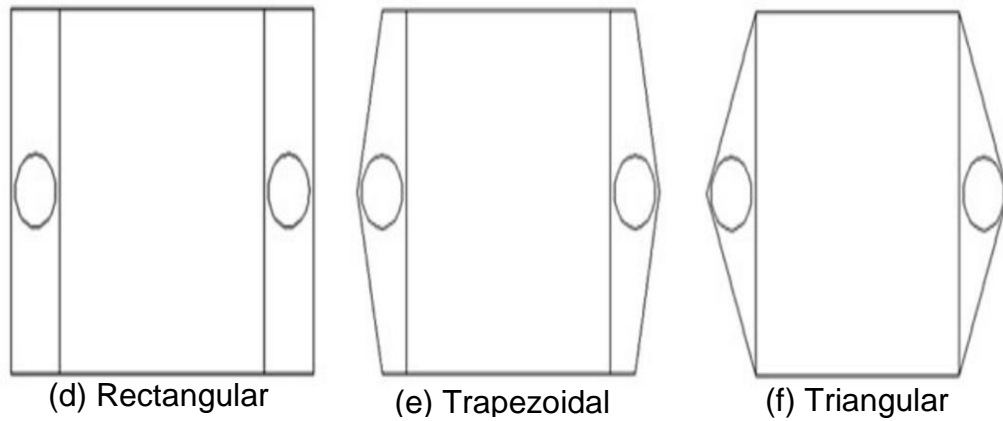


Figure 2.3: Different inlet and outlet positions and header shapes of micro-channel heat sinks [84].

Heat transfer can be enhanced by applying a magnetic field on water based Fe_3O_4 as indicated by the study of Ghasemian et al. [85]. They investigated the heat transfer characteristics of a rectangular channel with a width of 0.2 *cm* and length of 2 *cm* subjected to constant and variable magnetic fields under laminar flow. The finite volume method was used to solve the governing equations and two phase mixture flow was implemented in the study. The results showed that three parameters enhanced heat transfer, namely frequency and locations (a, b) of magnetic fields as shown in Fig. 2.4. Noticeable enhancement of heat transfer appeared at fully developed flow, especially when applying the magnetic field. Moreover, it is found that using an alternating magnetic field was better than a constant one by approximately 1.6 times. Using alternating magnetic field will act as a vortex generator to disturb the fluid frequently.

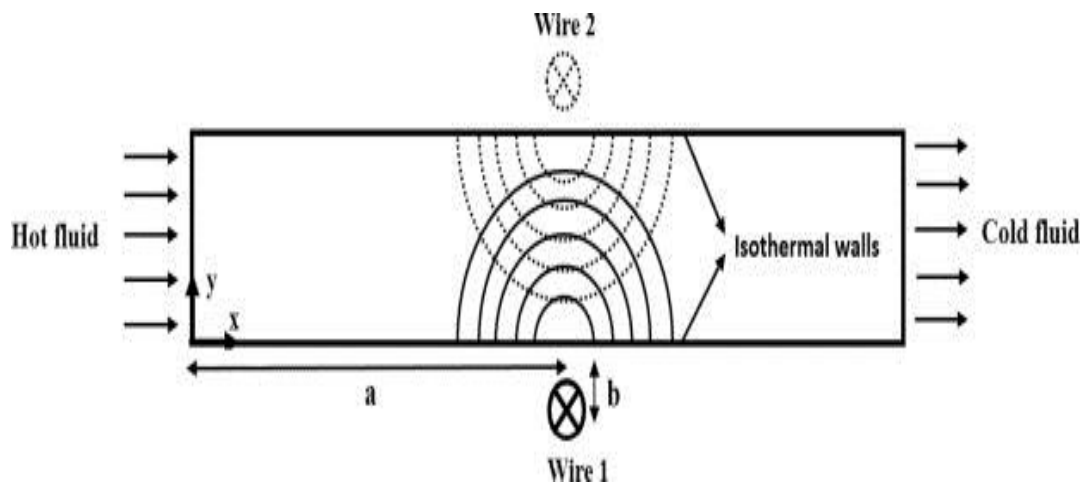


Figure 2.4: Magnetic fields distribution to enhance the heat transfer [85].

A review of numerical and experimental investigations focusing on the heat transfer and air-side flow using a fin and tube heat exchanger was presented by Pongsoi et al. [86]. The study summarises a significant effect such as tube arrangement, operating conditions, and fin configurations. More than 35 articles related to heat exchangers were considered, representing the experimental studies from the very early period. The study used geometry design by comparing circular and spiral fins. It concluded that 57% of the heat exchangers used spiral fin, thus, the recommendation of the investigation was to use spiral fin instead of circular fin in heat exchangers. Moreover, Pan et al. [87] presented the effect of different inlet distribution manifold for different width of rectangular micro-channels. The investigation considered different dimensions of the inlet design of a Z-shape to examine the effect of inlet distribution and the width of the channel on optimal design of a micro-channel. The results showed that the width of the channel had significant influence on optimisation results.

Another review of micro and mini channel geometries is that of Dixit and Ghosh [7]. The study illustrated previous work in a single-phase flow with heat exchangers and heat sinks in various types of flow such as laminar, turbulent, developing flows, and fully developed flow. It also presented the heat transfer performance such as convective heat transfer under the condition of constant wall temperature and constant heat flux. The application and fabrication of micro and nano-scales were also adopted in this investigation. It was concluded that, there is still difficulty to produce channels of micro-size, due to manufacturing limitations, however, micro-channels can be produced as parts, but it is still not easy to combine the parts to produce micro-channels. Many issues can be found when producing micro-channels from parts such as the accuracy of having equal distance between channels. Moreover, the reliability of the glue for a specific application, the conductivity of the glue used to combine the parts, and avoiding having a layer of the glue, might influence the heat transfer performance.

A numerical and experimental investigation of heat transfer and fluid flow performances in a bronze rectangular micro-channel with dimensions of 1 and 0.3 mm was presented by Gamrat et al. [88]. Water as a working fluid with

Reynolds number in the range of 200-3000 was considered to investigate mixed convective heat transfer performance. The results of the numerical study showed that there was no sensible influence on Nusselt number when the channel dimension changed from 1 to 0.1mm. Due to the limitation of the experimental measurement, the impact of this change has not been measured.

Laminar flow in different rectangular copper micro-channels with width and height 231 μm and 713 μm respectively, was studied experimentally and numerically by Qu and Mudawar [89]. Deionized water at Reynolds number in the range of 139- 1672 was considered as the working fluid. Two heat flux values (100 and 200 W/cm^2) were applied on the bottom wall to investigate fluid flow and heat transfer performance. It was found that the outlet temperature of the fluid decreased at high Reynolds number while the pressure drop increased. It was also found that there was not much difference in temperature at the top wall of the micro-channels, therefore, it can be considered as an adiabatic wall.

However, most recent numerical studies considered the top wall (the wall which is opposite the wall where heat flux was applied to) as an adiabatic wall. This is because the low heat transfer at the top wall might transfer from the walls by conduction and the fluid by convection, especially when using a plastic top wall.

2.2.2 Two-phase flow

There are considerable numbers of studies that have been carried out on the design of micro-channels using two-phase model as can be seen in the following paragraphs.

An experimental investigation of heat transfer performance was conducted by Hsu et al. [90] using different orientations of copper rectangular micro-channels with hydraulic diameter of 440 μm , heat flux of 25 kW/m^2 , mass flux 100 and 200 $\text{kg}/\text{m}^2\text{s}$. Two-phase boiling flow and HFE-7100 as a working fluid was considered. The setup investigated the effect of the inclination from the horizontal to the vertical position on boiling heat transfer. It was found that the

heat transfer coefficient rose with the vapour quality and peaked when it reached 0.6 for the upward position.

Suwankamnerd and Wongwises [91] studied two-phase air-water flows in a copper rectangular micro-channel having $267 \mu\text{m}$ hydraulic diameter with low Reynolds number. The setup used a separate flow model as well as a homogeneous flow model to estimate the pressure drop using the Friedrel correlation which is used to measure the pressure drop in two-phase flow. The investigation showed enhancement in Nusselt Number of 120% compared to single-phase flow.

In addition, Mirmanto [92] studied the heat transfer coefficient in various dimensions of a single copper rectangular micro-channel with a horizontal position. Boiling deionized water at $98 \text{ }^\circ\text{C}$ at the inlet as a working fluid, 125 kPa as inlet pressure, 800 kg/m^2 of mass flux, and various values of heat flux were used in this study. The results showed that there was good agreement between the experimental measurements and the numerical simulation especially in the pressure gradient. It was effective at low pressure generated. At fixed heat and mass flux it was found that the heat transfer coefficient went down with the quality in the smallest hydraulic diameter, while it was increased significantly with the other diameters.

Konishi et al. [93] studied the effect of boiling flow on flow and heat transfer maps. The geometry was a copper rectangular channel consisting of two heating walls fixed opposite each other with liquid and mass inlet velocities ranging from 0.1 to 1.9 m/s , and 224.2 to $3347.5 \text{ kg/m}^2 \text{ s}$, respectively; and the temperature of inlet sub-cooling in the range of 2.8 - $8.1 \text{ }^\circ\text{C}$. Heat transfer and fluid flow measurements were adopted to examine flow performance. It was found that the temperature distribution improved as the gravity rose, while it decreased in micro-gravity.

Gan et al. [94] investigated experimentally the pressure drop characteristics of two-phase flow in a triangular silicon micro-channel with dimensions of 300 , 212 , $155.4 \mu\text{m}$ in width, depth, and hydraulic diameter respectively. Acetone was considered as a working fluid under various ranges of inlet temperature and pressure, mass velocity, superheat, outlet quality, and heat flux. The pressure drop and boiling flow were performed. The outcome of the study was

a new correlation which considered the functionality of mass flux, therefore, the error of predicting the acetone data with 12.56% of mean absolute error.

Fang et al.[95] proposed a correlation of flow boiling to investigate the heat transfer regime using a copper rectangular tube. The study adopted H₂O, R718 as a working fluid, two-phase laminar and turbulent flows. More than 1050 data points of water boiling flow for mini and micro-channels were collected. The results showed that the proposed correlation was applicable to many refrigerant fluids especially for R410 and NH₃.

Shojaeian and Koşar [96] reviewed previous experimental studies on micro and nano geometries using boiling flow. These geometries were in various shapes such as rectangular, triangular, and cylindrical cross section. Heat transfer and fluid flow characteristics were presented and compared with different parameters such as single-phase and two-phase flows. It is found that the nano and micro-structures enhanced the heat transfer rate of systems. Furthermore, the manufacturing ability has increased to produce such complex shapes of nano/ micro-channels. Consequently, manufacturing nano/micro configurations had some finishing issues related to the surface. This can be tackled by coating the surface.

Asadi et al. [97] reviewed the validity of experimental correlations on pressure drop and heat transfer characteristics in single and two phase flows with different geometries of micro-channel. The investigation used 219 papers of experimental and numerical studies (from 1982 to 2013). It was found that, before 2003, the researchers focused on experimental and analytical investigations, while after 2003 the focus turned to be on numerical studies. It also indicated that, approximately, 76% of researchers considered the laminar flow using single phase flow. This is because the behaviour of the laminar flow can be predicted and agreed with the experimental data. However, an important factor has not been considered in this study which is the energy consumption of using turbulent flow. For example, using turbulent flow will cost more pumping power to derive the flow resulting in more energy consumption.

In summary, straight micro-channels represented the starting stage in converting from using conventional channels to micro-sized channels in various applications of micro-electrical and micro-electronical chips. As

reviewed in the previous sections, micro-channels have rapidly received high attention by many researchers in different investigations, both numerical and experimental as presented in Fig. 2.5.

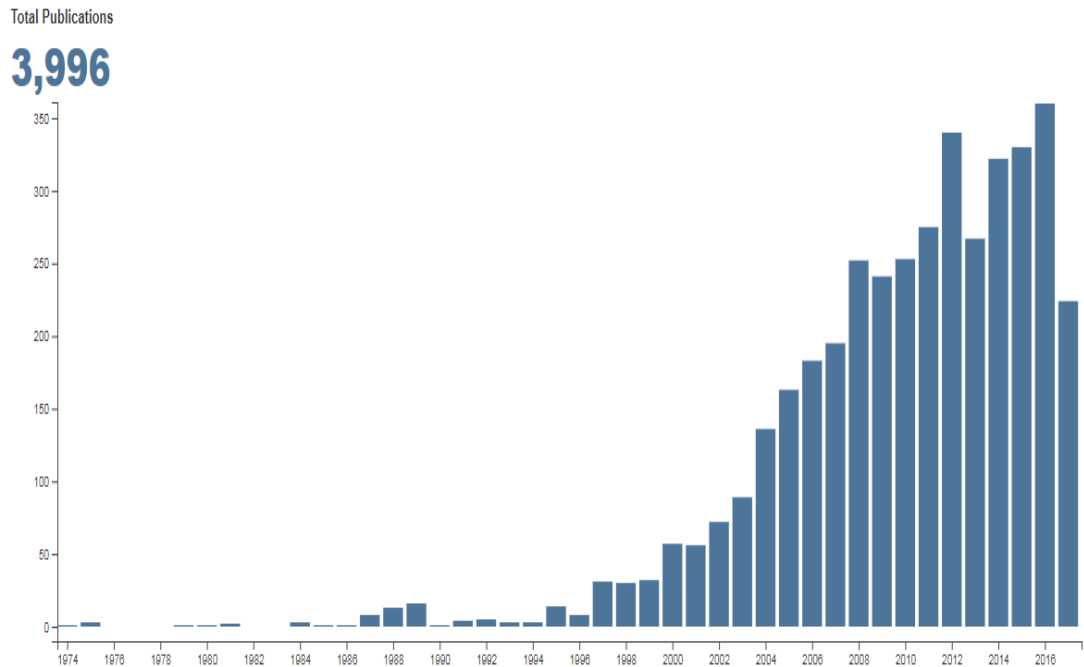


Figure 2.5: Growth in number of publications of micro-channels [98].

The limitation in manufacturing micro-channels was a reason for a reduction in experimental studies. Another reason is the high price incurred to manufacture micro-channels. It is to be expected that in the near future, the manufacturing developments will allow production of the micro-sized channel easily. Therefore, there is a real need to develop the straight micro-channels to have some complex shapes such as zigzag, wavy and curved micro-channels to enhance the heat transfer. In addition, increasing the surface area and developing the secondary flow in the micro-channels also contributes to enhance the heat transfer rate. This can be achieved by adding some objects to increase the surface area and disturb the flow to develop the secondary flow.

2.2.3 Curved and tapered rectangular micro channels

Research on curved micro-channels has also received recent attention by many researchers because of the high thermal and flow performance produced by these geometries as elaborated in the following paragraphs.

Numerical simulation of laminar flow using water as a cooling fluid was done by Guo et al. [99]. They investigated the influence on heat transfer performance of a curved micro-channel with square cross section as presented in Fig. 2.6. This micro-channel had a width and curve radius of 0.2 mm, 30 mm respectively and Reynolds number in the range of 100-865. It was found that at high convection heat transfer, synergy principle method can be applied. Note that this method applied to increase the accuracy of the solution because it considers the heat transfer at the outer wall. This method is applicable for such a curved channels because it presents the heat transfer accurately for the outer walls with consideration of fluid flow.

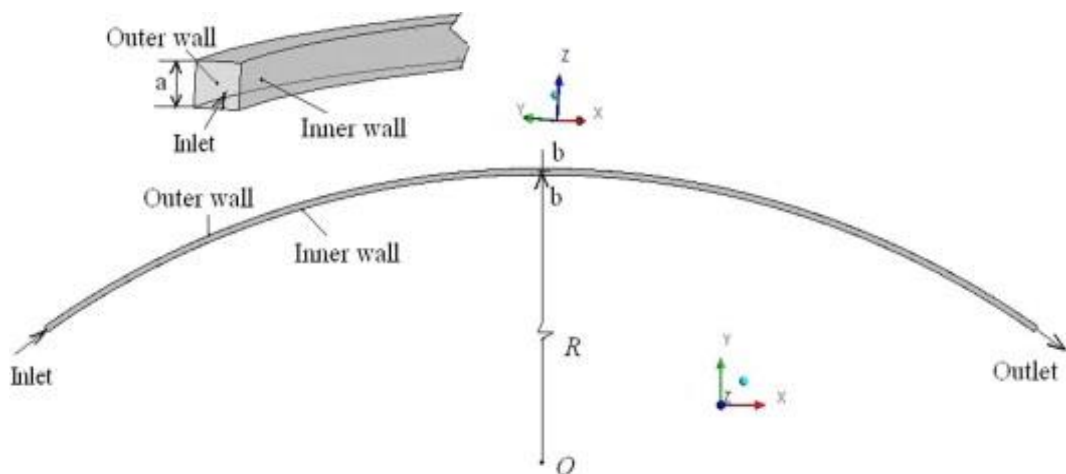


Figure 2.6: Curved duct with square cross sectional area [99].

Chu et al. [100] performed both experimental and numerical investigations of curved rectangular micro-channels with different diameters to study the influence of different diameters of the curve on flow characteristics. Reynolds number was in the range of 80-876 and deionized water as a working fluid was considered. The results showed good agreement between the simulation and experiments. It was found that the curvature of channel geometry

increased the velocity at the outer wall, this leading to enhancement of the heat transfer performance but increase in the friction factor.

A numerical study of a tapered aluminium micro-channel by Dehghan et al. [101] investigated the influence of different tapering geometries on pressure drop reduction using laminar flow and a constant heat flux of 100 W/cm^2 . The width of the channel was fixed at the inlet to be $200 \mu\text{m}$ while the outlet width was in the range of 75 to $200 \mu\text{m}$ with the channel length being $12000 \mu\text{m}$. It was found that Poiseuille number and Nusselt number rose with tapering. The optimum heat transfer characteristics was found at an outlet to inlet width ratio of 0.5 . However, no consideration of the pressure drop in this study, it might be worth to consider the pressure drop effect using the channel inlet which can be taken a range from 75 to $200 \mu\text{m}$.

2.3 Non-uniform channels and vortex generators

The effect of vortex generators (VGs) on heat transfer and fluid flow characteristics were investigated experimentally in 1969 [73]. Two types of vortex generators were classified based on the direction of the axis of rotation of the vortices generated as briefly discussed in chapter one (sec.1.4).

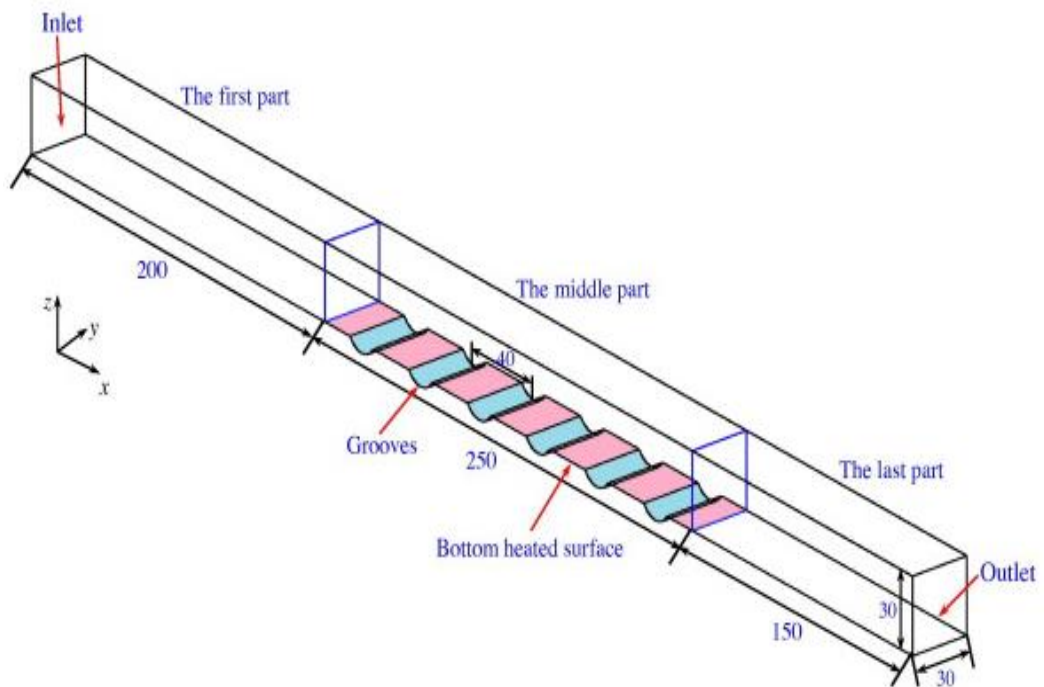
Several parameters such as the geometry, shape, and the position of VGs might play a crucial role to enhance heat transfer, and the VGs shape can be classified into rectangular, delta wings and winglets as presented earlier in [39]. However, the wing and winglet VGs are only suitable for air-based heat sinks. Various investigations have also indicated potential benefits of using VGs with laminar flow at different Reynolds number [37, 43, 102].

2.3.1 Non-uniform channels

Many experimental and numerical investigations have considered geometrical modifications of uniform channels to enhance the heat transfer performance. Liu et al. [103] conducted an investigation of the influence of geometry on heat and flow maps using turbulent air flow in a modified square channel having cylindrical slots of various diameters as shown in Fig. 2.7 a. The finite volume

method was used to solve the governing equations utilizing FLUENT 12.1. The results emphasized that using cylindrical grooves and square ribs in the channel (see Fig. 2.7b) enhanced the heat transfer characteristics compared to the uniform channel due to the extended surface area and the generation of vortices by disturbing the flow. However, the pressure drop of square-ribbed channel was higher than the cylindrical grooves channel and the uniform channel. This study agreed with the results of cylindrical grooves in mini channels done by Tang et al. [104].

(a)



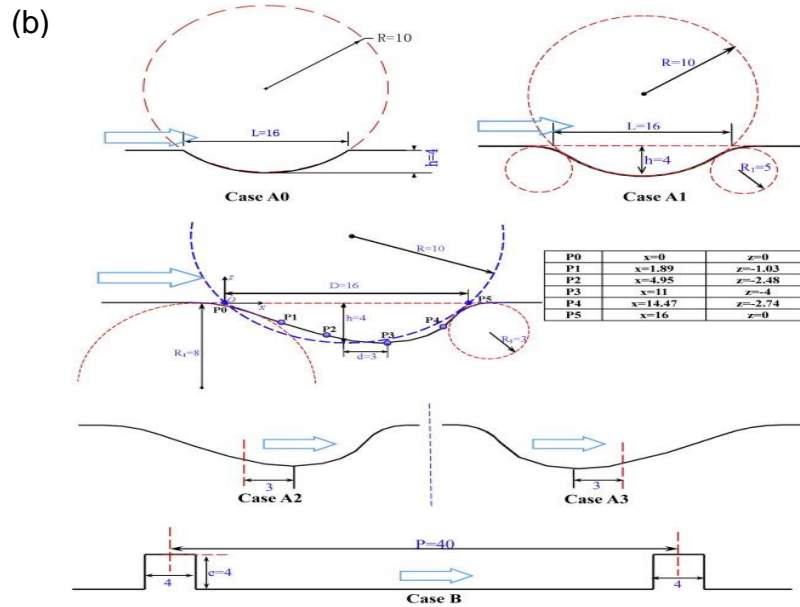


Figure 2.7: Rectangular micro-channel [103]; (a) Geometry description, (b) various cylindrical grooves (cases A0-A3) and square ribs (case b).

Zhai et al. [105] simulated the flow in micro-channels with six types of cavities and ribs in the single micro-channel walls. These were “triangular-cavities with circular-rib (a) (Tri.C-C.R for short), (b) triangular-cavities with triangular-rib (Tri.C-Tri.R for short), (c) triangular-cavities with trapezoidal-ribs (Tri.C-Tra.R for short), (d) trapezoidal-cavities with circular-rib (Tra.C-C.R for short), (e) trapezoidal-cavities with circular-rib (Tra.C-C.R for short), (f) trapezoidal-cavities with trapezoid-rib (Tra.C-Tra.R for short)” as seen in Fig. 2.8. De-ionized water was used as a coolant with Reynolds number ranged from 300 to 600 and a constant heat flux of 10^6 W/m² was applied at the bottom wall of the micro-channel. The finite volume method and FLUENT software was adopted to investigate the flow and heat transfer characteristics. The results showed that using triangular cavities and ribs (see Fig. 2.8f) offered better heat transfer compared to a uniform rectangular micro-channel due to better interaction between the solid and the fluid.

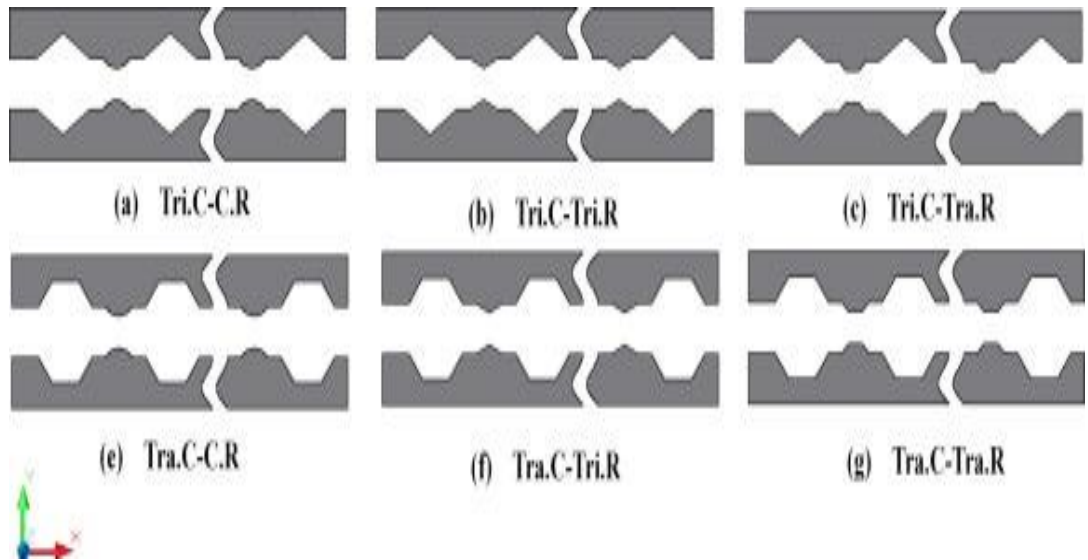


Figure 2.8: Square channel having different ribs and cavities [105].

Knupp et al. [106] proposed a hybrid simulation method to solve the heat transfer and fluid flow characteristics via a single domain strategy and generalized integral transform technique (GITT). This was applied to laminar flow in non-uniform channels as shown in Fig. 2.9. The results showed that the GITT method was suitable to be applied for multiphysics applications found to be in a good agreement with finite element calculation form in the commercial software COMSOL Multiphysics. It is clear that this study agreed well with the literature that using COMSOL Multiphysics provides sufficient agreement with the experiments studies due to the temperature dependent equations implemented in the software, and it is used widely for solving problems, especially those with Multiphysics applications.

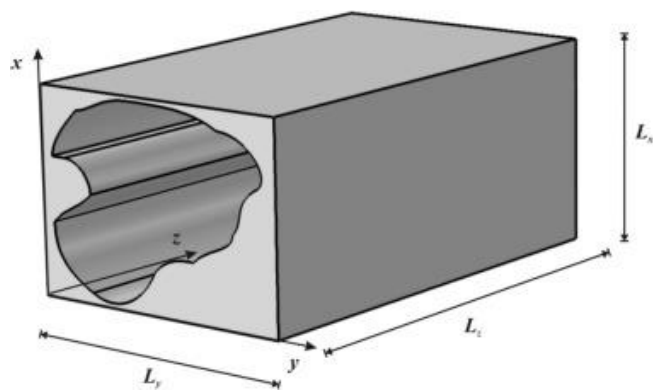


Figure 2.9: Irregular channel [106].

Henze and Wolfersdorf [107] experimentally investigated the impact of tetrahedral VGs on Nusselt number and the flow velocity. The results showed that using the VGs enhanced the heat transfer rate compared to the uniform channel. In addition, it was found that the highest VGs offered highest heat transfer enhancement. It was also indicated, as to be expected, that the heat transfer enhanced with increasing Reynolds number. However, the pressure penalty has not been considered, which determines the pumping power required compared to the uniform channel.

Dai et al. [108] investigated experimentally the influence of zigzag and sine wave micro-channel structures on laminar water flow and heat transfer maps. They used Reynolds number in the range of 50 to 900 with heat flux of 19.1 W. A uniform duct was simulated to understand the behaviour of hydraulic heat transfer. The results showed that the zigzag geometry enhanced heat transfer, while the pressure drop increased.

Karathanassis et al. [109] investigated the heat and flow characteristics in an array of fin plate heat sinks. The geometry was designed to be three sections, for each section, the hydraulic diameter was decreased by increasing the number of plates. The FVM was applied to solve the governing equation of the numerical part, while a closed rig with flow rate ranging from 20-40 ml/s was used in the experimental part. It was found that the heat transfer enhanced in the third section due to the buoyancy. Also the temperature was uniform when Reynolds number decreased. Nevertheless, the pressure drop increased due to increasing the number of plates.

An analytical investigation has been conducted to study the effect of extended surface area in heat sinks with four types of fins that were (a) longitudinal rectangular fin array (LRFA), (b) longitudinal trapezoidal fin array (LTFA), (c) annular rectangular fin array (ARFA), and (d) annular trapezoidal fin array (ATFA), as shown in Fig. 2.10 [110]. The results showed that the triangular fin offered the best heat transfer rate compared to the other three models. It was found that the optimum individual fin was different from the optimum value of heat sink as a component. This is because the individual fin was taken shorter than the fin in the fins array of the heat sink.

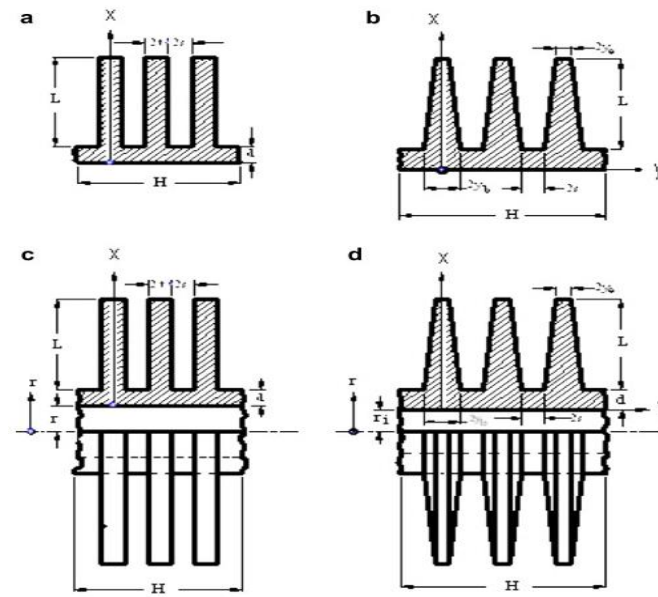


Figure 2.10: Various types of fins (a) LRFA, (b) LTFA, (c) ARFA, and (d) ATFA [110].

Ebrahimi et al. [26] studied the impact of using linear VGs to generate vortices in micro-channel on fluid flow and heat transfer regimes. Different orientations of the VGs and deionized-water under laminar flow were considered to simulate three dimensional geometry utilizing finite volume method. The results showed that Nusselt number rose from 2-25% when Reynolds number ranged from 100 to 1100. However, the friction factor increased by up to 30% when using longitudinal VGs. This friction factor penalty could be acceptable if space were limited and certain heat transfer rate had to be achieved.

Hong et al. [111] sought to improve the uniformity of the temperature distribution in micro-channel heat sinks by considering a heat sink in which the micro-channels formed a rectangular fractal-shaped network. Their numerical analysis of the 3D conjugate heat transfer revealed hotspots in regions where the channel density was sparse, but these could be overcome by local modifications of the channel size. The modified network was found to have lower thermal resistance, lower pressure drop and much improved uniformity in temperature compared to parallel-channel heat sinks.

2.3.2 Cylindrical vortex generators

The above examples show that there are many ideas for geometrical modifications of micro-channels, some of which are rather complex. A somewhat simpler - yet effective - class of geometrical modifications are ribs or cylindrical added to the channel walls, base, or interior. These act as transverse vortex generators, and have been shown to enhance the heat transfer [28, 112-116].

A two-dimensional numerical study by Cheraghi et al. [6] considered a smooth channel with fixed heat flux through the wall sides and an adiabatic cylinder at various locations inside the channel. The Reynolds number was of 100 and Prandtl number ranged from 0.1 to 1. The authors found that the maximum enhancement occurred when the cylinder was fixed half way from the base to the top of the channel. The results also showed that the low Prandtl number had a positive effect on heat transfer enhancement.

Turbulent flow in a channel having cylindrical vortex generators was investigated numerically by Wang and Zhao [117]. It was found that utilizing a cylindrical vortex generator enhanced the heat transfer by 1.18 times compared corresponding the uniform channel. However, this study did not take into account the thermal conductivity of the rib which might distribute the heat to the fluid due to the high thermal conductivity of metals compared to fluids resulting in further enhancement of the heat transfer in micro-channels.

Chai et al. [118] investigated numerically the effects of ribs on the side walls of a silicon micro-channel heated from below and cooled by laminar water flow. The ribs were arranged in an offset manner on both side walls, and had various cross-sectional shapes, namely rectangular, backward triangular, forward triangular, isosceles triangular and semi-circular, each with a protrusion of 25 μm into the channel. For Reynolds number in the range of 190-838, Nusselt numbers up to 1.95 times that of a smooth channel were achieved, with the apparent friction factor increasing up to 4.57 times. Performance evaluation criteria values of 1.02 to 1.48 were found, with forward triangular ribs performing best for $\text{Re} < 350$, and semi-circular ribs for

$Re > 400$. In a further three-part work, the same authors also studied aligned versus offset fan-shaped ribs on the opposite side walls [119-121]. Various other side-wall rib shapes and configurations have also been considered by others, e.g. [122, 123] .

2.4 Nanofluids overview

As remarked in chapter 1, an alternative to modifying the geometry to enhance the heat transfer is to modify the working fluid. The last decade has seen a dramatic increase in the nanofluids, as can be seen in Fig. 2.11. Compared to previous years, it is expected to see more publications this year as the data is for only up to April-2018.

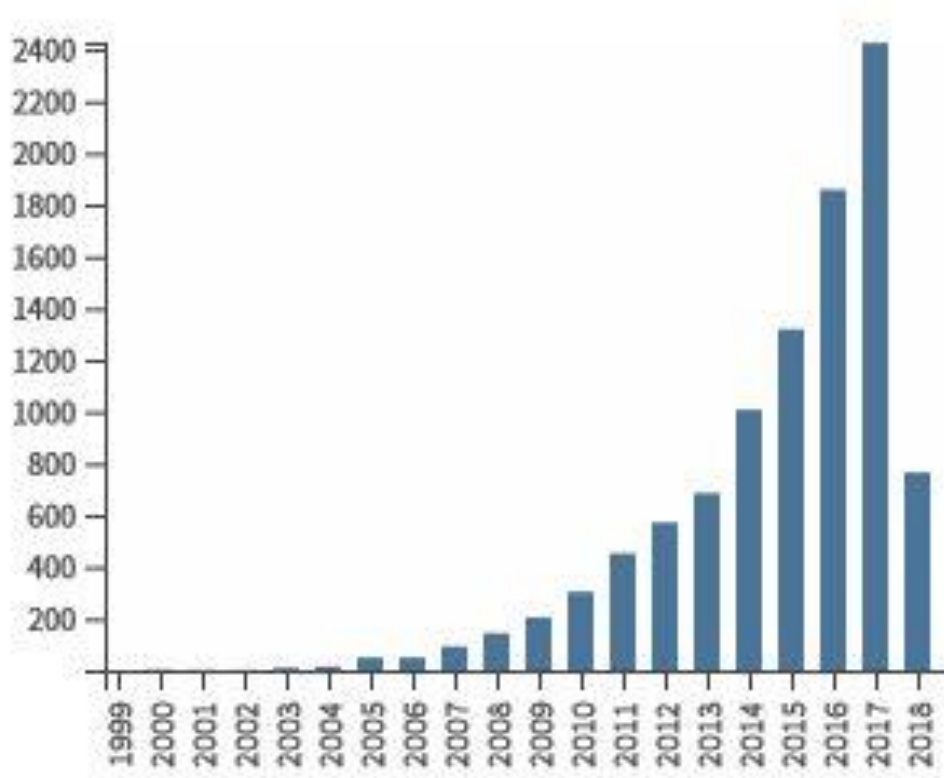


Figure 2.11: Growth of publications in nanofluids [98].

Using nanofluids increases the pumping cost to drive the flow of cooling systems. Thus, researchers have extensively studied the effects of nanofluids on conjugate heat transfer in various ways such as the effect of fluid temperature, nanoparticles shape, clustering of nanoparticles and the effect

of pH (potential of hydrogen). However, the most related factors to this study are explained below.

2.4.1 Nanofluids preparation

A nanofluid is a solid-liquid combination fluid obtained by dispersing nano-sized particles up to 100 nm in a base fluid to improve thermal conductivity of the base liquid [124-127]. Nanofluids can be prepared using several approaches such as single-step method and two-step method.

The single-step method is a direct evaporation method by which nanoparticles are dispersed directly into a working fluid. In 1996, this method was used to prepare Al_2O_3 and CuO nanoparticles by Eastman et al. in Argonne National Laboratory in the USA [128]. The same procedure was employed by Lee et al. [129], Choi and Eastman [130], Choi et.al. [52]. After this Zhu et al. [131] produced Cu-ethylene glycol nanofluid from copper sulphate anhydride ($\text{CuSO}_4 \cdot 5\text{H}_2\text{O}$) and sodium hypophosphite ($\text{NaH}_2\text{PO}_2 \cdot \text{H}_2\text{O}$) reaction under microwave irradiation. This one-step method produced nanofluid with good stability.

In a two-step procedure, the first step introduces an inert gas to produce a dry powder of nanoparticles. Then these nanoparticles are dispersed in the conventional fluid. Li and Xuan [108] used the inert gas method which can produce clean nanoparticles and, as a result, produce a stable nanofluid. However, this method is difficult and expensive for nanoparticle requirements. Consequently, many other techniques may produce dry nanoparticles such as chemical techniques study [132], aerosol spray method [133], metal vapour [134], arc discharge for nano-carbon tubes [135], laser ablation [136], a catalytic process [137], or another successful method called VEROS (Vacuum Evaporation on Running Oil Substrate) method [138]. In this technique, direct evaporation in a vacuum onto the surface of running oil was used to produce nanoparticles in small size (10 nm). However, VEROS technique is not suitable for substances of more than one component like metal oxides and separation of nanoparticles from the fluid is difficult to produce the dry

nanoparticles. VEROS method was modified by Eastman et al. [139], they replaced the oil by ethylene glycol to produce Cu-ethylene glycol nanofluid.

2.4.2 Thermo-physical Properties of Nanofluids

Nanofluids have high thermo-physical properties [140]. As a result of having high thermal conductivity, nanofluids can offer high heat transfer performance compared to the base fluid without nanoparticles. Various considerations of nanofluid properties have been made to evaluate and prepare nanofluids, such as the effect of base fluid, dispersion and distribution [141], particle shape [142, 143], volume concentration [144-147], particle-shell structure [148, 149], and thermal contact resistance [150, 151]. Furthermore, different factors affect the heat performance of nanofluids such as thermal conductivity, density, viscosity and heat capacity.

Nanofluids can be used with different shapes of different channels to enhance the heat transfer, for example, a V shape wavy plate channel was studied numerically using various types of nanoparticles and base fluids [152]. The study used a large range of Reynolds number from 8000 to 20000. The FVM was used to solve the governing equation with the $k-\epsilon$ standard turbulent model to investigate the heat transfer performance. It was found that the best nanofluid was silicon oxide particles in glycerine base fluid to enhance Nusselt number. However, the pressure drop increased using nanofluids. Such studies should consider an optimisation between heat transfer enhancement and pressure drop increase, or a simple optimisation factor such as hydraulic thermal performance also gives an indicate about overall enhancement [153].

2.4.2.1 Experimental data of thermal conductivity

Investigators focused on providing a comprehensive data of thermal conductivity and the factors which play a major role to enhancing the thermal conductivity of nanofluids. They found that the base fluid, nanoparticles size, material and concentration are the most effective parameters. Therefore, Table 2-1 illustrates a brief survey of thermal conductivity studies.

Table 2.1: Heat transfer enhancement using different fluids.

Base fluid	particles	Size [<i>nm</i>]	$\phi\%$	Enhancement
Water [5]	Al ₂ O ₃	30	0.3-2	h>57%, Nu=62%
Water [128]		33	5	29%
Water [129]		24.4, 38.4	4	10%
EG			5	17%
Water [154]		28	3	12%
EG			8	40%
EO			7	50%
Water [155]		38.4	4	24.3%
Water, EG,PO [156]		12.2-302	5	30%
Water [157]		36	10	29%
Water [158]		27-56	1.6	10%
Water [159]		48	1	4%
Water [160]		20	14.5	20%
Water [161]		110-210	1	0%
Water [162]		36, 47	6	28%
Water [163]		8-282	4	18%
EG		12-282	3	16%
Water [164]		36, 47	18	30%
Water	CuO	36	5	60%
Oil			5	44%
Water [129]		18.6, 28.6	3.5	12%
EG			4	20%
Water [154]		23	4.5	12.3%
EG			6	12.5%

Water [155]		28.6	4	36%
Water [156]		29	6	58%
water[160]		33	5	18%
Water [159]		33	1	5%
EG			1	9%
Water [164]		29	3.3	8%
Water [165]		L=50-100	0.4	9.6 %
Water [166]	TiO ₂	10,15*40 rod	5	30, 33%
Water [167]		165	0.72	6.5%
Water [160]		40	2.5	6%
Water [168]		95	2	22%
Water [159]			1	14.4%
Water [169]			3	9.6%
Water [170]	Fe ₃ O ₄	9.8	5	38%
EG [159]	WO ₃	38	0.3	14%
Water [160]	ZrO ₃	20	10	15%
Water [161]		110-250	0.1	0%
Water [161]	SiO ₂	20-40	0.1	0%
Water [171]		12	1	3%
EG [172]	Cu	< 10	0.3	40%
Water [173]		100	7.5	75%
Oil			7.5	44%
Water [174]		50-100	0.1	23.8%
EG [175]	Fe	10	0.55	18%
EG [176]		10	0.2	18%
EG [159]		10	0.55	18%

Water [177]	AG, Au	10-20	0.001	4%
Toluene			0.001	9%
Toluene [178]	Au	2	0.04	1.5%
Ethanol		4	0.03	1.4%
Toluene	Fullerene C60-C70	0.5-0.6	0.8	0%
Mineral oil [178]		10	0.8	6%

Increase in the thermal conductivity of the working fluid improves the efficiency of the associated heat transfer process. However, investigations about the convective heat transfer of nanofluids indicated that the enhancement of heat transfer coefficient exceeds the thermal conductivity enhancement of nanofluids [179-182]. Moreover, other parameters like density, heat capacity, and the viscosity have less effect than thermal conductivity.

2.4.2.2 Theoretical development of nanofluid equations

Investigators have started from the Maxwell equation [183] to predict the thermal conductivity of nanofluids. Improving the Maxwell equation offered better understanding of the behaviour of thermal conductivity since 1935 when Bruggeman [184] reported that high concentration on nanoparticle cannot be neglected. Moreover, Hasselman [185] in 1987 modified the theory of Maxwell considering the size of the of the composite dispersed phase in addition to the volume concentration. However, these studies under-predicted the experimental measurements.

Many investigations have tried to improve the Maxwell equation to produce a modified thermal conductivity equation which offers good agreement with the experimental data. Modern techniques were utilized to enhance the prediction of nanoscale equations such as nanoparticle-matrix interfacial layer [186, 187], nanoparticle Brownian motion [188, 189], and nanoparticle cluster/aggregate [190].

Nie et al. [191] used the exact expression for the heat flux vector of the base fluid plus nanoparticle system to estimate the contribution of nanoparticle Brownian motion to thermal conductivity. It was found that its contribution is too small to account for the abnormally high reported values. The mean free path and the transition speed of phonons in nanofluids were estimated through density functional theory. It was found that a layer structure can form around the nanoparticles and the structure does not further induce fluid–fluid phase transition in the bulk fluid.

In contrast to Nie et al. [152] , Ghasimi and Aminossadati [192] showed that considering Brownian motion would enhance the thermal conductivity. They used CuO-water nanofluid in a right triangular enclosure. The results also reported that heat transfer was enhanced with increasing of nanoparticles.

Xuan and Roetzel et al. [193] suspended ultrafine particles to change the properties and heat transfer performance of the nanofluid, which exhibited a great potential in enhancing the heat transfer. Based on the assumption that the nanofluid behaves more like a fluid rather than a conventional solid-fluid mixture, they proposed two different approaches for deriving the heat transfer correlation of the nanofluid. The effects of transport properties of the nanofluid and thermal dispersion were also included.

2.4.2.3 The effect of base fluid

Base fluid can be water, oils or ethylene glycol. Researchers have investigated the effect of base fluid on heat transfer enhancement for two decades [48, 194, 195].

Xie et al. [196] studied the enhancement ratio of thermal conductivity between the base fluids and nanofluids. They considered three types of base fluid (Water, glycerol, ethylene glycol and pump oil) with α -Al₂O₃ as nanoparticles. The results showed that the water-based nanofluid was the lowest thermal conductivity compared to other nanofluids, while the thermal conductivity of the water itself was higher compared to the other base fluids.

However using nanofluids with water-based nanofluid was most common in many heat transfer and fluid flow applications as it clearly shown in Table 2.1.

2.4.2.4 The effect of nanoparticles concentration

The influence of the concentration is an effective factor to enhance the thermo-physical properties of nanofluids. It is the portion volume of nanoparticles to the base fluid. Many researchers declared that having solid particles in the base fluid would enhance the thermal conductivity of nanofluids, increasing the viscosity and the density of nanofluids [194, 197-202]. Furthermore, nanofluids showed non-Newtonian behaviour when using nanoparticles of more than 5% [182, 203]. However, due to the high thermal conductivity of metallic nanoparticles, they offer the highest thermal conductivity of nanofluids compared to the oxides and non-metallic nanoparticles. Yulong et al. [204] studied the effect of volume concentration on thermal conductivity enhancement. They found that the thermal conductivity enhanced with the nanoparticles as shown in Fig. 2.12.

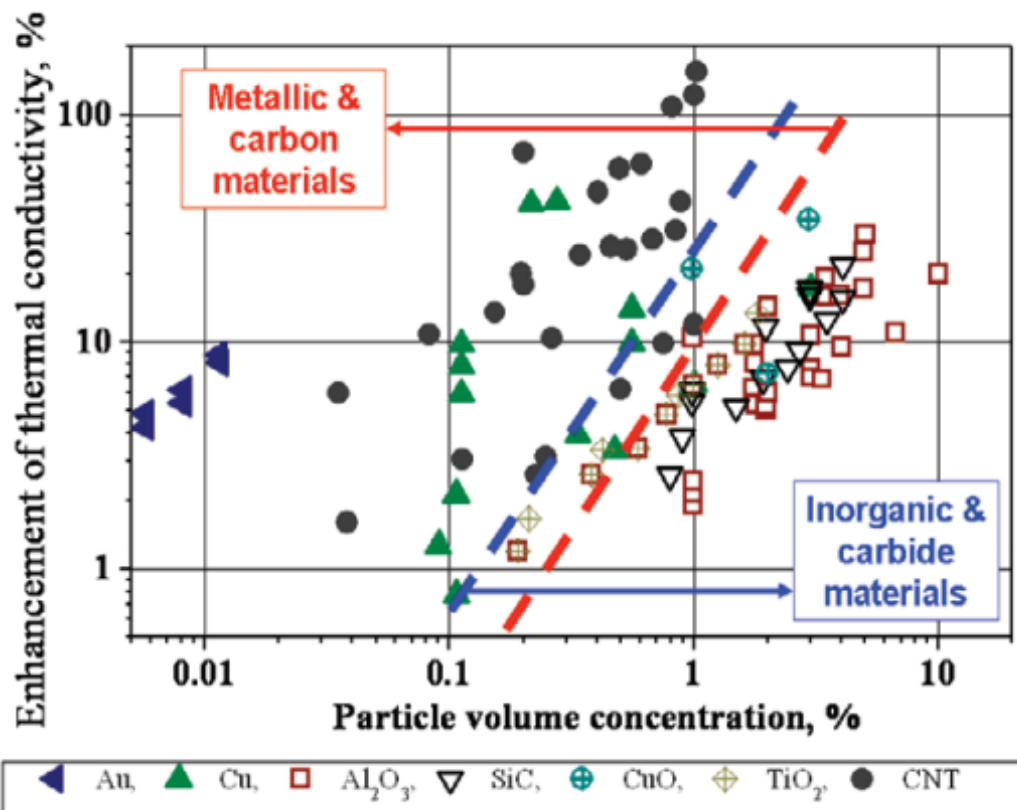


Figure 2.12: The influence of nanoparticle concentrations on thermal conductivity [204].

Another study by Kumar et al. [205] investigated the impact of thermal conductivity and base fluid on conjugate heat transfer. They utilized CuO and TiO₂ up to 1% of volume concentration and different base fluid of water and ethylene glycol under temperature range from 30 °C to 50 °C. The study found that the thermal conductivity enhanced as the nanoparticles concentration increased for both cases, an example is shown in Fig. 2.13. The very famous study on thermal conductivity done by INPBE [206] reported that the enhancement relation between the thermal conductivity and nanoparticles concentration were approximately linear.

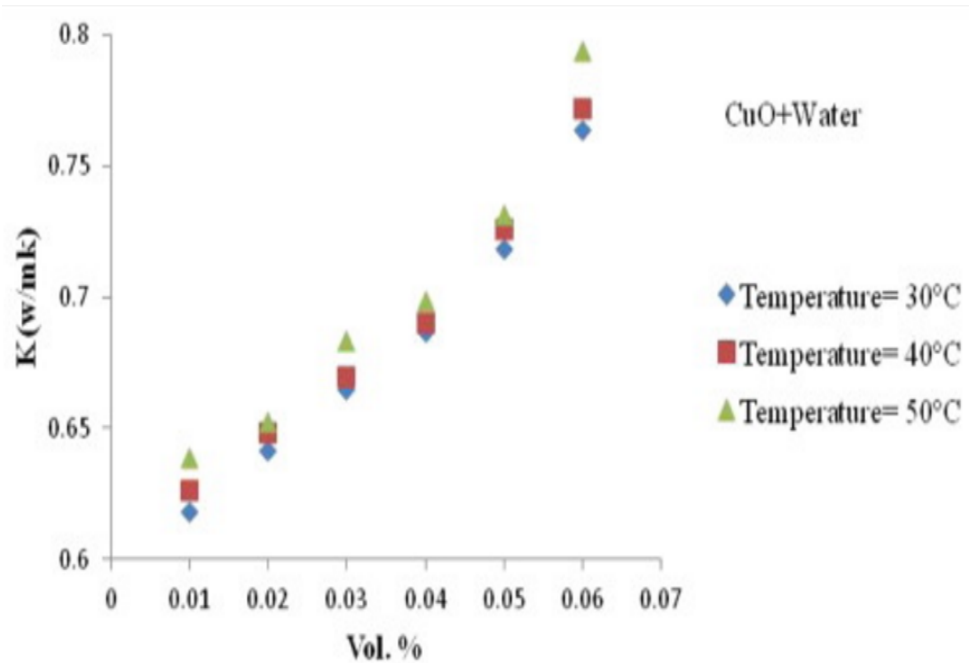


Figure 2.13: The influence of nanoparticle concentrations on thermal conductivity [205].

2.4.2.5 The influence of nanoparticle materials

As one might expect, the nanoparticle material has an effect on resulting nanofluid properties. Nanoparticles can be metallic (Fe, Cu, Ag, Au, Al), carbon or metallic oxide (Fe₃O₄, CuO, Al₂O₃, TiO₂, SiC, SiO₂, ZnO) [207-211]. Metallic oxide and nanoparticles are commonly used with water as a base fluid. This is because the oxides are considered more stable than the pure

metals in fluids. Moreover, the oxygen in the dioxides makes nanoparticles disperse easily and stable in the base fluid. However, Al_2O_3 and SiO_2 / water nanofluids offer the highest heat transfer enhancement among the common nanofluids. Some researches indicated that SiO_2 / water nanofluids offer higher heat transfer enhancement compared to Al_2O_3 / water [201, 212-214], while others report the opposite findings [215-217].

2.4.2.6 Thermal conductivity

Thermal performance of a working fluid can be enhanced by increasing its thermal conductivity. This is because, solid nanoparticles have higher thermal conductivity than the base fluid; for instance, at room temperature, the thermal conductivity of copper is 700 times higher than that of the water. Therefore, adding solid nanoparticles to the base fluid improves the thermal conductivity of the working fluid. A ratio between the nanofluids and the base fluid can be applied k_{nf}/k_{bf} to calculate and evaluate the enhancement of the thermal conductivity of nanofluids. The enhancement of thermal conductivity achieved 40% in some cases, despite of the concentration of the nanoparticles not exceeding 10% [52, 128, 154, 172, 218-220].

In the last two decades some researchers indicated that there was no agreement between the theoretical equations and experimental data in terms of thermal conductivity, while Keblinski et al. [221] reported that most results of numerical and experimental investigations showed good agreement. However, the study of Keblinski et al. [221] was supported by a benchmark study of thermal conductivity done by the International Nanofluid Properties Benchmarking Exercise (INPBE) [206]. INPBE sent samples to 30 organisations worldwide to measure the thermal conductivity. The results showed that the thermal conductivity showed $\pm 10\%$ or less average differences between the experimental data and theoretical equation of thermal conductivity. Nanofluids have high thermo-physical properties compared to the base fluid in terms of thermal conductivity [222-226] and heat transfer coefficient [227-229]. Therefore, theoretical and experimental surveys are presented in the next sections.

2.5 Nanofluid equations

2.5.1 Thermal conductivity:

Modern equations of effective thermal conductivity [230] are presented based on the basic correlation [231] which was developed [232] to be two equations which are static and Brownian thermal conductivity (see eq.2.1). The static thermal conductivity is proposed by [192] (see eq.2.2) as below:

$k_{eff} = k_{static} + k_{brownian}$	2-1
$k_{static} = k_f \left[\frac{(k_s + 2k_f) - 2\varphi(k_f - k_s)}{(k_s + 2k_f) + \varphi(k_f - k_s)} \right]$	2-2

where k_s and k_f are the thermal conductivities of the particles and the fluid respectively.

The Brownian motion thermal conductivity equation [232] is :

$$k_{brownian} = 5 \times 10^4 \beta \varphi \rho_f C p_f \sqrt{\frac{KT}{\rho_s d_s}} f(T, \varphi) \quad 2-3$$

where

$$f(T, \varphi) = (2.8217 \times 10^{-2} \varphi + 3.917 \times 10^{-3}) \left(\frac{T}{T_0} \right) + (-3.0669 \times 10^{-2} \varphi - 3.91123 \times 10^{-3})$$

with K being the Boltzmann constant, T is the fluid temperature, and T_0 is the reference temperature.

2.5.2 Viscosity equation

The viscosity of the nanofluid is approximately the same as the viscosity of a base fluid if containing dilute suspension of fine spherical particles, as shown below [192]:

$$\frac{\mu_{eff}}{\mu_f} = \frac{1}{1 - 34.87 \left(d_p / d_f \right)^{-0.3} \varphi^{1.03}} \quad 2-4$$

$$d_f = \left[\frac{6M}{N\pi\rho_{fo}} \right]^{1/3}$$

where μ_{eff} and μ_f are the viscosity of nanofluid and base fluid respectively, d_p is the nanoparticle diameter, d_f is the base fluid equivalent diameter and φ is the nanoparticles volume fraction. M is the molecular weight of the base fluid and N is the Avogadro number, and ρ_{fo} is the mass density of the base fluid calculated at temperature T=293 K.

2.5.3 The density equation:

The effective density consists of three main parameters which are nanofluid concentration (φ), nanoparticle density ρ_s and base fluid density ρ_f [5]:

$$\rho_{eff} = (1-\varphi)\rho_f + \varphi\rho_s \quad 2-5$$

2.5.4 The effective heat capacity equation:

With Cp_s being the heat capacity of the solid particles, and Cp_f being that of the base fluid, the effective heat capacity of the nanofluid is given by [200]:

$$(Cp)_{eff} = \frac{(1-\varphi)(\rho Cp)_f + \varphi(\rho Cp)_s}{(1-\varphi)\rho_f + \varphi\rho_s} \quad 2-6$$

2.5.5 The effective thermal expansion equation:

The thermal expansion for solid parts β_s and for base β_f fluid with φ can produce the effective thermal expansion as follow [233] [234]:

$$\beta_{eff} = \frac{(1-\varphi)(\rho\beta)_f + \varphi(\rho\beta)_s}{(1-\varphi)\rho_f + \varphi\rho_s} \quad 2-7$$

2.6 Drawbacks of nanofluids

Recent investigations have indicated that there is no benefit in using nanofluids. Moreover, Myers et al. [50] revealed that there is a lack of consistency between the mathematical and experimental studies. The authors also indicated that comparing nanofluids on the basis of non-dimensional parameters such as Reynolds number is misleading in drawing a correct conclusion of the real heat transfer enhancement. Furthermore, Haddad et al. [235] reviewed a natural convection using nanofluids. They indicated that, in numerical studies, the heat transfer was significantly enhanced using nanofluids, nevertheless, the experimental investigations showed the opposite results. However, this study reviewed the natural convection investigations only which can support the opposite results of the experimental studies, because there is perhaps not enough flow to circulate the nanoparticles in the system which lead to augmentation of the nanoparticles in one place of the system. This could cause hot spot zones, then, decrease the heat transfer performance of the system. The reason behind the discrepancy between the numerical and experimental of the same working condition might be the augmentation as the numerical studies do not take this issue into the account.

Another point of using a fixed Reynolds number and a fixed pumping power with nanofluids was highlighted by Haghghi et al. [236]. The results showed that there is no enhancement in heat transfer when using a fixed pumping power with nanofluids. However, using a fixed Reynolds number showed good enhancement of heat transfer. The same findings were concluded by Alkasmoul [237, 238].

Though nanofluids enhance the heat transfer rate, they attract more cost in pumping to drive the fluid [228, 239-244].

2.7 Evaluation of heat transfer improvement

In electronics, the main aim of enhancing a cooling system is to reject the generated heat and keep the electronics working in the range of a limited temperature 85 °C [153]. Recently, optimising the energy to reduce the power consumption of the cooling system has attracted many researchers, the power consumption can be the pumping power of the cooling system or the power reduction after enhancing the cooling system.

To help to evaluate the benefit reuses cost of a proposed modification of a cooling system, a performance evaluation criterion (PEC) index can be formulated which accounts for both change in heat transfer performance and fluid flow effects [245, 246]. The heat transfer term can be Nusselt number or thermal resistance, while the fluid flow term might be the friction factor or pressure drop. This formula can be used to evaluate the performance of the overall enhancement of the system.

Furthermore, the formula could be used to evaluate the performance of modification of the geometry by comparing basic and developed designs such as smooth and modified micro-channel as shown in the equation below [22, 23]:

$$PEC = \frac{Nu/Nu_s}{(f/f_s)^{1/3}} \quad 2-8$$

Where, Nu , Nu_s are the Nusselt numbers for modified and straight channels, and f , f_s are the friction factor for modified and straight channels.

This evaluation method was used by many researchers to examine the performance of proposed designs. Furthermore, it could be considered as a starting point of optimising the whole system.

2.8 Validation of numerical methods versus experimental investigations

Developments in numerical solution methods for heat transfer in system which made them more accurate and closer to the experimental data. For example, considering the temperature dependence of the thermo-physical properties [153]. Many investigations were done to improve the numerical methods such as Bushehri et al. [247]. They proposed a new method to deal with fluid and

solid with an equation utilizing (FVM) CFD software openFOAM with new boundary conditions for the temperature jump and flow slip. The equation was tested against previous works and showed a good agreement. It was applied to a micro-channel heat sink consisting of two parallel plate to investigate heat transfer performance. The results indicated that the heat transfer was accurately calculated using the proposed equation.

Moreover, many studies paid an attention to numerical simulation, because it is important to predict the experimental measurements such as heat flux, temperature, and fluid velocity. Using simulation offered low cost compared to the experimental set up [88]. Many investigations were also developed the numerical methods to be more accurate and efficient, for instance, improving a hybrid finite element method to solve solid-liquid equations of microchannel [11], also modified a technique such as generalized integral transform technique (GITT) for solving coupling equation which showed a very good agreement with the COMSOL Multiphysics® [12].

An example of good agreement between the numerical and experimental studies can be seen in Fig. 2.14. However, using temperature dependent equations for thermal properties give better results than temperature independent equations. This can be seen later in chapter 3 when the temperature dependent equations are used (see Fig. 3.11).

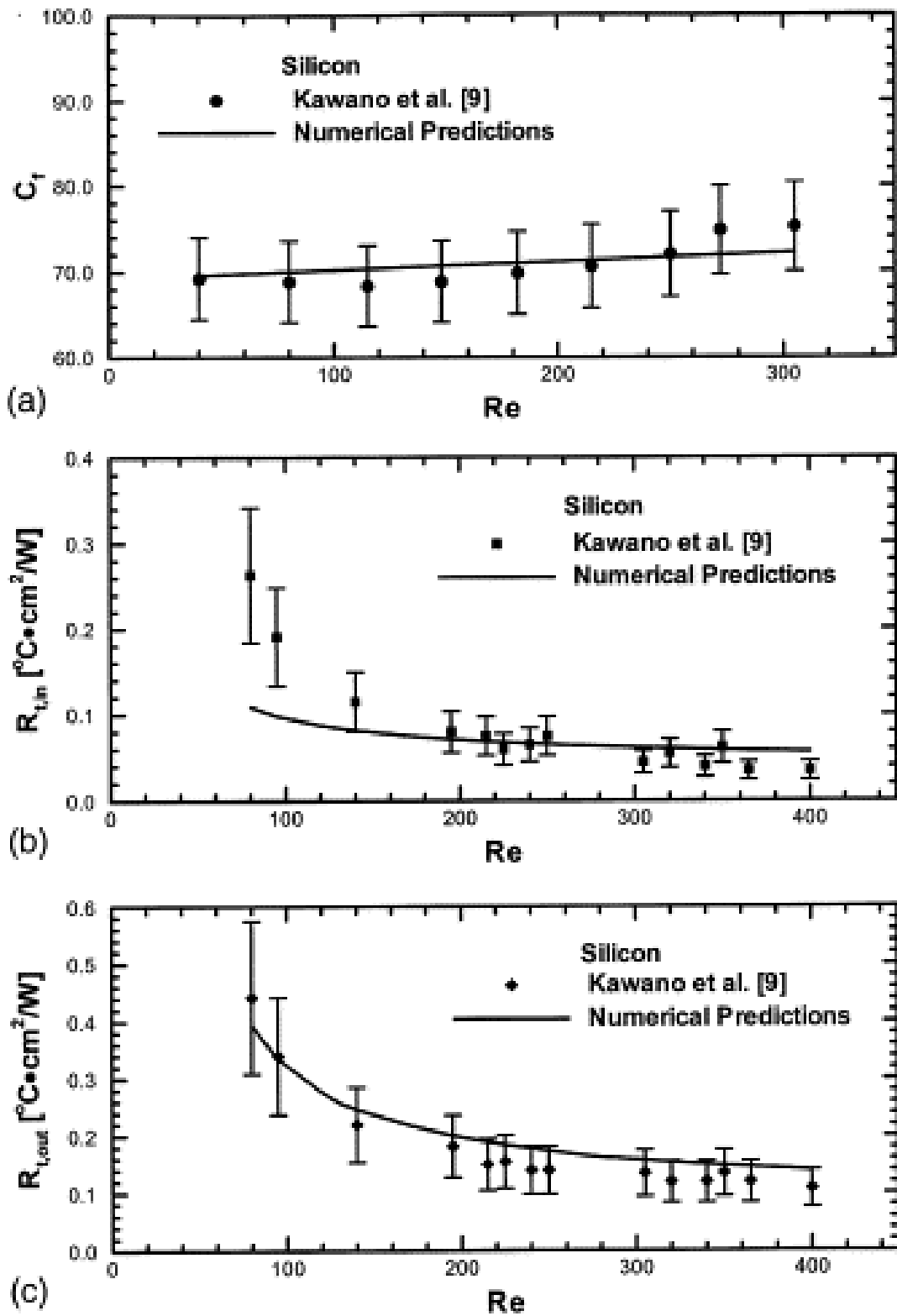


Figure 2.14: Validations between numerical and experiments, (a) friction coefficient, (b) inlet thermal resistance, and (c) outlet thermal resistance.

2.9 Conclusions from the literature

A comprehensive literature review has been provided in this chapter to understand the gaps in knowledge in the available published studies on micro-channel heat sink and nanofluids. Several conclusions can be drawn and they are summarized as follows:

- Applications demands capability to handle high heat flux, therefore, developing liquid cooling systems is increasingly important.
- All studies in the literature indicated that using extended surface area such as ribs or grooves in uniform channels offered better heat transfer enhancements compared to the uniform channels itself. However, there will be a pressure drop penalty caused by ribs and grooves partially disturbing the fluid flow.
- Although are many examples of geometrical modifications that offer some form of benefit in terms of heat transfer, most of these are rather complex.
- So far, simpler cylindrical vortex generators have only explored partially in two recent studies. However, have focused on flow disturbance, treating the VGs as adiabatic objects, and therefore conjugate heat transfer effects have not been precisely considered.
- Nanofluids have been extensively studied in the literature. However, there are still areas of disagreement in terms of the benefit of using them. Although thermal conductivity can be enhanced, the drawback of nanofluids is the increases in pressure drop required to drive the flow.
- SiO_2 and Al_2O_3 –water are generally accepted to be the best nanofluids in terms of heat transfer enhancement. However, comparing SiO_2 and Al_2O_3 nanoparticles in water at the same concentration, some researchers found that Al_2O_3 -water offers better heat transfer

enhancement than SiO₂-water, whereas, others indicated the opposite. However, the maximum percentage of nanoparticle concentrations is 4%.

As presented in the literature there is a gap of knowledge on using micro-channels with liquid coolants. Therefore, last sections of chapter 3 will investigate numerically the common air-based heat sink with water as a working fluid using COMSOL Multiphysics. Before presenting the investigation, it is important to illustrate the methodology of the present study which is presented in the next chapter (chapter 3).

Chapter 3: Numerical method

3.1 Introduction

As discussed in chapter 2, computational fluid dynamics (CFD) has been widely used to explore new ideas in small scale systems involving micro and mini channel heat sinks due to saving cost and time.

Therefore, CFD is also the key tool used in this thesis. All required details of applying CFD technique to investigate the fluid flow and heat transfer performance using micro-channel geometry are presented in this chapter. It is broken down to sections describing and explaining each step of solving the CFD problem starting by giving a background of CFD, the COMSOL Multiphysics® software package, governing equations, the boundary conditions, and ending with a summary.

3.2 Background of CFD

The importance of CFD is to provide an accurate solution at low cost and in less time compared to developing an experimental setup. For instance, modifying the design of a geometry several times using CFD takes much less time and cost than when manufacturing it [248, 249]. In addition, different phenomena combined with a conjugate heat transfer such as chemical reaction can be included to CFD to provide a prediction of solution [250, 251].

Therefore, CFD technique is used in industry widely because of its ability to provide simulations with acceptable error compared to experimental setup as clearly indicated in the literature.

Complex problems such as combined heat transfer and fluid flow in exchanging systems cannot be solved easily using analytical solution. Therefore a numerical approach is required for solving such complex problems. Several numerical methods are known and available such as finite difference, finite volume and finite element. In the current study, finite element method (FEM) is considered to solve the 3-D micro-channel model.

The FEM is a powerful engineering analysis tool that has been widely used in solving science and engineering problems. It first appeared in the 1950s, and is also known as finite element analysis. Basically, FEM cuts the geometry into sub-geometries known as elements. Each element consists of a number of nodes [252]. Over each element, the field variables are approximated as low-order polynomials, for example linear or quadratically. The geometry having all elements and nodes is known as a mesh which is shown in Fig. 3.1

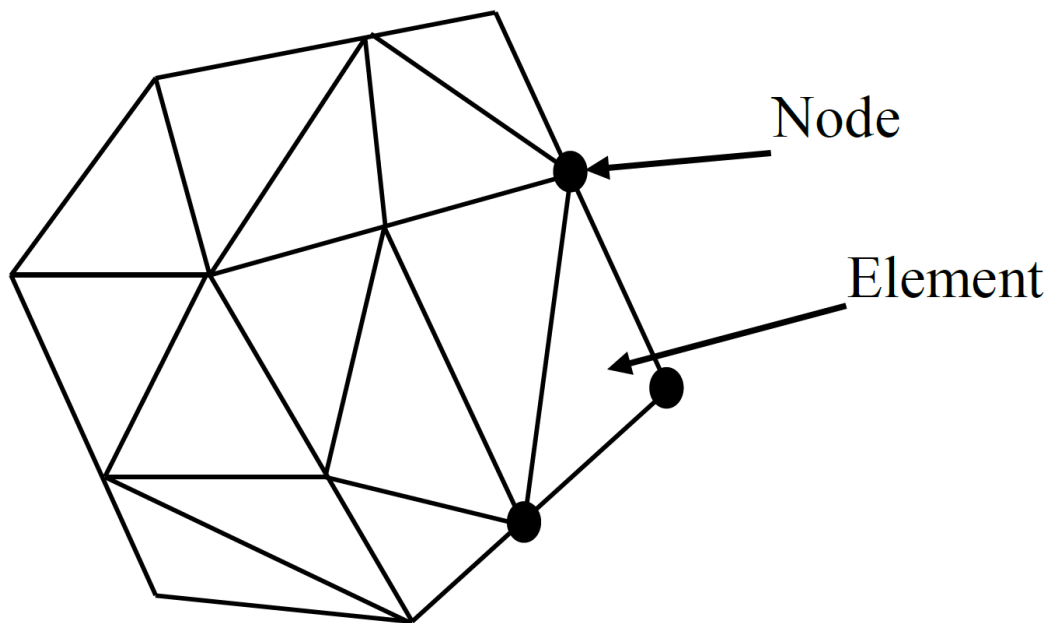
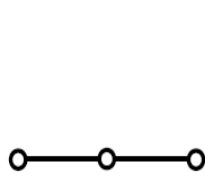
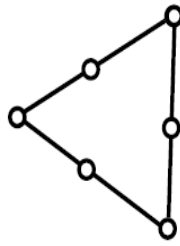


Figure 3.1: Mesh of a geometry having elements and nodes.

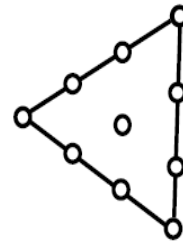
Furthermore, the shape of the mesh depends on the element shape, it can be 1D, 2D or 3D (See Fig. 3.2) which is also related to the dimensions and complexity of the geometry [253].



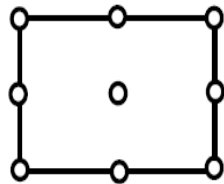
a) 1D
element



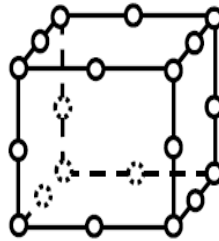
b) 2D 6 nodes
triangular
element



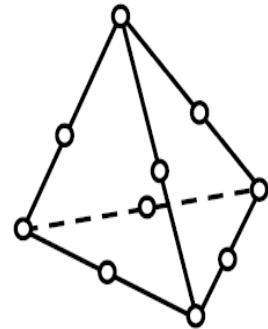
c) 2D 10 nodes
triangular element



d) 2D 9 nodes
rectangular
element



e) 3D
hexahedral
element



f) 3D
tetrahedral
element

Figure 3.2: Types of quadratic one, two and three-dimensional elements [253].

However, the process of solving governing equations using FEM can be described as in Fig. 3.3 [253].

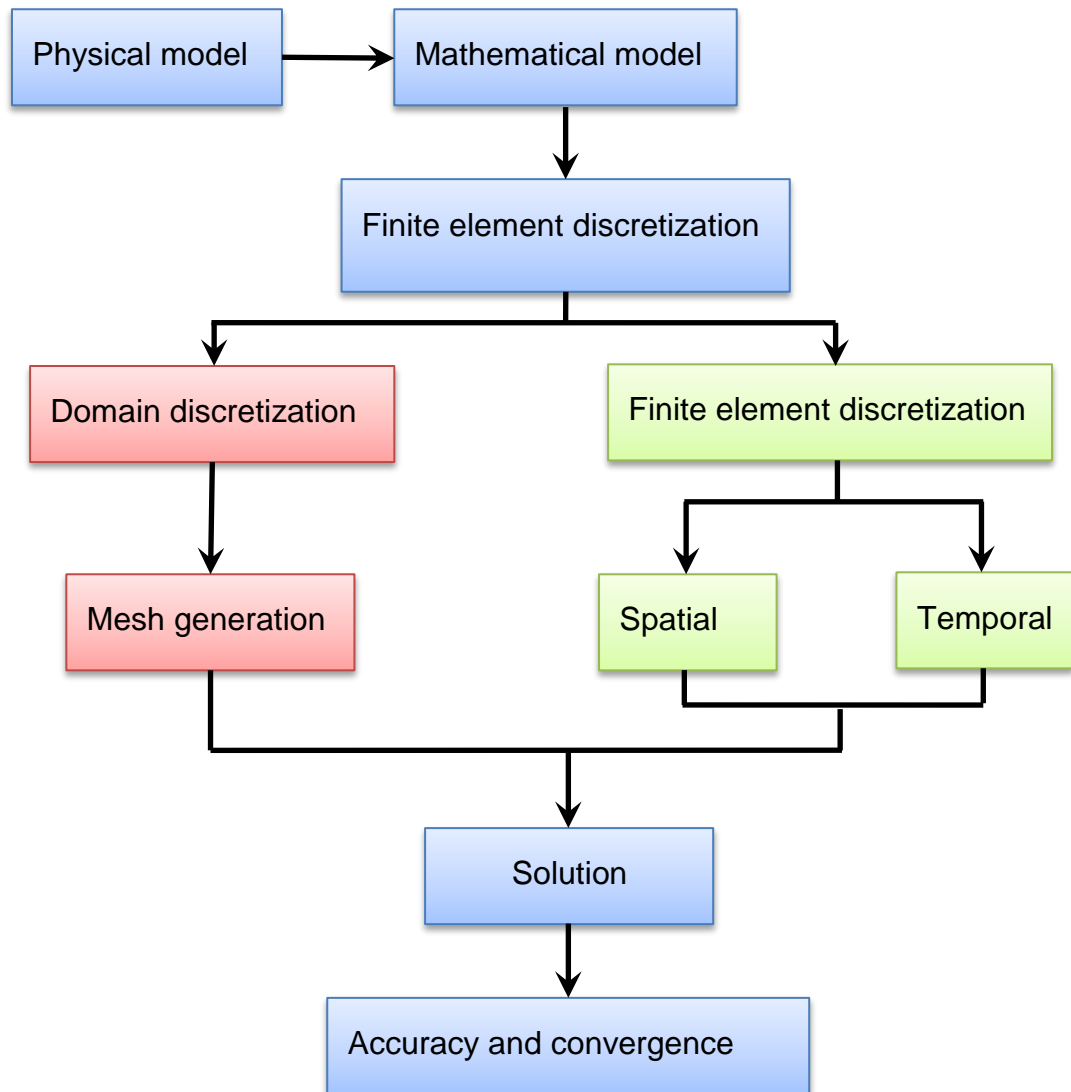


Figure 3.3: FEM process

The general procedure to solve CFD problems using FEM or any other method may have several steps namely, physics scenario, geometry, computational mesh, governing equations, solution algorithm, results and analysis. This procedure consists of three main stages namely, pre-processor, solver, and post-processor, which are connected together as described in Fig. 3.4.

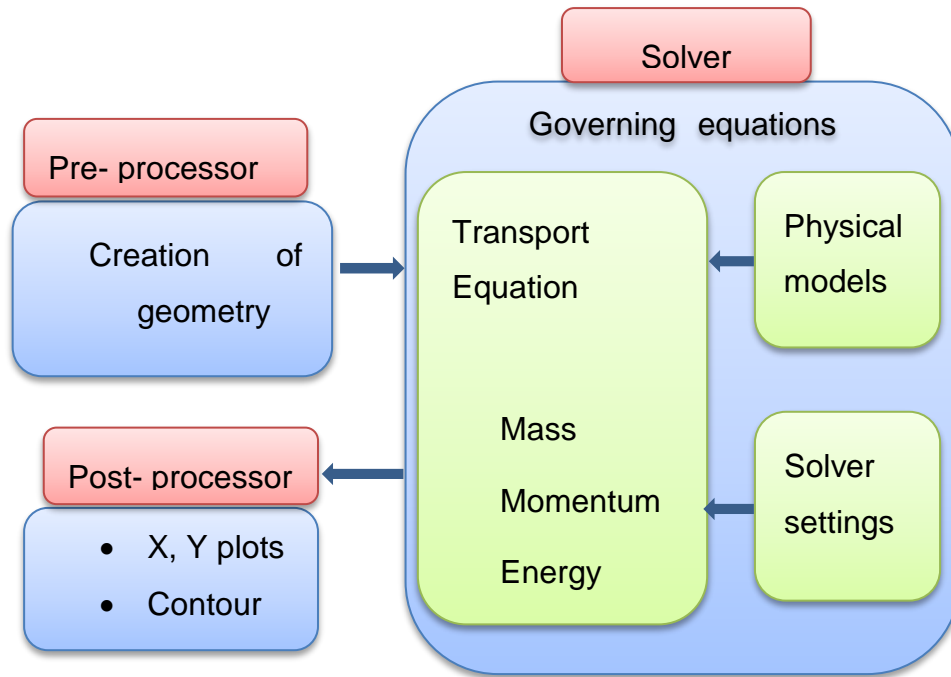


Figure 3.4: The connection between the three stages [254].

Generally, after creating the geometry and generating the mesh, the next stage is to solve the differential equations using a discretisation of FEM. This results in a large set of data giving the velocity, pressure, and temperature values at the mesh points. The final stage is to process this data to generate meaningful visualisations and plots.

3.3 Governing equations

The coolant in the channel is taken to be either water or nanofluid, with temperature-dependent density ρ and viscosity μ , flowing under steady laminar conditions. Gravitational effects are not important in this small, closed-domain forced convection system and, since fluid is Newtonian, the governing continuity and Navier-Stokes equations therefore take the form:

$$\nabla \cdot (\rho \mathbf{u}) = 0 \tag{3-1}$$

$$\rho(T_L)(\mathbf{u} \cdot \nabla) \mathbf{u} = \nabla \cdot \left[-p\mathbf{I} + \mu(T_L)(\nabla \mathbf{u} + (\nabla \mathbf{u})^T) - \frac{2}{3} \mu(T_L)(\nabla \cdot \mathbf{u})\mathbf{I} \right] \tag{3-2}$$

where $\mathbf{u} = (u, v, w)$ is the flow velocity in (x, y, z) Cartesian coordinate space, and p is the pressure. The energy equation for the fluid is

$$\rho C_p \mathbf{u} \cdot \nabla T_L = \nabla \cdot (k \nabla T_L) \quad 3-3$$

where C_p , T_L , and k are respectively the specific heat, temperature, and thermal conductivity of the liquid. Viscous dissipation is neglected since water viscosity is low. The solid parts of the domain are taken to be aluminium, since this is a common material from which heat sinks are made, though some results for copper are also presented in chapter 5. Heat conduction through the solid is governed by

$$\nabla \cdot (k_S \nabla T_S) = 0 \quad 3-4$$

where T_S and k_S are respectively the temperature and thermal conductivity of the solid.

The temperature dependence of the fluid properties is given by the following expressions built in to COMSOL based on experimental data:

$$\begin{aligned} \rho(T_L) = & 838.466135 + 1.40050603T_L - 0.0030112376T_L^2 \\ & + 3.71822313 \times 10^{-7}T_L^3 \end{aligned}$$

$$\begin{aligned} \mu(T_L) = & 1.3799566804 - 0.021224019151T_L + 1.3604562827 \times 10^{-4}T_L^2 \\ & - 4.6454090319 \times 10^{-7}T_L^3 + 8.9042735735 \times 10^{-10}T_L^4 \\ & - 9.0790692686 \times 10^{-13}T_L^5 + 3.8457331488 \times 10^{-16}T_L^6 \end{aligned}$$

$$\begin{aligned} C_p(T_L) = & 12010.1471 - 80.4072879T_L + 0.309866854T_L^2 \\ & - 5.38186884 \times 10^{-4}T_L^3 + 3.62536437 \times 10^{-7}T_L^4 \end{aligned}$$

$$\begin{aligned} k(T_L) = & -0.869083936 + 0.00894880345T_L - 1.58366345 \times 10^{-5}T_L^2 \\ & + 7.97543259 \times 10^{-9}T_L^3 \end{aligned}$$

These temperature dependent equations are valid for water. When water is the working fluid, they are used directly, and when the working fluid is a nanofluid, the above equations are used to provide the base fluid properties required in the nanofluid property equations given in section 2.5.

3.4 COMSOL Multiphysics®

In this study, the COMSOL Multiphysics® package is chosen to solve the problem of conjugate heat transfer based on FEM as a numerical technique. COMSOL Multiphysics® uses the Galerkin method to convert partial differential equations into FEM integral form. Also, COMSOL Multiphysics® has a built-in heat transfer module including all essential mechanisms such as conduction, convection and radiation. Furthermore, it contains capabilities of coupling Multiphysics to consider temperature and velocity fields in parallel with other physics such as chemical reactions or electrical circuits, also it can be used to solve phase change problems [255]. It is appropriate for such problems especially if the geometry is fixed to constant dimensions and the fluid flows in constant volume [256]. COMSOL is widely used to simulate cooling systems as they have a clear interaction between hot and cold surfaces using a combination of Multiphysics.

3.5 Nanofluid equations

As discussed in the literature, this study considers a nanofluid as one modified fluid having different properties from water. However, since the base fluid of the nanofluid is water, the water properties defined in COMSOL Multiphysics® as a function of temperature (see section 3.3) are used in combination with the nanofluid equations presented in chapter 2 (section 2.5) to obtain the nanofluid thermo-physical properties for different nanoparticle concentrations. The resulting values are validated against published experimental measurements – see Tables 3.4 and 3.5 and the results of chapters 6 and 7.

3.6 Geometry description and boundary conditions

The base geometry considered is a single uniform micro-channel with rectangular cross-section, as shown in Fig. 3.5(a). Such channels are common in the heat sinks designed for CPUs (Fig. 3.5b), where they form the gaps between the parallel fins of the heat sink, and that is the application considered here, with the base area of the heat sink taken as $A_s = 6.27 \times 10^8 \mu\text{m}^2$. Within the channel, a number of vortex generators are equally distributed

along the base. These have cross-sections that are either a rectangular, triangular (described in chapter 4) or circular having quarter-circle or half-circle (detailed in chapter 5), or the VGs can be elliptical and circular shape (presented in chapter 7). The micro-channel dimensions are given in Table 3.1.

Boundary conditions play a crucial role in solving the problem of conjugate heat transfer [257]. As indicated in Fig. 3.6, the symmetry of the flow was exploited to reduce computational effort, and symmetry conditions were applied at the left- and right-hand outer boundaries of the domain, corresponding to the centre of the channel and the centre of the wall between two channels respectively. A uniform heat flux was applied at the bottom boundary, as an idealised representation of a live CPU chip requiring cooling via the heat sink. It is assumed that the micro-channels in the heat sink are fed from a header chamber, so at the micro-channel inlet a uniform velocity was imposed. The inlet speed u_{in} was set to achieve the desired Reynolds number, defined in terms of the hydraulic diameter as:

$$Re = \frac{\rho u_{in} D_h}{\mu} \quad 3-5$$

The inlet temperature was fixed at 293.15 K. At the outlet, the pressure was set to zero, and on the micro-channel walls the no-slip condition was applied. On the top boundary, and the remaining walls, adiabatic conditions were applied. Table 3.2 summarises the boundary conditions together with the relevant equations.

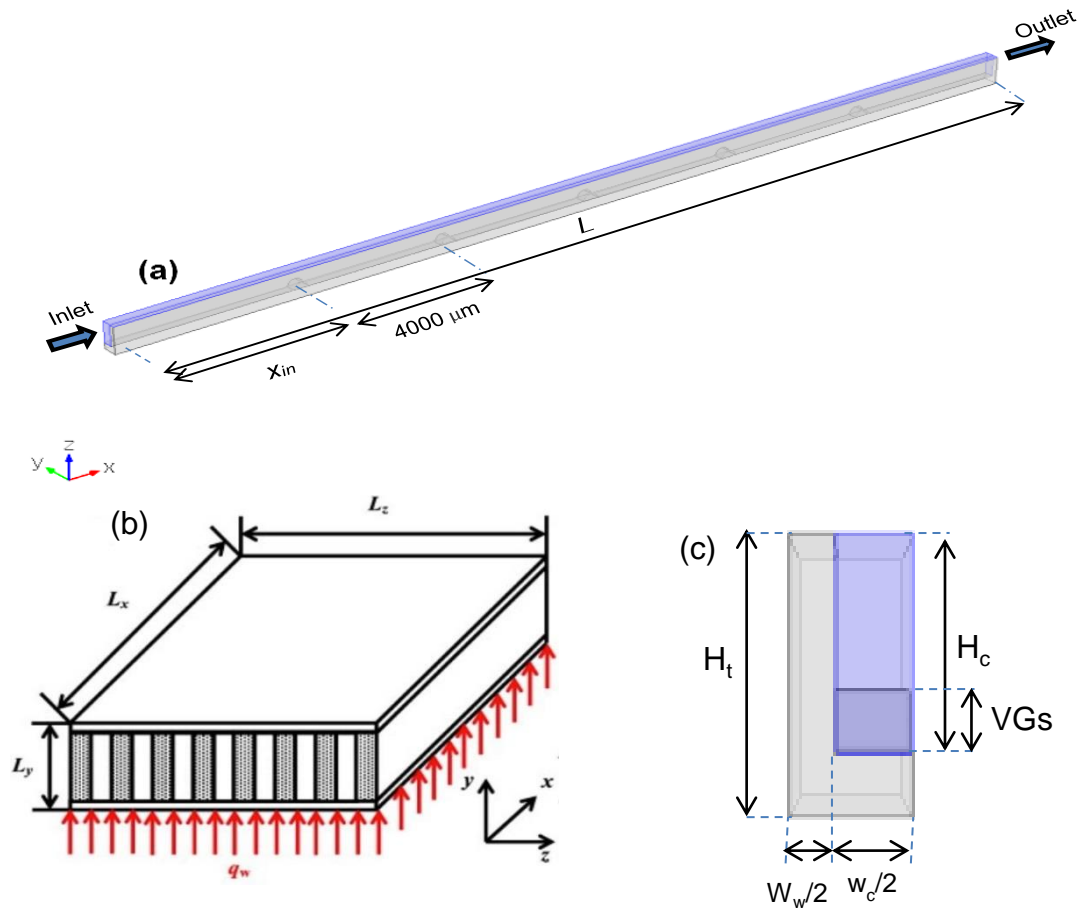


Figure 3.5: Geometry description: (a) rectangular micro-channel containing vortex generators; (b) 3-D view a heat sink comprised of a series of micro-channels [258]; (c) view along the channel showing the definition of parameters governing the dimensions of the geometry.

Table 3.1: Dimensions of the micro-channel and VGs models.

Micro- channel dimensions, μm					
L	25000	H_t	900	H_c	700
W_w	300	W_c	500	x_{in}	4000

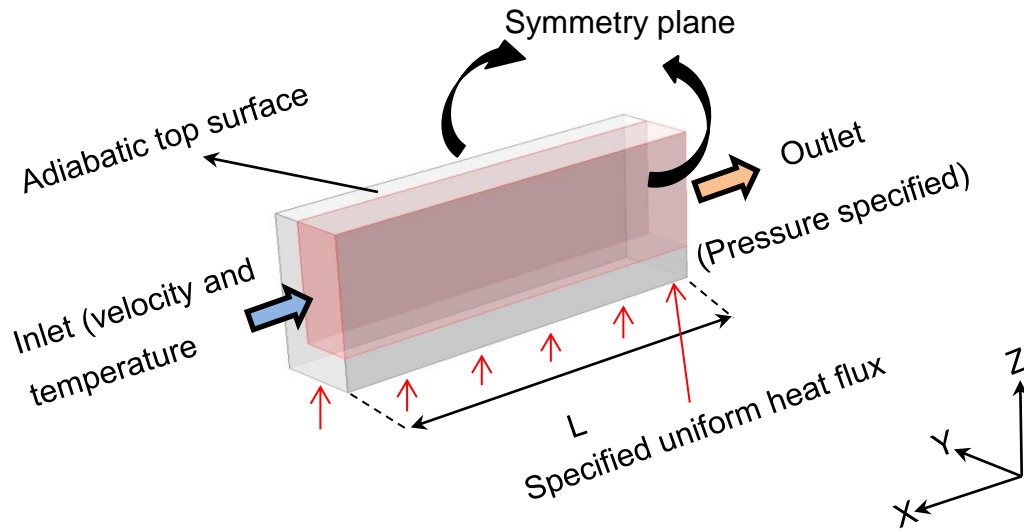


Figure 3.6: The boundary conditions of the geometry.

Table 3.2: The boundary conditions of the conjugate heat transfer model.

Locations	Fluid Conditions	Thermal Conditions
Inlet	$50 \leq Re \leq 2300$	$T_f = 293.15K$
Right and left sides (symmetry)	$\frac{du}{dy} = 0$	$\frac{dT}{dy} = 0$
Top wall and other walls	$\dot{m} = 0$	$\frac{dT}{dz} = 0$
Bottom wall of micro-channel	$\dot{m} = 0$	$\dot{q} = 100W/cm^2$ constant
Pressure outlet	$P = 0$	$\frac{dT}{dx} = 0$
Bottom of micro-channel heat sink	$\dot{m} = 0$	$k_{ai} \frac{dT_{air}}{dn} = k_s \cdot \frac{dT_s}{dn}$

3.7 Heat transfer performance characterisation

The heat transfer performance is quantified by the thermal resistance, defined as:

$$\theta = \frac{T_{ave} - T_{in}}{A_s q} \quad 3-6$$

where T_{ave} is the average temperature on the base surface in the system, T_{in} is the inlet temperature, and q is the heat flux through the base of the heat sink. A thermal-hydraulic performance evaluation criteria (PEC) index [22, 23] is also used to assess the effective heat transfer enhancement provided by VGs, taking into account the penalty paid in terms of the pressure drop. Rather than using the usual average Nusselt numbers and friction factors as the contrasted thermal and hydraulic measures [22, 23], here the PEC index is defined in terms of equivalent directly computed quantities, namely the thermal conductance of the system (i.e. the reciprocal of the thermal resistance) and the actual pressure drop. Hence the PEC index is defined as:

$$PEC = \frac{\theta_s / \theta}{(\Delta P / \Delta P_s)^{1/3}} \quad 3-7$$

where ΔP and θ are the pressure drop and thermal resistance in a microchannel containing VGs and ΔP_s and θ_s are the same quantities in the corresponding smooth (i.e. uniform) micro-channel.

The mass flow rate (\dot{m}) and the pumping power (P_p) used in this study are presented as:

$$\dot{m} = \rho u_{in} A \quad 3-8$$

$$P_p = u_{in} A \Delta P \quad 3-9$$

Where u_{in} is calculated based on the equation of Reynolds number (3-7), A is the cross sectional area of the inlet of the microchannel ($H_c * W_c$, see Table 3.1), and ΔP is the pressure drop.

3.8 Mesh sensitivity and code validation

Equations (3-1)-(3-4) were solved simultaneously using the finite element software COMSOL Multiphysics® version 5.2. A grid independence test was applied on both smooth channel and a VG-enhanced channel to assess the density of mesh required. For the smooth channel, five meshes were used, labelled as 'coarser', 'coarse', 'normal', 'fine', and 'finer', with number of elements 53554, 145869, 283944, 788230, and 2831904 respectively, and Fig. 3.7 shows the average temperature calculated using each mesh. As can be seen, the 'fine' mesh provided the best run time while ensuring mesh independence of the solution. Therefore, the standard fine 'physics-controlled' mesh was used as the base mesh. This was then modified to accommodate the VGs micro-channel models, and mesh sensitivity checked again with a sequence of increasingly finer meshes 'M1' to 'M5'. Using the maximum temperature as a measure, Fig. 3.8 confirms the suitability of mesh M1. The M1 details are modified to be 100 elements as the maximum size, while the minimum size is 10 elements. The growth ratio is 1.15 (very fine at the contact of the liquid and solid surfaces inside the channel).

To ensure the accuracy of the results, two simulation models were compared with previous numerical studies. The first validation model was compared with Shkarah et al. [78], who modelled a graphene micro-channel within a heat sink using the finite volume-based software FLUENT. Figs. 3.9 and 3.10 show a comparison of the present COMSOL simulations with the published calculations, with the inlet temperature set at 300 K, the flow rate at 8.6 cm³/s, and the heat flux at two values: 181 and 277 W/cm². Good agreement is seen between the two approaches. The second validation was with Abdollahi and Shams [259]. They investigated the impact on conjugate heat transfer of using rectangular vortex generators with various orientations and their inclination in a channel, with water as the working fluid. The validation was done with the

present study and showed good agreement, using an angle for the VG of 45° , a heat flux of 1 kW/m^2 , and values for Reynolds number of 233 and 350 as shown in Table 3.3.

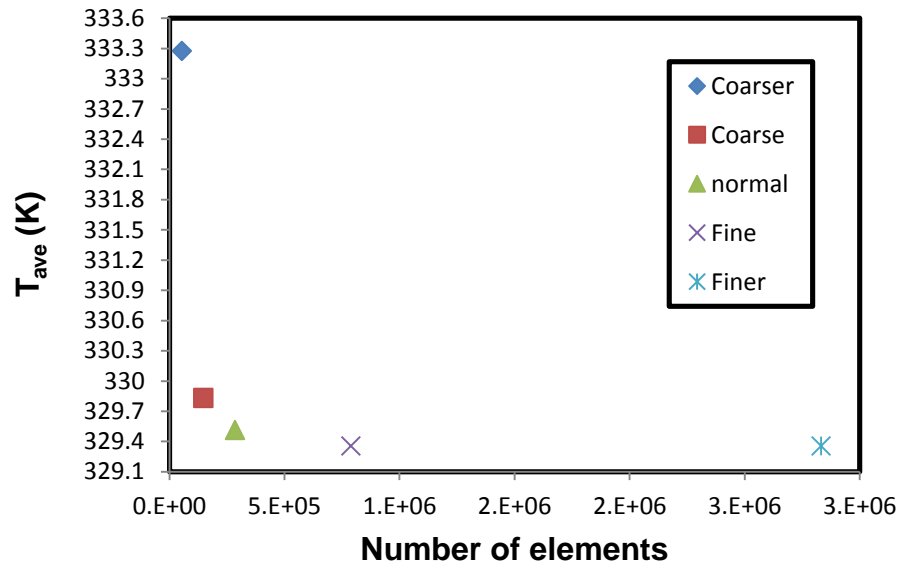


Figure 3.7: Grid independence test for a smooth channel, showing the maximum temperature calculated using increasingly refined meshes, with $q = 100\text{ W/cm}^2$ and $Re = 600$.

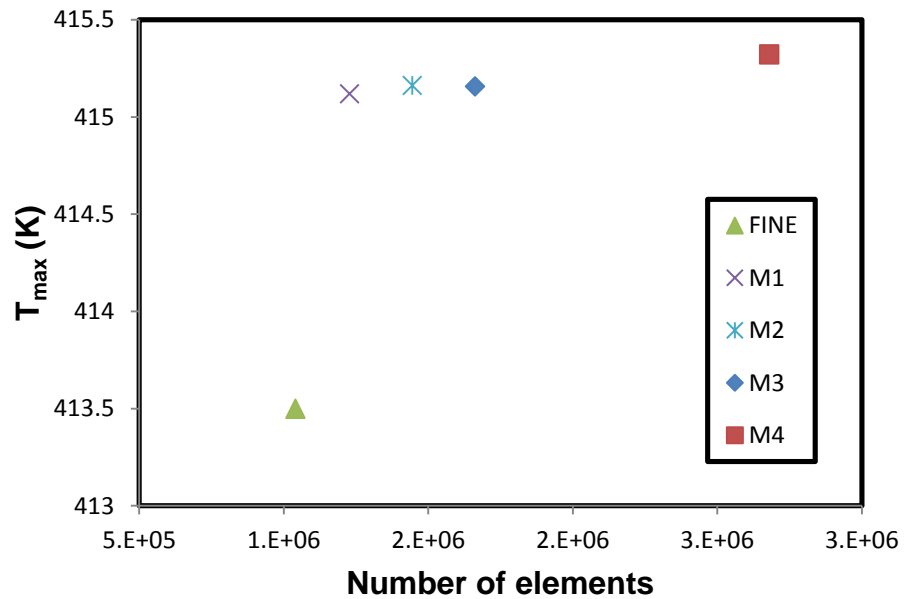


Figure 3.8: Grid independence test for micro-channel with VGs; $q = 100\text{ W/cm}^2$, $Re = 100$.

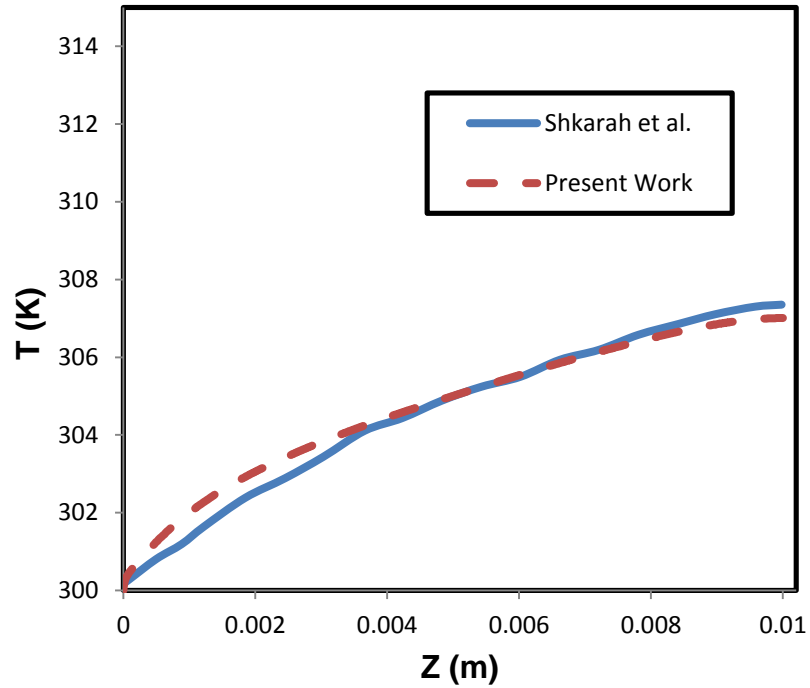


Figure 3.9: Code validation by comparison of calculated temperature distribution along a graphene micro-channel with heat flux 181 W/cm² and flow rate 8.6 cm³/s [78].

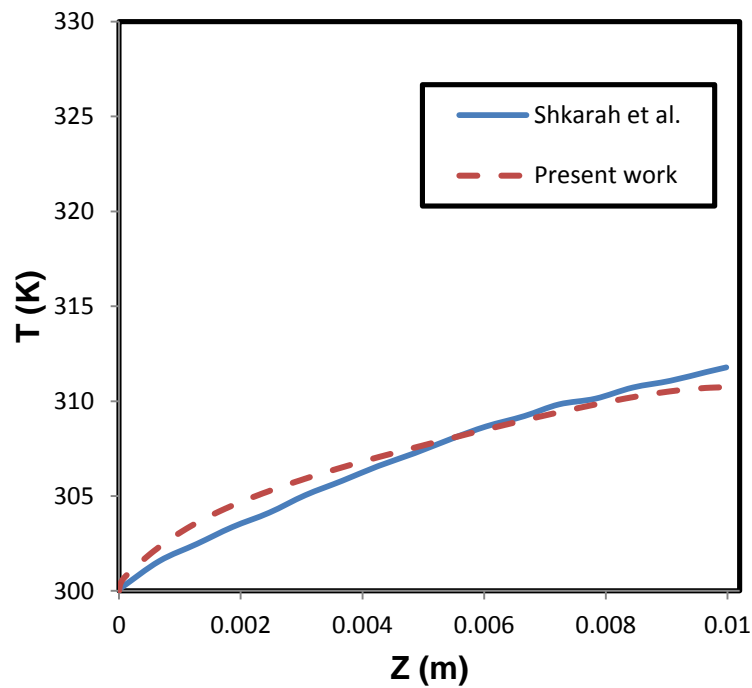


Figure 3.10: Code validation by comparison of calculated temperature distribution along a graphene micro-channel with heat flux 277 W/cm² and flow rate 8.6 cm³/s [78].

Table 3.3: Code validation with Abdollahi and Shams [259].

Angle of VG	45°	45°
Re	233	350
Heat flux	1kW/m ²	1kW/m ²
T (K) present	307	305
T (K) [259]	306.362	305.617

Another validation for a uniform channel consists of comparison with two further investigations. The first study was an experimental investigation of a straight micro-channel done by Kawano et al. [260]. The second validation was against numerical study presented by Qu and Mudawar [261]. Both studies used the same material (silicon) and the height, width and length of the micro-channel were 180 μm , 57 μm , 10 mm respectively. The top of micro-channel was subjected to a uniform heat flux of 90W, while the side walls were set to be symmetry, and the bottom wall was adiabatic. Laminar flow was used in the studies, with Reynolds number ranging from 80 to 400. To validate the present computational method, the same system was modelled and the resulting calculations of the thermal resistance (calculated in this instance as $R_{th, out} = (T_{surface, Max} - T_{fluid, in}) / q$) are shown in Fig. 3.11. As can be seen, excellent agreement with the experiments is found.

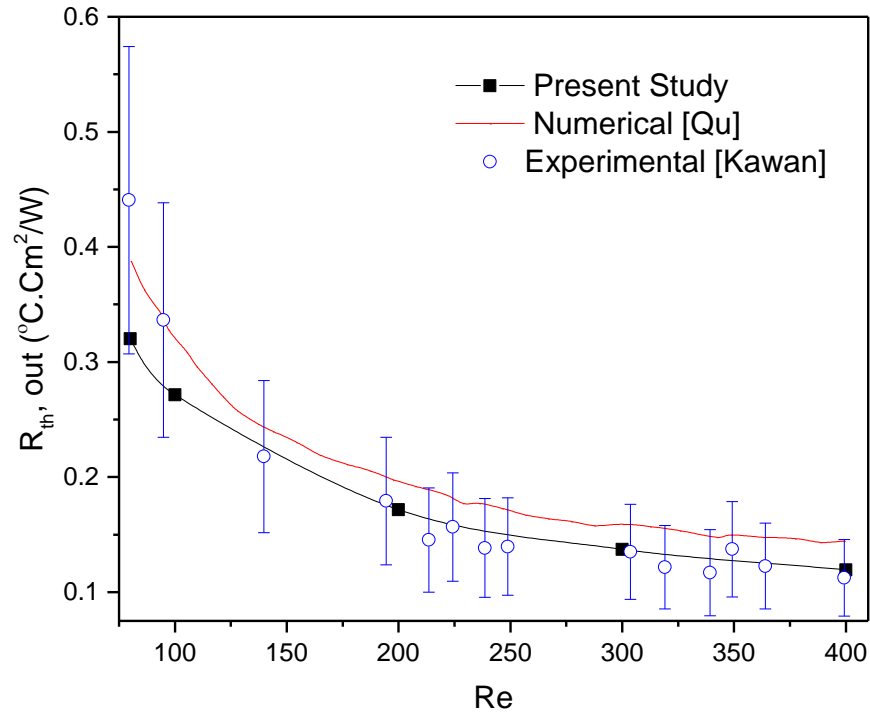


Figure 3.11: Validation of the present model against experimental data of Kawano et al. [260] and alternative numerical results of Qu and Mudawar [261].

3.9 Experimental and numerical validation of nanofluids

To ensure the validity of numerical equations (2-1 to 2-7), a validation of nanofluids thermo-physical properties between the experimental measurement of a study which was done by Ahmed et al. [262] and the numerical equations adopted here is shown in Table 3.4. A spherical shape of nanoparticles with 25 nm solid particles diameter was considered. Furthermore, different concentrations of nanoparticles were utilized in the water as a base fluid to produce the thermo-physical properties of nanofluid with 0.5% and 1% volume fraction. Two types of nanoparticles were mixed with the base fluid to present two nanofluids namely, SiO₂ water and Al₂O₃ water.

Table3.4: Comparison of predicted nanofluid equations with experimental work at 20° C [262].

	Al ₂ O ₃ -water						SiO ₂ - water									
	0.5%			1%			0.5%			1%						
	[1]	Present	[1]	Present	[1]	Present	[1]	Present	[1]	Present	[1]	Present				
comparison																
ρ (kg/m ³)	1010.101	1013.062	1025.021	1027.921	1001.011	1004.212	1007.023	1010.221	9.15×10 ⁻⁴	9.5×10 ⁻⁴	0.001105	0.001105	0.631397	4105.1	4106.432	
μ (pa.s)	1.02×10 ⁻³	0.00105	1.04×10 ⁻³	0.001105	0.612	0.634312	0.625	0.631397	0.612	0.634312	0.625	0.631397	4105.1	4106.432		
k (W/m.K)	0.6422	0.66881	0.649	0.675586	4142.8	4144.089	4105.1	4106.432	4142.8	4144.089	4105.1	4106.432	4105.1	4106.432		
Cp (J/kg.K)	4113.9	4115.243	4048.9	4050.222	4142.8	4144.089	4105.1	4106.432	4142.8	4144.089	4105.1	4106.432	4105.1	4106.432		

Table 3.5: Thermo-physical properties of nanofluids used in this study at the inlet temperature (293.15K)

SiO₂-water properties at different concentrations				
Concentration(ϕ)	ρ (kg/m ³)	μ (kg/(m*s))	k (W/(m*K))	C _p (J/(kg*K))
0.5%	1005.6	0.001	0.596	4148.8
1%	1011.6	0.001	0.598	4111.2
2%	1023.6	0.001	0.602	4037.2
4%	1047.6	0.001	0.610	3894.3
Al₂O₃-water properties at different concentrations				
0.5%	1014.5	0.001	0.602	4120.0
1%	1029.4	0.001	0.609	4054.9
2%	1059.0	0.001	0.624	3930.4
4%	1118.4	0.001	0.656	3701.1
Base fluid properties (water)				
ρ (kg/m ³)	μ (kg/(m*s))	k (W/(m*K))	C _p (J/(kg*K))	
998.2	0.001	0.589	4185.1	

3.10 Preliminary Investigation of perforated pinned heat sink

Before going on to explore liquid micro-channels, vortex generators and nanofluids in later chapters, this short section presents a brief preliminary study of an air-cooled heat sink. The purpose is to investigate whether geometrical modifications that are effective in enhancing the performance of air-based system also work when the coolant is switched to a liquid. This section is considered as an example to apply the methodology used in chapters 4 to 7.

The system in question is a common pinned heat sink (PHS), consisting of a square horizontal and vertical cylindrical pins in a regular array. Al-damook et al. [263] have recently shown that perforations in the pins have a beneficial effect on the performance of heat transfer and fluids flow. Here, the same system is modelled with water replacing the air, to evaluate how effective the design modifications are for water coolant.

3.10.1 Geometry description

The perforated PHS adopted from Al-Damook et al. [263] is shown in Figs. 3.12-3.14. The thermal performance of this model is examined using water in laminar flow (instead of the air for which the system was originally developed).

The base of the heat sink is taken to be 5 cm, 5 cm and 0.2 cm of length, width and thickness, respectively, while the pin height is 10 cm.

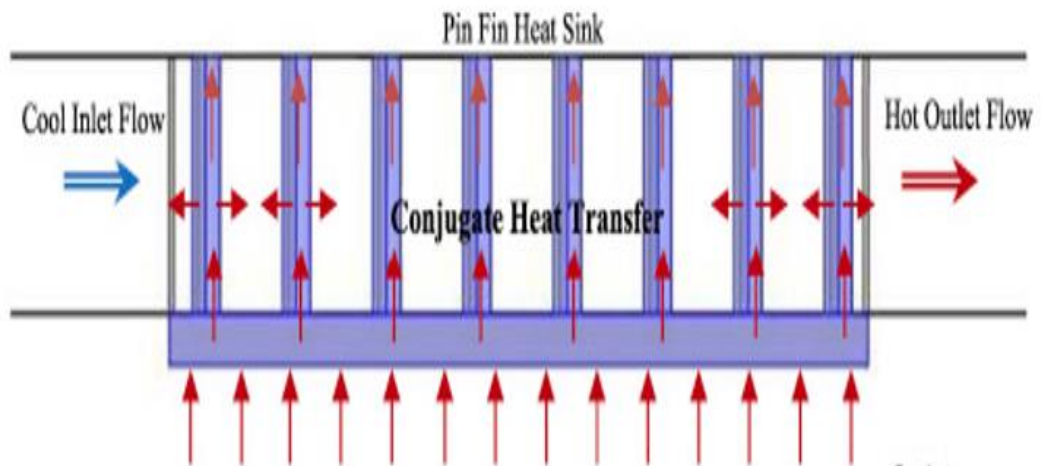


Figure 3.12: Pinned fin heat sink.

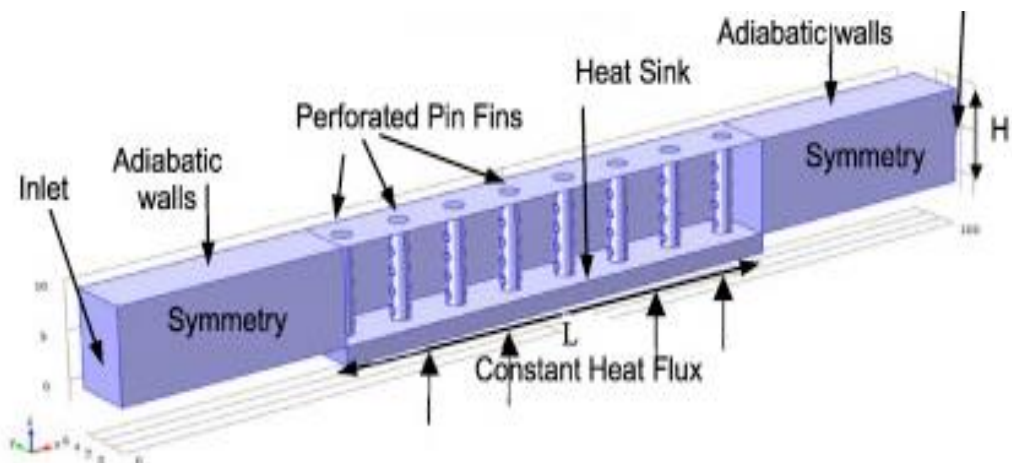


Figure 3.13: Boundary condition of perforated pinned heat sink.

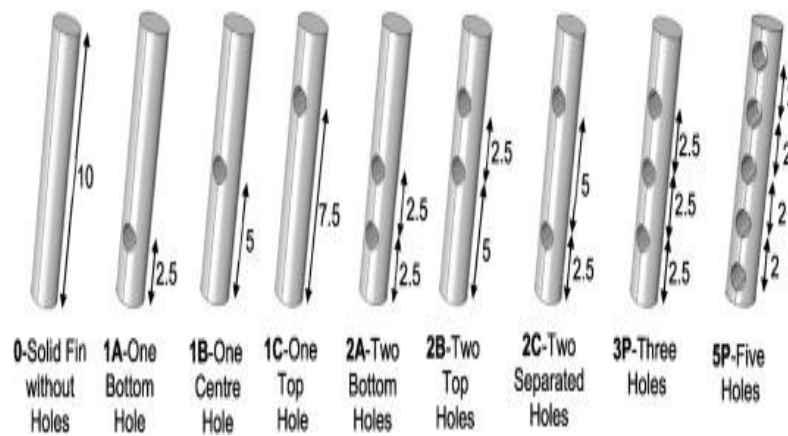


Figure 3.14: The pin fin model description, all dimensions in mm [263].

3.10.2 Perforated PHS using water

The perforated PHS model is compared with the solid PHS to examine the influence of using water on hydraulic and thermal performance. Fig. 3.15a presents numerical predictions of the pressure drop through the PHS. It is found that the pressure drop decreases only slightly when using the perforated model compared to the solid one. Fig. 3.15b describes the average temperature of PHS base plate, T_{case} , as a function of the Reynolds number in the range of $300 \leq Re \leq 1100$ for both solid and perforated pinned heat sinks.

The results show that there actually a slight increase in base temperature when perforations are introduced. Since water is more viscous than air, the flow path through the small perforations suffers a relating higher viscous resistance and consequently little water passes through. Hence the pressure drop is only marginally improved. Since flow through holes is slow, the gain in heat transfer through the thermal surface of the holes is outweighed by loss of the holes, and the loss of the conductive area along the pins. Hence the base temperature is slightly higher for perforated case, therefore, the focus of the research will be on the VGs of different shapes (see Fig. 3.14) using water as a coolant and exploring their effect on heat and flow characteristics.

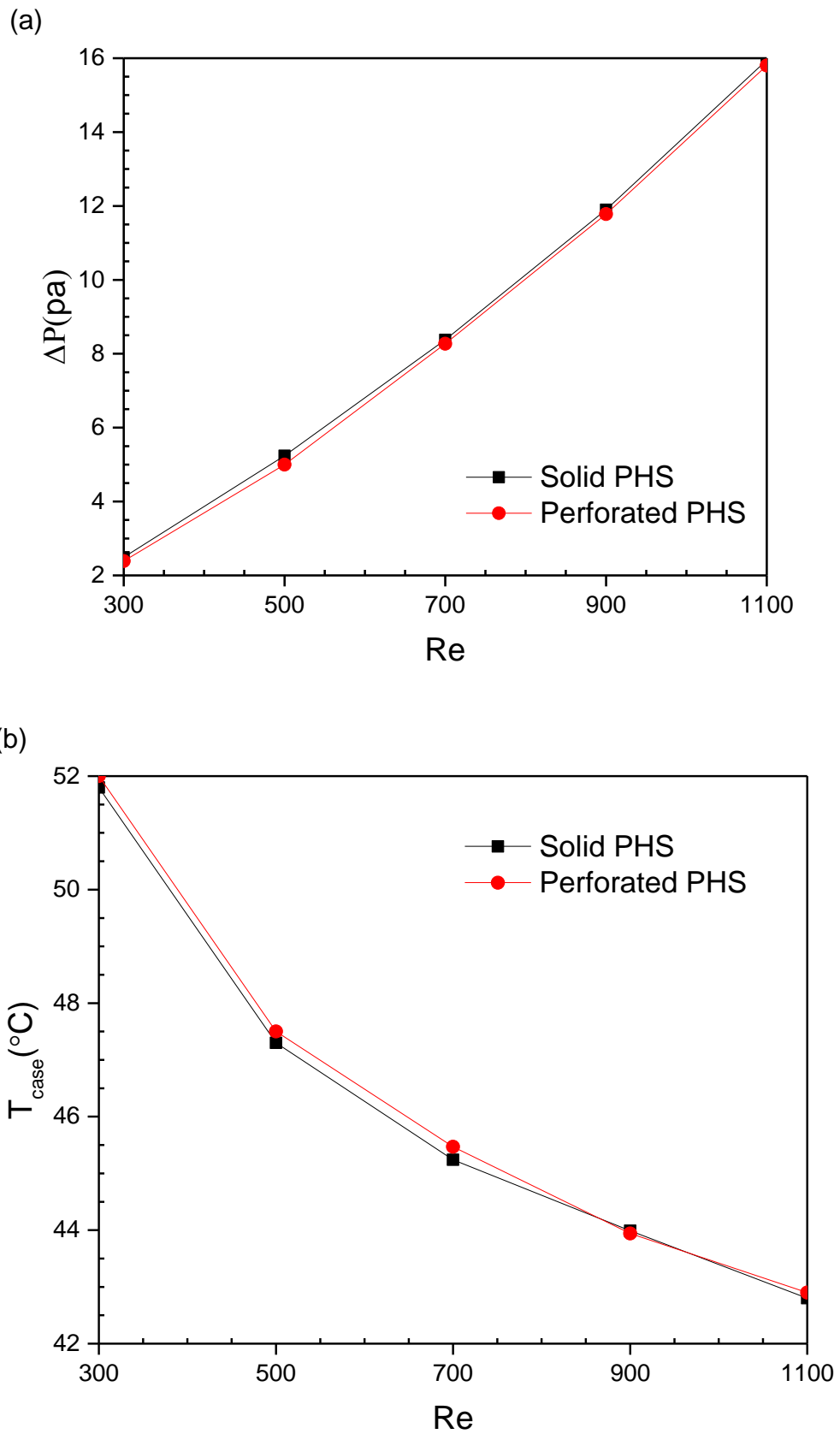


Figure 3.15: Comparisons between solid and perforated PHS (3 holes) with water as a coolant: (a) Pressure drop; (b) Base plate temperature.

The example of pin fin presented in Fig. 3.15 shows that the idea for enhancing the heat transfer performance in air-based cooling system do not necessary work with liquid coolants. Though liquids offer higher thermal conductivity than air, the higher viscosity must be taken into consideration.

3.11 Summary

This chapter outlined how to use CFD to solve a conjugate heat transfer problem in a micro-channel system. The adopted method has been shown to produce mesh independent results, and has been validated against published experimental and numerical work. The next chapters (4-7) focus on the numerical results of using different VGs shapes to enhance the heat transfer and reduce the pressure drop compared to the uniform micro-channel with water as the coolant. Nanofluids as coolants are presented in chapter 6, required pumping power explored in chapter the pin fin model is studied to examine the impact of the geometry and the fluid type on heat transfer and fluid flow characteristics. The model has been investigated under laminar flow ($300 \leq Re \leq 1100$) subjected to a uniform heat flux related to CPUs in electronic devices is 75 W/cm^2 .

Furthermore, in the present study, the perforated pinned heat sink showed insignificant enhancement in heat transfer rate or reduction in pressure drop compared to the solid pins. It does not necessarily follow that a geometrical modification that improves heat transfer for one fluid will also enhance performance for a different working fluid.

The remainder of this thesis is devoted to geometrical and/or coolant enhancements that are appropriate for liquid coolant heat sink.

Chapter 4: Heat and Flow Analysis of Circular Vortex Generators Design

4.1 Introduction

As discussed in the previous chapter, the results indicated that no enhancement in heat transfer is seen with the perforated pinned heat sink with water. Therefore, to enhance the thermal performance of a cooling system, a modified micro-channel having different shapes of VGs is proposed and compared to a base geometry which is a uniform micro-channel. The base geometry considered is a single micro-channel with rectangular cross-section, as described in chapter 3 section 3.6.

The model is a new design of a uniform micro-channel having different shapes of vortex generators (VGs) positioned at intervals along the base of the channel. The VGs shapes are circular, triangular and rectangular compared to each other based on constant volume of 0.0314 mm^3 . Models with Reynolds number in the range of 50 to 2300 are subjected to a uniform heat flux relevant to microelectronics air and water cooling.

The configuration is a micro-channel with the dimensions listed in Table 4.1 and as shown in Fig. 4.1. The computational domain consists of a single micro-channel with rectangular cross-section, with appropriate symmetry planes to represent the whole heat sink. The total base area of the heat sink is taken as $A_s = 6.27 \times 10^8 \text{ } \mu\text{m}^2$. The new shapes of VGs such as rectangular, square, forward triangular and backward triangular are seen in Fig. 4.2 (a-g). The key factor in examining the influence of different shapes on heat and flow performance is the constant volume of 0.0314 mm^3 for each VG.

This chapter also focuses on the effect of half-circle VGs having and a variable radius, r , ranging up to $400 \text{ } \mu\text{m}$ design on heat transfer and fluid flow characteristics. Note that the units to present the temperature is Kelvin and the velocity is m/s.

Table 4.1: Micro-channel and VGs dimensions in μm .

Micro-channel dimensions (μm)									
L	25000	H_c	700	H_t	900	W_c	500	W_w	300
VGs dimensions (μm)									
Triangle		Rectangle		Square		Circle			
h	300	h	315	h=b	250.6628	r	Up to 400		
b	418.879	b	200	r=200 for VGs comparison					

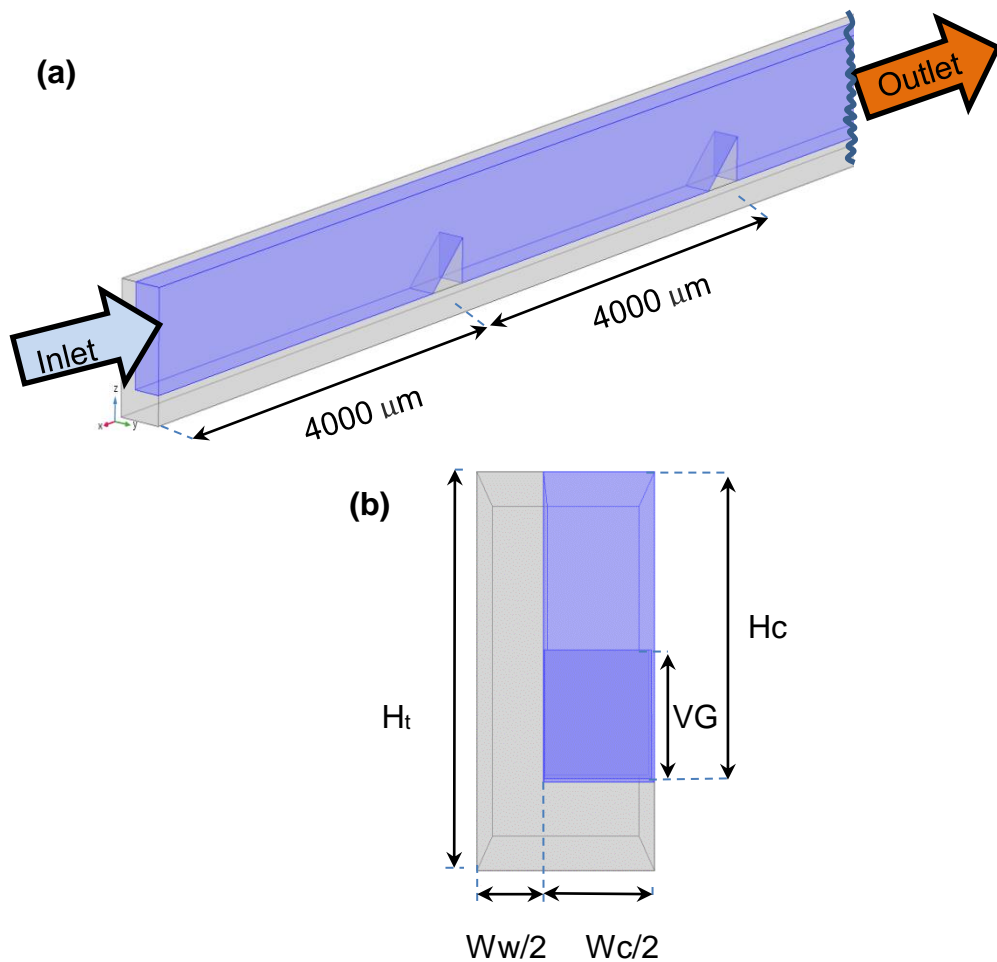


Figure 4.1: Geometry description: (a) rectangular micro-channel containing vortex generators; (b) view along the channel showing the definition of parameters governing the dimensions of the geometry.

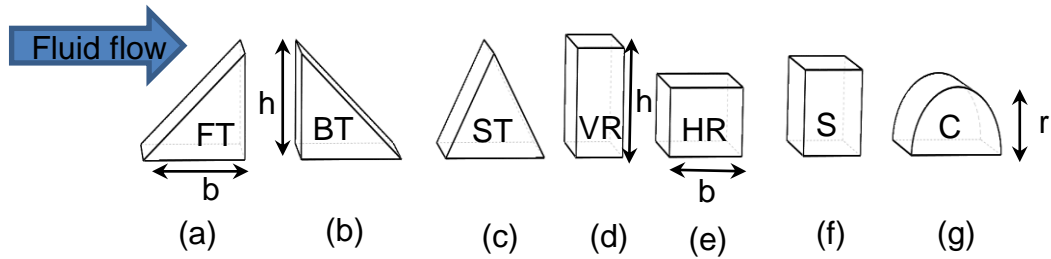


Figure 4.2: Side view of different shapes of VGs: (a) Forward triangular (FT); (b) Backward triangular (BT); (c) Symmetry triangular (ST); (d) Vertical rectangular (VR); (e) Horizontal rectangular (HR); (f) Square (S); (g) Half-circle (C).

4.2 Influence of VGs shape in the micro-channel

Proposed VGs shapes are compared to a uniform channel. The key factor of this comparison is that all VG configurations are considered to have an equal volume of 0.0314 mm^3 . The performance of heat transfer and fluid flow effect were examined using laminar flow and a constant heat flux ranging from 75 to 100 W/cm^2 and Reynolds number in the range of 50 to 2300. Before investigating the influence of different VG configurations on heat transfer and fluid flow, Fig. 4.3a shows the effect of heat flux on thermal resistance in a uniform micro-channel having no VGs. As to be expected, that thermal resistance increased with increasing heat flux for the given Reynolds number. However, systems using water as a coolant can dissipate high heat flux compared to air-base systems. Therefore, $75\text{-}100 \text{ W/cm}^2$ is considered in the following results. Furthermore, in particular applications there is a temperature limitation of operating electronic chips, as calculated results showed that the working temperature of 356 K is suitable for the experimental applications, which can be achieved using Re of 300. In addition, Fig. 4.3a also presents that at high Reynolds number (2000-2300) there is no significant improvement in thermal resistance. Hence, the later results are presented at Reynolds number in the range of 300-2000. Another important factor in heat transfer studies is the pressure drop, since it is directly related to the power consumption and hence the overall cost of the system for a long period of operation. Fig. 4.3b reveals that the pressure drop is very slightly higher at the

lower heat flux. This is due to the viscosity effect, as the viscosity of a cold water is slightly higher than the hot water, therefore this slightly increases the pressure drop. Thus Fig. 4.3b shows that no significant effect found utilizing heat flux ranging from 75-100 W/cm². Therefore, in all following results, a heat flux of 100 W/cm² is used. The detail of the effect of VGs shapes on conjugate heat transfer is presented in different sections as below.

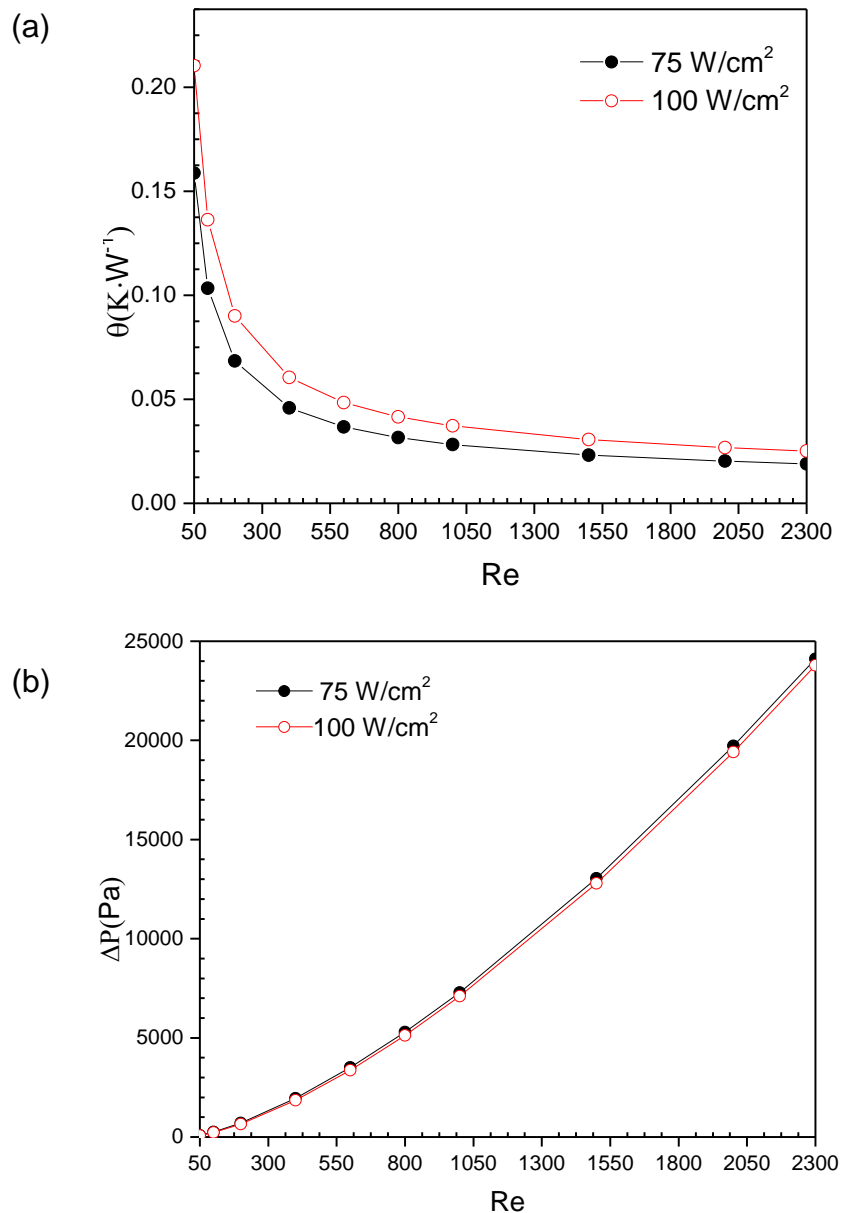


Figure 4.3: Different range of heat flux with the full range of Re using uniform channel: (a) thermal resistance; (b) pressure drop.

4.2.1 Triangular shapes

A uniform channel is taken as a reference to be compared to the three new VG configurations of triangular shape which are forward (FT) backward (BT) and symmetric (ST) (see Fig. 4.2). As discussed in the previous section (5.2), the heat flux is taken as 100 W/cm^2 and Reynolds number is ranging from 300 to 2000 to assess the impact of VGs on thermal resistance and pressure drop as shown in Fig. 4.4a and b. The influence of triangular VG shapes on thermal resistance is presented in Fig. 4.4a, where it is found that the symmetric (ST) VGs model offers the lowest thermal resistance, followed by forward (FT), then the backward (BT), while the highest thermal resistance is for the uniform channel. This is also seen in Fig. 4.5a (temperature contours) which shows that ST VGs model at $Re\ 800$ offers the lowest temperature. This is because of the VGs configuration related to the fluid flow, for instance, there is a stagnant zone before the VGs of model BT (see Fig. 4.5b) which generates a hot spot, while less effect can be seen for FT model due to the flow direction. However, the ST model has smaller stagnant zone compared to BT and FT models, this can be seen in Fig. 4.4b. It is clear that all triangular configurations offer heat transfer enhancement compared to the uniform channel. However, the price for thermal reduction of ST model paid for pressure drop as ST model has the highest pressure drop compared to all proposed models of triangular shapes which is shown in Fig. 4.4b. The next section presents the influence of rectangular VG models on conjugate heat transfer.

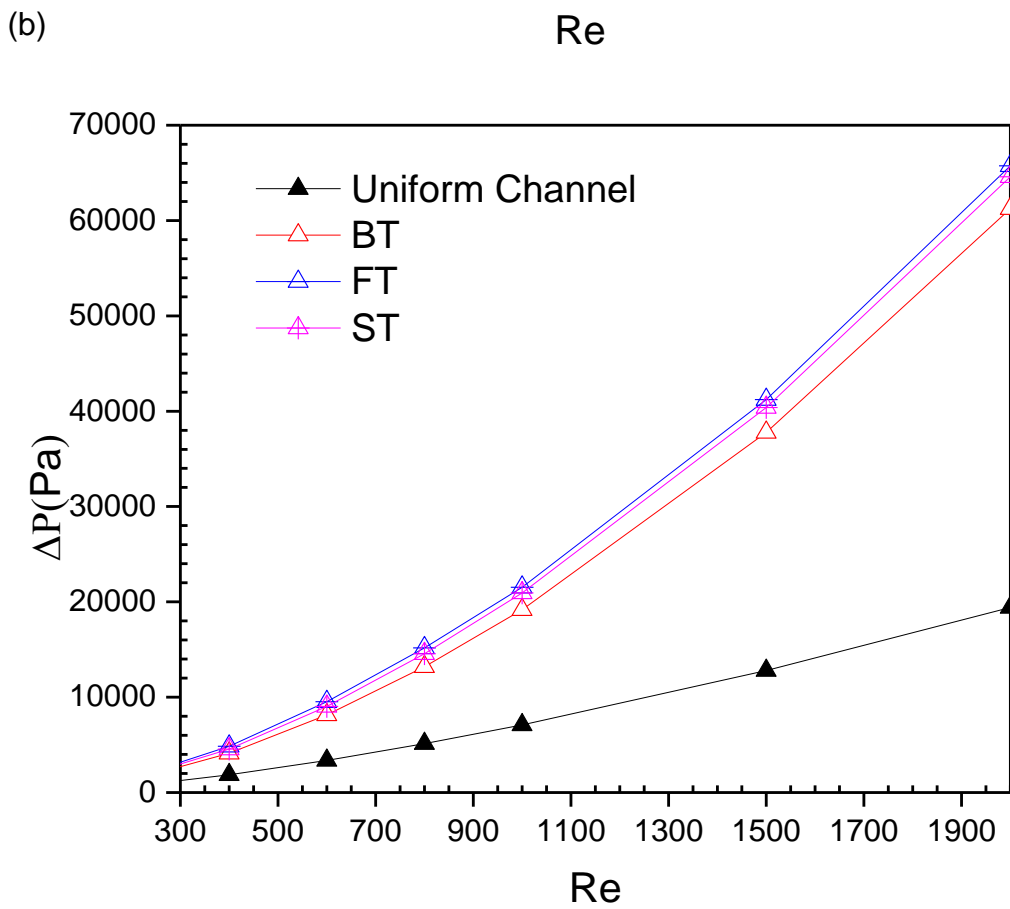
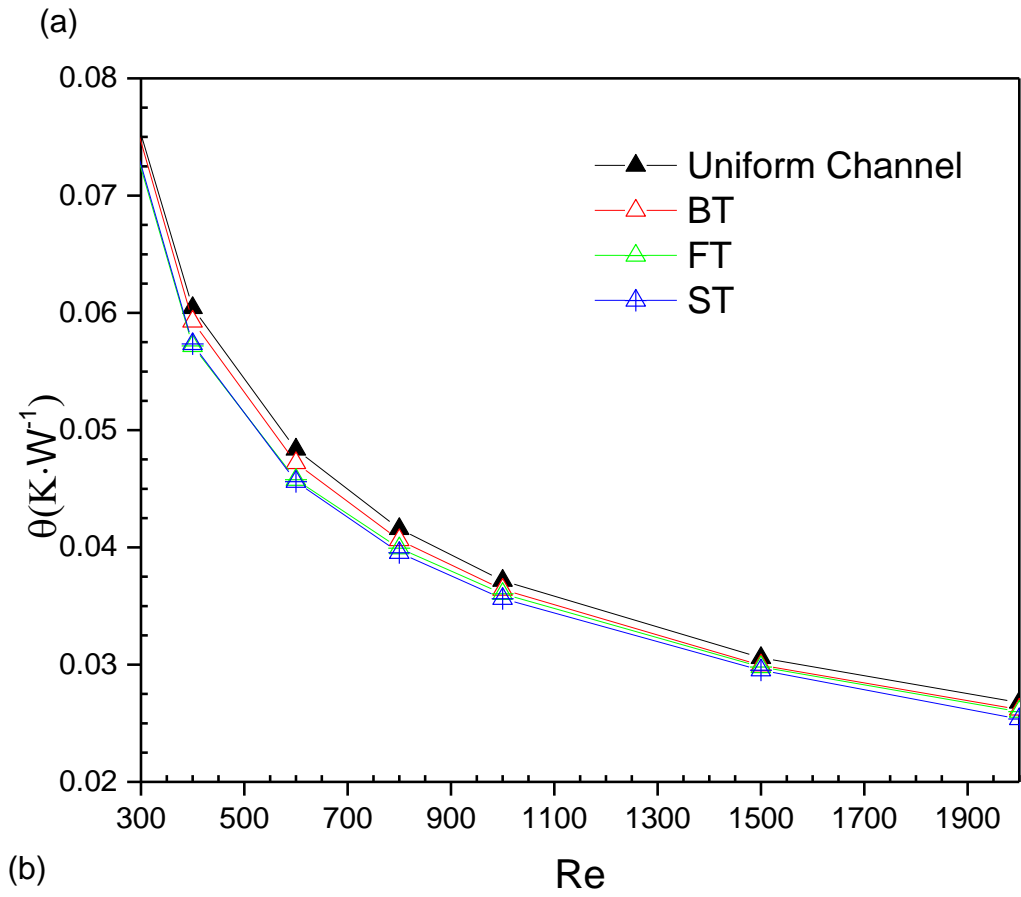


Figure 4.4: Different configurations of triangular VGs forward triangular (FT), backward triangular (BT) and Symmetric triangular (ST): (a) thermal resistance; (b) pressure drop.

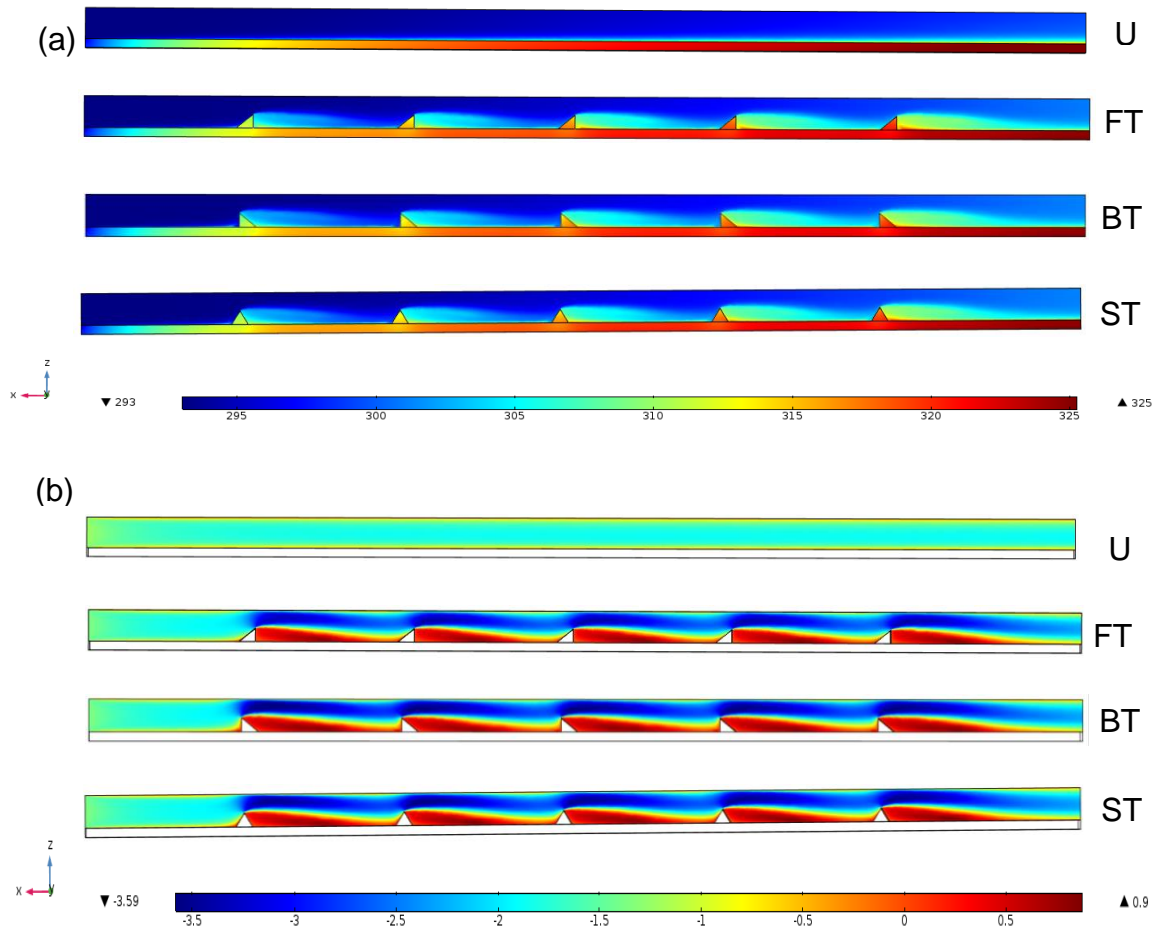
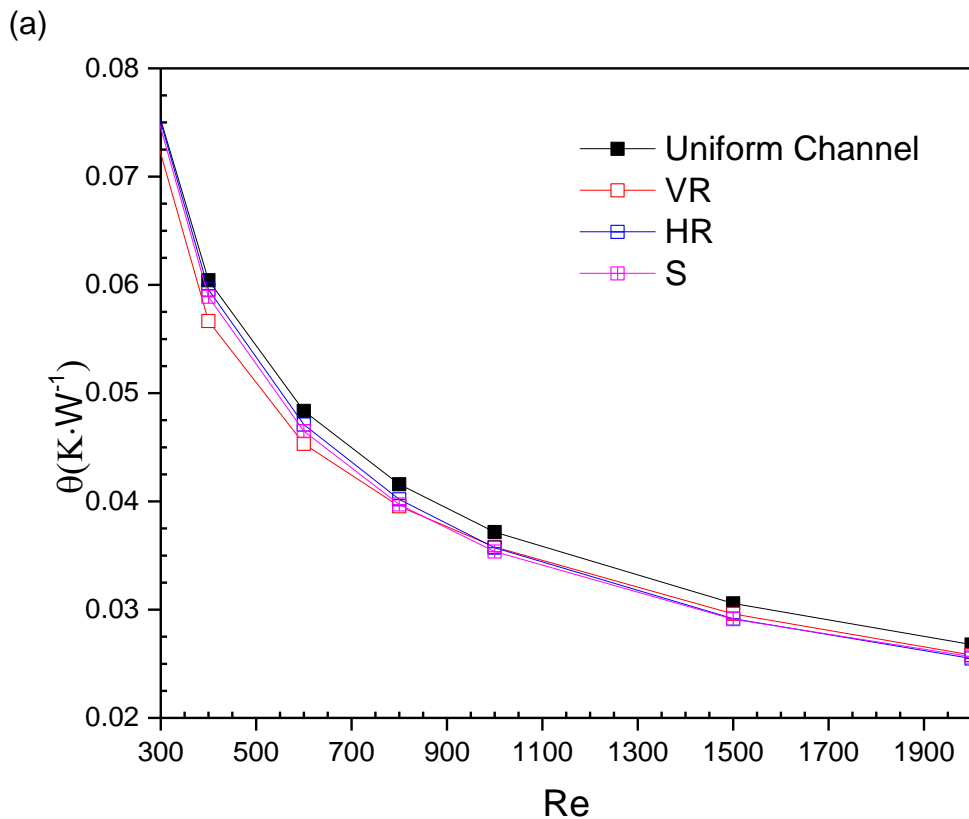


Figure 4.5: X-Z planes of various triangular VGs models with flow direction from the left to the right at Re 800: (a) temperature contour (K) at the wall of the channel; (b) contours of x velocity component (m/s) at the centre of the channel.

4.2.2 Rectangular shapes

In this section, various shapes of rectangular configuration (see Fig. 4.2d-f) are compared to the uniform channel to examine their effect on thermal resistance and pressure drop. Fig. 4.6a shows the effect of rectangular VGs in various models (Vertical rectangular (VR), Horizontal rectangular (HR) and Square (S)) on thermal resistance. It is found that the S VGs shape offers the lowest thermal resistance compared to VR, HR and the uniform channel especially at $Re \geq 900$, while model VR offers best thermal resistance at $Re \leq 800$. The reason behind that can be explained using Fig. 4.7a and b. Fig. 4.7a shows that the S model has lowest temperature because its dimensions make

a balance between the height of the VGs which act as fins in terms of heat transfer and the stagnant zone behind the VGs in terms of fluid. It can be seen that the effect of heat transfer is more than the effect of the fluid flow in the case of comparing VR and S models. Therefore, the VR model offers a better heat transfer rate compared to the S model at low Re (see Fig. 4.6a). This can be discussed in more detail through association with the fluid flow contours shown in Fig. 4.7b, which shows that the height of S model lies between VR and HR. Obviously generating a hot spot behind each VGs depends on the stagnant zone that also depends on VG's height. For example, Fig. 4.7b shows that S model has the larger stagnant area than HR model, but S model still the lowest thermal resistance (see Fig. 4.6a). This can be attributed to the fact the fast stream (blue stream) passing over the S model is more than the one passing over the HR model (see Fig. 4.7b). the results show that the HR model offers the lowest pressure drop compared to VR and S models as shown in Fig. 4.6b, this is due to the height (h) of the VGs facing the water (see Table 4.1).



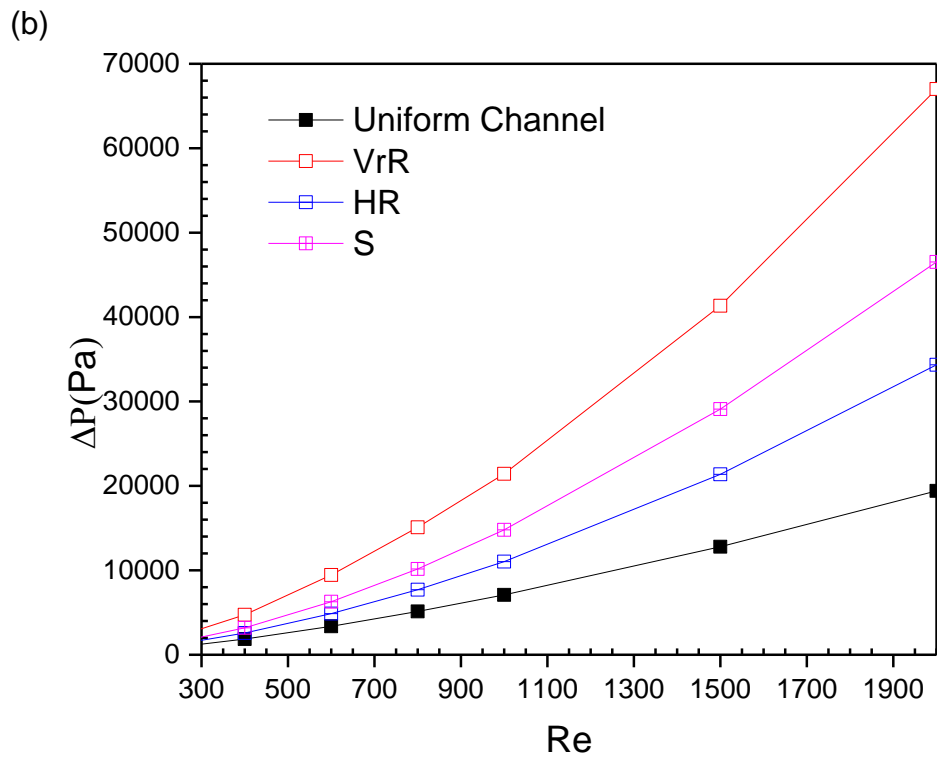


Figure 4.6: Different VGs of rectangular model (Vertical rectangular (VR), Horizontal rectangular (HR) and Square (S)): (a) thermal resistance; (b) pressure drop.

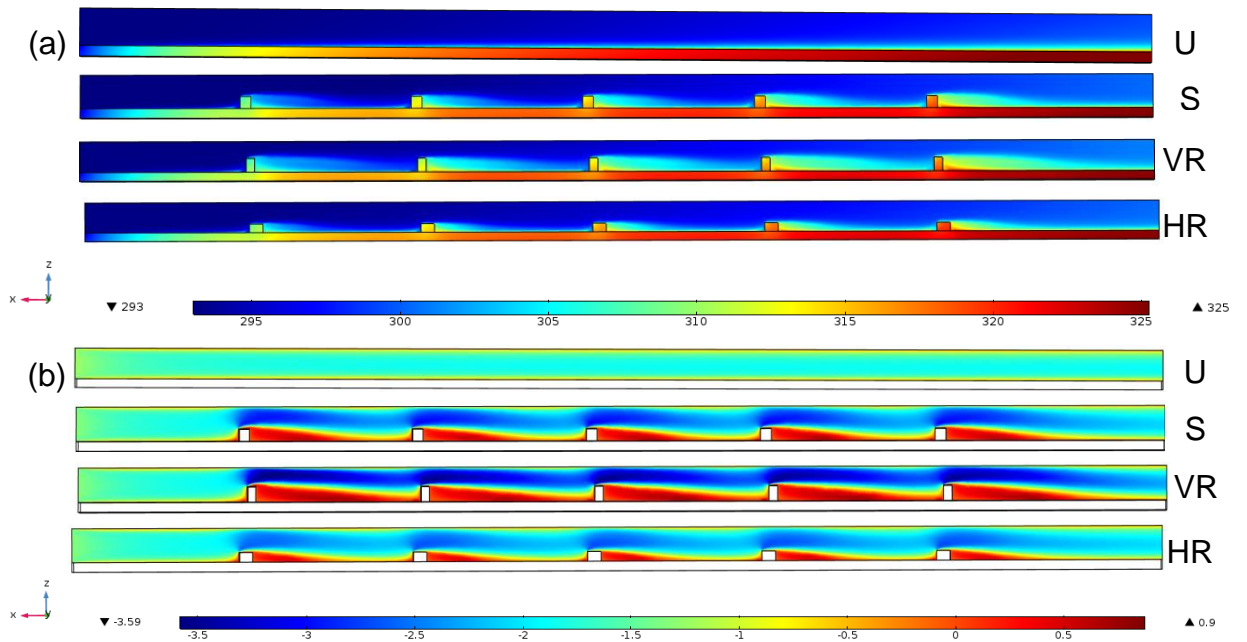
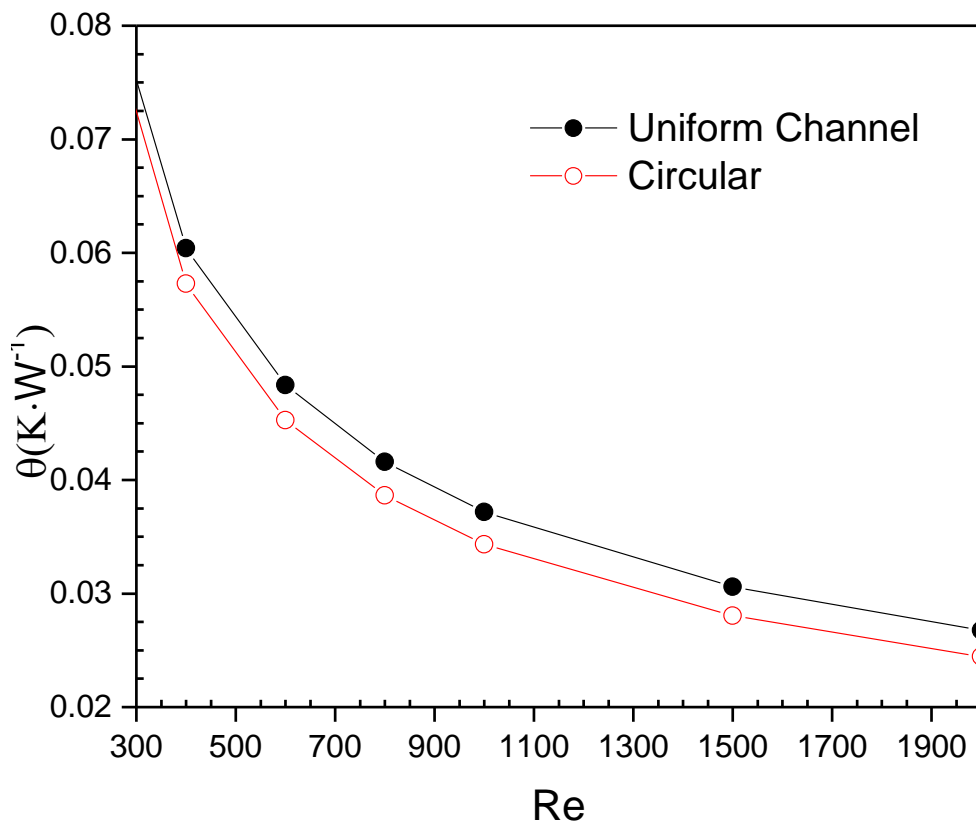


Figure 4.7: X-Z planes of various triangular VGs models (Vertical rectangular (VR), Horizontal rectangular (HR) and Square (S)) with flow direction from the left to the right at Re 800: (a) temperature contour (K) at the wall of the channel; (b) contours of x velocity component (m/s) at the centre of the channel.

4.2.3 Circular shapes

Circular VGs shown in Fig. 4.2g having dimensions presented in Table 4.1 compared to the uniform channel to study the shape effect on the conjugate heat transfer. Fig. 4.8a reveals that the thermal resistance decreased significantly using circular VGs compared to the uniform channel. However, the pressure drop of C-model is higher than the uniform channel due to the VGs which disturb the water in the micro channel as shown in Fig. 4.8b. The temperature contour of the circular VGs is compared to the uniform channel in Fig. 4.9a which reveals how the circular VGs assist to enhance the heat transfer by dissipating the heat from the base of the channel to the water. VGs help to develop the secondary flow by disturbing the flow (mixing the cold and hot fluids) which leads to reducing the boundary layer as shown in Fig. 4.9b.

(a)



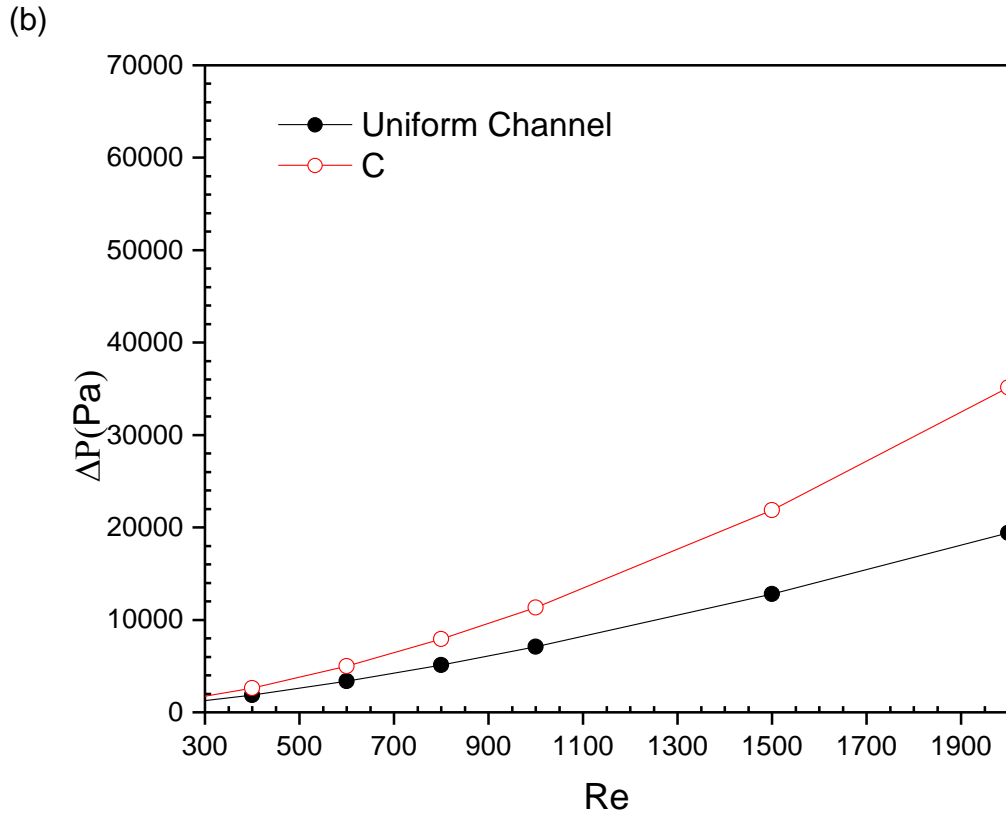


Figure 4.8: Circular VGs compared to uniform channel using Re from 300 to 2000: (a) thermal resistance; (b) pressure drop.

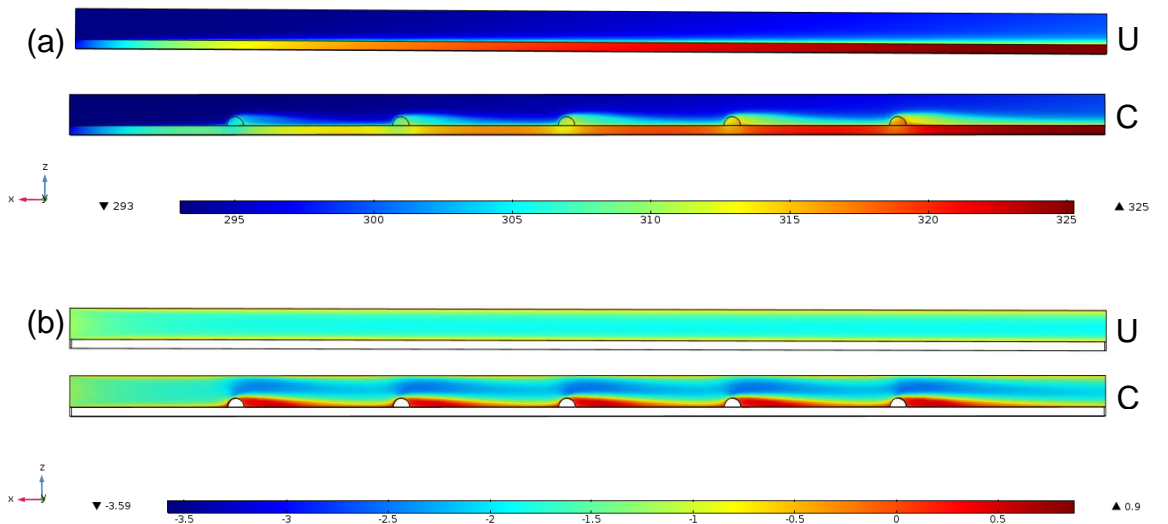
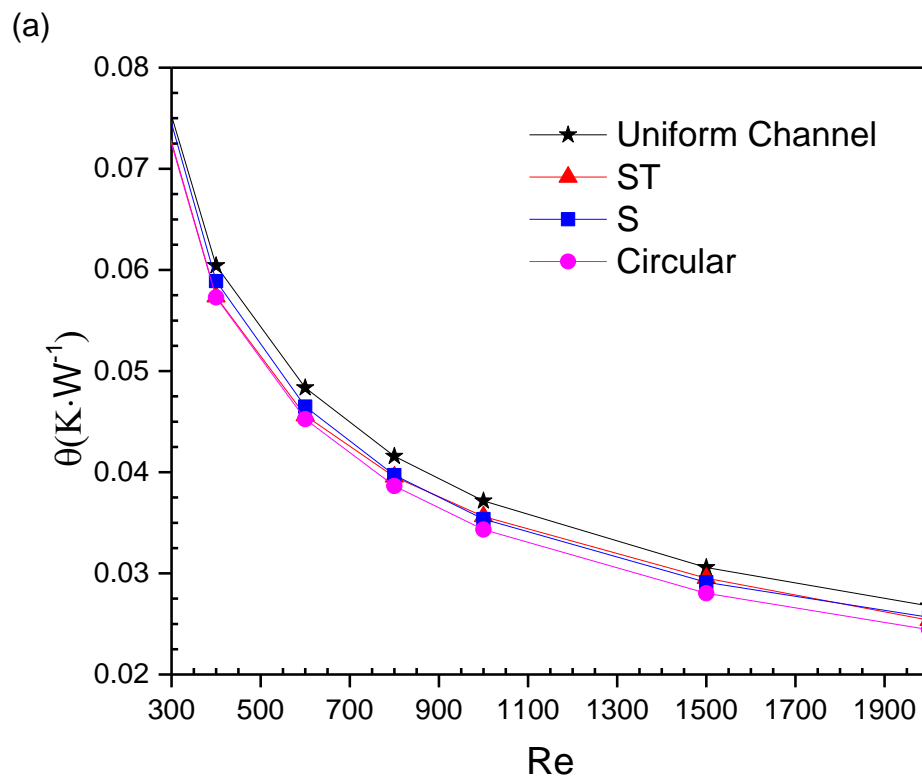


Figure 4.9: X-Z plane of uniform channel and circular VGs at Re =800: (a) temperature contour; (b) contours of x velocity component (m/s) at the centre of the channel.

4.2.4 Comparison of the VGs shapes

The sections above compared different VGs to the uniform channel for both thermal resistance and pressure drop. Overall, all proposed models enhanced the thermal resistance compared to the uniform channel, but all of them have higher pressure drop than the uniform channel. Hence, it is natural to ask what configuration is the best in terms of heat transfer and pressure drop. Therefore, Fig. 4.10a presents the lowest thermal resistance of each group of VGs shapes. It is found that the circular VGs shape has the lowest thermal resistance compared to S and ST models. In addition, Fig. 4.10b shows that the C-model also has a lower pressure drop than ST and S models, but still much higher than the uniform channel. VGs enhance the heat transfer, but this enhancement depends on the size of the spot area generated behind the VGs. For instance, the hot spot behind the C-model is less than for the ST and S models. Therefore, the C-model has the lowest thermal resistance as shown in Fig. 4.10a. This can be attributed to the fact that the main flow passes over the VGs and deflects it, generating a recirculation, which may act to reduce the thermal boundary layer and enhance the heat transfer by mixing hot and cold liquid [118, 264] as clearly presented in Fig. 4.11a.



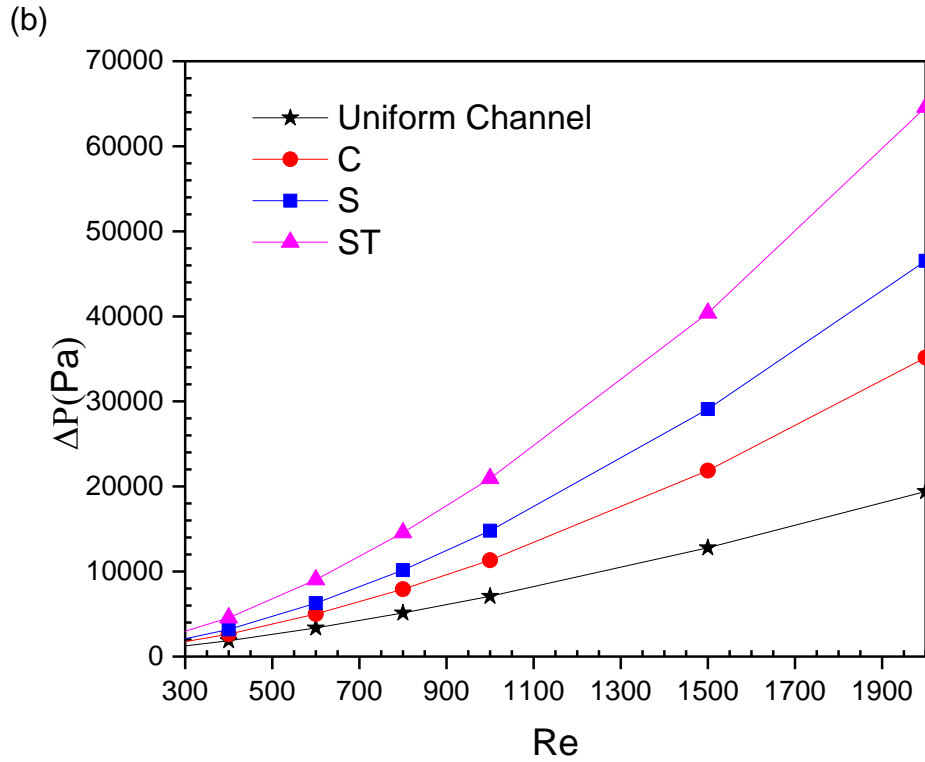


Figure 4.10: Comparison of the lowest thermal resistance configurations (ST, S and C models); (a) thermal resistance; (b) pressure drop.

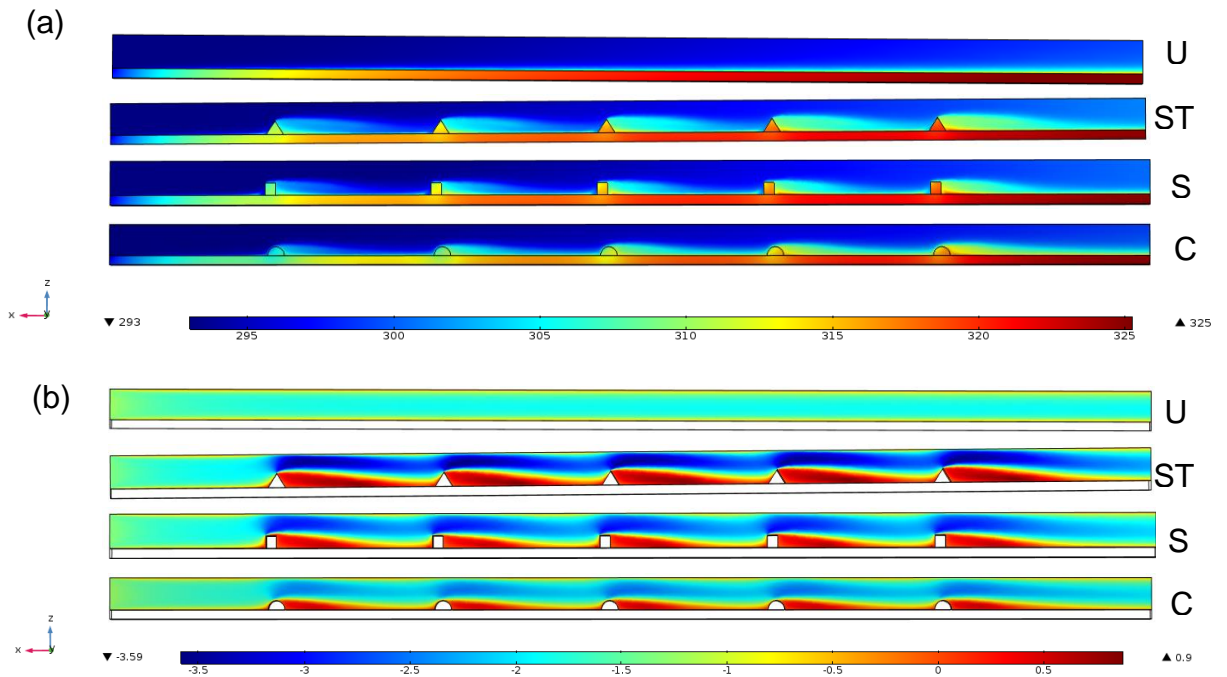


Figure 4.11: X-Z plane comparing the uniform channel to ST, S and C VGs models at Re =800: (a) temperature contour; (b) velocity contour.

4.2.5 Hydraulic thermal performance

The criterion used in this section is based on assessing by how much does increase in pressure drop outweigh combination of the heat transfer enhancement and the pressure drop increment when comparing the uniform channel and the proposed VG configurations (see Eq. 3-7). Fig. 4.12 shows the PEC index value for the best models in terms of thermal resistance (ST, S and C models, section 4.2.3). The results indicate that the lowest PEC is for ST model, then S model, and the highest PEC is for the C model. This can be attributed to the fact of how PEC applied (see Eq.3-7) to evaluate the overall heat transfer. This follows since the C model has the lowest thermal resistance and lowest pressure drop compared to the other VGs models (see Figs. 5.10 and 5.11). However, the C model still below 1 (PEC for the uniform channel).

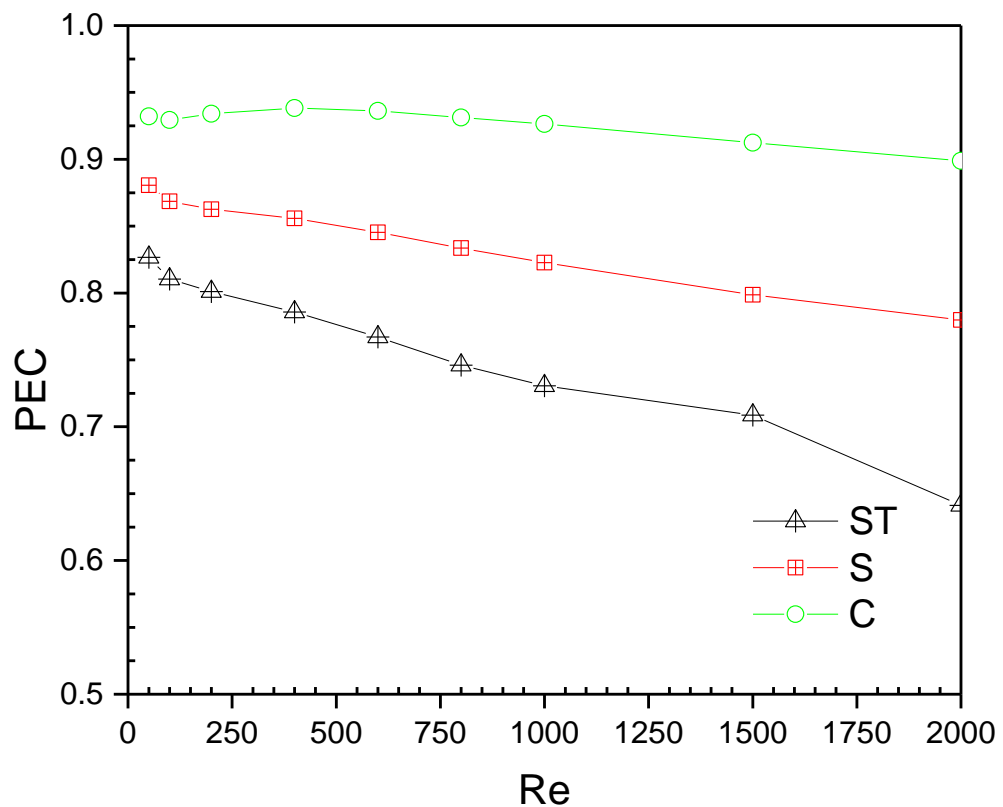


Figure4.12: PEC of the lowest thermal resistance models with the full range of Re.

Based on the above results, the C-model offers lower thermal resistance and pressure drop and higher PEC index than other suggested VG configurations. Therefore, the focus of the rest of the chapter is on the influence of half-section VGs having various radii on the heat transfer and fluid flow characteristics as illustrated in the next sections of this chapter.

4.3 Further exploration of half-circle VGs

The above results highlight that the half-circle VGs appear to be the most beneficial, thus these are now explored in more detail. The results presented below focus on the particular value of 100 W/cm^2 for the heat flux, because the system using water can achieve temperature reduction for high heat flux subjected to the system. However, higher heat flux cannot apply to the system due to the upper temperature limit for operation of electronic devices [30, 265-267].

The other VG geometry considered in this work is that of cylinders with a half-circle cross-section as shown in Fig. 4.2. Again the three different radii of spanwise configurations shown in Table 4.1 were considered. Fig. 4.13 presents the impact of the radius of full-span VGs on the thermal resistance and pressure drop for a range of Reynolds numbers, which is split into two plots for the sake of clarity. Unlike the quarter-circle VGs, for the half-circle case, the thermal resistance decreases monotonically with radius for all Reynolds numbers above 100. The thermal resistance also decreases as Re increases, but of course the pressure drop increases.

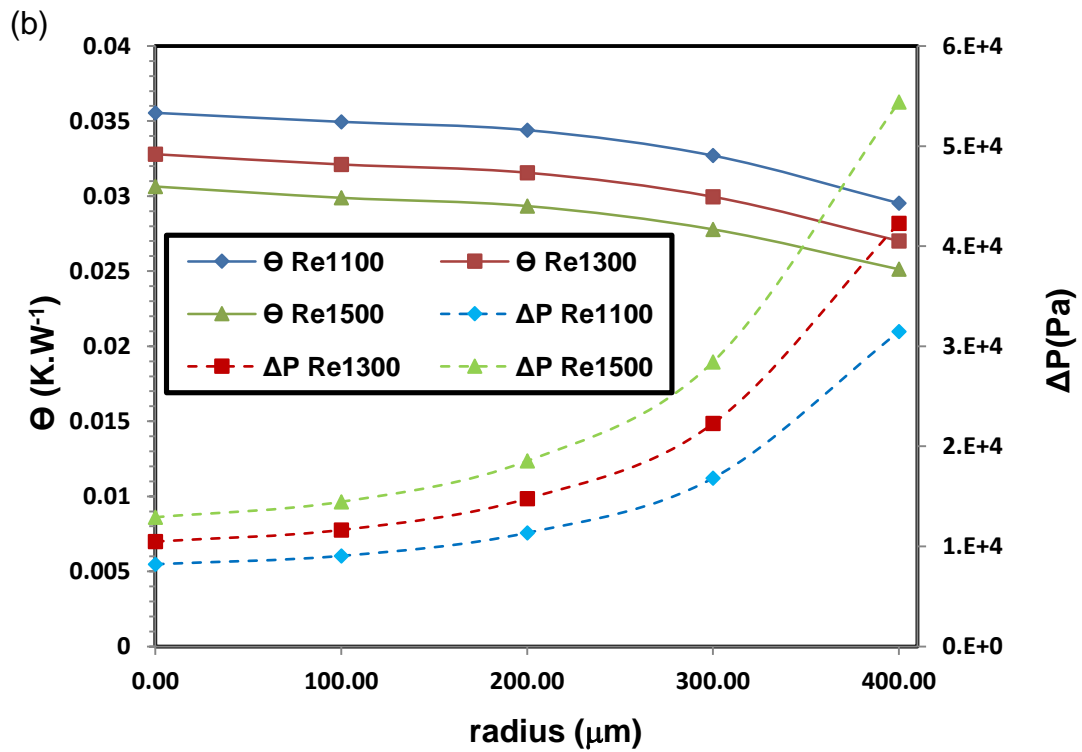
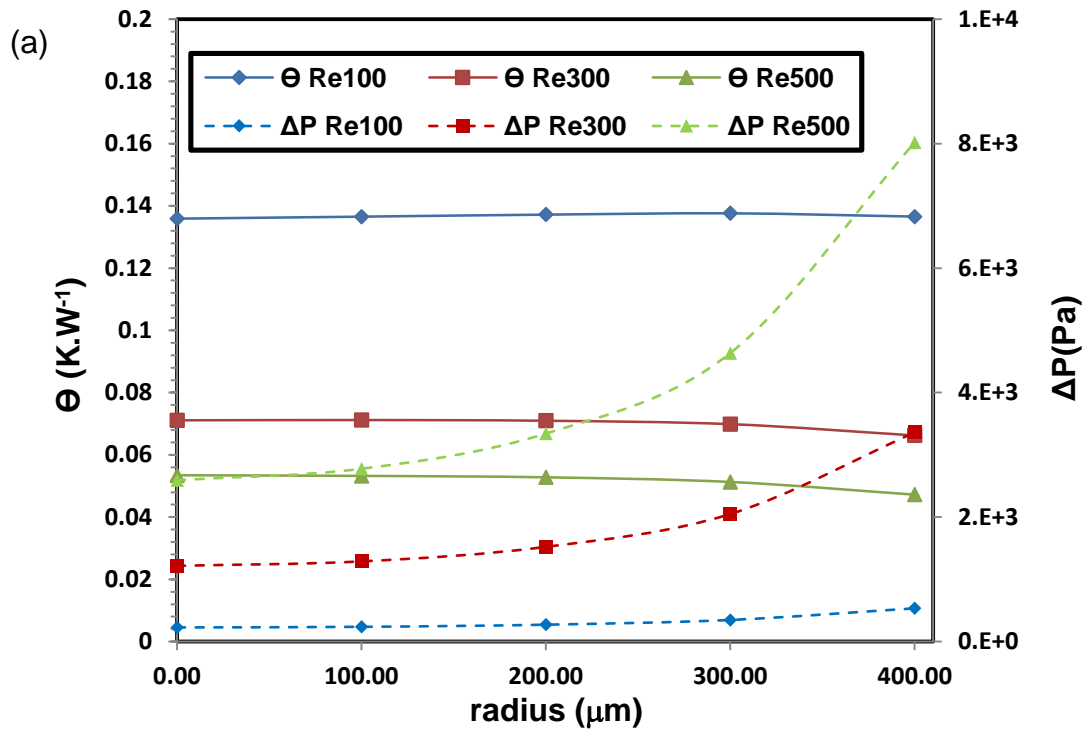


Figure 4.13: Thermal resistance and pressure drop as a function of VG radius for full-span half-circle VGs: (a) $Re = 100$ to 900 ; (b) $Re = 1100$ to 1500 .

Fig. 4.16 compares the thermal resistance and pressure drop observed using half-circle VG design, along with those of the smooth, uniform channel with no VGs present. The VG radius in each case is 200 μm . All VGs resulted in higher pressure drops than the uniform channel, as is to be expected. The lowest pressure drop with VGs present is seen with the uniform channel, then full-span VGs – i.e. the same ranking as for the thermal resistance.

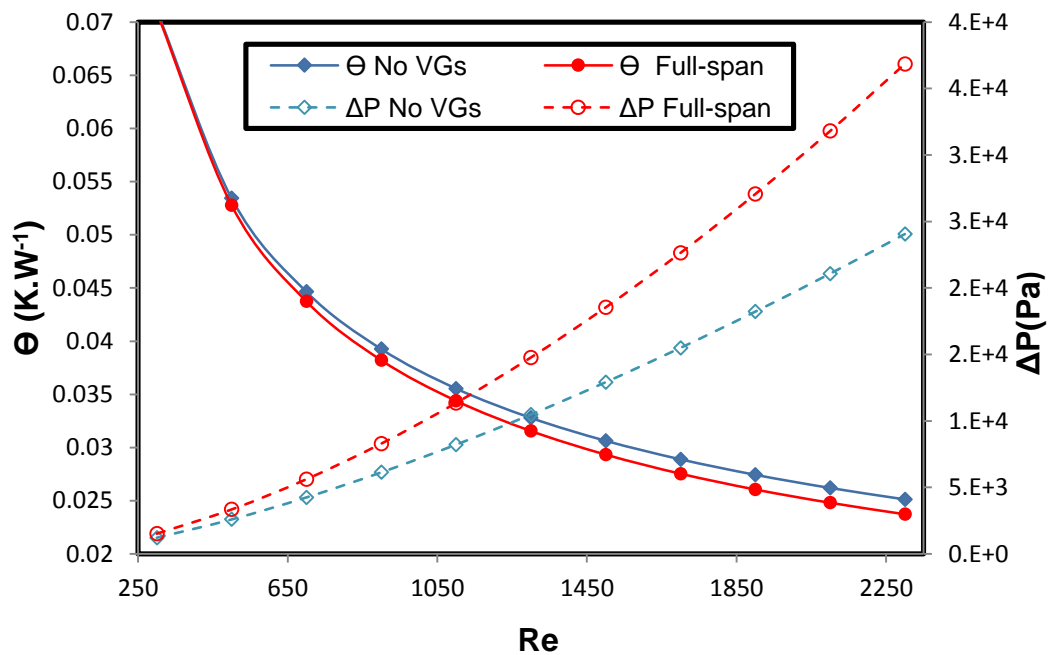


Figure 4.14: Comparison of the thermal resistance and pressure drop characteristics of the uniform channel and the half-circle VG considered, with radius equal to 200 μm .

4.3.1 Thermal-hydraulic performance

To assess the real practical potential for improving the efficiency of micro-channel heat exchangers using VGs, it is important to combine the heat transfer performance with an appreciation of the fluid flow penalty resulting from the constriction of the channel. Clearly there is a huge design space available for the optimization of cylindrical VGs, however a full optimization study is beyond the scope of this study. Instead, to illustrate the potential of such VGs, calculation of the performance evaluation criteria (PEC) index, equation (3-7), is made for the half-circle VG.

Fig. 4.15 plots the PEC index of the data, confirming that small-radius VGs offer good potential for improving the efficiency of micro-channels operating at low Reynolds number, with $r = 100 \mu\text{m}$ appearing to give the best performance over the widest range of Reynolds number. However, as seen in Fig. 4.1 that the thermal resistance increases with increasing the radius of VGs. But this reduction in thermal resistance leads to increase the pressure drop, as the PEC index is a ratio of the thermal enhancement and fluid flow, it can be concluded that no benefit of using large radius when presenting the data in PEC perspective.

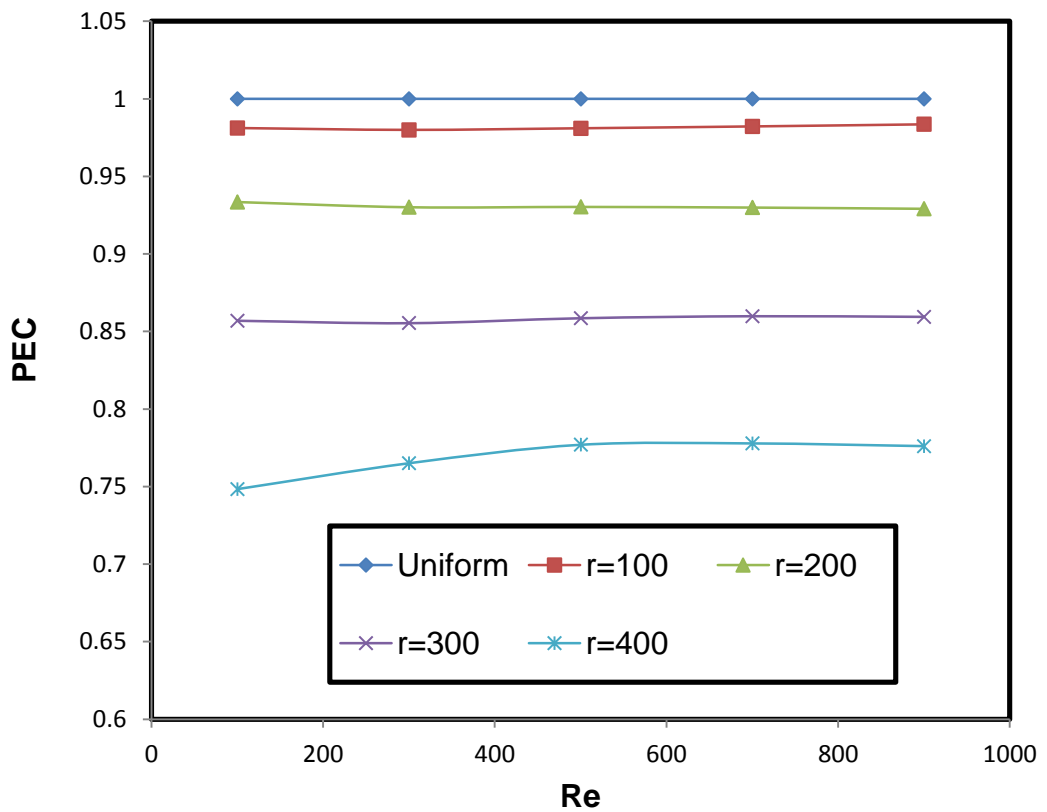


Figure 4.15: Variation of PEC index with Reynolds number for centred half-circle VGs of various radii.

4.4 Summary

In this chapter, a uniform micro-channel having different VG configurations has been studied to examine the impact of the geometry on heat transfer and fluid flow characteristics. The vortex generators (VGs) using different configurations which are forward triangular (FT), Backward triangular (BT), Symmetry triangular (ST), Vertical rectangular (VR), Horizontal rectangular (HR), Square (S) and Half-circle (C). The models have been investigated under laminar flow ($50 \leq Re \leq 2300$) subjected to a uniform heat flux of 100 W/cm^2 related to CPUs in electronic devices. The effect of the VGs was quantified in terms of the thermal resistance, pressure drop along the channel, and a combination of these forming a performance evaluation criteria (PEC) index. Therefore, the outcomes out of this research are summarised in the following points.

- For triangular VGs configurations (Forward triangular (FT), backward triangular (BT) and Symmetry triangular (ST)). It is found that the lowest thermal resistance is for the ST model, while the lowest pressure drop is for the BT model.
- For the rectangular VGs models (Vertical rectangular (VR), horizontal rectangular (HR) and Square (S)), the results show that the S model offers the lowest thermal resistance and pressure drop compared to VR and HR, but the S model still has a higher pressure drop than the uniform channel.
- Circular VGs offer the lowest thermal resistance, followed by rectangular and triangular VGs. However, the pressure drops of all proposed VGs models are much higher than the uniform channel, meaning that additional pumping power would be needed to drive the flow compared to the uniform channel.
- A thermal hydraulic performance criterion (PEC) is used to evaluate the combination of heat transfer and the pressure drop of the system and come out with an overall evaluation. It is found that the circular VG model offered the highest PEC ($PEC \approx 0.95$) in comparison to triangular

and square configurations, but still below that of the uniform channel (PEC=1). Reducing radius improves PEC, but it remains below 1.




As concluded above, the half-circle was the best VGs among all suggested VGs in enhancing the heat and flow characteristics. However the problem of high pressure drop of using VGs compared to the uniform micro-channel is still not solved here. Therefore, the next chapter suggests a new idea to enhance the heat transfer and reduce the pressure penalty simultaneously.

Chapter 5: Benefits of spanwise gaps in cylindrical vortex generators

5.1 Introduction

As seen in previous chapter, the cylindrical vortex generators placed transversely over the span of a micro-channel can enhance heat transfer performance, but adding full-span vortex generators incurs a substantial pressure drop penalty. This chapter examines the benefits of introducing various gaps along the length of the vortex generators, both for reducing pressure drop and improving the thermal conductance of the system. Three particular configurations are considered with varied dimensions: symmetrical gaps at each end of the vortex generator, i.e. adjacent to the channel side walls; a single central gap; and a combination of a central and end gaps as shown in Table 5.1 and Fig. 5.1. The performance is investigated numerically via 3D finite element analysis (see chapter 3) for Reynolds number in the range 300-2300 and under conditions of a uniform heat flux input relevant to microelectronics cooling. The results presented below focus on the particular value of 100 W/cm² for the heat flux, because this corresponds to the upper limit for operation of electronic devices [265-267].

Table 5.1: Dimensions of the micro-channel and VG configurations

Micro- channel dimensions, μm					
L	25000	H_b	200	H_c	700
W_w	300	W_c	500	r	0-500
Gap dimensions, μm					
Central gap (C)		End gap (E)		Central and End gaps (CE)	
					
C1	50	E1	50	CE1	250
C2	100	E2	150	CE2	300
C3	150	E3	200	CE3	350
C4	400	E4	250	CE4	400
C5	450	E5	300	CE5	450
		E6	350		
		E7	400		

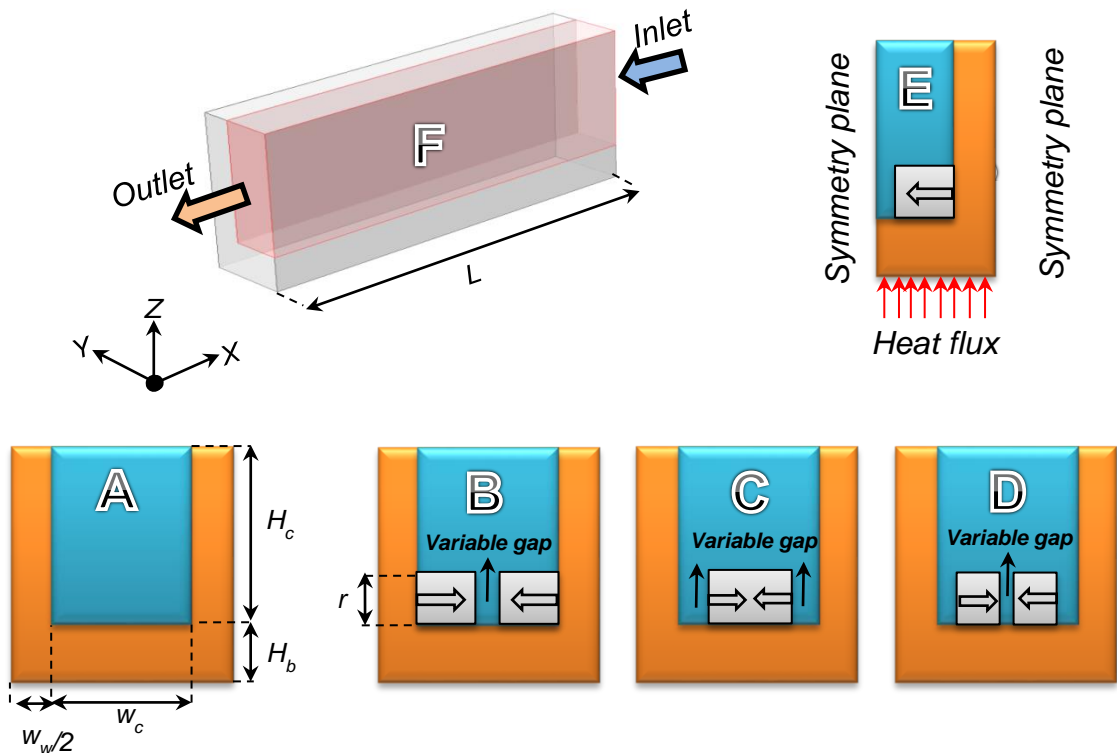


Figure 5.1: Geometry description: (a) uniform rectangular micro-channel with governing the dimensions of the geometry; (b) front-view cross-section of a 'central' ('C') gap VG; (c) front-view cross-section of an 'end' ('E') gap VG; (d) front-view cross-section of a 'CE' VG, with central and end gaps; (e) boundary conditions applied; (f) 3D view of the uniform channel.

5.2 The gap performance

In this study, three-dimensional laminar flow simulations were conducted with Reynolds number in the range 300-2300 to assess the effects of the various gaps in the VGs (described in Sec. 2) on the conjugate heat transfer, with water as the working fluid. There is a very large parameter space associated with the VG geometry: in addition to the gap positions and widths of primary interest, other parameters include the radii, longitudinal position, separation and number of VGs, as well as the conductivity of the VG and channel material. These will be considered in sub-sections below, but to begin we consider the same half-circle VG arrangement used in chapter 4, namely a series of 5 equally-spaced aluminium VGs of radius 400 μm .

5.2.1 End gaps (E-type vortex generators)

In previous chapter concluded that the full span half-circle VGs of the channel provided a lower thermal resistance and lower pressure drop than the other VGs. In other words, having a gap between the ends of the VG and the channel side walls might be beneficial. Therefore the starting point for the results presented here is an investigation of how the width of the end gaps affects the performance of the system, to see if there is an optimum gap.

5.2.2 The effect of end-gap width on conjugate heat transfer

Fig. 5.2 shows how the thermal resistance and the pressure drop along the channel vary with Reynolds number for a selection of different end-gap widths. Note that the gap size given in the legend refers to the combined width of the symmetrical gaps at each end. For clarity, not all gap sizes from Table 5.1 are shown is here labelled as 'E3' and consists of a 100 μm gap at each end of the VG. It is found that this gap width produces a lower thermal resistance than all larger gap widths, but inevitably does result in a greater pressure drop than VGs with larger gaps. However, it is possible to reduce the thermal resistance a little more by decreasing the gap further, as the curve for the E2 model (two 75 μm gaps) shows. Of course the pressure drop is increased, but the E2 pressure drop is still less than that for full-span VGs that have a much higher thermal resistance.

Reducing the gap size further than E2 does not provide any benefit. For example, the E1 VGs (two 25 μm gaps) produce the same thermal resistance as E2 VGs (not shown in Fig. 5.2 for clarity), but a much higher pressure drop. In fact this pressure drop (see Fig. 5.2) actually exceeds that for full-span VGs, as a result of the higher viscous drag caused by the very narrow gaps. Such small gaps would also be more challenging to manufacture. In terms of the achievable thermal resistance, the E2 VG with an overall gap of 150 μm (i.e. a 75 μm gap at each end) could therefore be considered as the optimum E-type VG, as it will produce a lower pressure drop than the VGs with the same thermal resistance but narrower gaps.

It is worth noting that the E7 VGs, which have two gaps of 200 μm each, show almost exactly the same thermal resistance as the full-span VGs, yet with a greatly reduced pressure drop. In fact the pressure drop is not much higher than for the uniform channel with no VGs present (see Fig. 5.2). The low pressure drop penalty is to be expected given that the gaps in the E7 VGs are 80% of the channel width.

5.2.3 Performance evaluation criteria index

In an attempt to give a quantitative indication of the benefit versus cost of having VGs present in the channel, the Performance Evaluation Criteria (PEC) index defined in equation (3-7) sets the relative change in the thermal conductance of the system (with respect to a uniform channel) against the relative change in the pressure drop. Fig. 5.3 shows the values of this index as a function of Reynolds number for a selection of end-gap widths (the legend gives the combined width of the two symmetrical gaps at each end of the VG). On this measure, the E2 VG is essentially 'neutral' for the higher Re values – i.e. its PEC values are close to unity, so its improvement in thermal conductance is in some way 'worth' the increase in pumping power required. In contrast, the PEC values for the E1 VG are rather lower, levelling out at about 0.85, consistent with the observations in the previous section that reducing the size of the end gap below that of the E2 VG simply raises the pressure drop with no improvement in thermal resistance/conductance.

Similarly, the E7 VG noted above reaches PEC values above one, since its relatively large gaps mean that the pressure drop is only a little higher than that of the uniform channel. However, this is not the largest PEC value that can be achieved with end gaps. The highest PEC value obtained is about 1.02 with the E6 VG, having end gaps of 175 μm each. This VG does however have a rather higher thermal resistance than the E2 VG (it is not shown in Fig. 5.2 but has a thermal resistance slightly lower than the E7 VG).

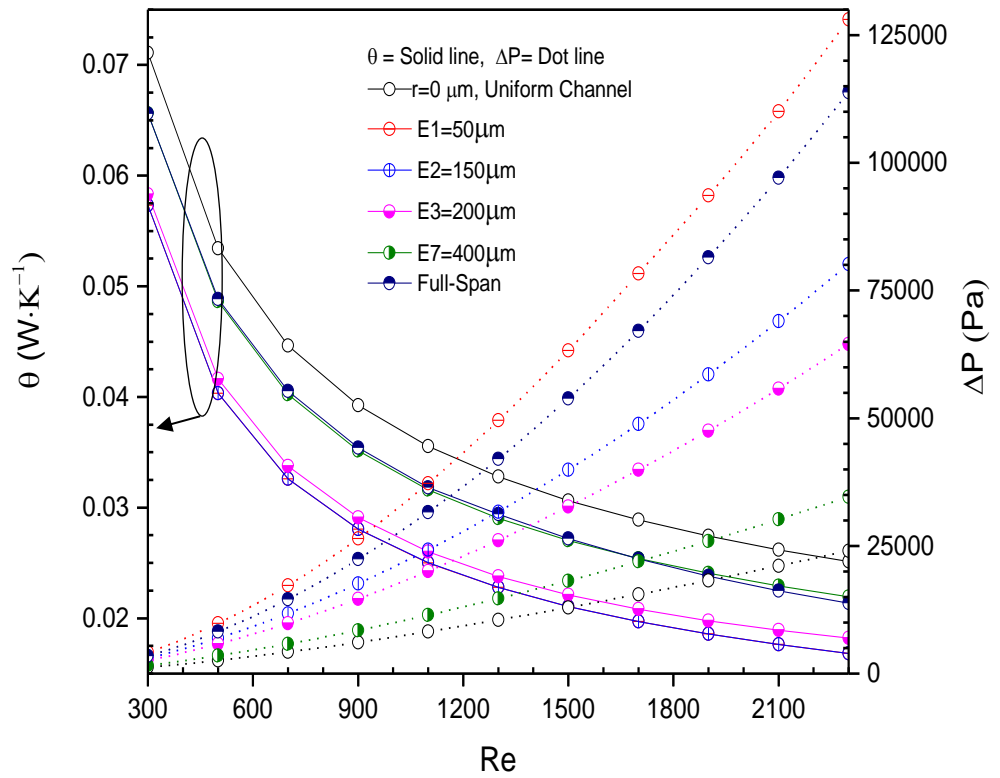


Figure 5.3: Thermal resistance and pressure drop versus Re for E-type VGs of radius 400 μm having various gaps of combined width indicated in the legend. The $r = 0 \mu m$ line refers to the uniform channel with no VG present.

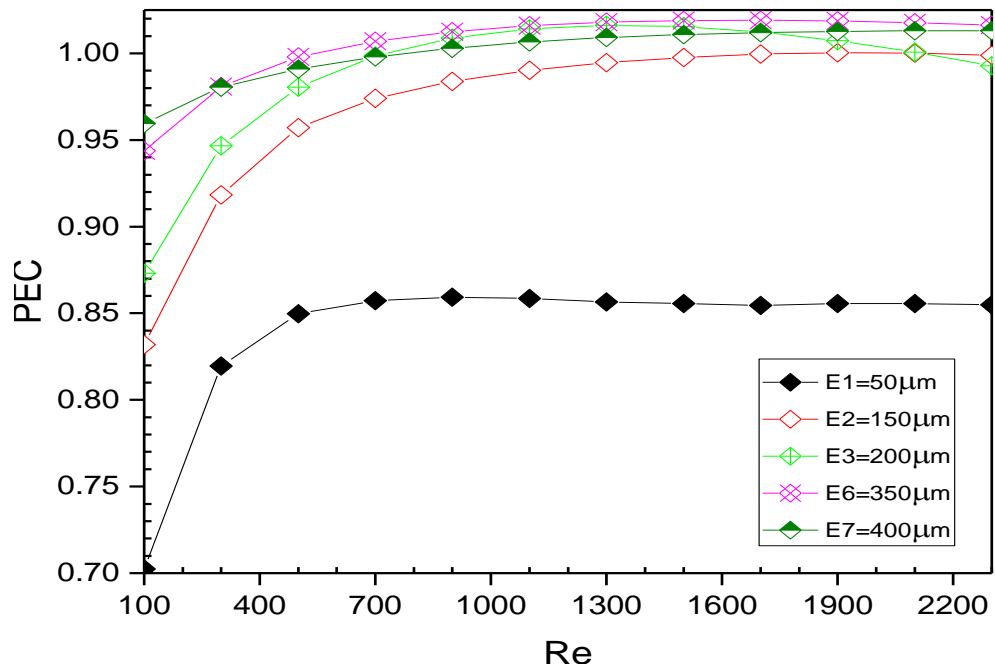


Figure 5.2: PEC index values for various end-gap widths.

5.2.4 Vortical flow structure and solid temperature distribution

The key effect of having a gap between the end of the VG and the channel wall, instead of a full-span VG, is that longitudinal vortices can be formed, i.e. with rotation axes parallel to the main flow direction. This can be seen clearly by tracing the 3D trajectories of passive particles in the flow, as shown in Fig. 5.4. A full-span cylindrical VG obviously completely blocks the flow in the lower part of the channel, and the inertia of the fluid passing over the VG results in an extended transverse vortex – i.e. with rotation axis perpendicular to the flow – see the blue trajectories in Fig. 5.4(a). There is also some weak large-scale rotation of the flow in the y - z plane, caused by the difference in boundary conditions at the solid side wall and symmetry plane, but the dominant effect is the transverse vortex.

With a gap present, the flow is very different and substantial longitudinal vortices arise – see the red trajectories in Fig. 5.4(b). Fluid which passes through the gap is swept upwards and towards the middle of the channel, as shown by the blue trajectories in Figs. 5.4(b) and (c), which is clearly beneficial for heat transfer from the solid surfaces of the base and side walls to the bulk fluid. Towards the middle of the VG there is still a transverse vortex element to the flow, but this is much more open than the clearly defined and essentially closed transverse recirculation behind the full-span VG seen in Fig. 5.4(a).

To illustrate the end gap effect on conjugate heat transfer, Fig. 5.5 shows temperature contours within the solid base and the solid side wall of the channel, on planes located $2\ \mu\text{m}$ from the solid-water contact surfaces. The plots compare full-span VGs with E2 VGs, with the flow from right to left, at $Re = 500$ as in Fig. 5.4. The contours for the full-span (F) VGs clearly show the influence of the VGs in reducing the local solid temperature via improved heat transfer to the fluid, though there are local hotspots behind each VG, corresponding to the enclosed transverse vortices seen in Fig. 5.4(a). In comparison, the E2 temperature contours show a consistent approximately 5K lower temperature at corresponding points in the channel. In particular, the side-wall contours (Fig. 5.4b) show a reduction in the vertical extent of the hotspots, and reduced temperatures in the upper areas of the wall, consistent

with the transport of fluid upwards and inwards (away from the wall) seen in Fig. 5.5(b).

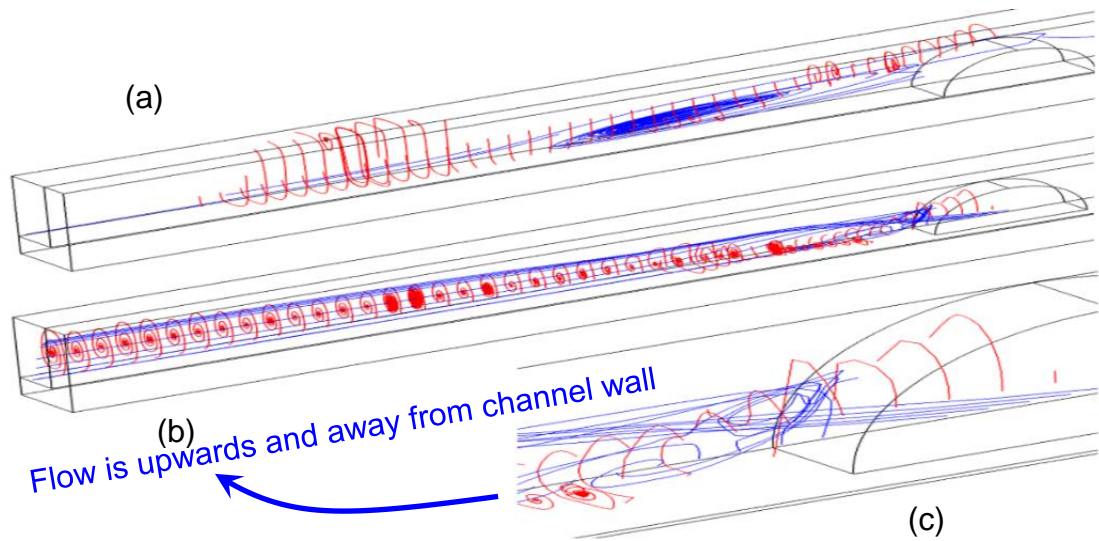


Figure 5.4: Paths of passive tracer particles in the flow, illustrating the effect of (a) a full-span cylindrical VG and (b) an E-type VG on transverse and longitudinal vortex generation. The VGs have radius $400\ \mu\text{m}$. The flow is from right to left with Reynolds number 500 and the gap at each end of the VG is $75\ \mu\text{m}$. Plot (c) is an enlarged view of (b).

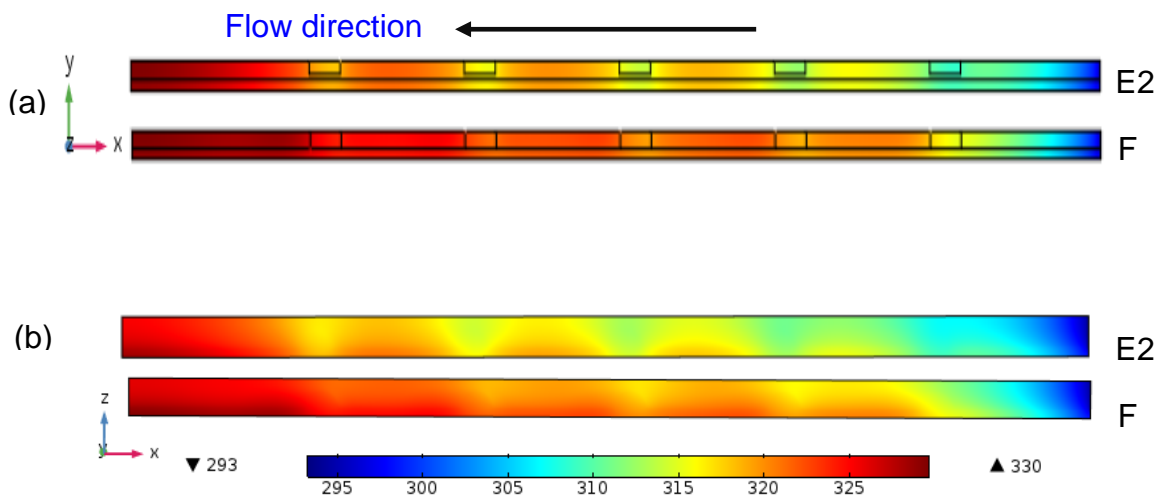


Figure 5.5: Temperature contours (in K) along channels containing five E2 or full-span (F) VGs. The planes shown are within the solid and located $2\ \mu\text{m}$ away from the water: (a) the base of the channel, (b) the side wall of the channel.

5.2.5 The effect of VG position and number

The results presented above are for a series of 5 equally-spaced VGs of radius $400\ \mu\text{m}$. Clearly this is just one configuration, therefore, it is interesting to explore the effect of changing that configuration. To illustrate the effect of VG position, a channel with a single E2 VG (of radius $400\ \mu\text{m}$) and vary the position, D , of the centre of the VG from the channel inlet considered. Fig. 5.6 shows that the VG position in the channel has barely any influence on the resulting thermal resistance of the channel, and only a small effect on the pressure drop due to the development of the flow from the inlet along the channel.

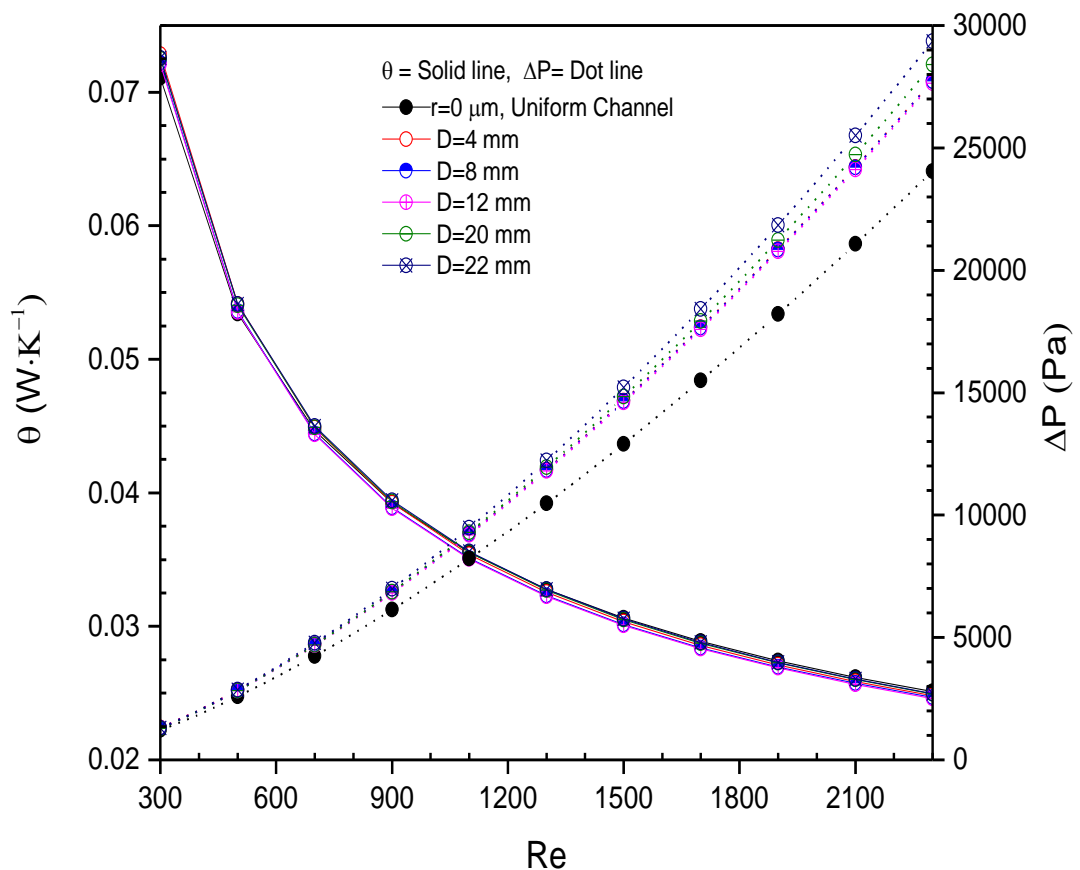


Figure 5.6: Effect of the number of E2 VGs on thermal resistance and pressure drop.

Though the position of the VGs is not important, the number of VGs will clearly influence both the thermal resistance and the pressure drop. Fig. 5.7 shows the values of these quantities for series of 4, 5 and 6 equally-spaced E2 VGs. As to be expected, adding more VGs lowers the thermal resistance but raises the pressure drop. However, in stepping from five to six VGs, the change in thermal resistance is rather less than the change in pressure drop, indicating that the benefit of decreased thermal resistance could be outweighed by the increased pumping power required. Indeed, this is confirmed by calculating the corresponding PEC values using Eq. (3-7), which are plotted in Fig. 5.8. The series of 5 VGs has an essentially neutral PEC (i.e. close to unity), especially for higher Re , indicating that increased pressure drop is balanced by a commensurate improvement in thermal performance. The series of 4 and

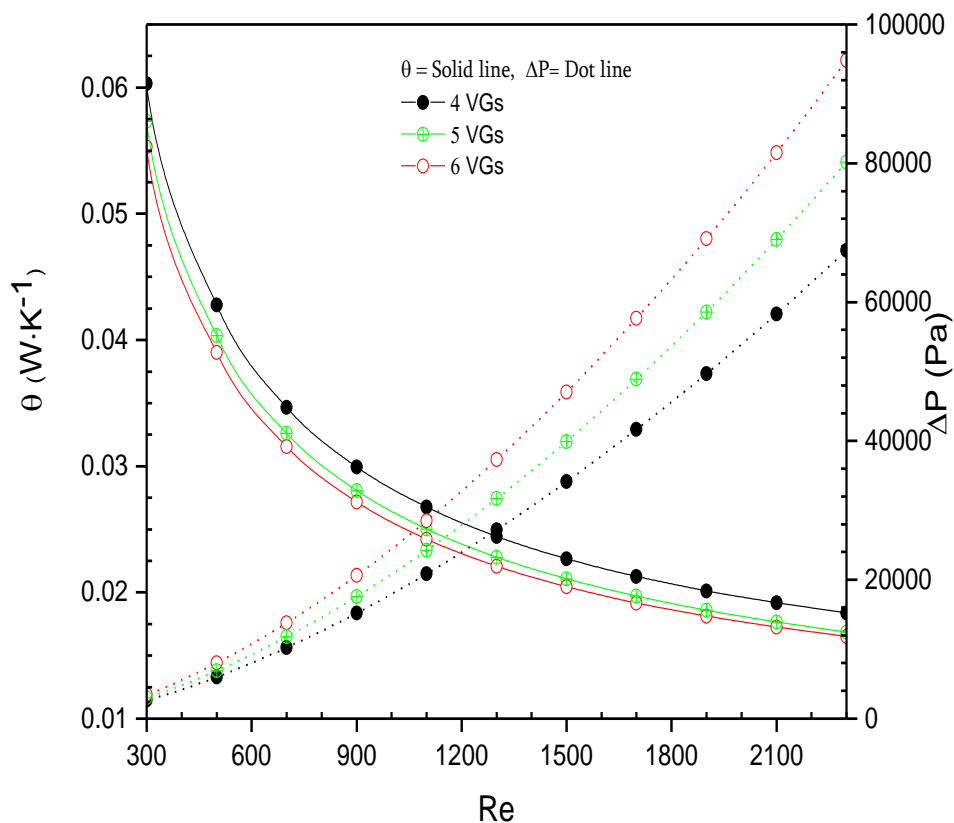


Figure 5.7: Effect of single E2 VG position on thermal resistance and pressure drop.

6 VGs have PEC also have values that are quite high, but they are both lower than for the 5 VGs. The cost of heat transfer enhancement in terms of the pressure drop penalty is therefore slightly higher than for the 5 VGs. All the remaining results presented here correspond to a series of 5 VGs.

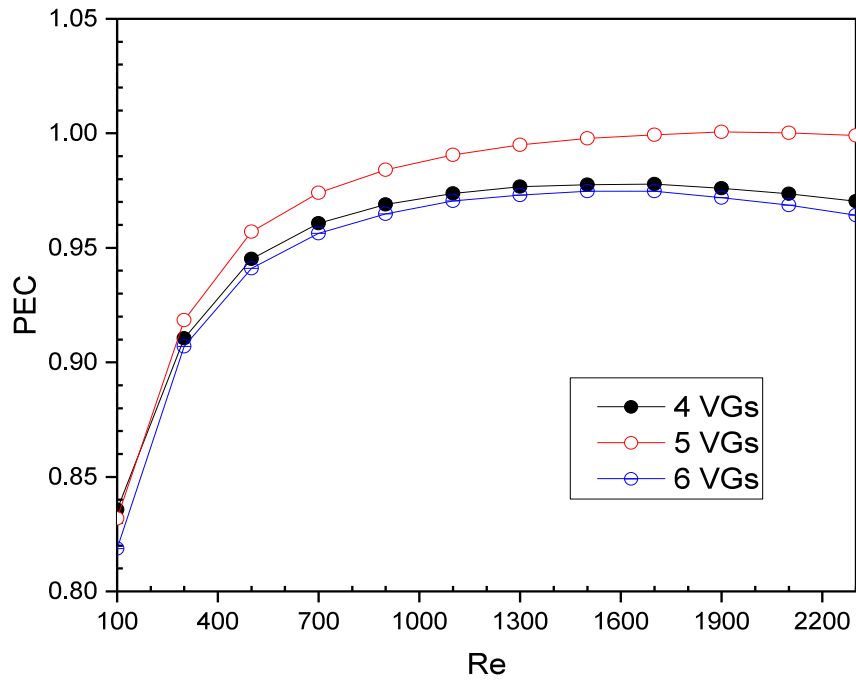


Figure 5.8: PEC versus Re for series of equally-spaced E2 VGs of radius $400 \mu\text{m}$.

5.2.6 The effect of VG radius

The results presented so far are all for VGs of radius $400 \mu\text{m}$ (as previously presented in chapter 4, section 4.3). This is to confirm that the thermal resistance decreased as the radius increased, while the pressure drop increased with the radius increment. Again, Fig. 5.9 shows how the VG radius affects the thermal resistance and pressure drop for a series of five E2 VGs. As is to be expected, increasing the radius generally reduces the thermal resistance. This is a result of an increased solid surface area in contact with the fluid and greater penetration of the (high-conductivity) solid into the bulk flow, as well as the mixing effects of the vortices generated. An exception to this is the very small-radius ($100 \mu\text{m}$) VGs at low Reynolds numbers. In that case, the thermal resistance is actually higher than that of the uniform channel. This is because at low Re the inertia of the flow passing over these small VGs is insufficient to generate a substantial recirculating wake. Instead, the fluid immediately behind the VGs is essentially stagnant, resulting in local hotspots and the associated increase in thermal resistance.

Clearly, increasing the radius of the VGs will increase the blockage of the micro-channel resulting in an increased pressure drop along the channel. This is evident in the pressure drop curves of Fig. 5.10, which highlight the dramatic increase in pressure drop for large radii. Similar observations are seen for the other VG configurations considered here.

Since the radius of the VGs produces a quantitative rather than qualitative change in behaviour (except for very small radii at low Re), for illustrative purposes the remainder of the results will be presented for VG radii of 400 μm . This is a convenient value for revealing the effects of the VG gaps prominently without too excessive a pressure penalty.

5.2.7 The effect of solid thermal conductivity

As stated in section 3.1, the solid material considered here is aluminium (thermal conductivity $238 \text{ Wm}^{-1}\text{K}^{-1}$), since this is a popular and economical material used for heat sinks. However, copper is also used for heat sinks and offers a higher thermal conductivity of $400 \text{ Wm}^{-1}\text{K}^{-1}$ (as well as a higher volumetric heat capacity). To assess the effect of the solid material on the

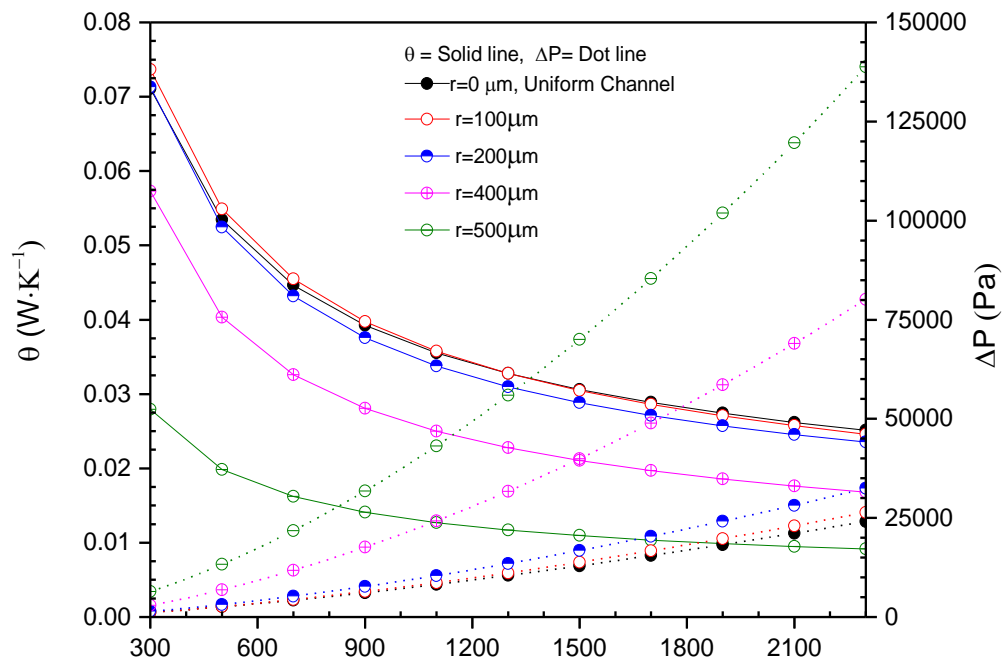


Figure 5.9: Effect of VG radius on thermal resistance and pressure drop for E2 VGs.

performance of the vortex generators, simulations with five E2-type VGs were repeated with copper as the solid material. Fig. 5.10 shows a comparison of the resulting temperature distributions in the channel side wall and channel base. The higher thermal conductivity of the copper of course results in faster heat conduction through the solid, which leads to greater heat transfer to the fluid occurring further upstream than with the aluminium. The thermal boundary layers develop more rapidly with the copper, such that downstream the boundary layer is thicker and heat transfer efficiency from solid to fluid is reduced. This results in higher downstream temperatures in the copper (see Fig. 5.10b and c). As a consequence, the calculated thermal resistance is slightly higher for the copper micro-channel, as can be seen in Fig. 5.11. The pressure drop (Fig. 5.11) is very slightly lower for the copper case because of the higher fluid temperature and consequential reduction in fluid viscosity.

Though there are clearly small quantitative differences in the calculated performance of the aluminium and copper micro-channels, the qualitative behaviour of the VGs is the same in both cases (see for example the temperature distributions in Fig. 5.10). Aluminium has several practical advantages over copper including its low density, lower cost and relatively easier manufacturability.

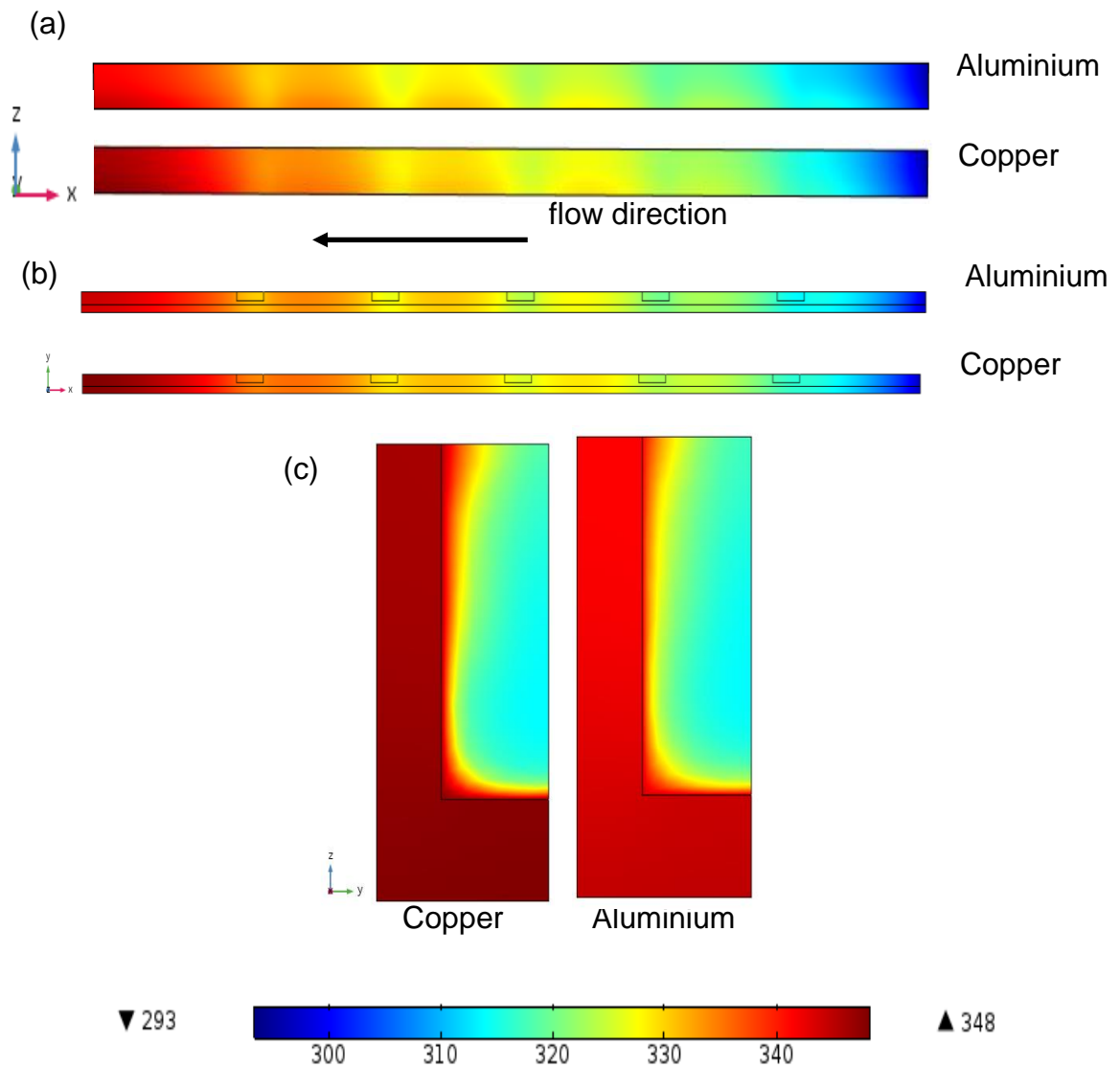


Figure 5.10: Temperature contours (in K) along copper and aluminium channels containing five E2 VGs of radius $400\ \mu\text{m}$ with flow at $Re=300$. The planes in (a) and (b) are within the solid, $2\ \mu\text{m}$ away from the water: (a) the side wall of the channel, (b) the base of the channel. The (y,z) cross-sections in (c) are at the outflow.

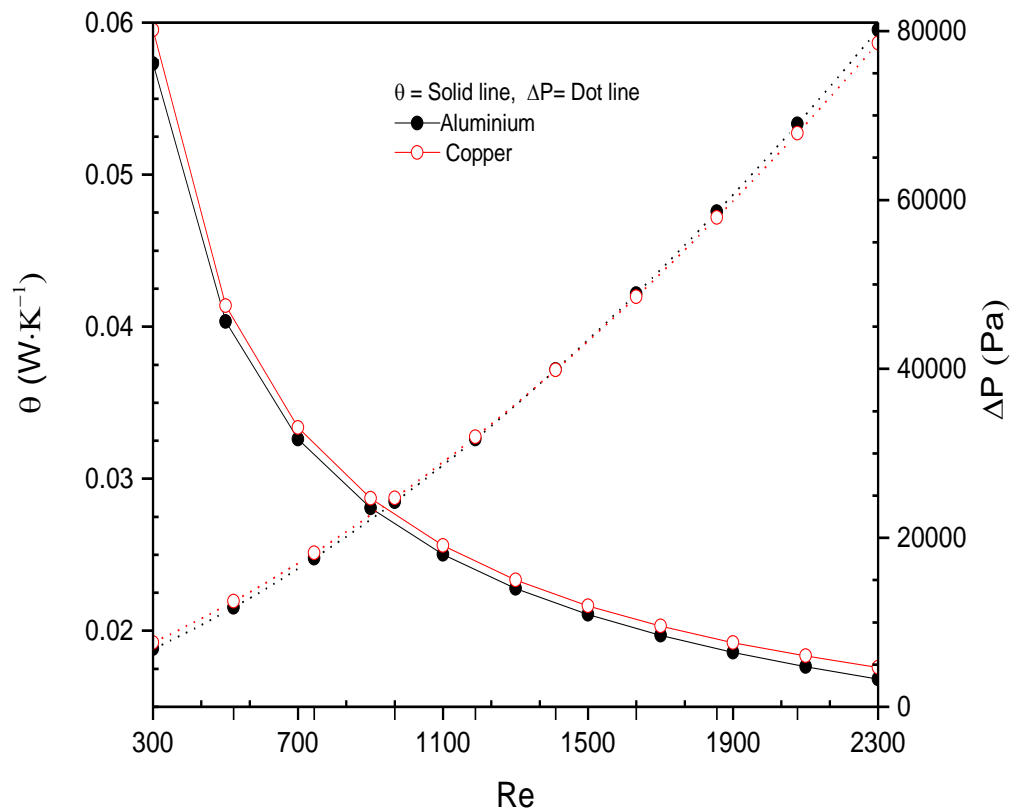


Figure 5.11: Performance of copper versus aluminium in terms of thermal resistance and pressure drop.

5.3 Vortex generators with a single central gap (C-type VGs)

Having seen the benefits of having a gap at each end of the VG, the effect of a single central gap is now assessed. Fig. 5.12 shows the corresponding thermal resistance and the pressure drop obtained for various gap widths, and compares this with the performance of the uniform channel and a channel with full-span cylindrical vortex generators present. For very wide gaps, the thermal resistance is similar to that of the uniform channel. As the gap is reduced, which is equivalent to extending two short VGs from each channel wall, the thermal resistance decreases. However, the change is not monotonic. For example, at $Re < 900$ the VGs with a 400 μm gap perform better than those with a 450 μm gap, but for larger Re the opposite is true. As in the case of small VG radii discussed in section 5.1.5, this is because at low Reynolds numbers the inertia of the flow is too weak to generate a substantial eddy behind the very short solid parts of the VGs. Improvement in heat transfer is primarily due to the increase in surface area and thermal bridging effect of the

higher conductivity solid. As Reynolds number and/or length of the VG increases, the additional benefit of the enhanced vortices leads to better thermal resistance. If the gap width is reduced further, thermal resistances better than that of the full-span VGs can be achieved, but there is an optimal gap of around $100\ \mu\text{m}$ below which the thermal resistance increases with decreasing gap. This is to be expected since as the gap width shrinks to zero, the performance should eventually tend to that of the full-span VGs.

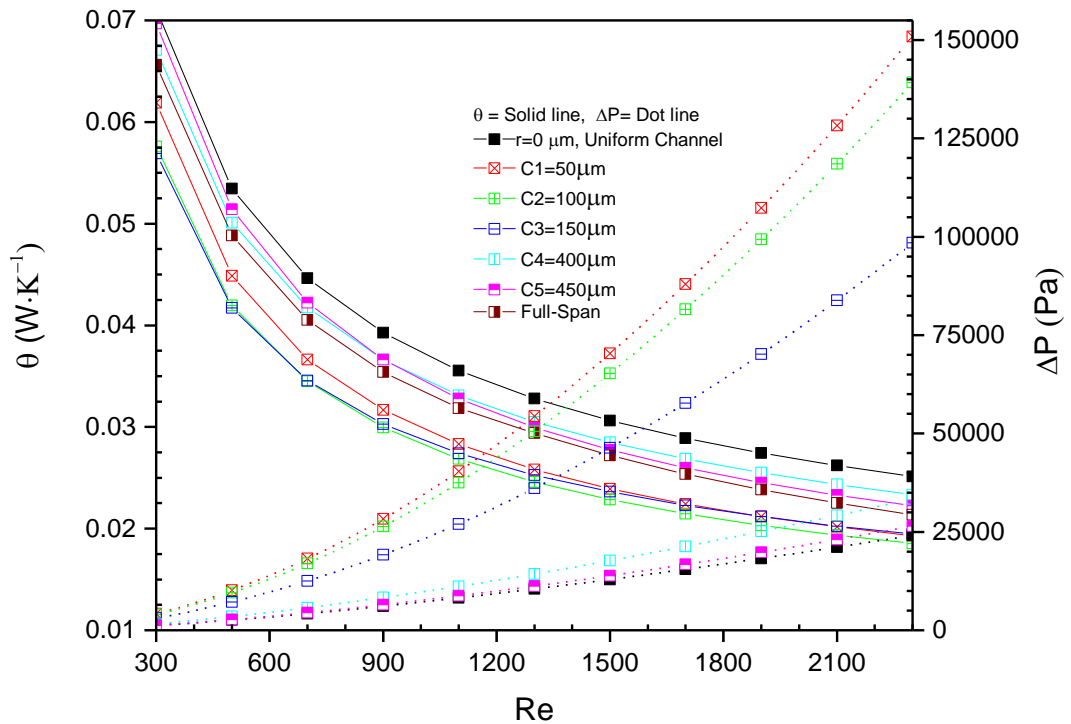


Figure 5.12: Thermal resistance and pressure drop calculated for C-type cylindrical VGs as a function of Reynolds number.

The pressure drop behaviour of the central-gap VGs is simpler and as to be expected: decreasing the gap monotonically increases the pressure drop from that of a uniform channel. Interestingly, the pressure drop for the central-gap VGs is somewhat higher than for the end-gap VGs with the same overall gap width. This results in a set of PEC curves with rather different shape – see Fig. 5.13 and compare with Fig. 5.3. In most cases the PEC value is quite low and diminishes substantially with Re . Only for relatively large gaps does the PEC value approach unity. For very wide gaps, the PEC value can exceed unity – notably for the C5 VG, which has a single central gap of width $450\ \mu\text{m}$,

and a corresponding PEC index of almost 1.1 for $Re = 2300$. Indeed this is the highest PEC value obtained from all the geometries examined here.

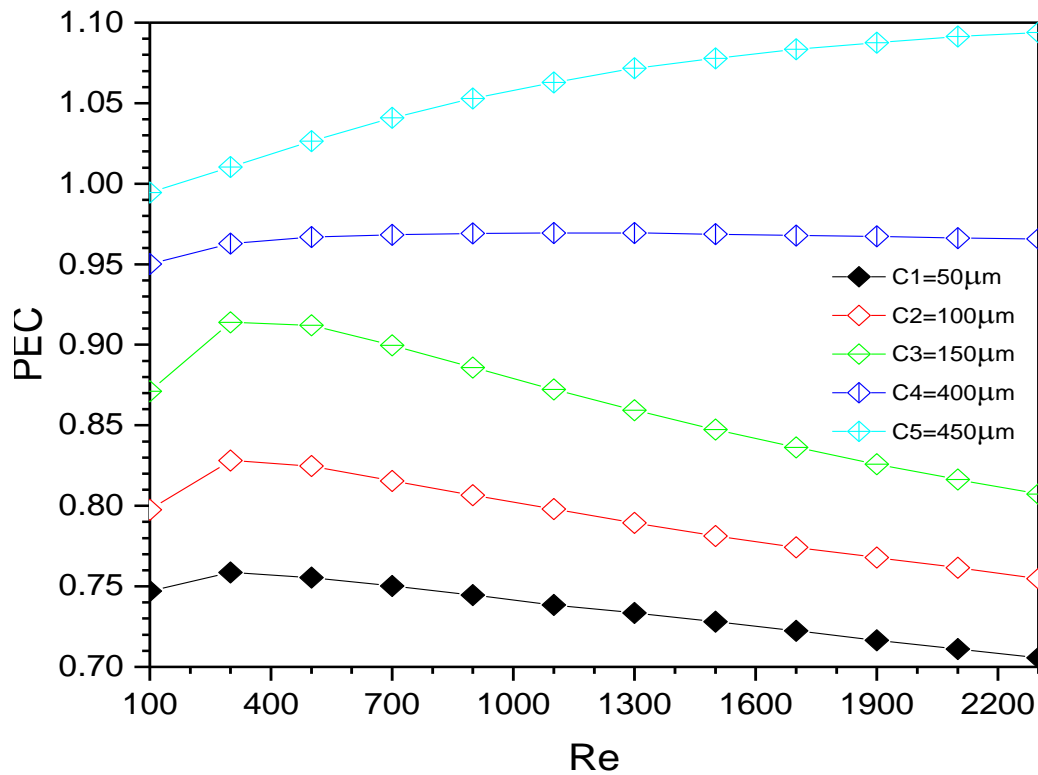


Figure 5.13: PEC values as a function of Reynolds number for the C-type VGs considered.

As Fig. 5.12 shows, the C5 VG provides a reduction in thermal resistance compared to a uniform channel, and the performance is almost as good as a full-span VG (the C5 thermal resistance is only 2% higher than the full-span value). However, there is a very large difference in the pressure drops associated with these VGs, which of course translates into the large difference in PEC index (1.1 versus 0.7 for C5 and full-span). Clearly, if the thermal resistance of the C5 VG is sufficiently low to maintain the required temperature of the system being cooled, it would appear to be a much preferable choice over the full-span VG as a result of the much lower pumping costs associated with it. This is considered further in chapter 7.

Though the pressure drop is quite high, the central gap VGs are effective in reducing the local temperature in the solid. To illustrate the temperature reduction that can be achieved relative to the full-span VGs, Fig. 5.14 compares (on the same scale) the temperature contours on a y - z cross-section through the fluid and solid, located just behind the first VG in the channel. Using VGs with a 100 μm central gap, the solid base at this point in the channel is cooled some 12K lower than with full-span VGs. Fig. 5.14 also indicates the more disturbed flow created by the C-type VG relative to the full-span VG, and the thinner thermal boundary layer. The temperature distributions along the channel are considered later, in section 5.5.3.

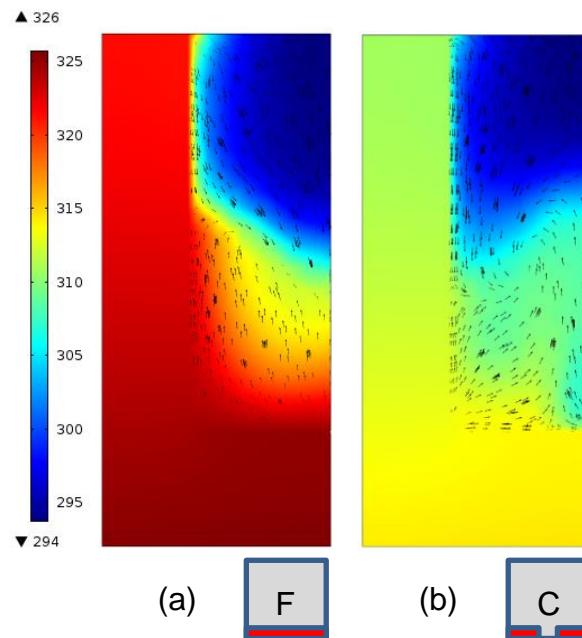


Figure 5.14: Temperature contours (in K) on a y - z plane located 100 μm downstream of the trailing edge of the first VG in the channel: (a) full-span VGs without gap, (b) C-type VGs with a central gap of 100 μm . The arrows indicate y , z velocity components at $Re=300$.

5.4 The effect of combining central and end gaps

Since a central gap and end gaps have each been shown to be beneficial, it is natural to ask if combining them in a single VG would provide even better performance. Fig. 5.15 shows the calculated thermal resistance of CE-type VGs which have a fixed gap of 100 μm at each end, and a central gap that is

varied from 50 to 250 μm . The gap widths indicated in the legend refer to the combined width of all three gaps. The end gaps in these VGs are equivalent to those in the E3 vortex generator (see Table 1). Comparing the E3 curve in Fig. 5.2 with the curves in Fig. 5.15 shows that introducing the central gap in addition to the end gaps actually degrades the performance in terms of heat transfer – i.e. the thermal resistance increases. Opening up a central route for the flow reduces the intensity of the flow through the end gaps, and consequently the strength of the longitudinal vortices generated near the channel walls and base. As the central gap is widened, the thermal resistance increases and approaches that of a uniform channel without VGs present.

Thinking in terms of the solid parts of the VGs rather than the gaps, an interesting corollary to the above observation is that two localised short cylindrical VGs are less effective in improving the thermal resistance than two small gaps at the ends of an otherwise solid VG. The PEC index values for the CE-type VGs are all less than unity; they mainly follow a similar profile to Fig. 5.3, with PEC values between 0.9 and 0.97, apart from the smallest gap (CE1), whose PEC index falls off more sharply with Re , reaching a value of 0.88.

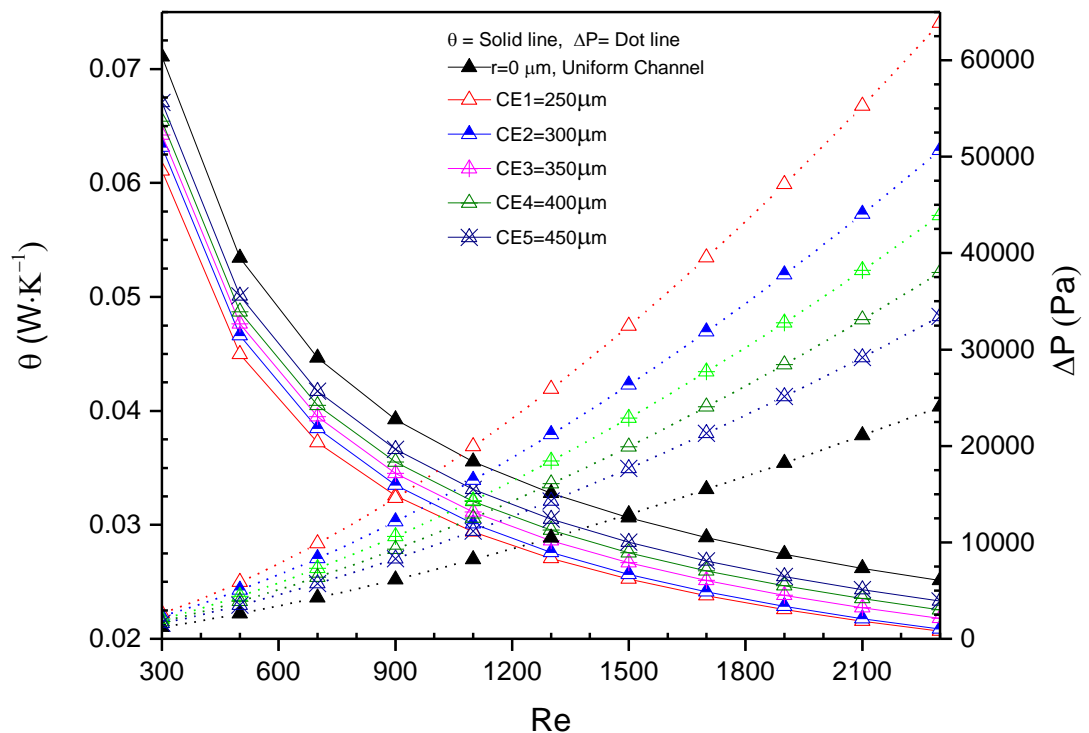


Figure 5.15: Calculated thermal resistance for CE-type VGs with a gap of 100 μm at each end and a variable width central gap. The width in the legend refers to the combined width of all three gaps.

5.5 Comparison of the ‘best’ of each vortex generator type

Having explored separately three different gap configurations, this section compares them against each other. Specifically the ‘best’ of each type of VG is considered, where ‘best’ refers to the gap width that provides the lowest thermal resistance for each VG type.

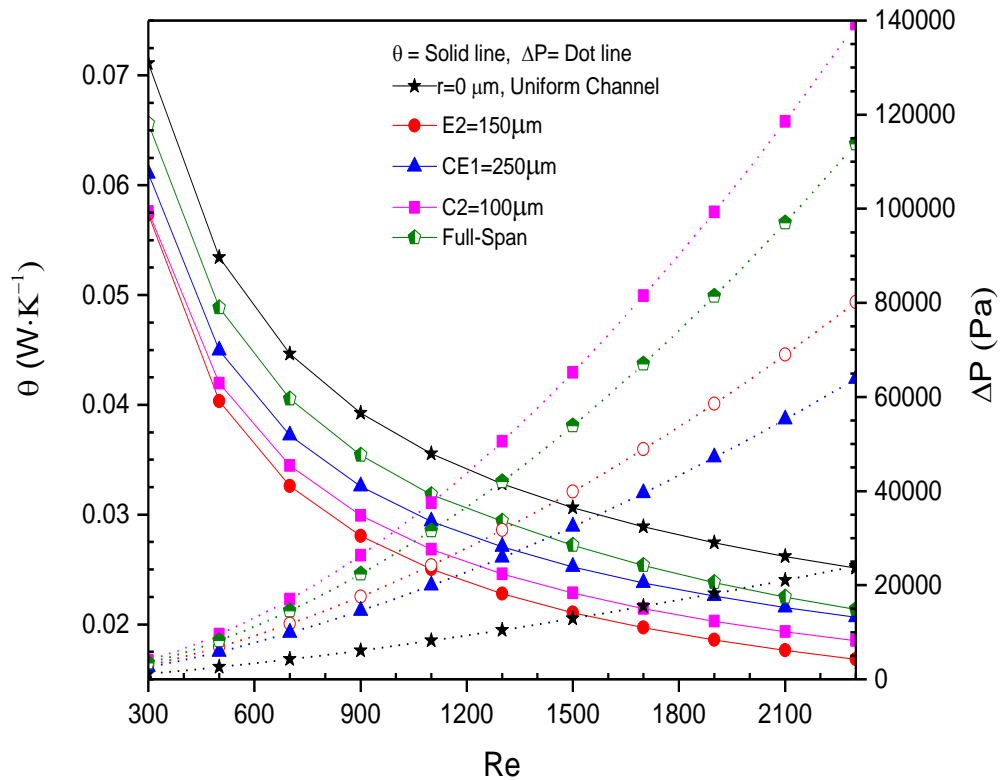


Figure 5.16: Comparison of the thermal resistances and pressure drops for the ‘best’ of each VG type.

5.5.1 Thermal resistance and pressure drop

As can be seen in Fig. 5.16, the lowest overall thermal resistance is that of the E2 vortex generators then, in order, the C2, CE1, and full-span VGs, all of which reduce the thermal resistance below that of a uniform channel. The end gaps of the E-type VGs are most effective as the longitudinal vortices are generated close to the side wall, meaning that they can improve the alignment of the flow with the temperature gradient normal to both the channel side wall and the base.

Of these VGs, the lowest pressure drop is that of the CE1 VG, followed in ascending order by E2, the full-span, and finally the C2 VG. Somewhat surprisingly, the C2 VG, with a single central gap of 100 μm , produces a higher pressure drop than the full-span VG. This is attributed to the increased viscous drag from the vertical sides of the narrow gap. For larger central gaps (wider than about 150 μm) the pressure drop is reduced below the level of the full-span VG, as the flow route through the gap opens up. The E2 VG, on the other hand, produces a lower pressure drop than the full-span VG, even though it has two narrow gaps of 75 μm . This is because at the ends of the VG the viscous drag is dominated by the much larger vertical side walls of the channel, and the more open flow path introduced by the gaps quickly outweighs any relatively small additional viscous drag. The CE1 VG has a larger overall gap width, so its low pressure drop is to be expected.

5.5.2 Thermal-hydraulic performance index

Fig. 5.17 plots the PEC index against Reynolds number for the VGs of each type that produce the greatest thermal conductance (i.e. lowest thermal resistance), and includes for reference the PEC index for the full-span VG system. Clearly the large increase in the pressure drop when full-span VGs are present is not compensated by a commensurate improvement in thermal conductance, and the PEC value is less than 0.8, falling to 0.7 at higher Re . Introducing gaps into the VGs improves the PEC index, but the high pressure drop of the C2 VGs means that the PEC value is not much better than the full-span VGs. Although the CE1 VG has a low pressure drop, its relatively poor improvement in the thermal conductance results in PEC values below unity but better than the C2 VG. The best PEC is that of the E2 VG, which, as seen already, has a good PEC index close to unity. This behaviour highlights the fact that the small end gaps promote more intense longitudinal flow disturbances along the length of the channel side wall, enhancing heat transfer from the side wall as well as the base surface.

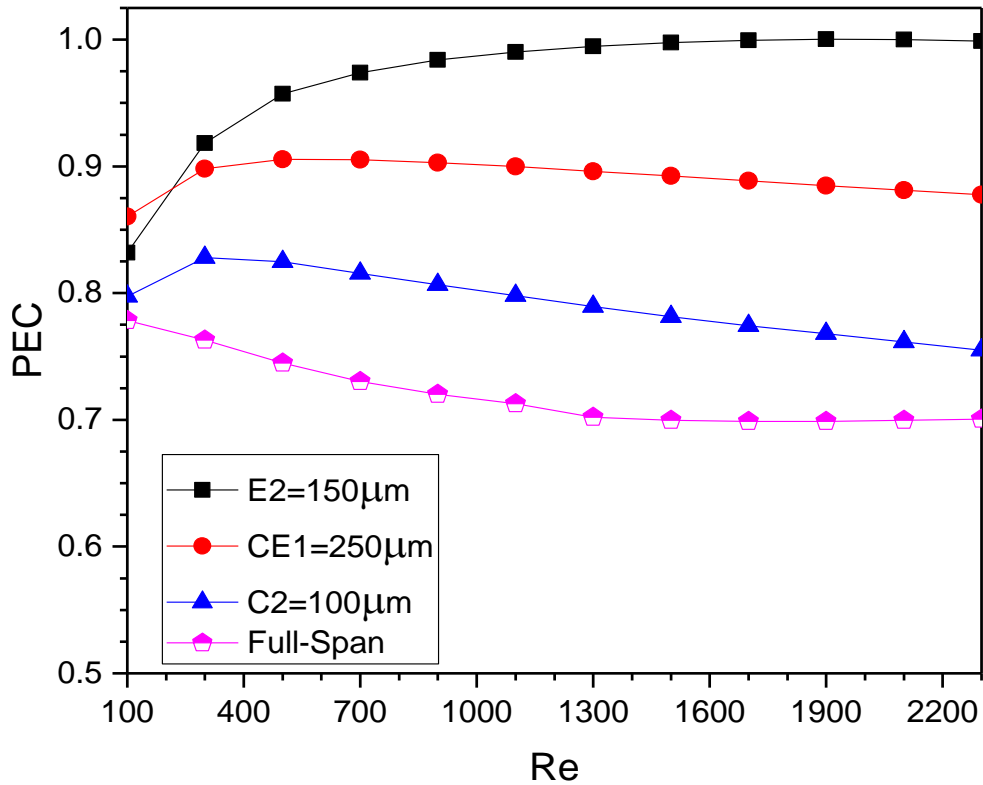


Figure 5.17: Performance Evaluation Criteria (PEC) index, equation (3.14), versus Reynolds number for the VGs of each type offering the lowest thermal resistance.

5.5.3 Solid and fluid temperature distributions

For a more visual picture of the performance of the different VGs in terms of the temperature distributions, Fig. 5.18 shows temperature contours on vertical and horizontal longitudinal cross-sections of the channel for the same VGs as in Fig. 5.16 operating at $Re = 300$. For comparison, corresponding contours for the uniform channel (i.e. without VGs) are also included. In the full-span VG plot in Fig. 5.18 (a) the presence of the closed transverse vortex generated behind each VG (see Fig. 5.4a) is clearly seen in the elevated temperatures of the fluid there, and there is some localised reduction in the solid temperature as a result (see Fig. 5.18b). Also shown well in Fig. 5.18(a), in the 'E2' plot, is the trail of hotter fluid that is transported upwards and into the bulk stream by the longitudinal disturbance generated by the gap between the VG and the channel wall. Compare this with the blue fluid trajectories

plotted in Fig. 5.4(b). This clearly leads to a substantially reduced temperature of the solid base, as can be seen in Fig. 5.18(b). A similar uplift of warmer fluid behind the VGs is seen in the 'CE1' plot of Fig. 5.18(a), but the effect is weaker as a result of the central gap diminishing the flow through the end gaps. The flow through the single 100 μm central gaps in the C-type VGs clearly improves the local heat transfer at each VG, as the temperatures of the VGs shows, but there is also a longitudinal effect visible on comparing the 'C2' and full-span plots in Fig. 5.18, which improves heat transfer to the fluid along the length of the channel downstream of the first VG.

To complement the side- and bottom-view plots of Fig. 5.18, Fig. 5.19 shows velocity and temperature plots on spanwise cross-sections of the channel. The velocity contours in Fig. 5.19(a) show the x-component, with positive values indicating flow towards the outlet and (dark blue) negative values corresponding to reverse flow. The cross-sections are located 100 μm downstream of the first VG (the position indicated approximately by the white dashed line in Fig. 5.18a), and also show the y-z velocity vectors. The full-span plot shows the strong down-channel flow above the VG and low-velocity flow immediately behind the VG. In contrast, the CE, C and E plots show the enhanced velocity arising from the gaps. The CE gaps are the widest, and this is reflected in the faster flow at the bottom left and the correspondingly reduced speed of the flow over the top of the VG. The swirling effect generated by the gaps in the three cases is also visible in the y-z velocity vectors. As discussed above, the end gaps generate a flow directed upwards along the channel wall, and this is visible in the circulatory patterns in Fig. 5.19 (indicated by the overlaid arrows). In contrast, when a single central gap is present, the circulation generated is in the opposite sense, leading to a flow down the channel wall.

Fig. 5.19(b) shows temperature contours on a cross-section located 2000 μm downstream of the centre of the last VG in the channel, which is the location indicated approximately by the black dashed line in Fig. 5.18(a). The plots also show y - z velocity vectors. The temperature contours clearly show that the E-type VG produces a significantly lower solid temperature than the other VG geometries. The longitudinal vortex created by the gap is also evident in the swirl of the velocity vectors in the rightmost plot of Fig. 5.19(b), and this allows better penetration of the cooler fluid into the the corner between the side wall and base. A similar vortex can be seen in the CE-type VG plot, but the intensity is much reduced by the presence of the additional flow route through the central gap. For the C-type VG, a substantial central plume of warmer fluid can be seen as a result of the single central gap promoting heat transfer from the base of the channel. However, the C-type and CE-type VGs both exhibit thicker thermal boundary layers in this region downstream of the final VG,

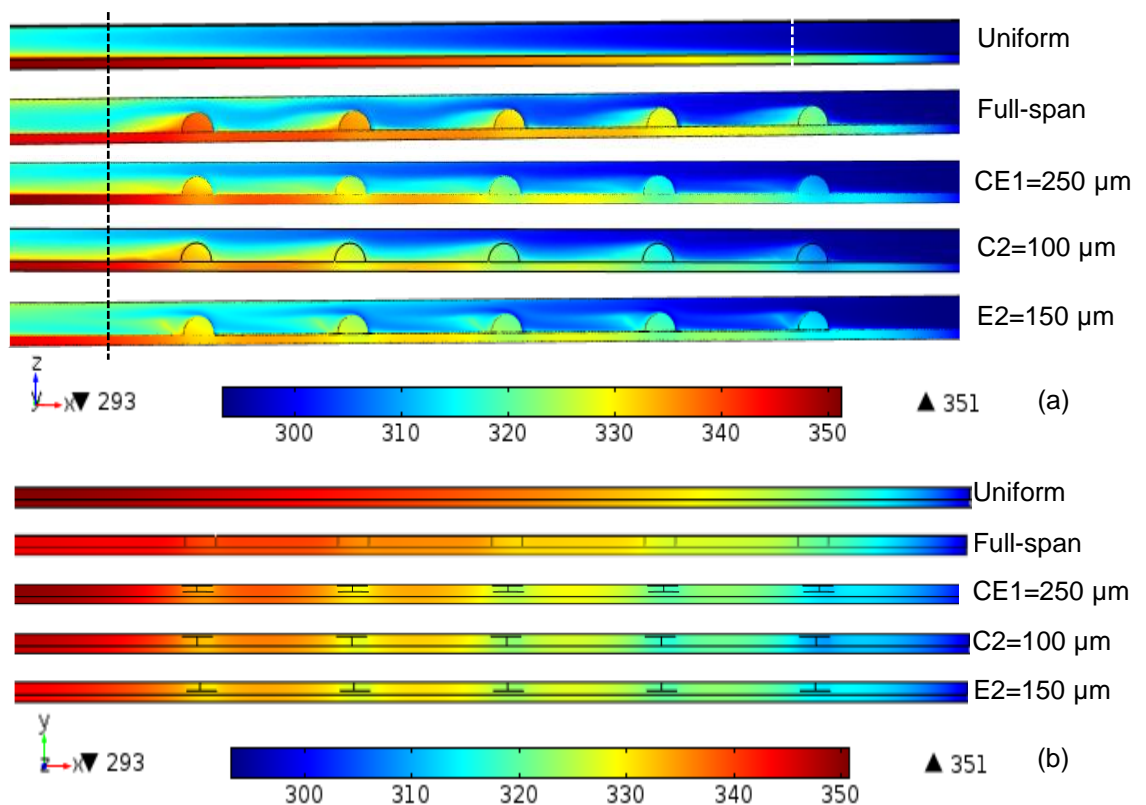


Figure 5.18: Temperature contours on (a) a plane parallel to the side wall located 100 μm from the wall, and (b) a plane parallel to the solid base located at 2 μm below the fluid flow, for different VG types operating at $Re = 300$. The flow is from the left to the right.

resulting in slightly higher solid temperatures here than for the full-span VG, despite the temperatures upstream being lower than for the full-span VG. This will be considered further in chapter 7.

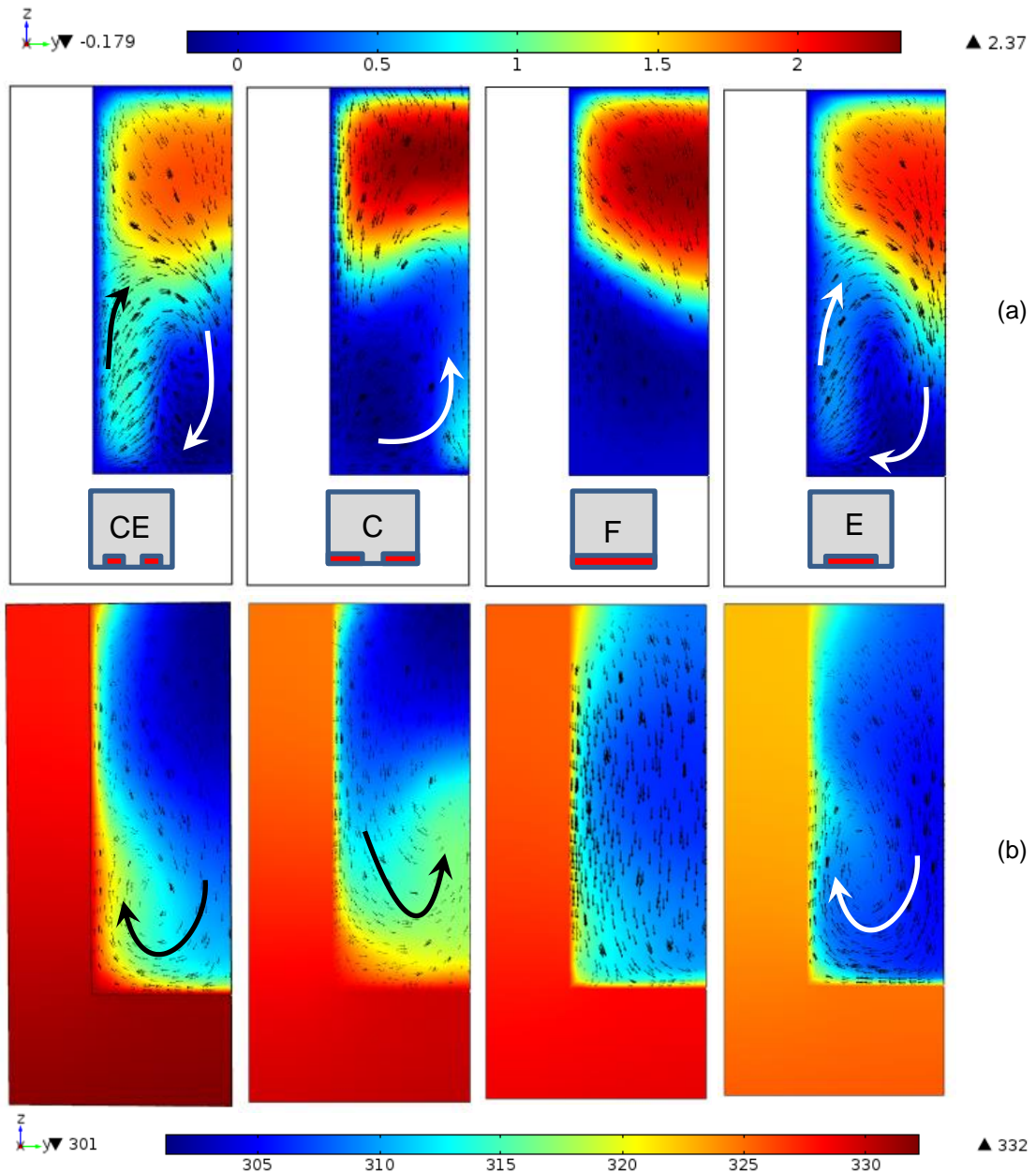


Figure 5.19: (a) Contours of the x component of fluid velocity (in m/s) and y,z velocity vectors on a spanwise cross-sectional plane located $100\ \mu\text{m}$ downstream of the first VG; (b) temperature contours and y,z velocity vectors on a cross-section located $2000\ \mu\text{m}$ downstream of the centre of the last VG in the channel. The Reynolds number is 500, and the VGs are (from left to right) CE1, C2, full-span, and E2 (see Table 5.1).

5.6 Summary

The 3D numerical analysis presented here set out to examine the benefits of having various gaps along the span of cylindrical vortex generators placed across the base of a water-filled micro-channel to enhance heat transfer. The geometries have been assessed at Reynolds number 300-2300 in terms of their thermal resistances, pressure drops, a performance evaluation criteria index combining both of these, and the maximum temperature of the base. The baseline geometry is a micro-channel containing solid full-span VGs, which generate transverse vortices.

It was found that, by all measures, having gaps between each end of the VGs and the channel side walls offers enhanced performance. Introducing these gaps produces longitudinal vortices adjacent to the channel side walls which enhance the heat transfer from those walls into the bulk flow. Importantly, three-dimensional tracer particle trajectory plots show that in addition to the longitudinal vortices generated downstream of the VGs, the fluid passing through the end gap is swept upwards and inwards, where it remains as it flows onwards to the outflow. This provides a significant additional heat transfer route for hot fluid to be transported directly away from the solid surfaces. The presence of the end gaps also reduces the pressure drop compared to the full-span VG, and for gaps of 100 μm at each end the PEC index is slightly above one for most Reynolds numbers, indicating that the pressure drop penalty compared to a uniform channel is more than compensated for by the improvement in thermal conductivity. The gap size offering the best thermal conductivity, and the lowest maximum base temperature, is 75 μm at each end, for which the PEC index is close to 1, i.e. neutral, especially at higher Re .

Having a single central gap was found to offer localised enhancement of heat transfer, which when considered over the whole base surface produced a lower average temperature and hence lower thermal resistance. However, the maximum temperature of the base, close to the outflow, is actually higher than that for a full-span VG, and close to that for a uniform channel without VGs present. From a practical perspective of maintaining the base of the heat sink at a given temperature, this is clearly undesirable. Small central gaps (e.g.

100 μm) are also found to increase the pressure drop relative to the full-span VG, and the PEC index for such gap sizes is correspondingly poor. On the other hand, large central gaps (e.g. 450 μm) have a high PEC index of up to 1.1, but produce average temperatures slightly above those for the full-span VG and maximum temperatures above even those for a uniform channel. This highlights that the PEC index should only be used in conjunction with specific actual rather than relative measurements of performance. Combining a central gap together with end gaps (of 100 μm) was found not to be beneficial, as the negative aspects of the central gap generally outweighed the positive effects of the end gaps.

The end-gap configuration outperforms the other configurations explored here, but there is an optimum end-gap width below which the pressure drop increases rapidly with no gain in heat transfer performance. For the system considered here, this gap was found to be 15% of the channel width.

There are of course many other configurations of VG gaps that could be considered for analysis, such as gaps that are staggered between consecutive VGs, rather than aligned as in the present study, and different spacing and distributions of the VGs within the channel. However, the clear conclusion from this work is that gaps at the ends of the VGs are beneficial in terms of the average temperature and in reducing the large pressure drop associated with full-span cylindrical vortex generators. Having said that, looking at the average temperature in the practical application of the micro-channels does not actually give a complete picture. It is also important to take the maximum temperature into the consideration, and this is discussed in chapter 7 in terms of energy management of heat transfer and fluid flow.

Chapter 6: Evaluation of nanofluid performance

6.1 Introduction

As indicated in chapter 1, an alternative to modifying the heat sink geometry to improve heat transfer is to modify the working fluid to enhance its thermal properties. Having explored VG geometries in the previous chapters, this chapter now explores the possibilities to use nanofluids. In this study, two types of nanofluids are used to assess the performance of the heat transfer and the fluid flow. The nanofluids consist of Al_2O_3 or SiO_2 nanoparticles in different concentrations up to 4% in water as a base fluid. The microchannel geometries considered are a uniform channel without VGs and channels with VGs. In the previous chapters, the performances of the different vortex generators were compared at equal Reynolds numbers. This was a reasonable and sensible approach since the properties of the working fluid were the same in each case, and the same conclusions would have been drawn had the VGs been compared on the basis of equal volumetric or mass flow rate. However, when comparing the heat transfer performances of different nanofluids, careful consideration must be given to the basis for comparison and the presentation and interpretation of the results. The reason for this is that increasing the nanoparticle concentration or changing the nanoparticle type in a nanofluid changes the viscosity and density of the nanofluid. Therefore an enhancement in heat transfer rate observed with one nanofluid compared to another at the same Reynolds number could in fact simply be due to an increase in the flow speed required to maintain the Reynolds number with a more viscous liquid. This issue has been recognised in a few previous studies [236, 237] and is discussed further in this chapter.

Using nanofluids themselves in a system need to be investigated in terms of fluid flow due to their thermo-physical properties change. Therefore, before applying nanofluids in a micro-channel having VGs, an important examination should be done to explore what is the suitable behaviour of the flow? Is it a fixed Reynolds number or a fixed mass flow rate? This is the first question that this chapter answers by exploring nanofluid performance in a uniform channel.

The next step in the current chapter is then to provide a clear picture of heat transfer performance of a combination of nanofluids with geometries having VGs. As illustrated in the literature, nanofluids have high thermo-physical properties compared to the base fluid. From a fluid flow perspective, the pressure drop of nanofluids is higher than for water at fixed flow rate due to high viscosity compared to water. Therefore, it is interesting to investigate the influence of the geometry on the pressure drop and suggest a new geometry which has lower pressure drop than those considered previously in thesis. Based on the findings of chapter 4, it was concluded that the micro-channel having the half-circular VGs (C-model, shown in Fig. 6.1a) offered lower pressure drop than triangular or rectangular VGs. Therefore, a new design of a half-elliptical VG (EL-model, shown in Fig. 6.1b with dimensions detailed in Table 6.1) is suggested which might offer lower pressure drop compared to the C-model.

Based on the suggested VGs, if there is a pressure drop difference between the half-circle and half-elliptical VGs, nanofluids can possibly be used with the geometry which has lowest pressure drop. Therefore, nanofluids in the half-elliptical VGs geometry are compared to the half-circle VGs geometry using water to assess the influence of different properties of fluids with association of different geometry on conjugate heat transfer. The key idea of this study is to examine the influence of nanofluids on the thermal resistance and pressure drop.

The results presented below focus on the particular value of 100 W/cm^2 for the heat flux, because this corresponds to the upper temperature limit for operation of electronic devices [153, 265-267].

This chapter is broken down into two main sections which are uniform channel and VG models, each section includes sub-sections which are fixed Reynolds number and fixed mass flow rate. Moreover, the sub-sections are also divided into two sub-sections represented by the thermal resistance and pressure drop effects.

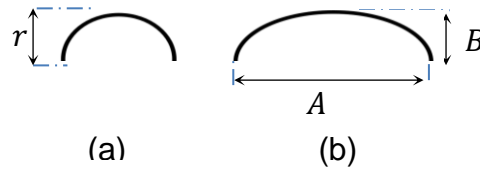


Figure 6.1: Side view of VGs: (a) half-circle (C); and (b) half-elliptic (EL).

Table 6.1: VGs dimensions in μm .

EL-model		C-model	
A	266	r	200
B	150		

6.2 Evaluating nanofluid performance in a uniform channel

In this section, two types of nanofluids are used in a uniform channel under laminar flow conditions. The nanofluids are Al_2O_3 - and SiO_2 -water nanofluids with different concentrations up to 4%, and they are compared to pure water to examine the resulting thermal resistances and pressure drops at fixed Reynolds number and at fixed mass flow rate.

Three-dimensional simulations were conducted with Reynolds number in the range of 50-1000 and mass flow rate ranging from 3.03×10^{-5} to 6.06×10^{-4} kg/s at a constant heat flux of 100 W/cm^2 . The uniform channel described in chapter 3 (see Fig. 3.5 with the dimensions shown in Table 3.1) is used to establish baseline behaviours of the different fluids.

6.2.1 Thermal resistance

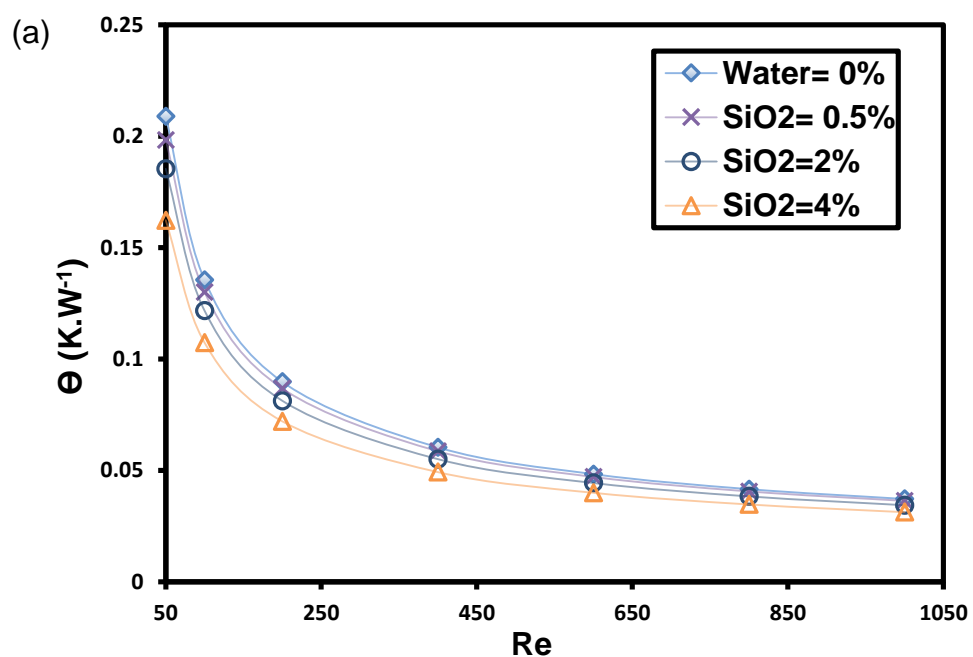
As in previous chapters, the thermal behaviour of the system is considered in terms of the thermal resistance detailed in eq. 3-6. To begin, the thermal resistances achieved with different nanofluids are compared on the basis of flow at equal Reynolds number. The impact of nanofluids can be introduced as three influences on thermal resistance which can be seen in Fig. 6.2. The first influence is that of nanoparticle concentration. A comparison of different

concentrations up to 4% of the Al_2O_3 and SiO_2 nanoparticles in water as a base fluid together with the pure water itself is shown in Fig. 6.2 a and b. It is found that thermal resistance decreased as the concentrations of nanoparticles increased. Since plotting as a function of Reynolds number effectively ignores changes in viscosity and density, this decrease in thermal resistance could be interpreted as being a result of the greater thermal conductivity of nanofluids compared to pure water.

The second influence is the impact of nanofluid type at the same concentration of nanoparticles. Fig. 6.2c shows that Al_2O_3 -water offered slightly better heat transfer rate than SiO_2 -water at the concentration of 4%. This is because of the higher thermal conductivity of the Al_2O_3 -water compared to SiO_2 -water (see Table 3.5).

The last influence is the reduction of thermal resistance using nanofluids compared to the pure water. This is because of the thermo-physical properties enhancement due to adding nanoparticles having high thermal conductivity into the water as a base fluid.

Again, the reduced thermal resistance could be interpreted as being because of the higher thermal conductivity of nanofluids compared to water. However, it is important to recognise the difference in the viscosity and density of the fluids.



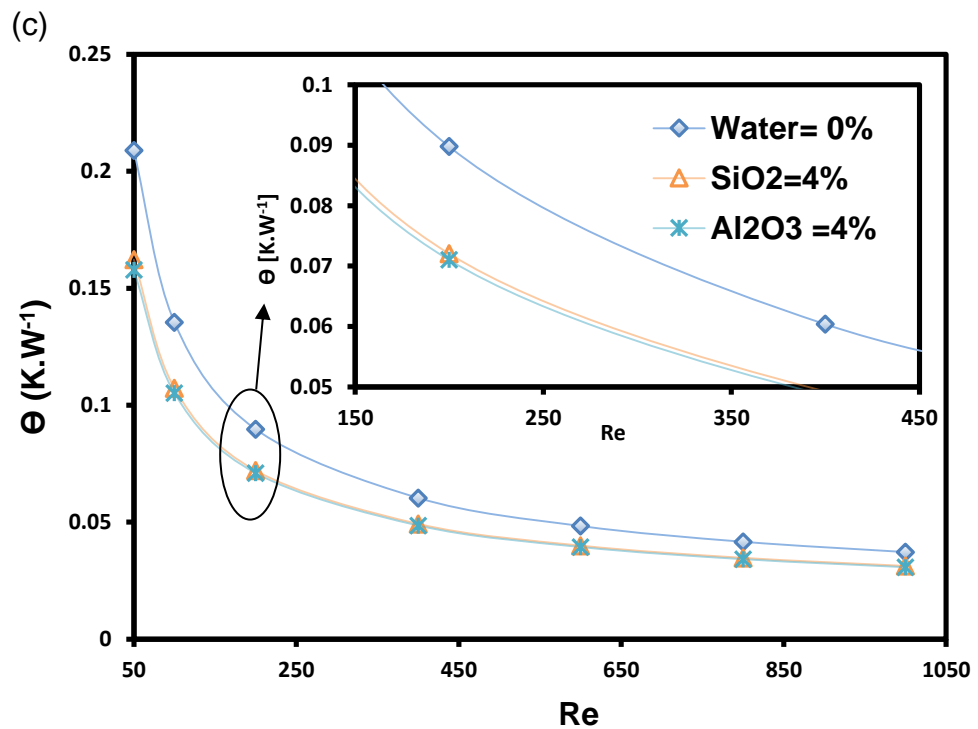
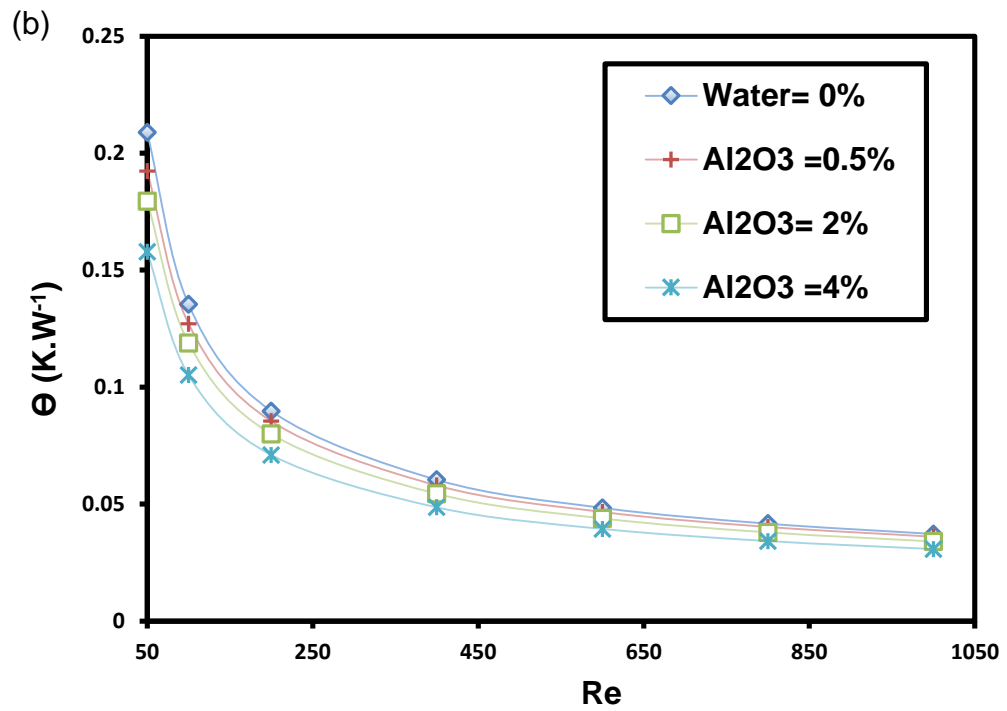


Figure 6.2: Thermal resistance of different working fluids with various concentrations in the uniform channel; (a) SiO₂-water at different concentrations up to 4% with water, (b) Al₂O₃- water nanofluids (4%) and water, (c) a comparison of Al₂O₃ and SiO₂ nanoparticles in the water (0 and 4) %.

The kinematic viscosity of nanofluids increases with nanoparticles concentration as shown in Fig. 6.3. Hence comparing the performance of a nanofluid with that of water at the same Reynolds number in the same geometry actually means that the nanofluid must be flowing in a higher speed.

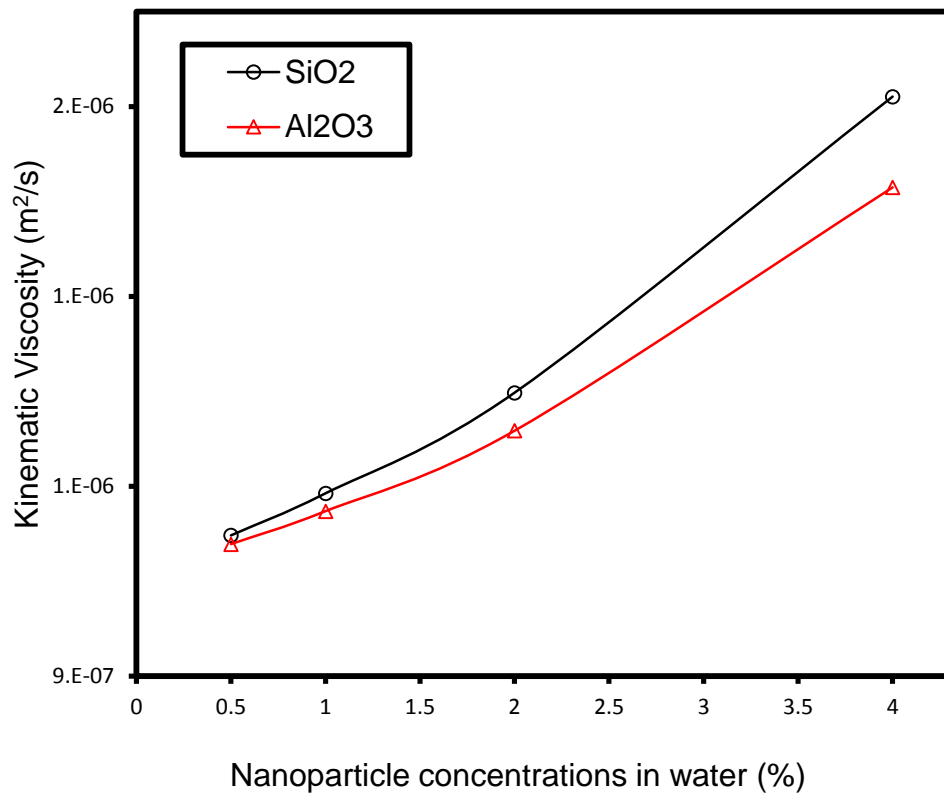


Figure 6.3: Kinematic viscosity of different nanoparticles concentration.

As many plots in this thesis show, the thermal resistance naturally decreases with increasing flow speed. Hence the apparent reduction in thermal resistance seen in Fig. 6.2 could be due to the change in flow speed.

To resolve this issue, Fig. 6.4 replots the thermal resistance as function of mass flow rate instead of Reynolds number. One can see that the data points are now shifted horizontally, reflecting the change in flow rate required to maintain the Reynolds number. Now, it can be seen that if nanofluids are compared on the basis of mass flow rate, there is actually negligible difference

in the thermal resistance. In fact, the nanofluid thermal resistance is slightly higher than that of water for flow rates below 3×10^{-4} kg/s.

A key question now is how the pressure drop is affected when nanofluids are used instead of water that is considered in the next section.

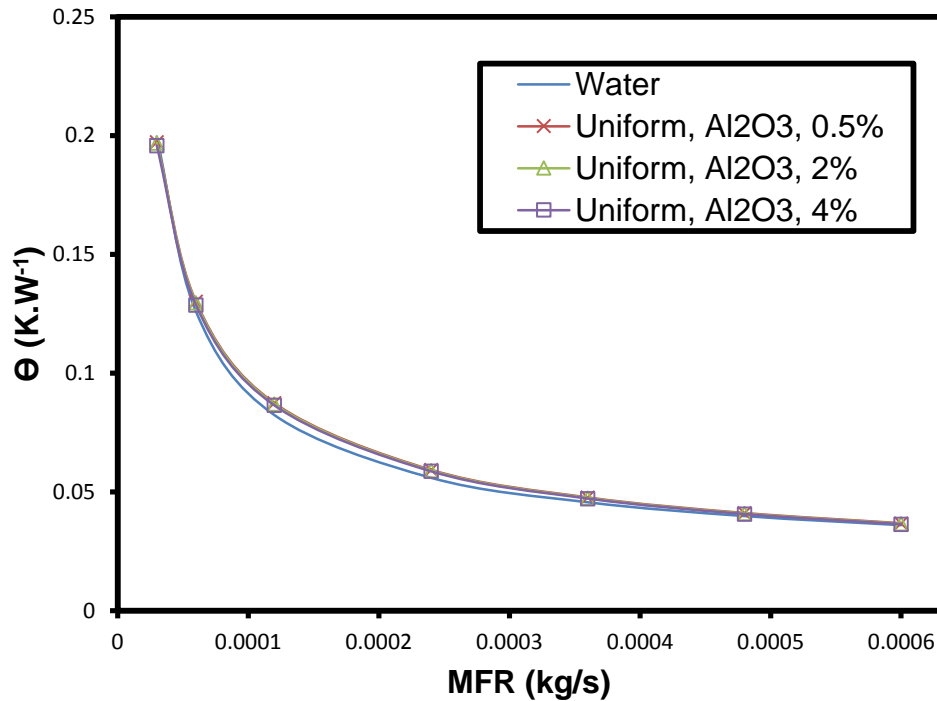


Figure 6.4: Thermal resistance for uniform channel model with nanofluid and pure water.

6.2.2 Pressure drop

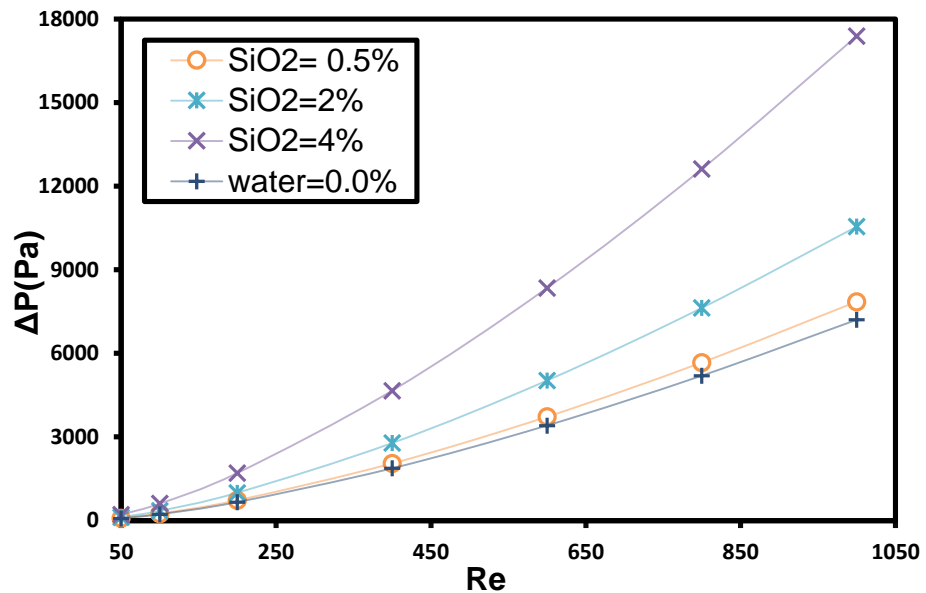
The pressure drop is presented in the full range of the given Reynolds number and mass flow rate. As to be expected, the pressure drop increases as Reynolds number increases for both pure water and nanofluids; this is the same behaviour when using mass flow rate instead of Reynolds number.

Fig. 6.5 (a and b) shows that the pressure drop increased as the concentration of nanoparticles increased, due to the associated viscosity increase. It is found that Al₂O₃-water has a lower pressure drop compared to SiO₂-water at the

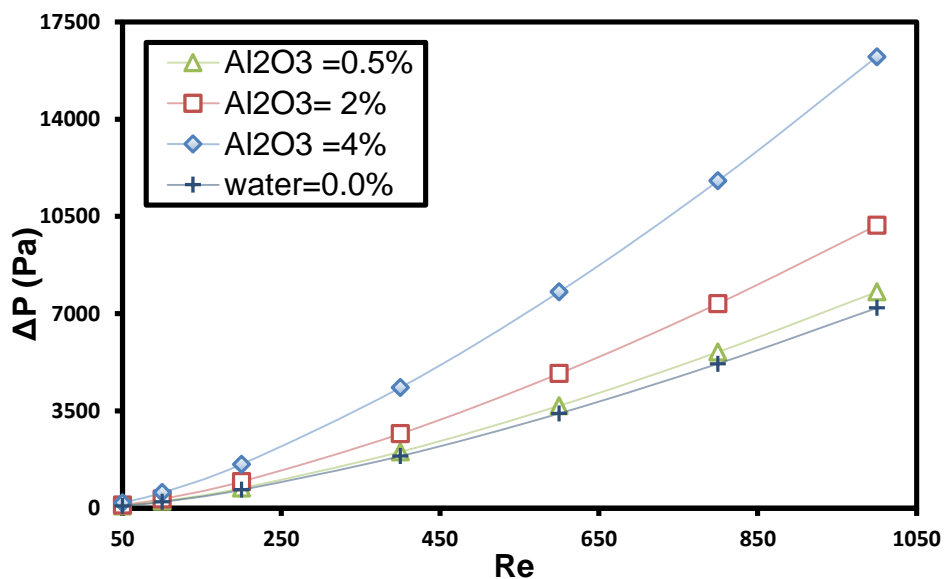
same concentration as shown in Fig. 6.5c. The figure also shows that pure water offered the lowest pressure drop among all fluid types.

When plotted as a function of mass flow rate, the increase in pressure drop does not appear as severe as in Fig. 6.5. However, the pressure drop does still increase with nanoparticles concentration. The fact that pressure drop increases with concentrations (see Fig. 6.6) while the thermal resistance remains essentially unchanged (see Fig. 6.4) has important consequences for the energy efficiency of cooling via nanofluids. This is explored further in chapter 7. The next section presents the influence of using nanofluids together with VGs on heat transfer and fluid flow performance.

(a)



(b)



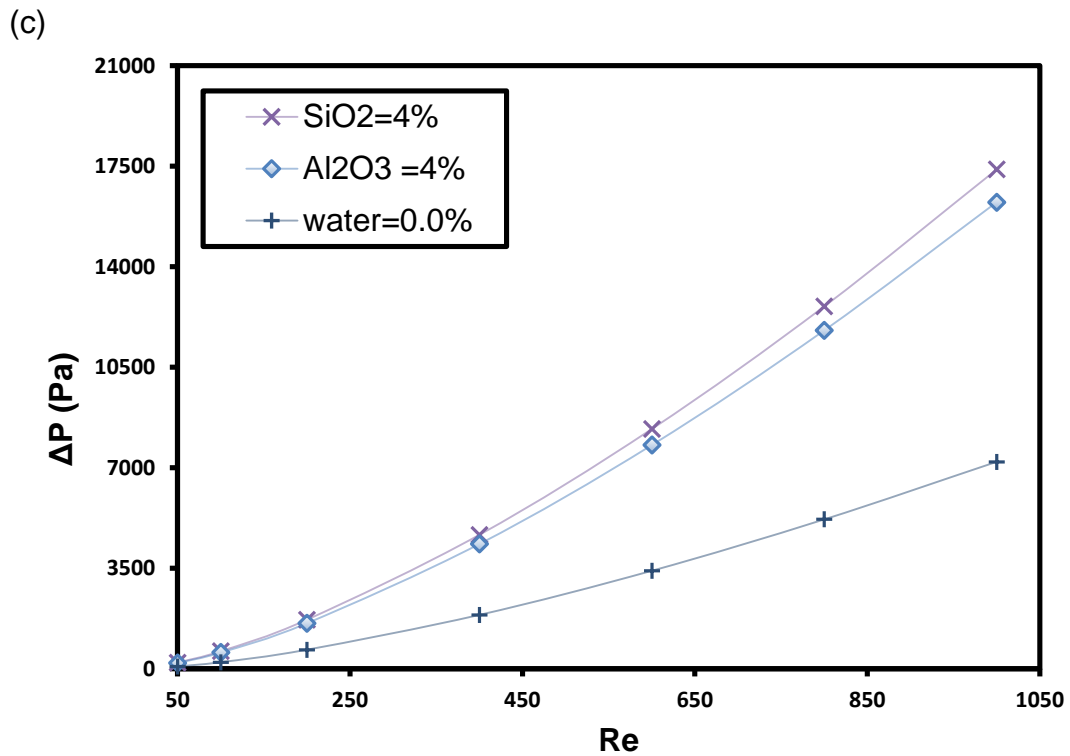


Figure 6.5: Pressure drop of pure water compared to different nanofluids in the uniform channel at given Re; (a) SiO₂-water at different concentrations up to 4% with water, (b) Al₂O₃- water nanofluids (4%) and water, (c) a comparison of Al₂O₃ and SiO₂ nanoparticles concentration of 4% in the water with pure water.

As to be expected, increasing the concentration of nanoparticles in the base fluid leads to increase in the viscosity and density, resulting in an increase in pressure drop as shown in Fig. 6.6. It is interesting to see that there is no significant difference in nanofluids velocity at different concentrations, but water velocity is higher than that of nanofluids at different concentrations as revealed in Fig. 6.7. This is due to density of nanofluids (see Eq. 3-8 and Table 3.5). This also can be attributed to the relation between the viscosity and density (kinematic viscosity) of nanofluids which increases with increasing nanoparticles concentration as can be seen in Figs. 6.8 and 6.9. It is found that the kinematic viscosity is constant at the inlet of the micro-channel due to the constant inlet temperature (see Figs. 6.8a and 6.9a), while the kinematic viscosity changed with temperature considerations at the outlet of the micro-channel (see the temperature dependent equations in sec.3.3). Moreover, Fig. 6.10 compares the kinematic viscosity of the SiO₂ and Al₂O₃ nanofluids at the concentration of 4%. The figure shows that the kinematic viscosity of SiO₂ nanofluid is higher than the Al₂O₃ nanofluid at the same concentration, this

also explains the reason of the high pressure drop of SiO_2 nanofluid compared to Al_2O_3 nanofluid. In addition, Figs. 6.8-6.10 also presents that the kinematic viscosity increases with nanoparticles concentration at the same mass flow rate either at the inlet or at the outlet of the micro-channel.

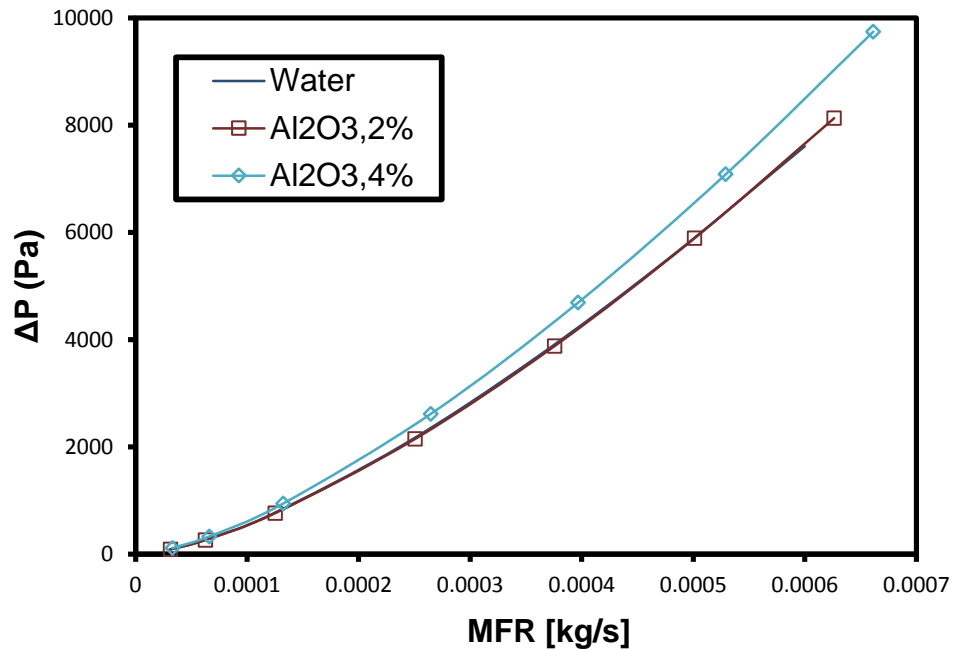


Figure 6.6: Pressure drop for the uniform channel model with water and Al_2O_3 nanofluid at different concentrations.

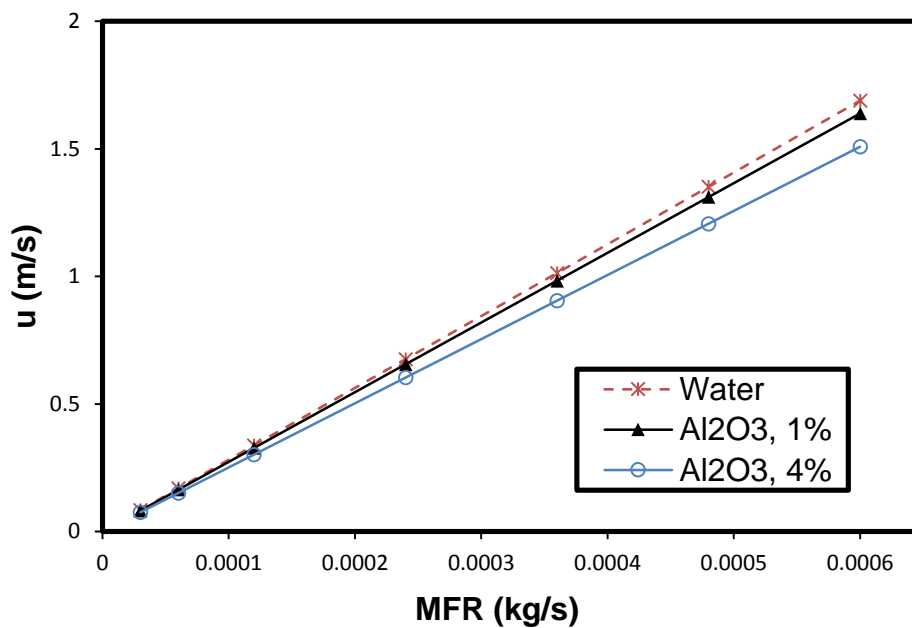


Figure 6.7: X-component of fluid velocity for water and Al_2O_3 nanofluid at different concentrations in the uniform channel.

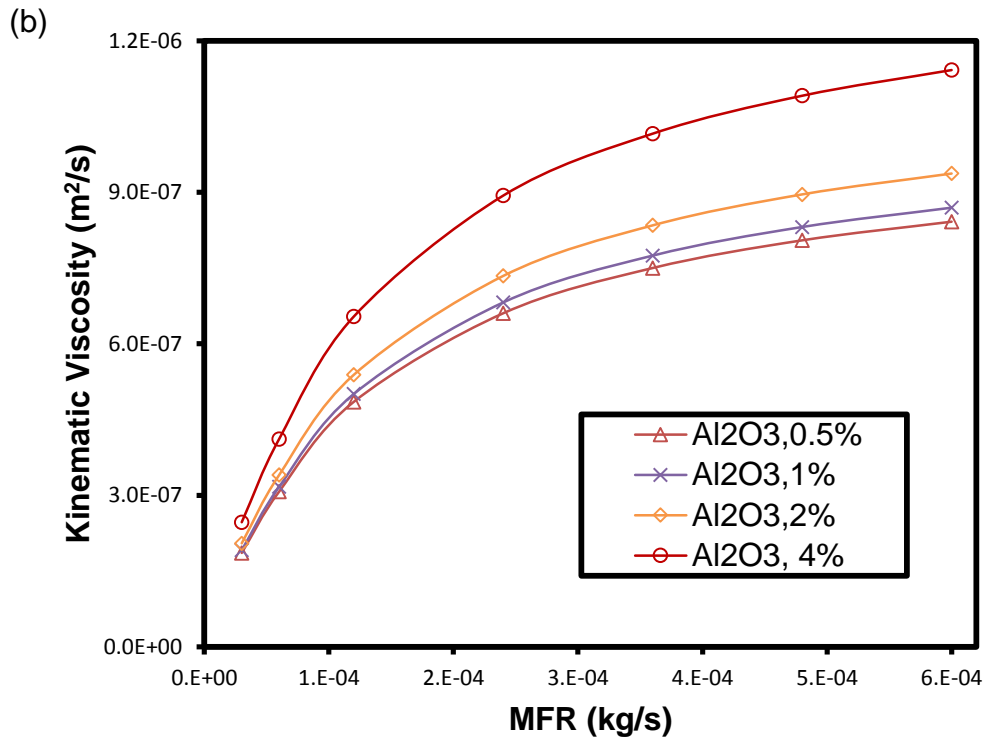
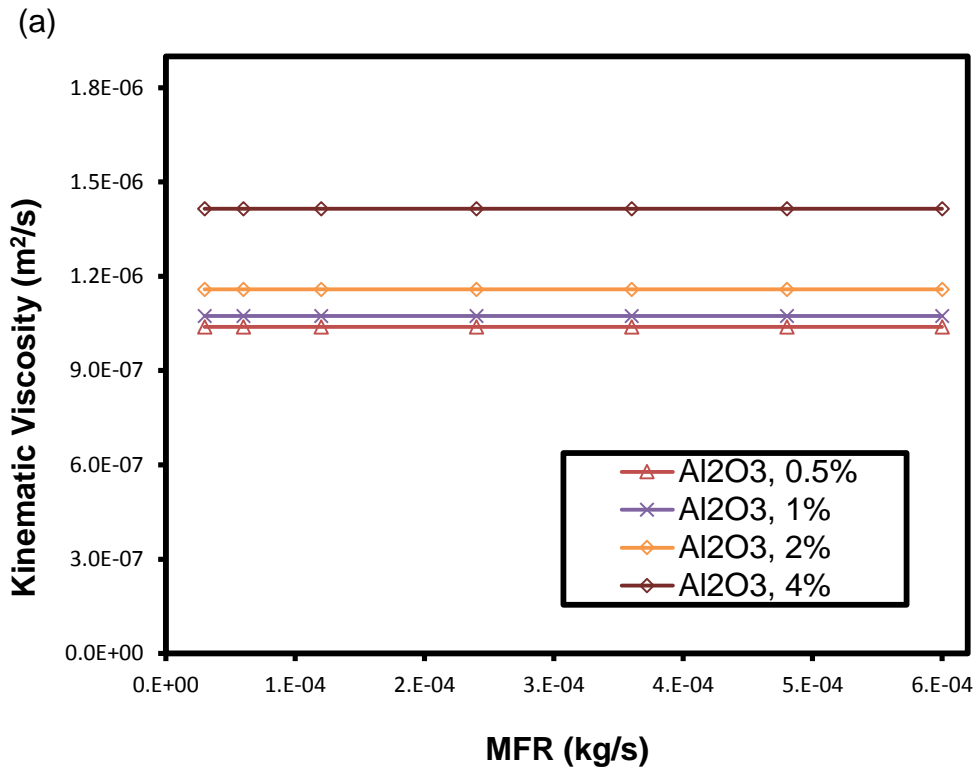


Figure 6.8: Kinematic viscosity of Al₂O₃ nanofluid at various concentrations; (a) at the inlet of the micro-channel (at the inlet temperature), (b) at the outlet of the micro-channel (temperature dependent).

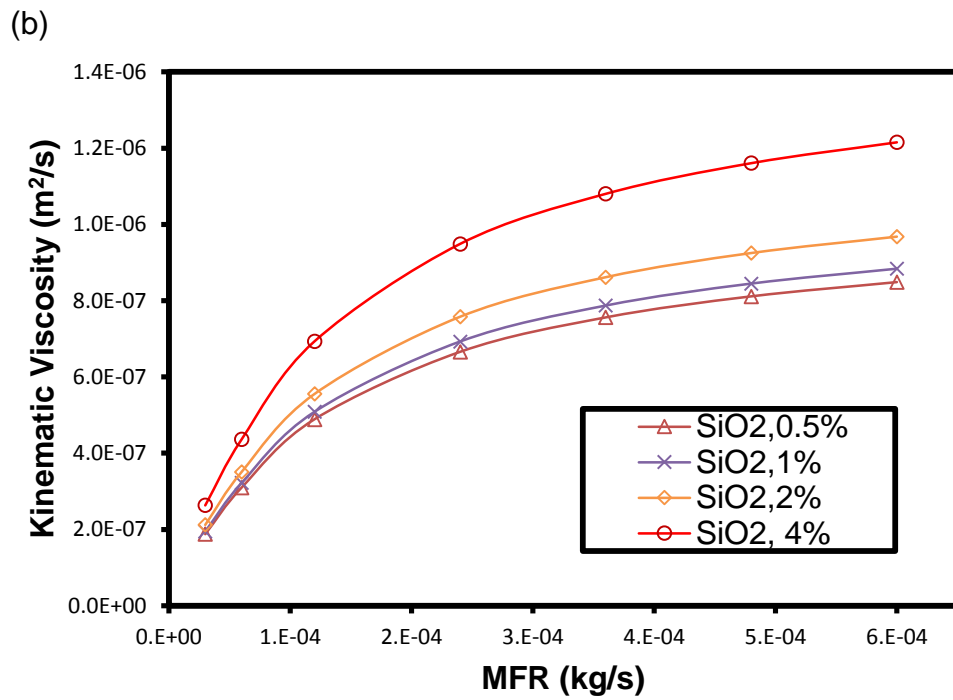
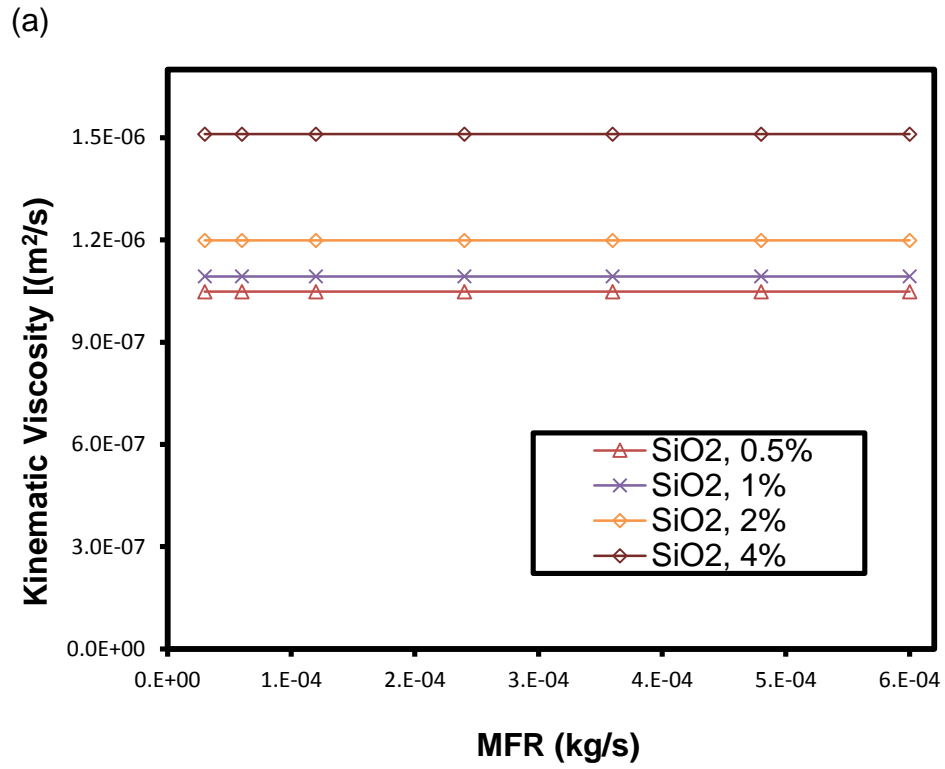


Figure 6.9: Kinematic viscosity of SiO₂ nanofluid at various concentrations; (a) at the inlet of the micro-channel (at the inlet temperature), (b) at the outlet of the micro-channel (temperature dependent).

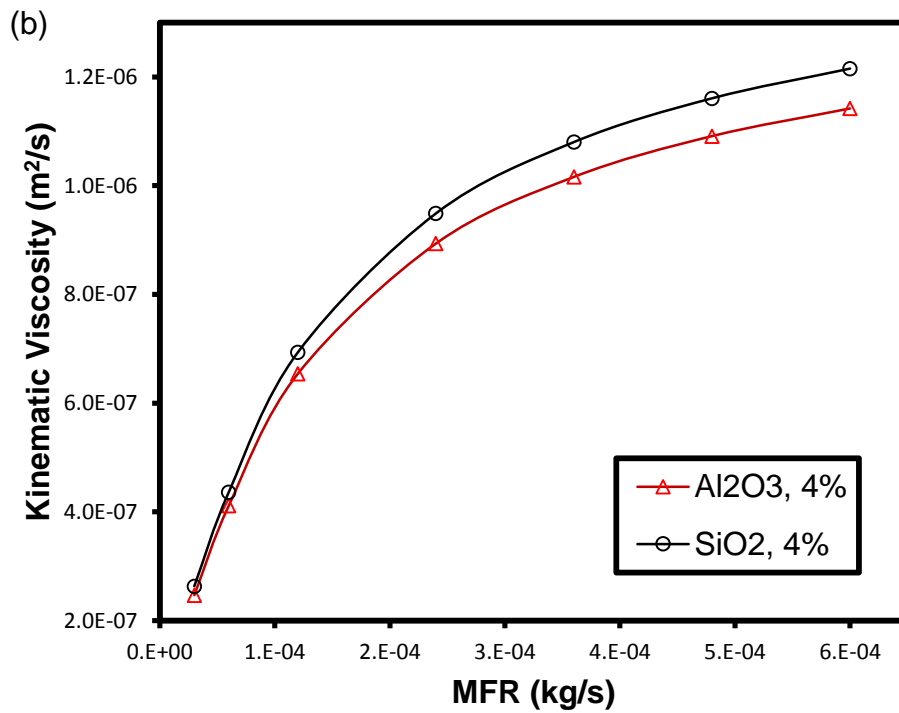
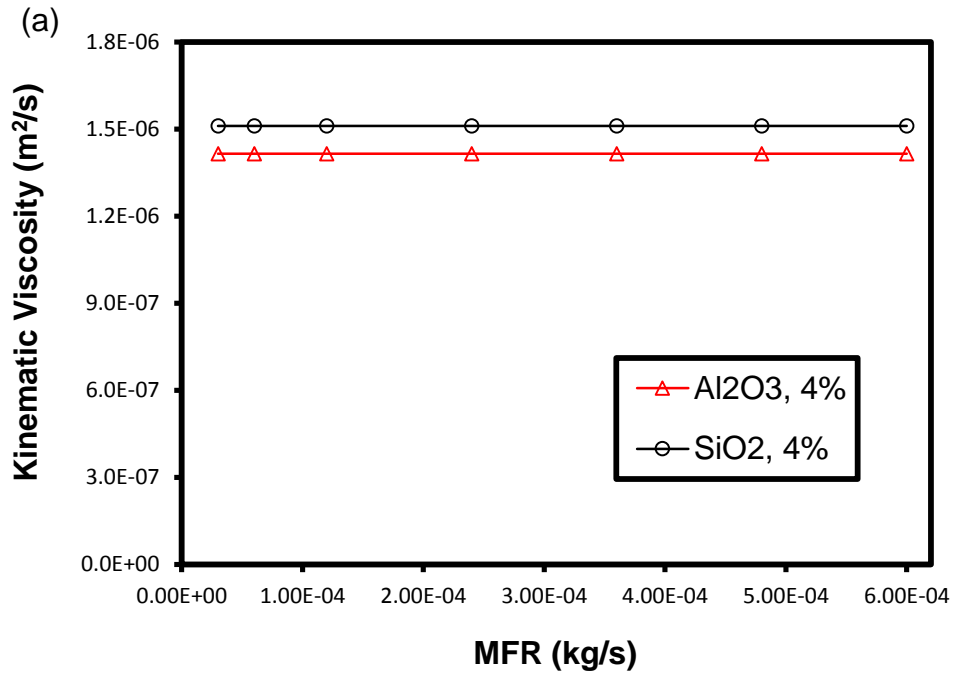


Figure 6.10: Comparison of Kinematic viscosity of Al₂O₃ and SiO₂ nanofluids at 4% of nanoparticles concentration; (a) at the inlet of the micro-channel (at the inlet temperature), (b) at the outlet of the micro-channel (temperature dependent).

6.3 Nanofluid performance with half-circle (C-model) VGs

Based on the findings in sec. 7.2 the Al_2O_3 nanofluid offered better heat transfer and lower pressure drop than the SiO_2 . Therefore, only the Al_2O_3 nanofluid is considered in this section.

Having seen the behaviour of nanofluids in a uniform channel in the last section, this section introduces vortex generators into the channel to assess their influence on the nanofluid performance. Full-span half-circle VGs (C-model) are chosen as these offered lowest pressure drop of the full-span VGs considered in chapter 4.

6.3.1 Thermal resistance

The influence of using nanofluid with the C-model and the uniform channel water as a reference to evaluate the improvement in heat transfer is considered here. Fig. 6.11a shows that the thermal resistance decreased when using Al_2O_3 nanofluid at the concentration of 4% compared to water for the C-model at the same Reynolds number. This is due to high thermal properties of nanofluid compared to water and/or an increase in the velocity calculated based on nanofluid thermal properties as discussed in sec 7.2. Moreover, Fig. 6.11b reveals that the C-model offers a lower thermal resistance than the uniform channel either with nanofluid or water.

As discussed in section 6.2.1, when the data is plotted in terms of flow rate instead of Reynolds number, the thermal resistance is shifted horizontally, this means that no reduction in thermal resistance using nanofluids at a fixed mass flow rate there is. Now, Fig. 6.11 shows that the C-model with water offered lower thermal resistance than Al_2O_3 nanofluid at the concentration of 4%. This can be attributed to the viscosity difference between water and nanofluid at the same flow rate. Interestingly, in spite of the high thermal conductivity of nanofluid compared to water, the main effect to enhance the heat transfer is still the velocity. In other words, to enhance the heat transfer, no matter how much the enhancements in thermal properties of a working fluid unless increasing the speed of this fluid. The figure also confirms that the C-model

offers lower thermal resistance than the uniform channel with the same working fluid.

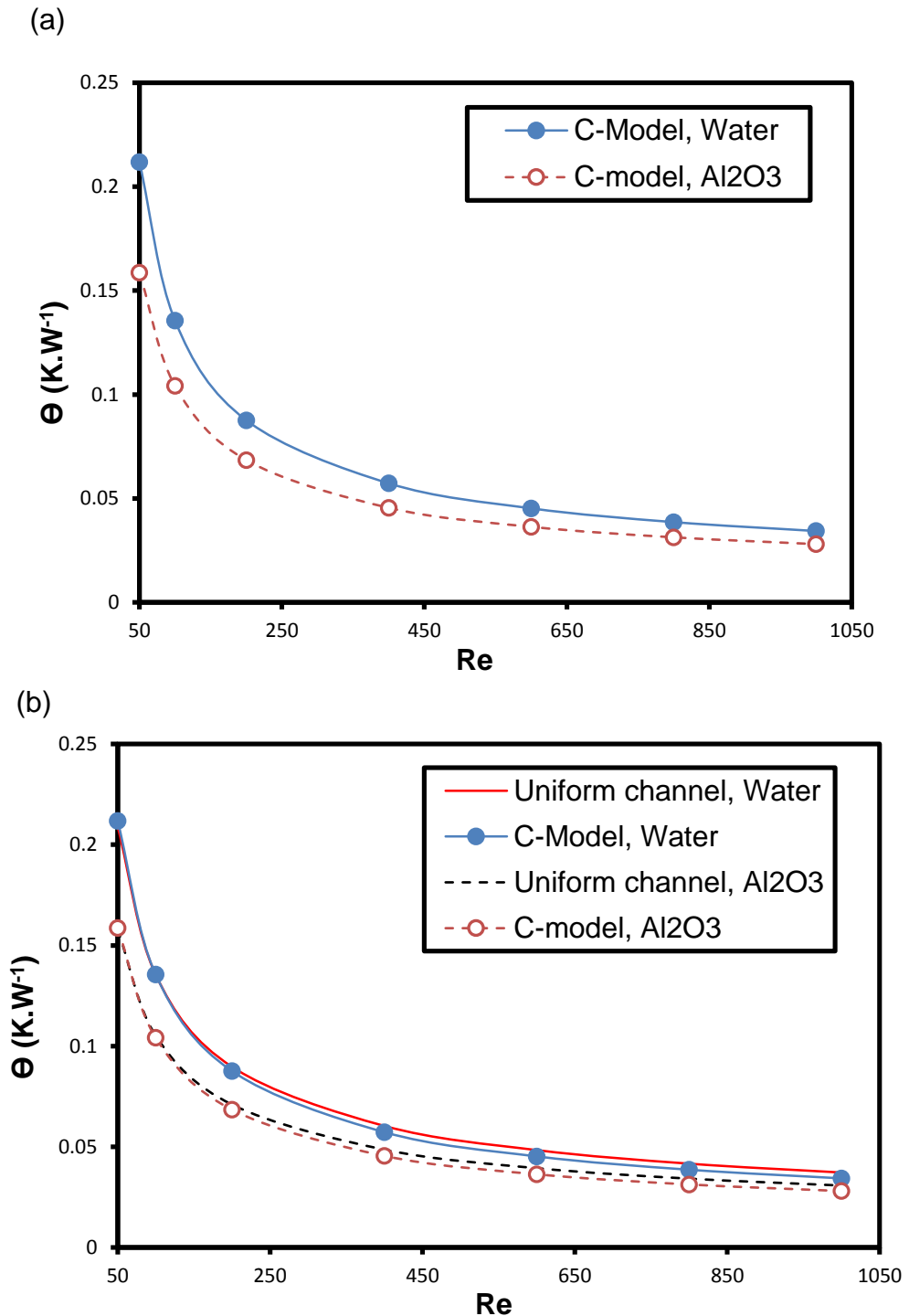


Figure 6.11: Thermal resistance comparison of the uniform channel and C-model with water and Al_2O_3 nanofluid at the concentration of 4%; (a) C-model with nanofluid and water, (b) comparison of the uniform channel and C-model with water and nanofluid.

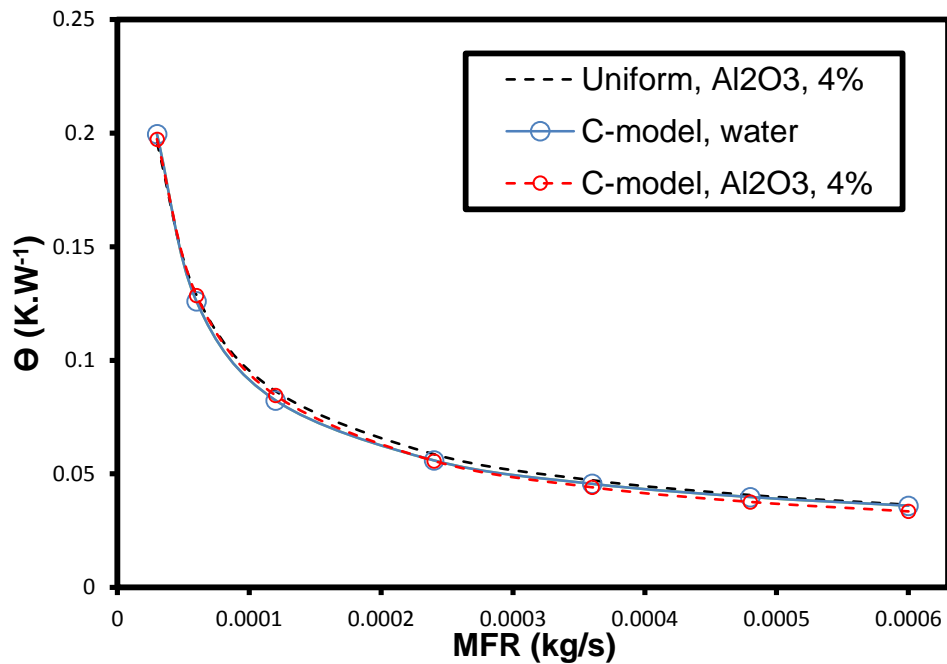


Figure 6.12: Thermal resistance Vs MFR for geometries and fluids, C-model and uniform channel with water and Al₂O₃ nanofluids at the concentration of 4%.

6.3.2 Pressure drop

As to be expected, the price for the reduction in thermal resistance is the increase in pressure drop. Fig. 6.13 highlights the significant increase in the pressure drop when using nanofluids compared to water. For instance, the uniform channel with nanofluid shows a higher pressure drop even than the C-model with water. This is due to the velocity and viscosity changes of nanofluid with respect to the Reynolds number compared to water.

However, as discussed in previous chapters of this thesis, it is clear that using nanofluid increases the pressure drop, also VGs in a uniform channel shows an increase in pressure drop compared to the uniform channel having no VGs. But different behaviour appears in Fig. 6.14 when using mass flow rate. The behaviour is, the uniform channel with nanofluid offers lower pressure drop than the C-model with water, this is opposite of what is shown in Fig. 6.13 when using Reynolds number. The reason for this, is that the velocity changes with Reynolds number as it is a function of the viscosity and density of nanofluid, meaning that increasing the nanoparticle concentration increases

the velocity required to achieve a given Reynolds number, as seen in Fig. 6.15a (see Eq.3-5 and Table 3.5). However, at a given mass flow rate, The higher density of the nanofluid compared to water (see Eq. 3-8 and table 3.5) means that the corresponding nanofluid velocity is lower than that of water. This can be seen in Fig. 6.15b which compares the water and nanofluid flow velocities in a uniform channel at specified mass flow rate.

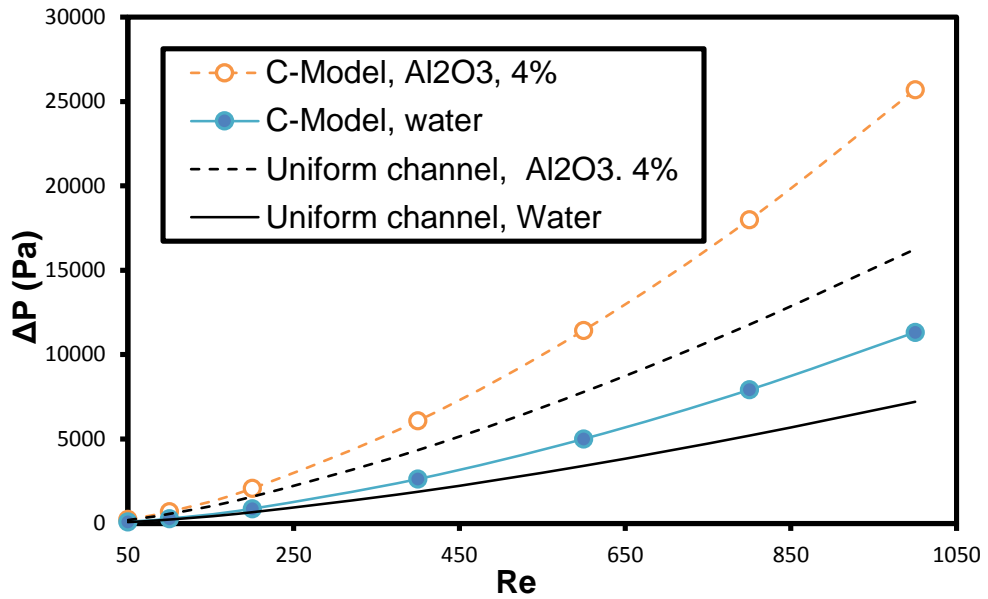


Figure 6.13: pressure drop with Reynolds number for C-model and uniform channel using water and Al₂O₃ nanofluid at 4% of concentration.

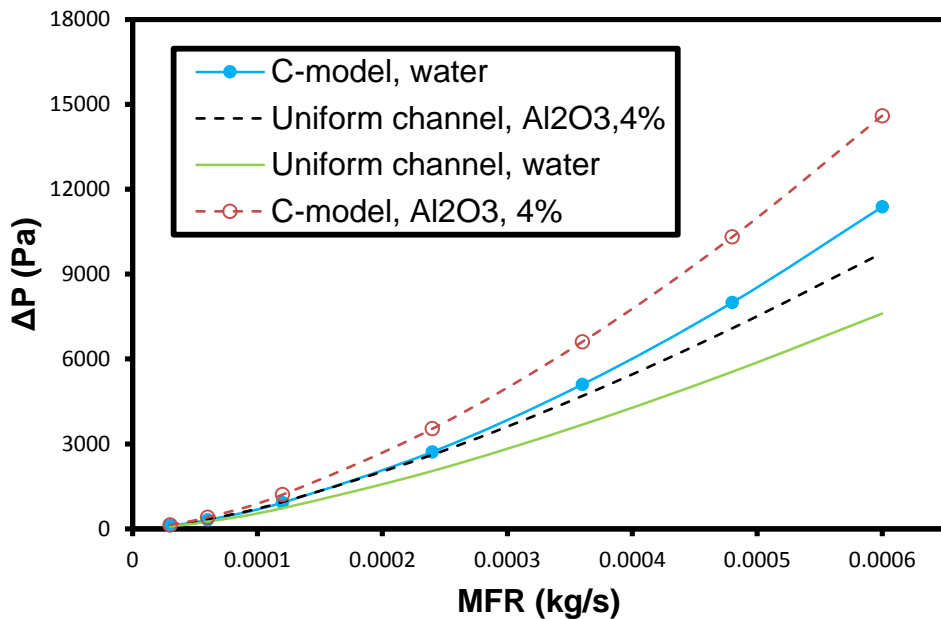


Figure 6.14: Pressure drop comparison of the uniform channel and C-model using water and nanofluid.

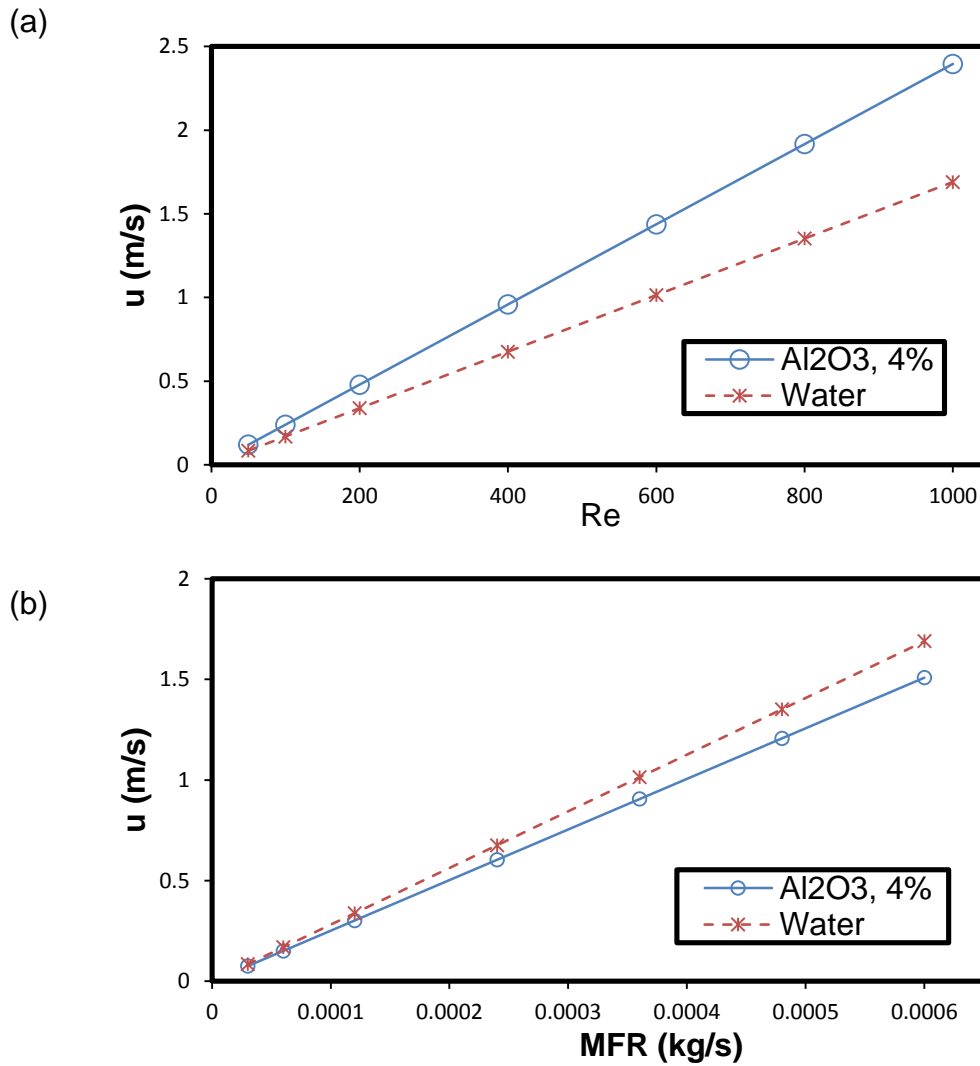


Figure 6.15: Velocity comparison of different fluids in the uniform channel with respect to: (a) Reynolds number; (b) MFR.

Now, the issue of the increase in the pressure drop with nanofluid still motivates this research to find a solution to keep enhancing the heat transfer performance and reduce the pressure drop. This directs the research to a new suggestion geometry to tackle the issue of the increasing in pressure drop. Therefore, there is an interesting question appears here: can the C-model be modified to be another similar shape to offer lower pressure drop than the C-model but enhance the heat transfer or at least keep it the same as the C-model. The suggestion is, for instance, an elliptical VG? It seems that suggesting elliptical VGs (EL-model) might solve the issue of the increase in pressure drop and enhances the heat transfer as presented in the next section.

6.4 Combining nanofluids and elliptical (EL-model) VGs

The EL-model is shown in Fig. 6.1 and described in Table 7.1, and has the same volume as the C-model at the radius of 200 μm . Both the C-model and EL-model have equal number of VGs which are 5 VGs in the base of the uniform micro-channel, also they have the same distribution and location. Now, the impact of combining nanofluids and various VGs shapes (C and EL models) on conjugate heat transfer is the aim of the current section. Therefore, the common question is, can the suggested geometry (EL-model) enhance heat transfer performance and reduce the pressure drop? This is with association of pressure drop difference between EL-model and C-model. The answer is detailed in the next sub-section.

6.4.1 Thermal resistance

The effect of combining nanofluids and VGs on thermal resistance is presented in terms of Reynolds number and mass flow rate. The geometry is the uniform channel having vortex generators (C-model and EL-model) which are considered and compared based on their constant volume (0.0314 mm^3).

The suggested model (EL-model) used with nanofluid at nanoparticles concentration of 1 and 4% and C-model with water is presented in Fig. 6.16 which shows the influence of the geometry and Reynolds number on thermal resistance. The figure shows that the C-model offers slightly lower thermal resistance than EL-model where water is used as the working fluid. Moreover, as to be expected that using nanofluid reduces the thermal resistance. It is also found that the thermal resistance decreased with increasing nanoparticle concentration from 1% to 4% which can be seen even in Fig. 6.2. The reason is that, Reynolds number is a function of the density and viscosity of nanofluids. Therefore increasing nanoparticles concentration increases the density and the viscosity which lead to increase Reynolds number.

Based on the results above, the question is, can EL-model with nanofluid offer lower pressure drop than the C-model with water which is mentioned earlier in the introduction? The answer is presented here.

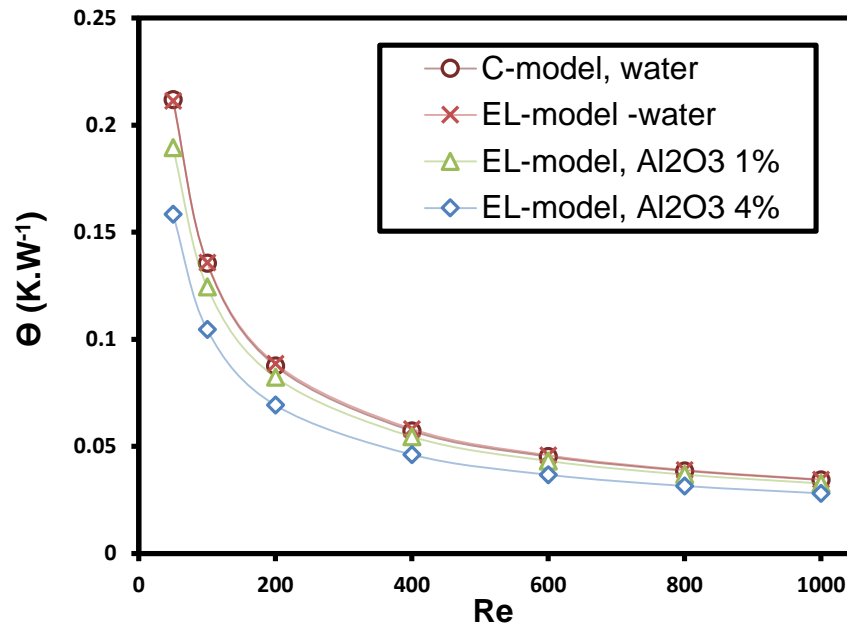


Figure 6.16: Thermal resistance of various shapes and fluids with different Reynolds number.

Fig. 6.17 shows the thermal resistance for various MFR values using EL, C models compared to each other at concentrations of Al₂O₃-water nanofluid up to 4%. The figure also demonstrates that EL-model with nanofluid offered lower thermal resistance compared to C-model with water at low mass flow rate. However, the results indicated that, only very little reduction in thermal resistance can be achieved when the MFR and nanoparticles concentration are low values. This can be attributed to the viscosity of nanofluid at constant MFR. The viscosity of nanofluids increased with the concentration of nanoparticles as illustrated in Figs. 6.7-6.10 also in Table 3.5. The increment in the viscosity led to decrease the velocity of nanofluids compared to water as presented in Fig. 6.15, this resulting to decrease the heat transfer enhancement.

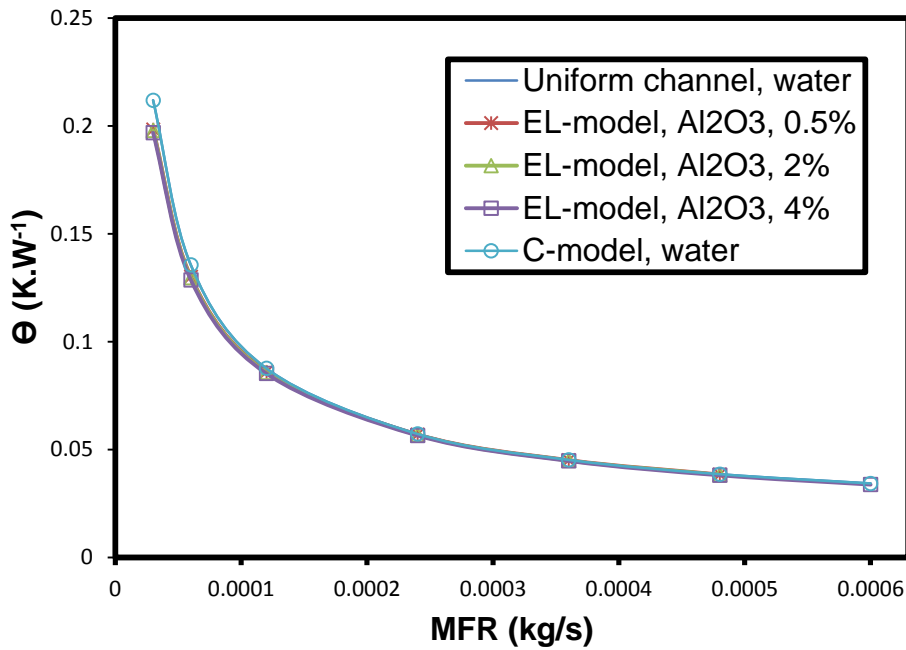


Figure 6.17: Thermal resistance for EL, C and uniform channel models.

6.4.2 Pressure drop

The impact of using different VG configurations with nanofluids is presented in Fig. 6.18, based on chapter 4, section 4.2.4 (see Fig. 4.15), the results showed that the half-circle VGs offered better pressure drop performance compared to different VGs configurations (rectangular or triangular VGs). The question which interestingly appeared here is, can the suggested geometry offer lower pressure drop than the half-circle VGs, then use the suggested geometry with nanofluids?

The answer is presented in Fig. 6.18 that the half-circle VGs (C-model) have higher pressure drop than the elliptical VGs (EL-model) with water as the working fluid. The results demonstrate that the EL-model with Al₂O₃ and SiO₂ nanofluids at the concentration of 1% is a successful suggestion to reduce the pressure drop (see Fig. 6.18) and the thermal resistance simultaneously when using fixed Reynolds number. However, C-model with water has higher pressure drop than the EL-model up to 3%. While, the EL-model with Al₂O₃ nanofluid at the concentration of 4% is higher than the C-model with water as presented in Fig. 6.19.

The key idea of using different geometry is to reduce the pressure drop and enhance the heat transfer simultaneously with advanced fluids such as nanofluids.

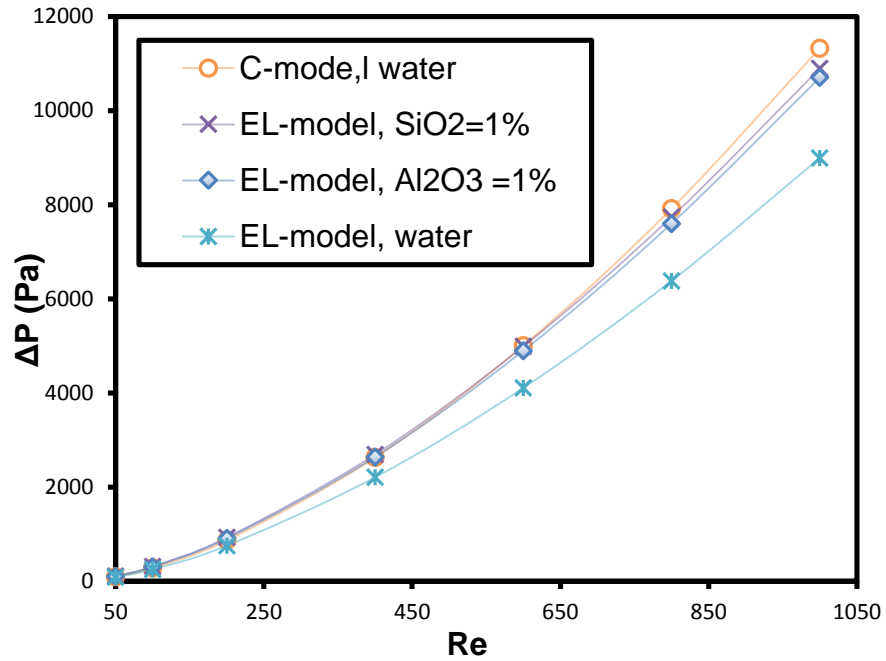


Figure 6.18: Pressure drop comparison of elliptical VGs with (0-1) % nanofluids and half-circle VGs using pure water.

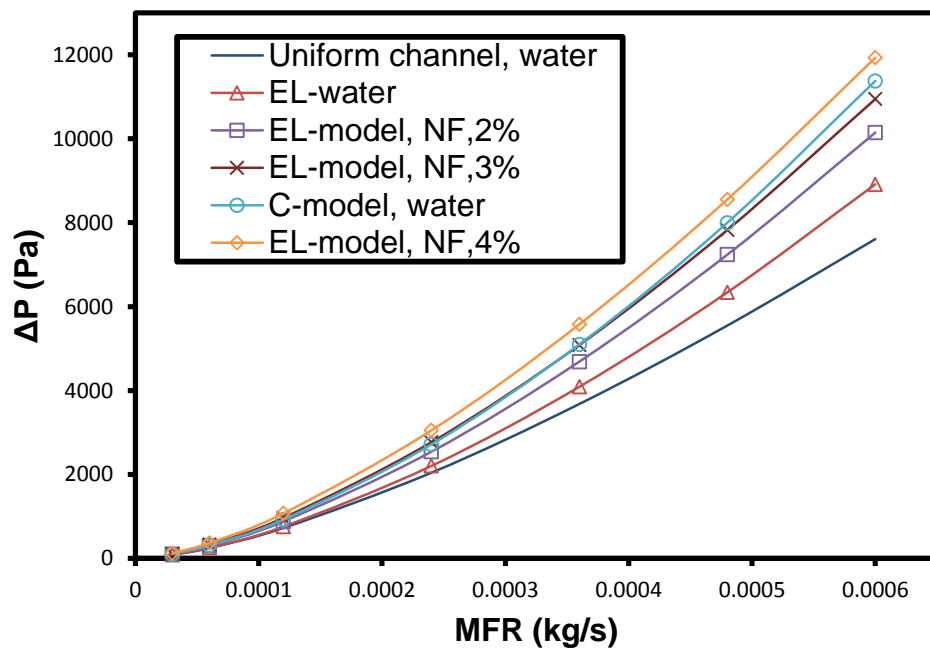


Figure 6.19: Pressure drop for C-model and uniform channel with water and EL-model with Al₂O₃ nanoparticles concentration in water (0-4) %.

6.5 Summary

In this study, various VG models are studied to examine the impact of the geometry and the working fluid on heat transfer and fluid flow characteristics. All models were investigated under laminar flow submitted to a uniform heat flux related to CPUs in electronic devices. The aim of this chapter was to suggest a suitable setup of fluids and geometries to meet the rapid developments of the electronic devices, therefore the outcomes are:

- Using fixed Reynolds number, the thermal resistance decreased using various nanofluids in different concentrations compared to pure water.
- The thermal resistance decreased as the concentrations of nanoparticles increased.
- Al₂O₃-water nanofluid has low thermal resistance and pressure drop compared to SiO₂-water nanofluid at the same concentration due to its thermo-physical properties.
- With a fixed Reynold number, the new suggested model (elliptical-model) with nanofluids up to 4% of nanoparticles offered lower thermal resistance and pressure drop, but the pressure drop of EL-model with nanoparticles concentration of 4% is higher than the half-circle model with water.
- Using MFR showed that there is a slight reduction in thermal resistance of EL- model with nanofluid compared to C-model with water, but not the same reduction as shown with Reynolds number using nanofluids with different geometries.
- The thermal resistance and the pressure drop increased with the nanoparticle concentrations when using MFR.

From the points above, it can be concluded that this chapter highlights that care must be taken when comparing the performance of different nanofluids, because the key fluid properties of viscosity and density increase with nanoparticles concentration. Importantly, the kinematic viscosity increase with nanoparticles concentration, meaning that the flows of two nanofluids in the same geometry at the same Reynolds number actually correspond to flows at different speeds. Hence apparent enhancement in heat transfer performance at different flow rates.

It is also shown that modifying a half-circle (C-model) VGs to a half-elliptical VGs (EL-model) produces little change in thermal resistance but substantial reduction in pressure drop. This can be exploited by combining geometrical modifications (using VG geometries) with coolant modifications (using nanofluids), and it is found that Al_2O_3 or SiO_2 nanofluids in a micro-channel with elliptical VGs can replace pure water as a coolant.

Based on the finding of this chapter, the practical perspective is important to be taken in to consideration in this thesis. Furthermore, the energy management of heat and flow characteristics plays a crucial role in practical and commercial applications. Therefore the next chapter focuses on the energy management analysis of heat transfer and fluid flow in micro-channel heat sink.

Chapter 7: Energy Management considerations

7.1 Introduction

In the practical application of a micro-channel heat sink (e.g. in cooling a micro-processor chip), as was the motivation for the present study, a vital quantity of interest is the actual surface temperature that can be achieved with a given micro-channel geometry, under a given heat load. Therefore, as a final observation, this chapter present the data in terms of energy management.

In previous chapters, the heat transfer performance has been presented primarily in terms of thermal resistance and pressure drop. However, as indicated in the introduction of this work, a key motivation for the present study is the cooling of electronic chips producing a certain heat flux through their surface. Since there is an upper limit of the temperature at which a chip can operate reliably, key practical questions about the cooling system are (a) can a sufficiently low chip temperature be achieved for a given heat flux, and (b) how much energy is needed to achieve an acceptable temperature? Hence this chapter revisits the findings of earlier chapters focusing on the temperatures of the base of the heat sink where the heat flux is applied and the pumping power required to achieve them. One of the ways to evaluate the energy management in a system is to consider the heat transfer performance based on the maximum and/or average temperature. Therefore, the results of chapter 4 are represented in terms of average and maximum temperatures with water as a coolant, and this will be the first section in this chapter. To develop the investigation a further step, chapter 5 is also revisited to explore the average and maximum temperatures of the best VGs that offer high thermal performance (see Fig. 5.16). The VG configurations are end gap model with gap=150 μm (E2), central gap model with gap=100 μm (C2), central and end gaps with gap=250 μm (CE1), no gap (full-span) and the uniform channel (seeTable6.1). The second section of this work studies the effect of heat transfer and fluid flow performance.

The influence of using different VG geometries to enhance the heat transfer and reduce the pressure drop is previously investigated in chapter 6 in terms

of thermal resistance and pressure drop. However, in the third section of this chapter, the heat transfer is presented in terms of the maximum and average temperatures, and the fluid flow will appear as pumping power.

The motivation for introducing gaps in chapter 5 was to reduce the pressure penalty, though it was found that heat transfer also improved. In this chapter the gap idea is explored further by applying it to the configuration that produced the highest pressure drop presented in chapter 4.

This is to evaluate the energy management in terms of pumping power and heat transfer performance. Chapter 4 concluded that the lowest pressure drop was for half-circle, rectangular and triangular VGs, respectively (see Fig. 4.10).

Therefore, here is an interesting question: is the idea of having gaps valid to be applied on triangular VGs which have the highest pressure drop (see Fig. 4.10) to reduce the pressure drop and enhance the heat transfer performance? Then, based on pressure drop difference, is it beneficial to use the triangular VG having gap with nanofluids? Does the suggested model (Triangular VGs with gap) work better than half-circle VGs to enhance the heat transfer and reduce the power consumption? The questions are answered in the first part of fourth section of this chapter.

Another important aspect in practical application is the optimisation of the geometry which is presented as the fifth section of this chapter.

7.2 Full-span VGs with water coolant

The results in chapter 4 are re-introduced as an average and maximum temperatures on the solid base of the micro-channel to assess the energy management of heat transfer performance. As presented in chapter 4, the lowest thermal resistance and pressure drop were for the half-circle, then the rectangular, then the triangular VGs (see Fig. 4.10). This is reflected in the average temperatures shown in Fig. 7.1. However, the figure illustrates that the C-model has the highest maximum temperature compared to R and T models and the uniform channel. This can be attributed to the overall heat transfer performance along the channel from the inlet to the outlet in terms of the average and maximum temperatures. The reason can be clarified when a

temperature distribution along the channel is drawn. This line is located at the centre of the channel bottom to show the temperature distribution for the uniform channel and the other VGs as illustrated in Fig. 7.2. The figure indicates, the C-model has the lowest temperature along the channel up to the distance of 21000 μm (after the fifth VG), then the temperature increases dramatically to be the highest temperature for a short distance only from 21000 μm to 25000 μm (at the channel outlet). Now, the reason of the hot temperature for the C-model at the outlet is the high temperature of the fluid at the outlet as seen in Fig. 7.3. Again, this is related to the fluid flow, as the average velocity for the C-model is the lowest among the other VGs. This means, more heat transfers from the base to the fluid, then the temperature of the fluid increases, this leads to less heat transfer at the channel outlet because of the low velocity for the C-model as indicated in Fig. 7.4.

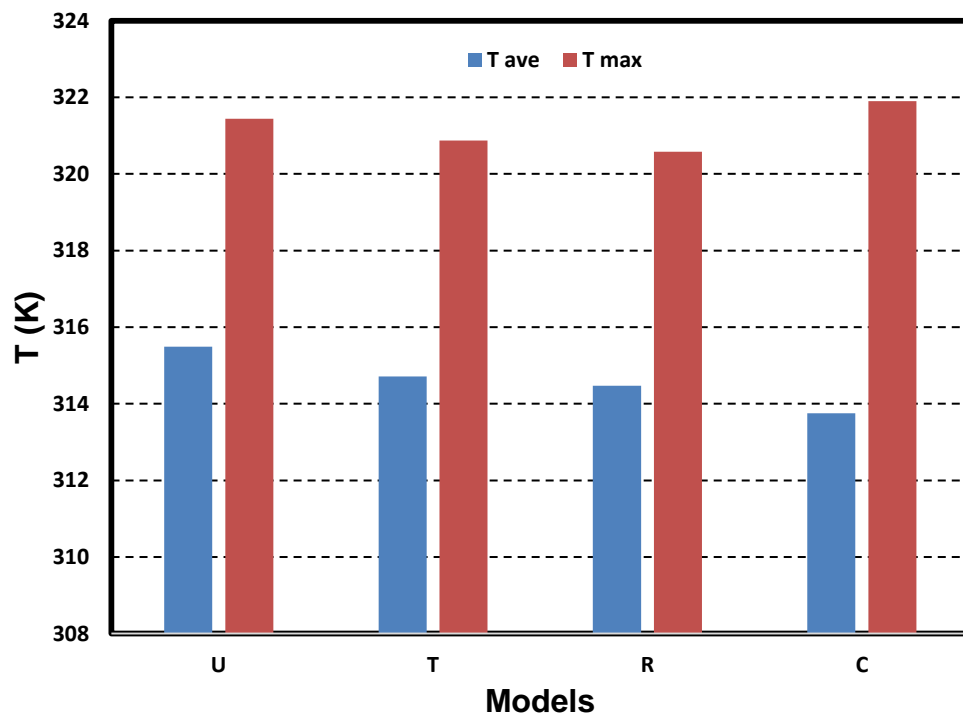


Figure 7.1: Average and maximum temperatures of the solid base achieved with various vortex generators at Reynolds number 1000 using water.

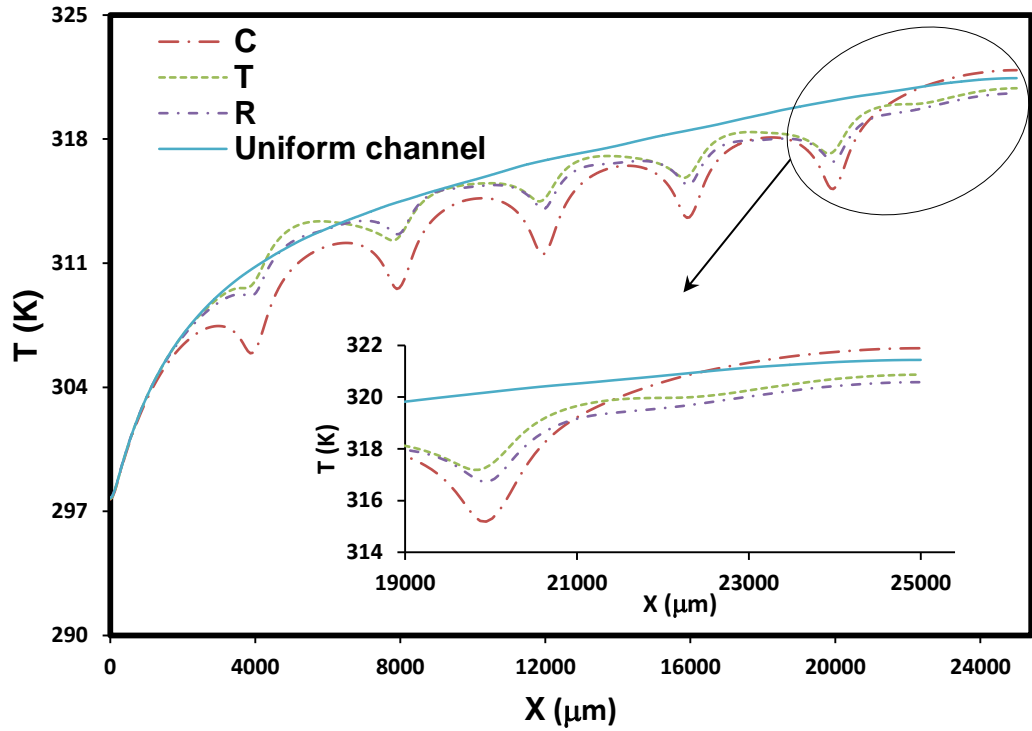


Figure 7.2: actual temperature distribution along the centre line of the microchannel.

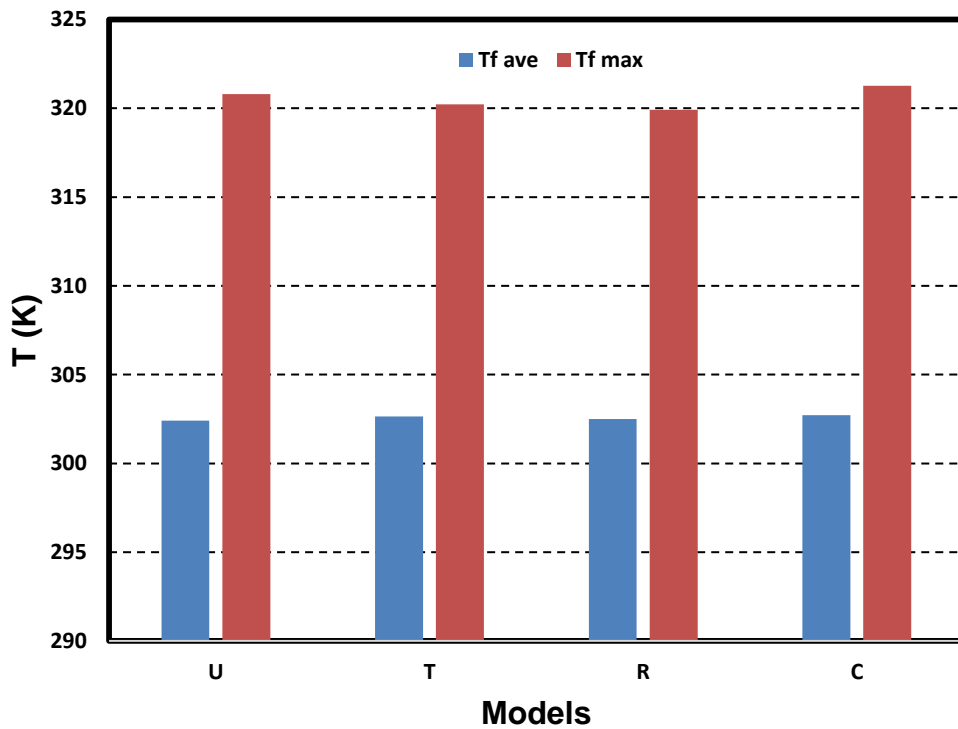


Figure 7.3: Maximum fluid temperature at the outlet for C, R and T models at $Re=1000$.

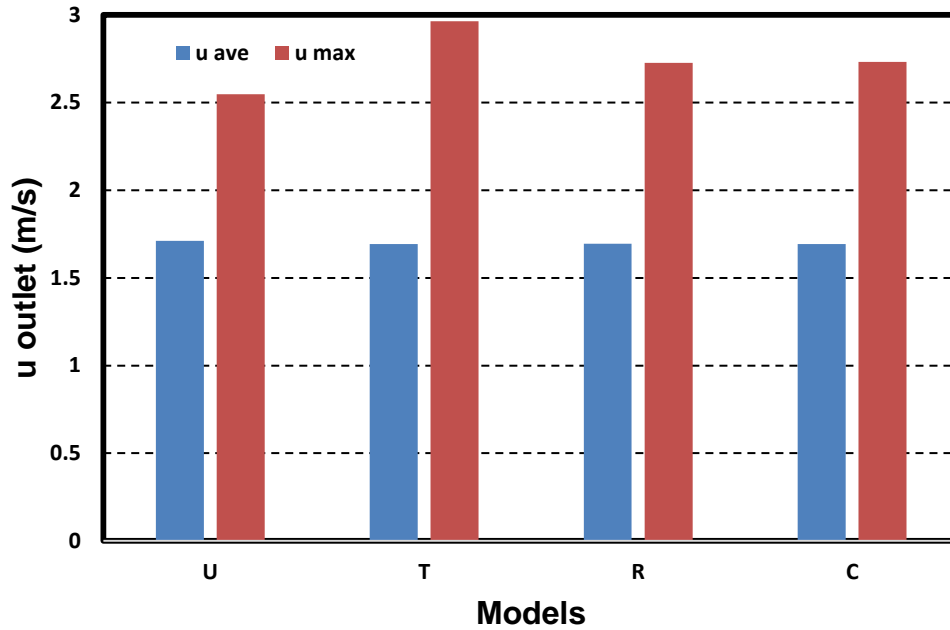


Figure 7.4: Average and maximum water velocities at the outlet of the uniform channel and various VGs at Reynolds number of 1000.

From the results above, the variation of using the average and maximum temperatures to evaluate the heat transfer performance needs to be investigated using the effect of the gap which appears in the next section.

7.3 Effect of gaps on energy management

As indicated in chapter 5, having gap in VGs enhances the heat transfer and fluid flow (reduces the pressure drop). It is found that the best heat transfer performance was for the end gap model with gap=150 μm (E2), then the central gap model with gap=100 μm (C2), central and end gaps with gap=250 μm (CE1), no gap (full-span) and the uniform channel (see Table 6.1 for geometry discription). Therefore, the results are represented with respect to the average and maximum temperatures as shown in Fig. 7.5. The figure presents the average and, importantly, maximum temperatures achieved on the bottom surface of the heat sink operating at $Re = 1500$ with channels containing the C2, E2 and CE1-model VGs offering the lowest thermal resistance. Recall that the heat flux entering the solid base from below is 100 W/cm^2 , the inlet fluid temperature is 293.15 K, and all models are half-circles

with the radius of 400 μm . Also included for comparison is the corresponding data for a uniform channel with no VGs, a channel with full-span VGs (no gap), and a channel with C5- model VGs which have the highest PEC index of 1.08 at this Reynolds number (see Figs. 5.13 and 5.17).

First, it can be seen that the channels with vortex generators all produce a lower average temperature than the uniform channel, as has already been seen through the thermal resistance equation in chapter 3 (3-6), which is based on the average temperature. However, the maximum temperatures obtained (at the outflow) show a rather different behaviour. The full-span VG provides a 2 K reduction in the average surface temperature and a 2.5 K reduction in the maximum temperature compared to the uniform channel. Introducing the end gaps to create the E2 VGs produces a further 4 K reduction in the average and 1.6 K reduction in the maximum temperature, and is clearly beneficial. However, the C-model and CE-model VGs do not significantly reduce the maximum temperature relative to the uniform channel – in fact the CE1 VG actually results in an almost 1 K increase in the maximum temperature. Similarly, the C5 VG offers no reduction in the maximum temperature compared to the uniform channel, despite providing a similar thermal resistance and hence average surface temperature to the full-span VG, as remarked above. This suggests that the improvements in heat transfer offered by the C2-model and CE1-model VGs are somewhat more localised, such that over the whole surface the net effect is a reduction in average temperature, but at the expense of other areas where the local heat transfer is worse. Indeed, this effect can be seen at the left-most ends of the contour plots in chapter 5, section 5.5.3 (see Fig. 5.18), where the C2 and CE1 VGs have a thicker thermal boundary layer on the base surface than the other VG models.

The temperature plots in chapter 5, section 5.5.3 (see Fig. 5.18) suggest that the E2-model and full-span VGs are essentially independent of each other at this spacing between the VGs; the transverse vortices generated by the full-span VGs do not extend as far as the next VG, and for the E2-model VG, the fluid passing through the gaps is swept upwards and inwards away from the gaps in the next VG.

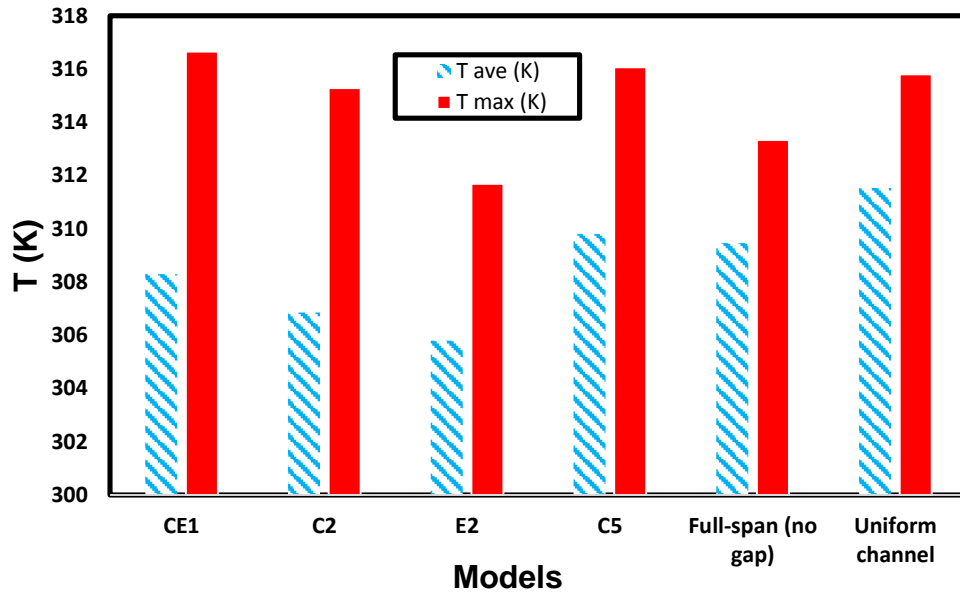


Figure 7.5: Average and maximum temperatures on the solid base achieved with various half-circle VGs with gaps and without gaps and Reynolds number 1500. See Table 5.1 for a description of the VG types.

In contrast, the C2 and CE1 VGs show more interaction, with a more closed region of higher temperature fluid between consecutive VGs. Hence for the C2 and CE1 VGs, the flow downstream of the final VG is more different from the upstream flow than in the E2-model and full-span (no gap) cases. This indicates that placement and distribution of the VGs within the channel is an important additional design factor for consideration, this is presented in the next sections.

The base surface temperature results highlight that, although the PEC index can be useful in comparing designs, it does not provide a complete picture of performance in terms of the practical objective maintaining temperature below a given threshold. The results of Fig. 7.5 do however show further evidence that having gaps between the ends of the VGs and channel walls is beneficial.

However, when analysing data from a pumping power perspective, it is found that the C5-model requires lower pumping than the other circular shapes as drawn in Fig. 7.6. This is because of the lower pressure drop offered by the C5-model due to having large gap (450 μm) as indicated in chapter 5 (see Fig. 5.12). Therefore, at limited pumping power the C5-model and the uniform

channel are the best designs to be manufactured to enhance the heat transfer at low power consumption.

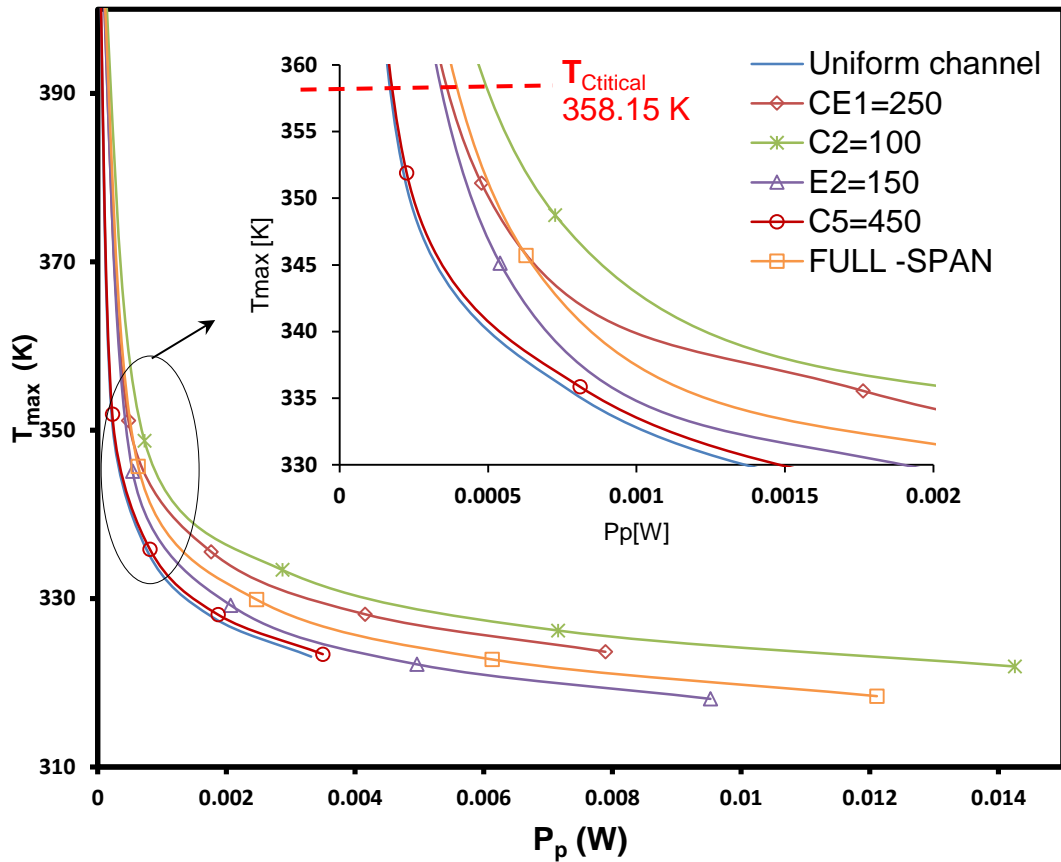


Figure 7.6: Maximum temperatures for different half-circle VGs compared to the uniform channel at different pumping power using water as a coolant.

7.4 Performance of nanofluids

7.4.1 Effect of VGs shape

Based on chapter 6, results showed that using elliptical VGs offered lower thermal resistance and pressure drop using fixed Reynolds number (see Figs. 6.3 and 6.5). However, no significant reduction for both thermal resistance and pressure drop can be seen when using mass flow rate (see Figs. 6.7 and 6.10). Therefore, it is worth to evaluate the heat transfer performance in terms of pumping power. Therefore, the actual temperature is presented by temperature contour as shown in Fig. 7.7a. The figure shows that the temperature of the EL-model is less than that of the C-model, this is because, the

nanofluid is used with the EL-model. Also, the velocity contour in Fig. 7.7b confirms that the fluid flow is enhanced for EL-model compared to the C-model by the reduction in the low velocity zone of the EL-model (Red zone). Thus, the influence of the C-model and the EL-model (VGs) on the maximum base temperature and pumping power are shown in Fig. 7.8. The uniform channel is taken as a reference to compare the influence of using the C-model with water and EL-model with water and SiO₂ nanofluid at the concentration of 1%. It is found that there is enhancement in heat transfer (temperature reduction) and in pressure drop when using different VG geometries and fluids, for the reduction in pressure drop (see Fig. 6.5).

Now, the suggested model (EL-model with 1% of SiO₂ nanofluid) does offer better heat transfer enhancement from a practical perspective than the C-model with water at the same pumping power. In other words, less pumping power is required to achieve a given temperature for the EL-model compared to the C-model. Hence, the idea of combining a geometry offering low pressure drop use of a nanofluid is successful. This will open a wide range of experimental design area. Therefore, researchers can find the easiest design to manufacture with no additional pumping power and produce enhancement in heat transfer when using the effect of different geometries as shown in Fig. 7.8.

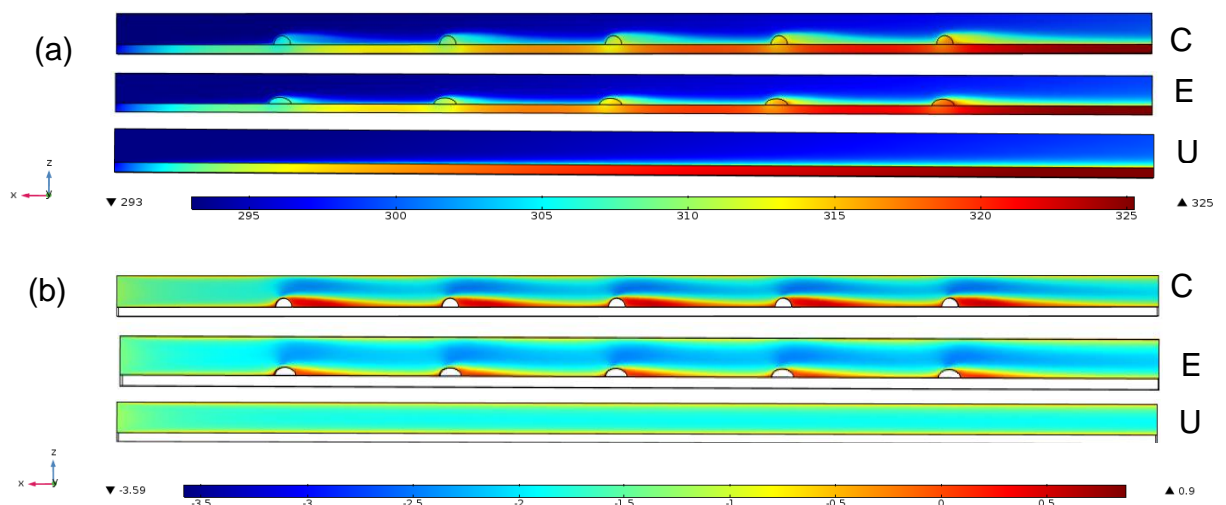


Figure 7.7: X-Z plane comparing the uniform channel to C-model, EL-model and the uniform channel at Re =800: (a) temperature contour; (b) velocity contour.

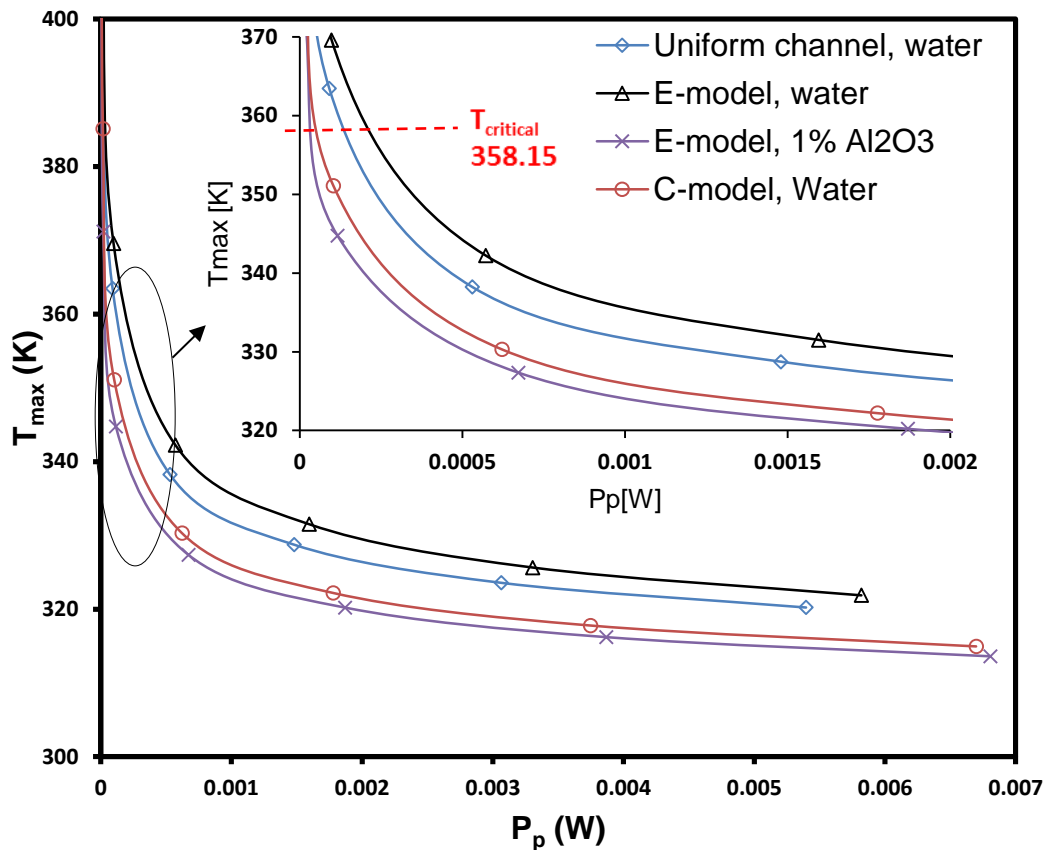


Figure 7.8: Maximum temperature with pumping power for various VG models compared to the uniform channel.

7.4.2 Effect of gaps

The purpose of this section is to draw a clear picture of the effect of the gap in VGs on the temperature and the pumping power, which is one of the most important factors in energy management terms. Therefore, one of the keys to manage the energy is to reduce the pressure drop. VG shapes presented in chapter 4 are re-presented here to introduce the impact of the gap with nanofluids, the VG shapes are Triangular (BT), rectangular (R) and half-circle (C). The results show the same behaviour of pressure drop when using either water or nanofluids, but with different values. However, the required pumping power for nanofluids is higher than for water due to the kinematic viscosity as discussed in chapter 6 (see Figs. 6.7-6.9). Thus, Fig. 7.9 compares the effect of the full-span (no gap) VG shapes on pressure drop. It can be seen that the lowest pressure drop is for the half-circle, then the rectangular and the

triangular VGs, respectively. This is for both, water (Fig. 7.9a) and nanofluids (Fig. 7.9b). As the results show that the highest pressure drop is for the triangular VGs, they are taken as an example to examine the effect of having a gap on the pressure drop, thermal resistance and pumping power. Now, the triangular model is considered as an example to suggest a model which has two gaps near the walls of the micro-channel, each gap has 50 μm .

The key idea of using the gap in VG models is to reduce the pressure drop and enhance the heat transfer simultaneously as detailed in chapter 5. The concept of having gap in VGs applied here, is exactly the same as when having different VGs with pressure difference to tackle the issue of high pressure drop of nanofluids as presented in previous section, but here, is based on the gap instead of geometrical effect.

Fig. 7.10a indicates that there is a reduction in the maximum temperature at the same pumping power for different VG shapes. Equivalently, to achieve a given temperature, lower pumping power is required by some VG shapes. Again, the same behaviour of thermal resistance can be seen for water and nanofluids as shown in Fig. 7.10b. Therefore, an interesting question appears here: can introducing a gap in triangular VGs (having the highest pressure drop) enhance the heat transfer using nanofluids or reduce the pumping power?

Fig. 7.11 reveals that, for a given pumping power, the half-circle VGs achieve the lowest thermal resistance.

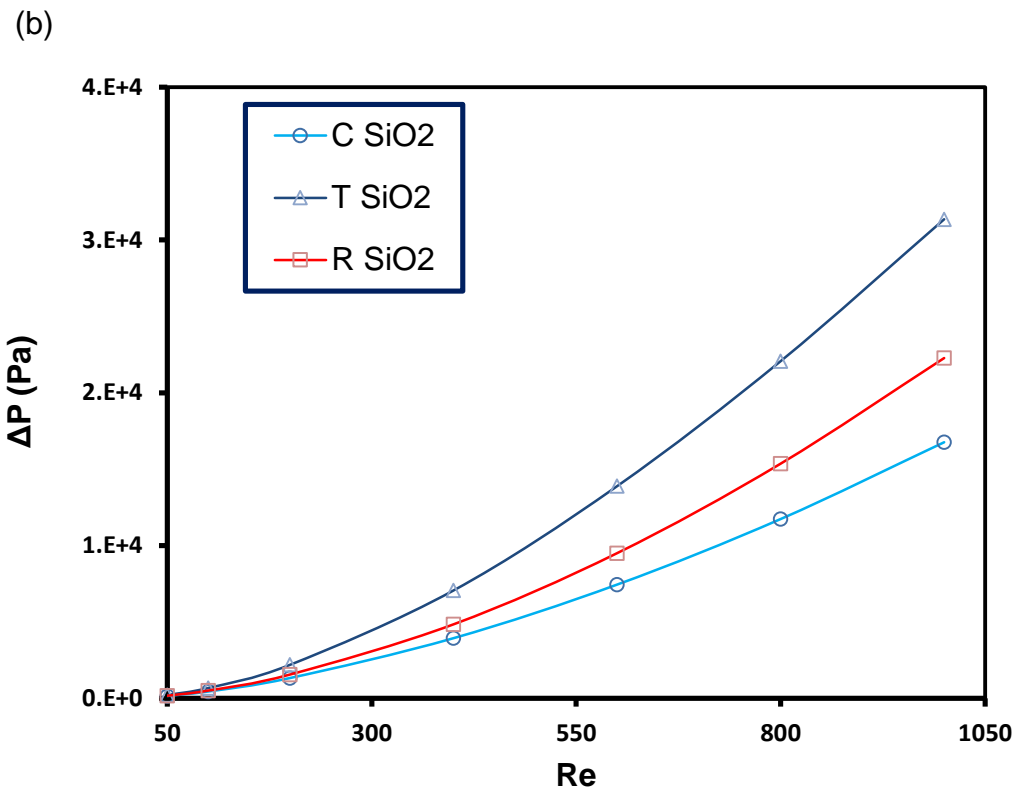
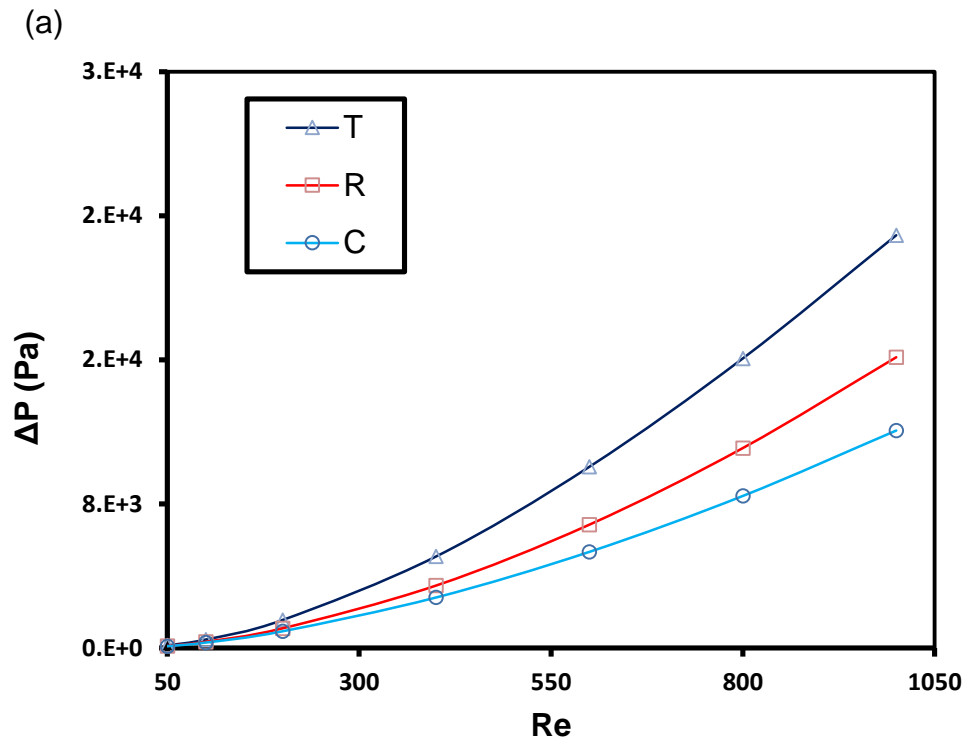
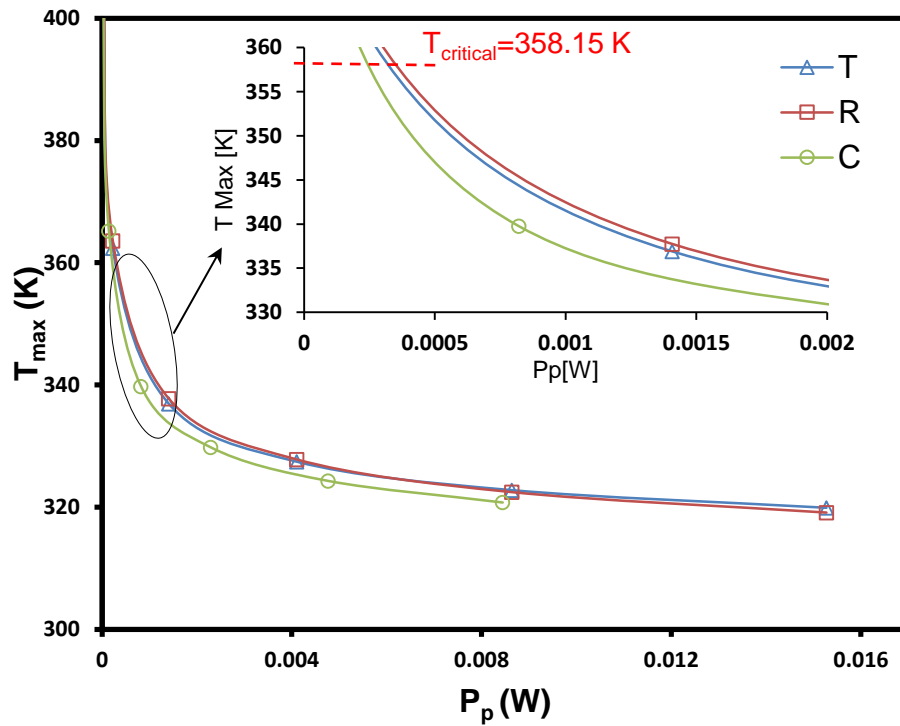


Figure 7.9: Pressure drop for different VGs shapes; (a) water for wide range of Re , (b) using SiO_2 -water nanofluids at the concentration of 2%.

(a)



(b)

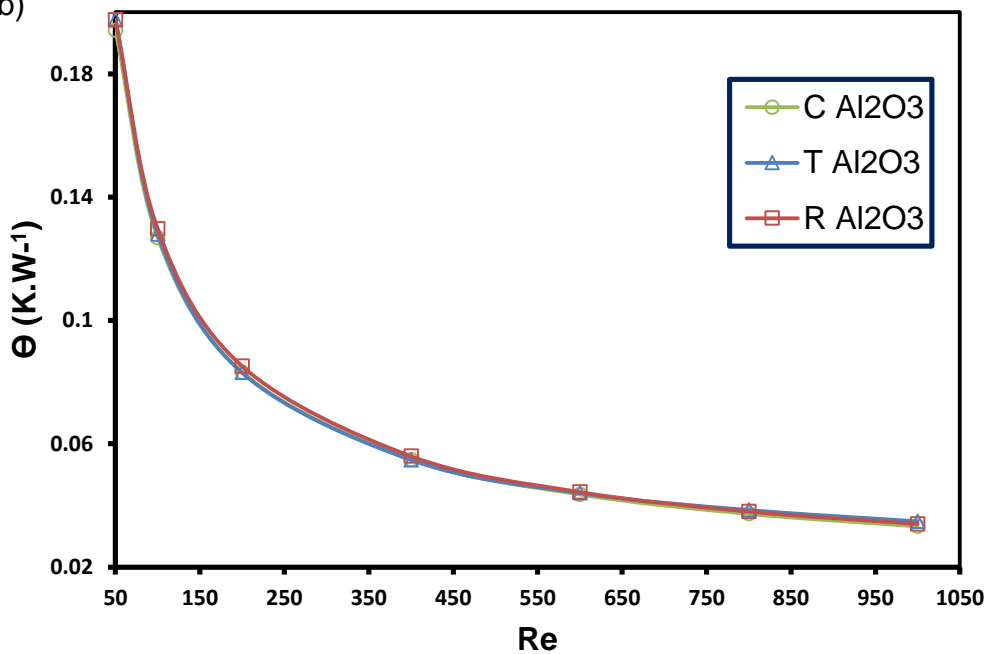


Figure 7.10: Different VG shapes with Al_2O_3 nanoparticles at the concentration of 0.5% in water; (a) Maximum temperature Vs pumping power; (b) thermal resistance using average temperature Vs Re .

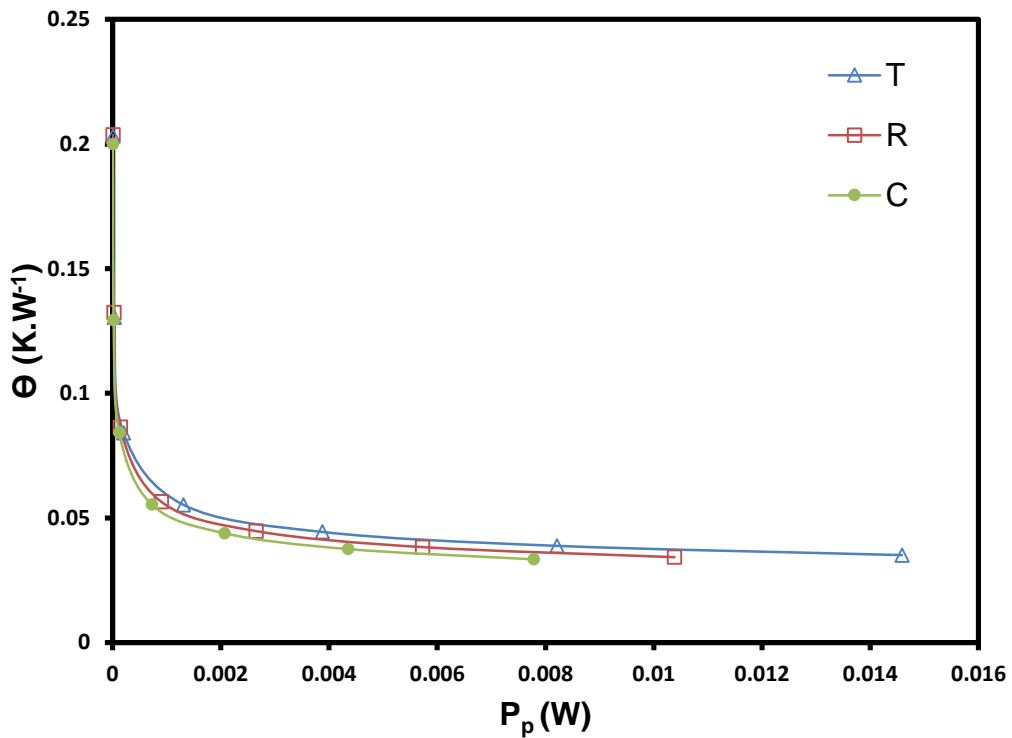


Figure 7.11: Thermal resistance with different pumping power of various VG shapes using SiO₂ of 0.5% in water.

Indeed, introducing the gap in triangular VGs can enhance the heat transfer for a given pumping power. A satisfactory answer to the question mentioned earlier can be presented in Fig. 7.12 with SiO₂-water at the concentration of 0.5%. This is because, the gap in triangular VGs can reduce the pressure drop which leads to reduction of the required pumping power and enhancement of the heat transfer performance. This can be clearly seen in Fig. 7.13. The figure shows reduction in the average and maximum temperatures. Fig. 7.14 shows velocity contour and temperature contour. The figure confirms that there is a relation between the enhancement of the fluid flow and the heat transfer in energy perspective.

In fact, enhancing the flow by having gaps in the triangular VGs (see Fig. 7.14a) leads to enhancing the heat transfer not only compared to the triangular VGs without gap but even better than the C-model.

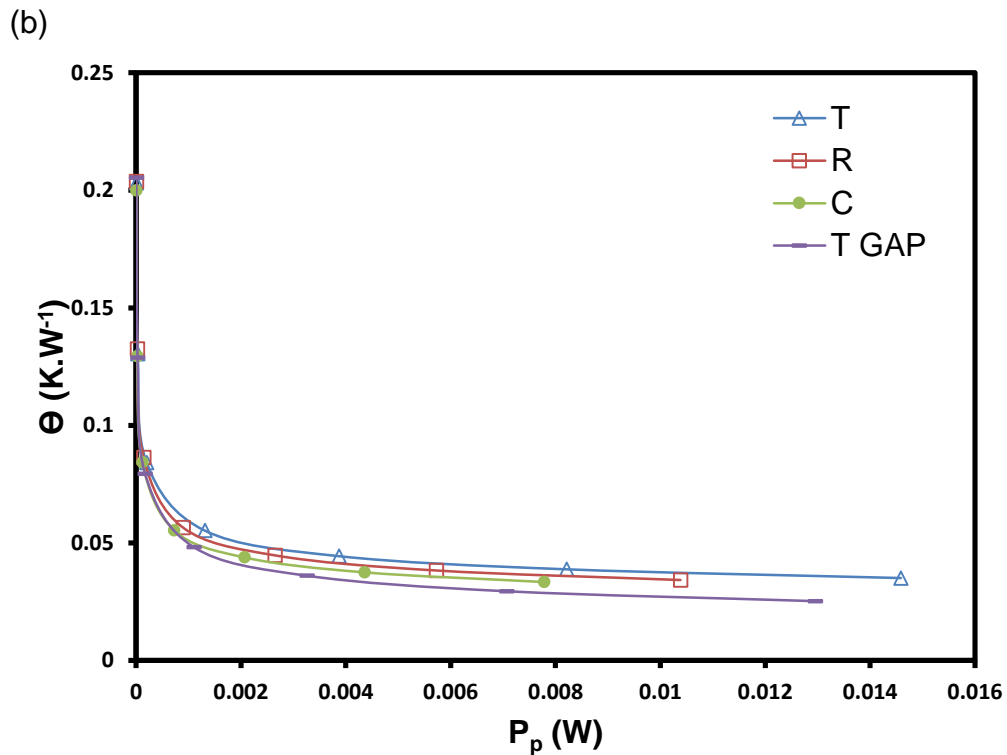
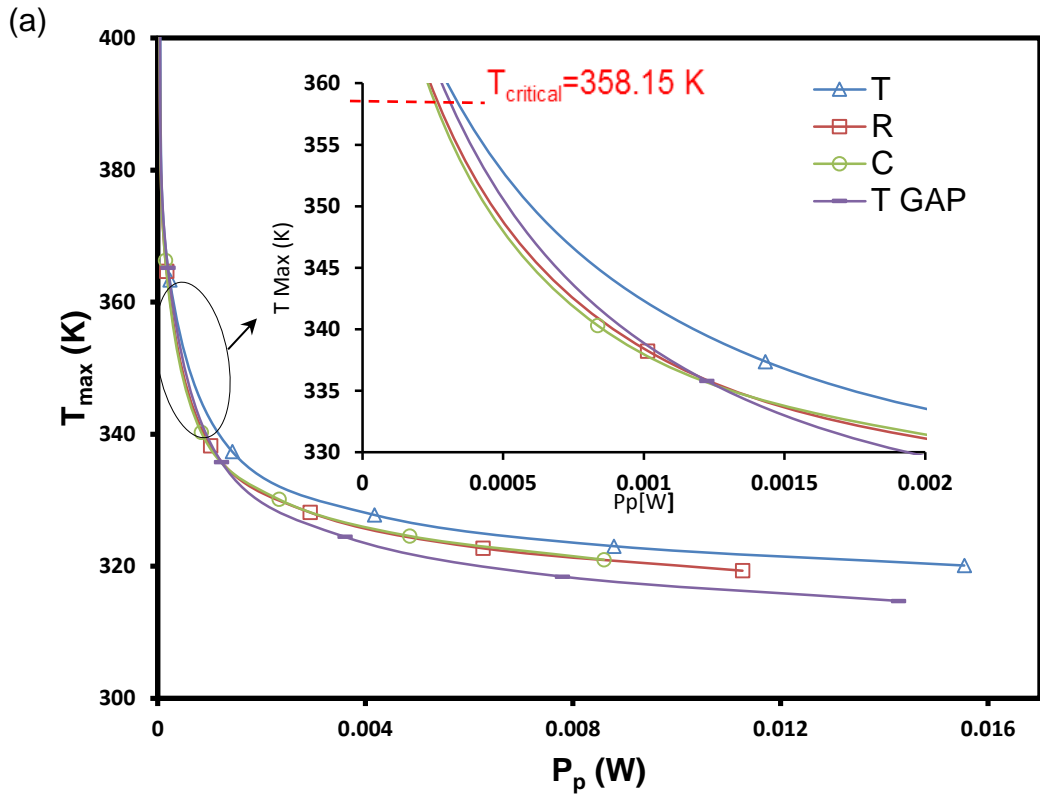


Figure 7.12: Pumping power for different VG shapes compared to triangular VGs having gap of 100 μ m (50 μ m each side near the walls) using SiO₂-water at the concentration of 0.5%; (a) maximum temperature (K); (b) thermal resistance using average temperature.

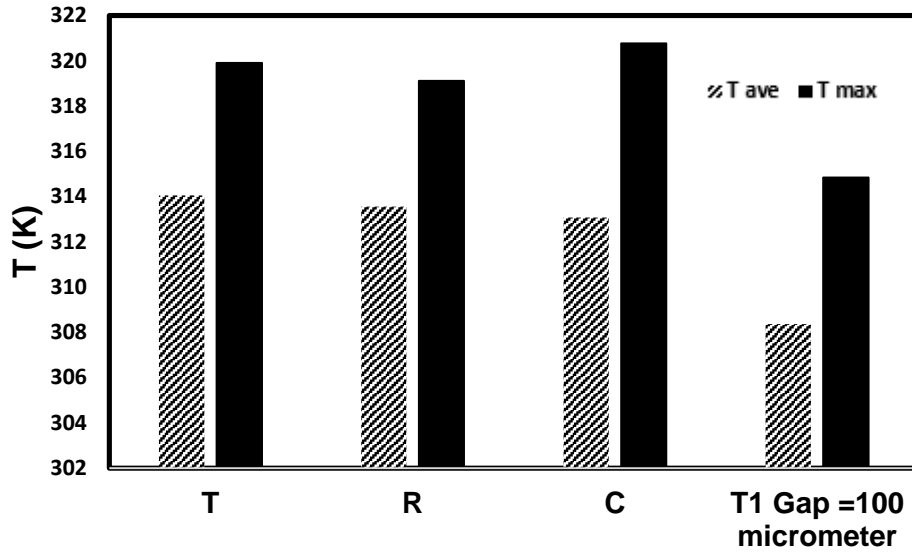


Figure 7.13: Average and maximum temperatures on the solid base achieved with various vortex generators at Reynolds number 1000 using SiO₂-water at the concentration of 0.5%.

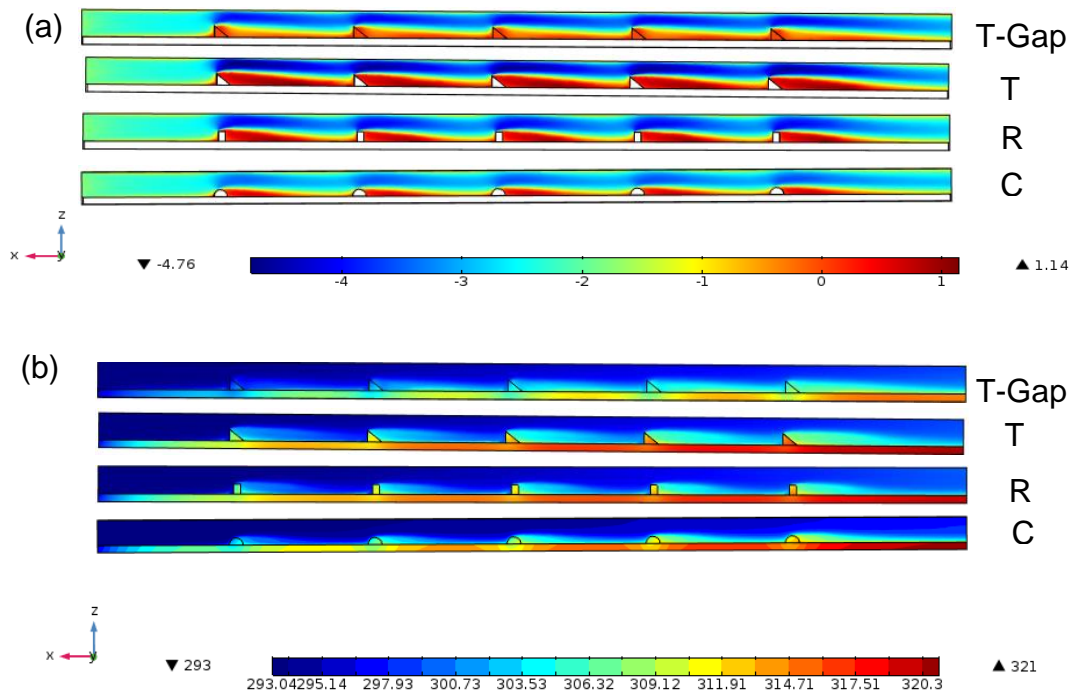


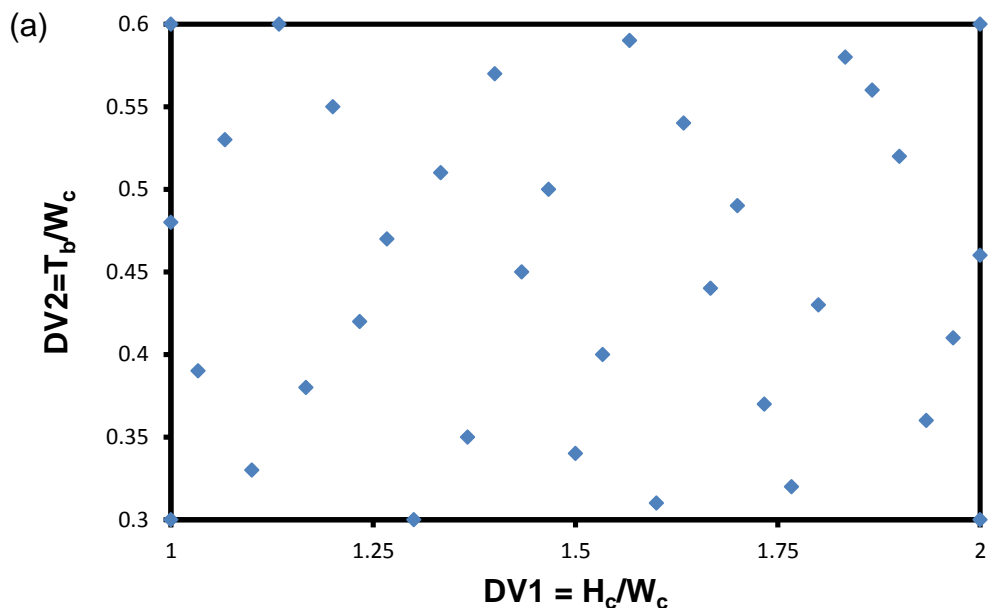
Figure 7.14: X-Z plane comparing the T-model having Gap of 100 μm to full-span T-model, R-model and the C-model at $\text{Re} = 1000$ with SiO₂-water at the concentration of 0.5%: (a) Velocity contour; (b) Temperature contour.

7.5 Optimisation of the uniform micro-channel

As indicated in previous chapters, a huge design space exists for the micro-channel system. Therefore, this section present a simple attempt to optimise the dimensions of the micro-channel to enhance the heat transfer performance. The objective is to reduce of the thermal resistance and the pressure drop simultaneously.

The thermal resistance and pressure drop are parametrised in terms of two dimensionless design variables $DV1$ and $DV2$, namely $DV1 = H_c/W_c$ and $DV2 = T_b/W_c$, with the channel height H_c and thickness $T_b = (H_t - H_c)$ and channel width $W_{ch} = 500 \mu\text{m}$ as described in chapter 3 in Table 3.1. A multi-objective design optimisation process is carried out with the goal to minimise both the thermal resistance and pressure drop. Due to the computational requirements of the 3D CFD analysis described in this thesis, a surrogate modelling approach is adopted for the optimisation study, a methodology that has been successfully applied for a range of engineering applications, e.g. the design optimisation of heat transfer. A 3D CFD-based design of experiments (DOE) approach based is used to generate 35 points spread within the design space $(DV1, DV2) \in [1, 2] \times [0.3, 0.6]$.

The distribution of points in the design variable space is shown in Fig. 7.15 along with the distribution corresponding to the explicit microchannel dimensions.



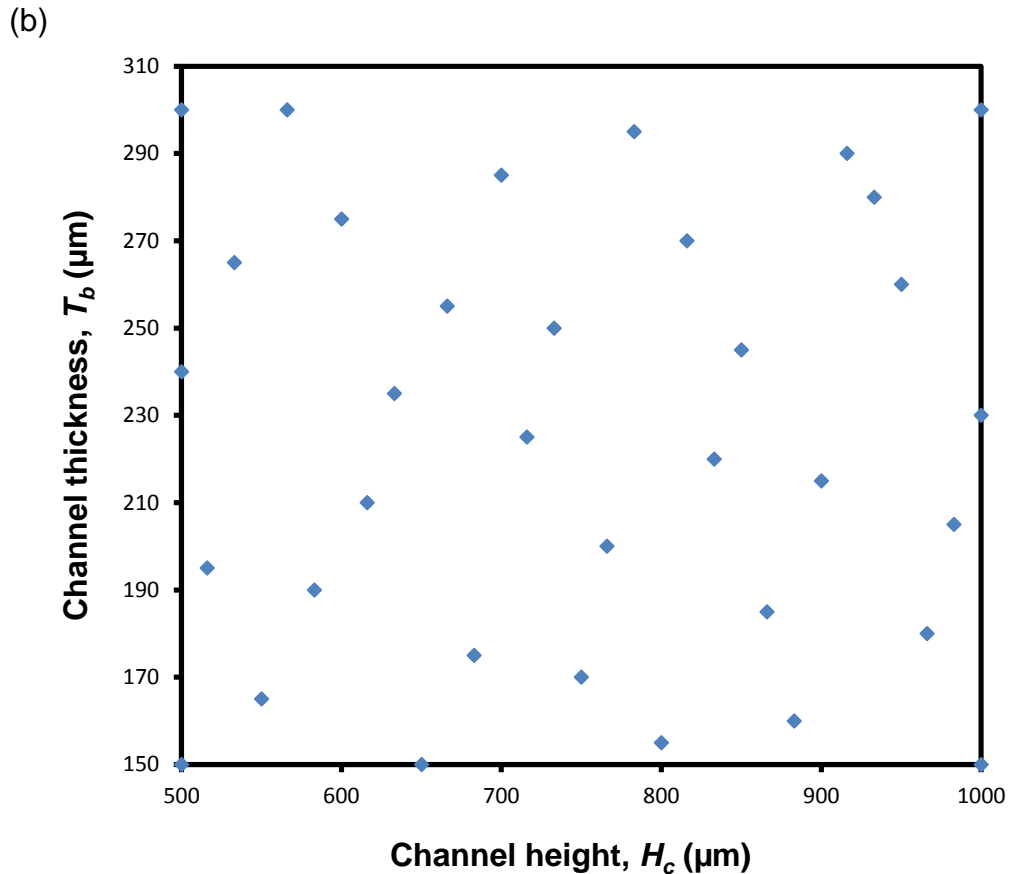


Figure 7.15: Distribution of design points for the design variables in: (a) Design variable space and (b) Corresponding microchannel dimensions.

The full dimensions of the geometry described in chapter 3, section 3.6 (see Fig. 3.1c) are included in Table 7.1. The Table shows the maximum temperature and pressure drop to build the optimisation.

In this study a constant Reynolds number is taken for each change of the height of the channel (H_c). Therefore, the velocity (u_u) is presented based on the Reynolds number using water as a coolant. The velocity is calculated based on Reynolds number of 700 for the dimensions of $H_c=670 \mu\text{m}$ and $W_c = 500 \mu\text{m}$.

Table 7.1: Dimensions with temperature and pressure drop at fixed Reynolds number.

H_c	H_t	U_{in} (m/s)	Temperature (K)	Pressure (Pa)
500	740	1.4025	329.34	14028
516	711	1.3808	328.81	13543
533	798	1.3591	328.36	13283
550	715	1.3388	327.99	12831
566	866	1.3208	327.37	12676
583	773	1.3027	326.9	12316
600	875	1.2856	326.88	12160
616	826	1.2705	326.35	11818
633	868	1.2552	325.97	11602
650	800	1.2407	325.56	11385
666	921	1.2277	325	11346
683	858	1.2146	324.64	10986
700	985	1.2022	324.53	10996
716	941	1.191	324.11	10661
733	983	1.1796	323.8	10594
750	920	1.1688	323.52	10388
766	966	1.159	323.16	10310
783	1078	1.1491	323.18	10159
800	955	1.1396	322.53	10046
816	1086	1.131	322.41	9790.5
833	1053	1.1222	322.22	9846.6
850	1095	1.1138	322.32	9546.3
866	1051	1.1061	321.73	9358.9
883	1043	1.0984	321.38	9695.7
900	1115	1.0909	321.81	9051.5
916	1206	1.084	321.94	8870.2
933	1213	1.0771	321.74	8654
950	1210	1.0703	321.37	8517
966	1146	1.0642	320.91	8580
983	1188	1.058	320.7	8446.5
1000	1230	1.0519	320.74	8350.8
500	650	1.4025	329.19	13800
500	800	1.4025	329.13	14065
1000	1150	1.0519	321.2	8175.8
1000	1300	1.0519	320.97	8243.4

A Radial Basis Function (RBF) method [268], proven to be a successful design tool for engineering applications such as heat transfer processes [269] and combustion systems [270] for instance, is employed to build the surrogate models of T and ΔP , where a cubic radial power function is used to determine the weighting of points in the regression analysis at each point:

$$w_i = r_i^3$$

8.1

The RBF-based surrogate models for the thermal resistance and pressure drop are built by carrying out 3D CFD calculations and solutions respectively at each of the DOE points and using these values to build surrogate models of their dependence on the design variables throughout the design space.

7.5.1 Multi-objective design optimisation

The design goal is formulated as the unconstrained, multi-objective optimization problem of minimising the temperature T and pressure drop ΔP simultaneously. The global minimum of the surrogate model for T and ΔP is found using a multi-objective genetic algorithm (GA) approach based on [271, 272]. Graphical examples of surface functions T and ΔP in terms of the design H_c and T_b are shown in Figures 8.16 and 8.17 respectively.

In a multi-objective optimisation problem, a Pareto front can be used by designers to select the most suitable compromise between the various objective functions that have been distinguished and for which the goal is to minimise the objective functions. It is not possible to move along the design points on the Pareto front to decrease any of the objective functions without increasing at least one other objective function, and Pareto points are often referred to as being 'non-dominated'. In the present case with two objective functions the Pareto front showing the impact of the two objectives of interest here is shown in Fig. 7.18. This data provides a convenient and scientifically-rigorous means by which designers can quantify the effect of their design criteria on both on both manufacturability and energy efficiency of micro-channels.

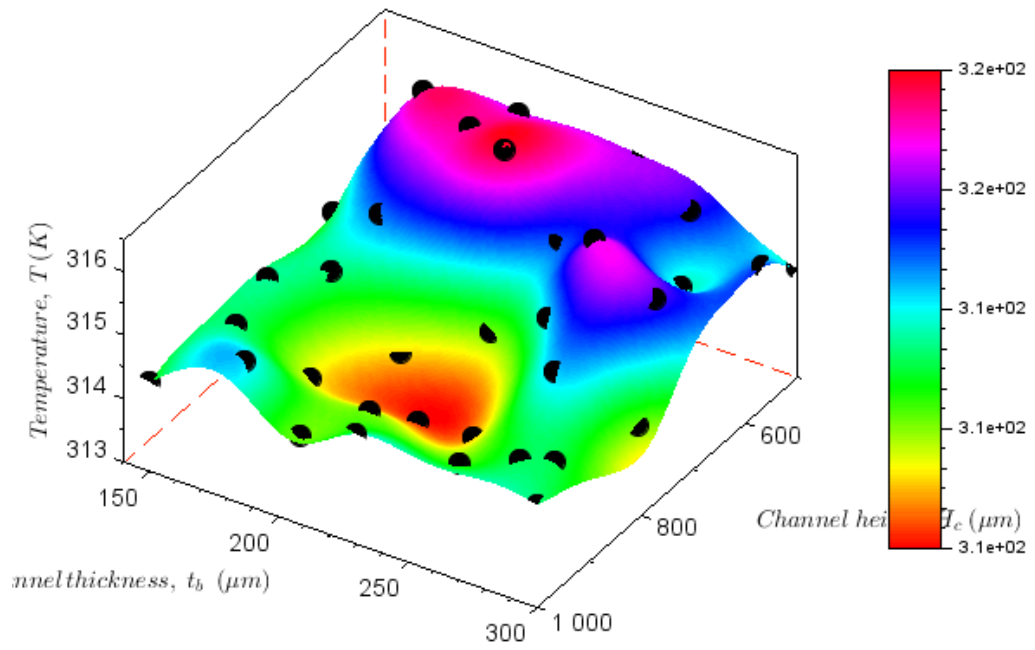


Figure 7.16: Response surface of function T from the surrogate model together with the DOE points.

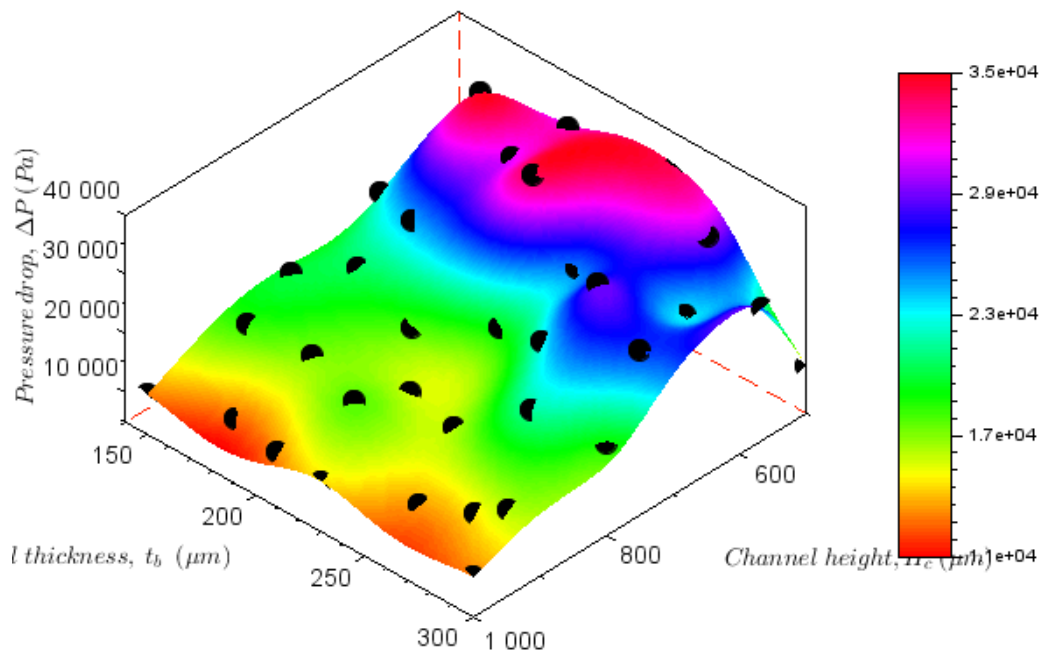


Figure 7.17: Response surface of function ΔP from the surrogate model together with the DOE points.

As a demonstration, 5 microchannel designs lying on the Pareto front in Fig. 7.18 (a and b) are detailed in Table 7.2. The corresponding design variables, namely H_c and T_b with the two objectives T and pressure drop ΔP are also specified.

For the five designs, the performance of maximum temperature and pressure drop predicted by surrogate model and the full CFD analysis is also included in Table 7.2.

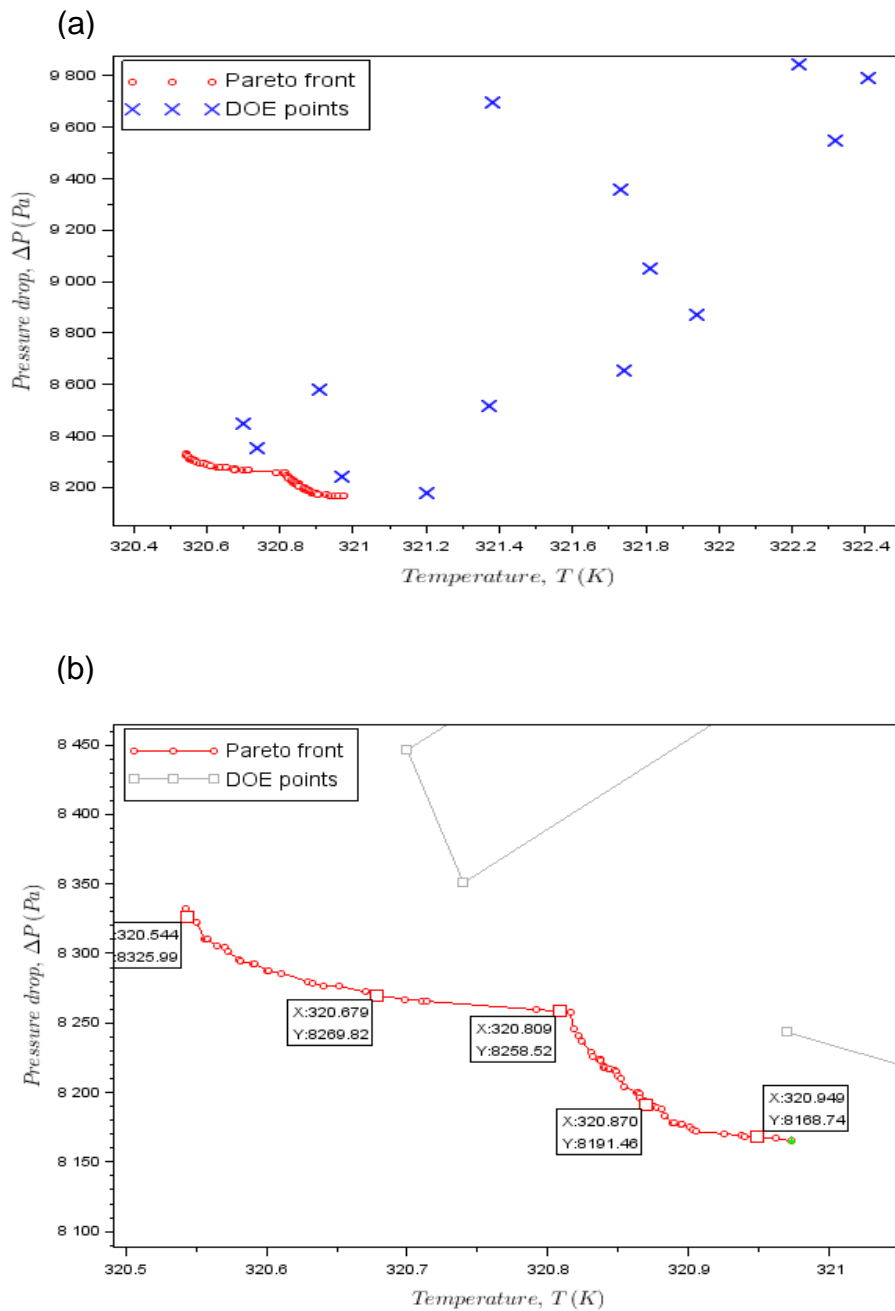


Figure 7.18: Pareto front for; (a) the design given in Table 7.1, (b) predicted points adopted from the Pareto front.

Table 7.2: Microchannel design performance at five operating conditions points located on the Pareto front together with CFD validation.

Pareto front	Hc	Ht	Predicted results		CFD results	
			Tmax	ΔP max	Tmax	ΔP max
	μm	μm	K	Pa	K	Pa
p1	997.47019	1197.19	320.5435	8325.986	320.91	8199.7
p2	997.55157	1181.082	320.67858	8269.82	321.15	8116.8
p3	997.81853	1171.693	320.80871	8258.52	320.85	8553.2
p4	996.78504	1256.879	320.8702	8191.461	321	8333.8
p5	995.59267	1265.096	320.94879	8168.737	321.06	8389

The validation of the points given in Table 7.2 are also presented in Fig. 7.19 (a and b). Fig. 7.19a shows very good agreement between the predicted temperature and the temperature of simulation results. The pressure drop is drawn in Fig. 7.19b, it is also found to be in good agreement between the predicted data and CFD results.

The optimum design points obtained by the surrogate models and GA and the CFD models are comparatively identical. Hence, confirming that the CFD model is able to predict the GA-based surrogate models results with high confidence. It is worth noting that in terms manufacturing, our CFD-validated surrogate model can be used as a reliable design tool to develop microchannels with desired anticipated thermal resistance and pressure drop (R_{th} , ΔP) belonging to the region $D=[0.123, 0.156] \times [1544.24, 9084.58]$ with consequential design variable $(W_{ch}, N_{ch}, \Theta) \in [0.8, 1.486] \times [9, 11] \times [20.28, 39.58]$.

Fig. 7.19 shows that the Pareto front showing the compromises that can be struck in minimising the maximum value of both T and ΔP together with five representative design points (e.g. P₁, P₂, P₃, P₄ and P₅) used for the microchannel performance analysis illustrated in Table 7.2.

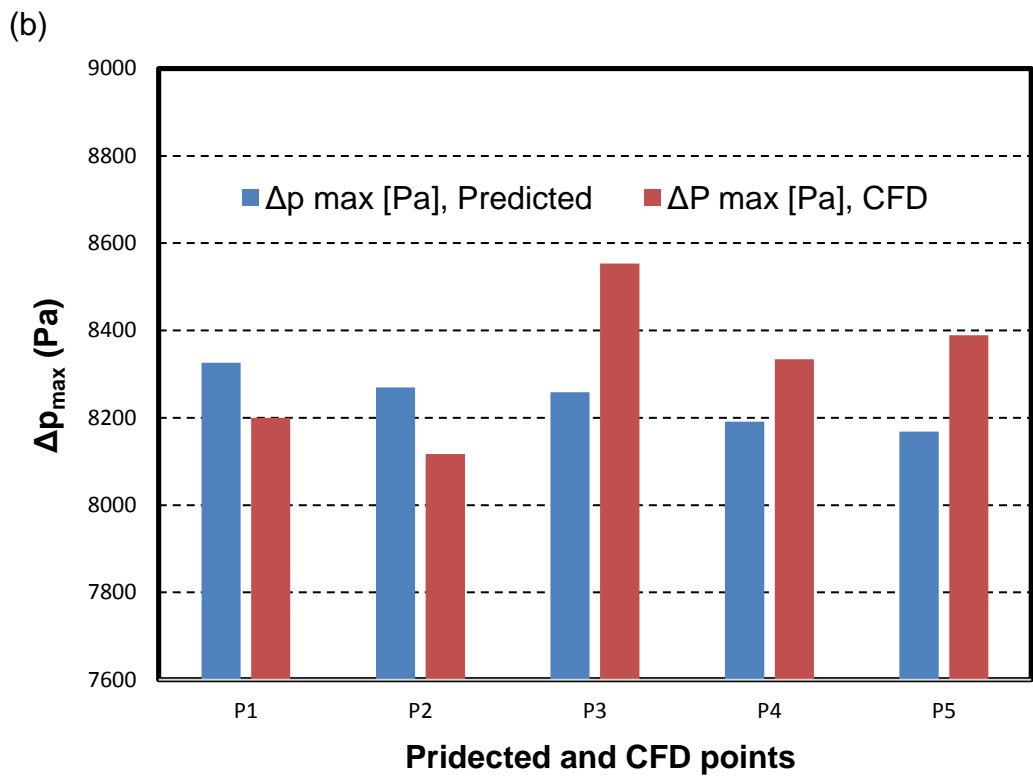
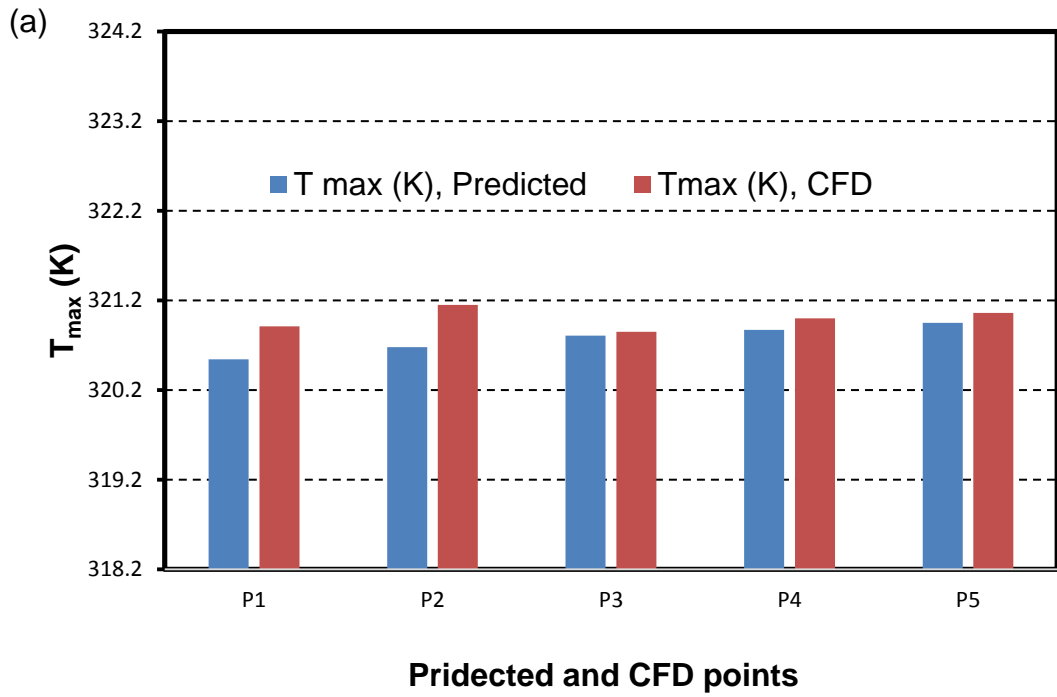


Figure 7.19: Validation between predicted data and CFD results; (a) maximum temperature, (b) maximum pressure drop.

7.6 Summary

This chapter examines the results of previous chapters together from a practical perspective. The aim of the study was to suggest a new geometry which meets the rapid developments of the electronic devices; shrinking the size of the micro-channel and increasing in the thermal efficiency simultaneously. This can be achieved by designing a micro-channel which offers high thermal performance for low input energy. Two ways are used to assess the performance of the heat transfer and fluid flow characteristics. The first way is to present the results as average and maximum temperatures which has been done in the first and second sections with water as a working fluid. The second way is to evaluate the coolant performance in terms of pumping power as was done in the third section, where the SiO_2 and Al_2O_3 nanofluids in different concentrations were considered. The fourth section deals with optimising the straight micro-channel to suggest a modified design to reduce the maximum temperature and pressure drop, simultaneously. The findings of the chapter are drawn to be:

- The half-circle model offers lower average temperature than the triangular and rectangular models as indicated in chapter 3. However, it produced the highest maximum temperature among the VGs due to the high outlet temperature of the fluid (see Fig. 7.2).
- Gaps at the ends of the VGs are beneficial in terms of the average and maximum temperatures that can be achieved for a given heat load, and in reducing the large pressure drop associated with full-span vortex generators. Half-circle VGs offers the lowest thermal resistance and pressure drop among the full-span VG models when using pure water or nanofluid as a working fluid. However, when considering the need to achieve a base temperature below a critical value, the C5 VG (with a wide central gap) is found to achieve this with the lowest pumping power requirements.
- Although nanofluids are generally associated with higher pumping power costs, here it is found that careful combination of nanofluids and VG geometries can produce net benefits. In particular it is found that 1% Al_2O_3 -water nanofluid in combination with an elliptical VG requires less

pumping power to achieve a required based temperature than the same VG used with pure water or even the half-circle VG with pure water. Therefore, more flexible options for manufacturing designs can be achieved with the effect of using different geometries with no additional cost to be paid for pumping power.

- There is considerable reduction in pumping power using nanofluids with VGs having gaps compared to the VGs without gaps.
- The results indicate that triangular VGs having gaps used with nanofluid provide a lower thermal resistance compared to the full-span triangular VG, and even better than the half-circle VGs with pure water at the same pumping power. This opens the door to the use of nanofluids without additional pumping power cost to enhance the heat transfer performance when using the gap in VG models.
- Surrogate models of the system behaviour built using radial basis functions are used to predict the system performance very accurately, enabling multi-objectives optimisation to be performed.
- There is a huge space key and the illustrative example presented here, but further optimisation is beyond the scope of this thesis.

Chapter 8: Conclusion and recommendation for future work

8.1 Achievements – general discussion

As indicated in previous chapters, many objectives have been achieved using geometrical and fluids influences to enhance the heat transfer and reduce the pressure drop. The numerical method used in this study is the finite element method which is built in COMSOL Multiphysics. To ensure the accuracy of the results, validations of previous experimental and numerical studies have been done and found in good agreement. The study investigated the conjugate heat transfer under laminar flow ($50 < Re < 2300$) subjected to a uniform heat flux ranging from 75 to 100 W/cm² related to CPUs in electronic devices. The results concluded that perforated pinned heat sink with water struggles to enhance the heat transfer. Therefore the vortex generators (VGs) with different shapes, namely forward triangular (FT), backward triangular (BT), symmetric triangular (ST), vertical rectangular (VR), horizontal rectangular (HR), square (S) and half-circle (C) are suggested to enhance the heat transfer using liquid coolant (water or nanofluid). Therefore, the outcomes out of this research are summarised in the following sections.

8.2 Vortex generators

From the analysis of the pinned heat sink, and the investigation of vortex generators, the following points have been identified:

- It does not necessarily follow that a geometrical modification that improves heat transfer for one fluid will also enhance performance for a different working fluid. In the present study, the perforated pinned heat sink that is effective with air does not work with water as a coolant.
- All proposed VG models offer heat transfer improvement (thermal resistance reduction) while, as to be expected, the price paid is the additional pumping power needed to drive the flow compared to the uniform channel.

- For triangular VG configurations (forward triangular (FT), backward triangular (BT) and symmetric triangular (ST)), it is found that the lowest thermal resistance is for the ST model, while the lowest pressure drop is for the BT model.
- For the rectangular VG models (vertical rectangular (VR), horizontal rectangular (HR) and square (S)), the results show that the S model offers the lowest thermal resistance and pressure drop compared to VR and HR, but the S model still has a higher pressure drop than the uniform channel.
- Circular VGs offer the lowest thermal resistance (2% reduction in thermal resistance compared to the uniform channel), followed by rectangular and triangular VGs. However, the pressure drops of all proposed VGs models are much higher than for the uniform channel. For the VGs with half-circle cross-section spanning the whole width of the microchannel, the thermal resistance was shown to decrease monotonically as the VG radius increases. However, as expected the pressure drop increased with radius as a result of the increasing constriction in the flow.
- A modification of the full-span half-circle VG to produce a shorter, centred VG showed a greater reduction in the thermal resistance, while also showing a smaller increase in the pressure drop, compared to the full-span VG. It is found that the E2 model offers reduction in thermal resistance (up to 7% compared to the uniform channel and 2% compared to full-span model) and pressure drop compared to the full-span VGs.
- Based on the PEC index, which offsets the improvement in thermal resistance against the pressure penalty. For example there is a reduction in thermal resistance for all proposed models. However, few models offer heat transfer enhancement with respect to the increase of pressure penalty. Thus, small-radius centred VGs offer good potential

for improving the efficiency of micro-channels. It is found that VGs with very large gap (C5-model - 450 μm of gap) offer the best PEC for half-circle models, with a value of up to 1.08, which corresponds to a net improvement of 8% in the efficiency of the system compared to the uniform channel.

8.3 Nanofluid performance

As indicated in chapters 6 and 7, care must be taken when implementing nanofluids in systems, especially dealing with non-dimensional factors such as Reynolds number. This can mislead the results as the Reynolds number is a function of density and viscosity of nanofluid. Therefore, increasing the density and viscosity (increasing nanoparticles concentration) increases Reynolds number. However, using a physical unit such as mass flow rate does not offer the same enhancement in heat transfer compared to non-dimensional factors (Reynolds number), based on this, it is found that:

- The thermal resistance decreased using various nanofluids in different concentrations compared to pure water, it is also decreased as the concentrations of nanoparticles increased.
- Al_2O_3 -water nanofluid has low thermal resistance and pressure drop compared to SiO_2 -water nanofluid at the same concentration due to its thermo-physical properties.
- The new suggested model (elliptical-model) with nanofluids up to 4% of nanofluid concentration offered lower thermal resistance and pressure drop, but the pressure drop of EL-model with nanoparticles concentration of 4% is higher than the half-circle model with water.
- No significant reduction in thermal resistance is found compared to the use of a fixed Reynolds number with different geometries.
- The thermal resistance and the pressure drop increased with the nanoparticle concentrations when using MFR.

From above points, it is found that there is possibility of combining geometrical modifications (using VG geometries) with coolant modifications (using nanofluids), and it is found that Al_2O_3 or SiO_2 nanofluids in a micro-channel with elliptical VGs can replace pure water as a coolant.

Based on the above findings, the energy management of heat and flow characteristics plays a crucial role in practical and commercial applications. It is found that having gap in VGs enhances the heat transfer performance and reduces the power consumption. The results show that the using nanofluid with geometrical modification (elliptical model) provides efficient system with low pinging power.

8.4 Limitations of this study

Although the finite element model used here was validated against published experimental data for a uniform channel, this study is an entirely CFD-based investigation, and therefore experimental validation of the new ideas presented has yet to be achieved. CFD does not suffer the same restriction in terms of manufacture that limits experimental and practical systems, and it is recognised that some of the VG designs considered here may not yet be feasible to manufacture. As has been stated earlier in the thesis, there is a huge design space in terms of VG/microchannel geometry, working fluid, and even a combination of these. The optimisation study presented in chapter 7 considers only a limited investigation of that design space, but does illustrate the potential for exploiting optimisation methods in this type of system.

- **Lack of experiments:** Limited practical applications of using a micro-channel heat sink with water or nanofluids, while several experiments have used low thermal conductivity liquids such as Novec. There is also lack of using closed cycle cooling system compared to open and immersing systems such as those used in data centres.
- **Manufacturing issues:** High accuracy manufacturing machines are required to produce high quality experiments that agreed with the results of numerical studies. The common issues of lack agreement between the numerical and experimental investigations could be the error in dimensions of the experiment compared to the actual design, the finishing of the experiment surfaces (surface roughness), the accuracy of measuring devices or their setup due to limited space (micro- size).

8.5 Future Work

In this section, further work possibilities are listed:

1. This study has not been done experimentally, therefore, it can be a new experimental study which can be used in practical applications. The experimental study also could be compared to the existing numerical study of this work.
2. Investigate the effect of tapered geometry with vortex generators on a conjugate heat transfer and fluid flow characteristics. This is to reduce the issue of the increase of pressure penalty and enhance the heat transfer which leads to offer efficient cooling system with low power consumption.
3. Study and optimise the impact of nanofluids on heat and flow performances using equations established in the literature (see Ch2, section 2.5) and compared them with experimental studies. Also, different types of nanoparticles such as CuO and TiO₂ in the base fluid such as water and/or glycerine with various concentrations can be investigated.
4. The optimization objectives can be extended to be three design variables by including the fluid type such as water or nanofluids. The optimization study can be done in two ways, the first way is based on the thermal and fluid performance such as PEC index, however, the second optimization could be for the whole project that is include the cost, the design, using different shapes of VGs, and the fluid type.
5. An important study of energy management can be based on the

optimisation results. Saving power, materials, space and the operating conditions for a system due to the reduction in temperature and power consumption when using modified micro-channel and/ or nanofluid is one way of energy management which depend on the outcome of the optimisation.

REFERENCES

1. McCartney, S., *ENIAC: The triumphs and tragedies of the world's first computer*. 1999: Walker & Company.
2. Gong, L., J. Zhao, and S. Huang, *Numerical study on layout of micro-channel heat sink for thermal management of electronic devices*. Applied Thermal Engineering, 2015. **88**: p. 480-490.
3. Li, H.-Y., et al., *Enhancing heat transfer in a plate-fin heat sink using delta winglet vortex generators*. International Journal of Heat and Mass Transfer, 2013. **67**(0): p. 666-677.
4. Dutschk, V., et al., *Smart and green interfaces: From single bubbles/drops to industrial environmental and biomedical applications*. Advances in Colloid and Interface Science, 2014. **209**: p. 109-126.
5. Albadr, J., S. Tayal, and M. Alasadi, *Heat transfer through heat exchanger using Al₂O₃ nanofluid at different concentrations*. Case Studies in Thermal Engineering, 2013. **1**(1): p. 38-44.
6. Cheraghi, M., M. Raisee, and M. Moghaddami, *Effect of cylinder proximity to the wall on channel flow heat transfer enhancement*. Comptes Rendus Mécanique, 2014. **342**(2): p. 63-72.
7. Dixit, T. and I. Ghosh, *Review of micro- and mini-channel heat sinks and heat exchangers for single phase fluids*. Renewable and Sustainable Energy Reviews, 2015. **41**(0): p. 1298-1311.
8. Mehendale, S.S., A.M. Jacobi, and R.K. Shah, *Fluid Flow and Heat Transfer at Micro- and Meso-Scales With Application to Heat Exchanger Design*. Applied Mechanics Reviews, 2000. **53**(7): p. 175-193.
9. Kandlikar SG, G.W., *Evolution of microchannel flow passages: thermohydraulic performance and fabrication technology*. Proceedings of the ASME international mechanical engineering congress exposition, 2002.
10. Tuckerman, D.B. and R.F.W. Pease, *High-performance heat sinking for VLSI*. Electron Device Letters, IEEE, 1981. **2**(5): p. 126-129.
11. Nonino, C., et al., *Conjugate forced convection and heat conduction in circular microchannels*. International Journal of Heat and Fluid Flow, 2009. **30**(5): p. 823-830.
12. Knupp, D.C., R.M. Cotta, and C.P. Naveira-Cotta, *Heat Transfer in Microchannels with Upstream–Downstream Regions Coupling and Wall Conjugation Effects*. Numerical Heat Transfer, Part B: Fundamentals, 2013. **64**(5): p. 365-387.
13. Zhai, Y.L., et al., *Characteristics of entropy generation and heat transfer in double-layered micro heat sinks with complex structure*. Energy Conversion and Management, 2015. **103**: p. 477-486.

References

14. Manglik, R., *Heat transfer enhancement*. 2003, Wiley, New York. p. 1029-1130.
15. Ebrahimi, A., et al., *Heat transfer and entropy generation in a microchannel with longitudinal vortex generators using nanofluids*. Energy, 2016. **101**: p. 190-201.
16. Promvonge, P., et al., *Enhanced heat transfer in a triangular ribbed channel with longitudinal vortex generators*. Energy Conversion and Management, 2010. **51**(6): p. 1242-1249.
17. Chompookham, T., et al., *Heat transfer augmentation in a wedge-ribbed channel using winglet vortex generators*. International Communications in Heat and Mass Transfer, 2010. **37**(2): p. 163-169.
18. Dezan, D.J., L.O. Salviano, and J.I. Yanagihara, *Heat transfer enhancement and optimization of flat-tube multilouvered fin compact heat exchangers with delta-winglet vortex generators*. Applied Thermal Engineering.
19. Song, K., et al., *Quantitative relationship between secondary flow intensity and heat transfer intensity in flat-tube-and-fin air heat exchanger with vortex generators*. Applied Thermal Engineering, 2016. **103**: p. 1064-1070.
20. Wu, J.M. and W.Q. Tao, *Numerical study on laminar convection heat transfer in a rectangular channel with longitudinal vortex generator. Part A: Verification of field synergy principle*. International Journal of Heat and Mass Transfer, 2008. **51**(5–6): p. 1179-1191.
21. Wang, C.-C., et al., *Flow visualization of wave-type vortex generators having inline fin-tube arrangement*. International Journal of Heat and Mass Transfer, 2002. **45**(9): p. 1933-1944.
22. Manca, O., S. Nardini, and D. Ricci, *A numerical study of nanofluid forced convection in ribbed channels*. Applied Thermal Engineering, 2012. **37**(0): p. 280-292.
23. Ahmed, M.A., et al., *Effect of corrugation profile on the thermal-hydraulic performance of corrugated channels using CuO–water nanofluid*. Case Studies in Thermal Engineering, 2014. **4**(0): p. 65-75.
24. Wang, C.-C. and J.-S. Liaw, *Air-side performance of herringbone wavy fin-and-tube heat exchangers under dehumidifying condition – Data with larger diameter tube*. International Journal of Heat and Mass Transfer, 2012. **55**(11–12): p. 3054-3060.
25. Li, L., et al., *Numerical simulation on flow and heat transfer of fin-and-tube heat exchanger with longitudinal vortex generators*. International Journal of Thermal Sciences, 2015. **92**(0): p. 85-96.
26. Ebrahimi, A., E. Roohi, and S. Kheradmand, *Numerical study of liquid flow and heat transfer in rectangular microchannel with longitudinal vortex generators*. Applied Thermal Engineering, 2015. **78**(0): p. 576-583.
27. Ahmed, H.E., H.A. Mohammed, and M.Z. Yusoff, *An overview on heat transfer augmentation using vortex generators and nanofluids*:

References

- Approaches and applications*. Renewable and Sustainable Energy Reviews, 2012. **16**(8): p. 5951-5993.
28. Min, C., et al., *Experimental study of rectangular channel with modified rectangular longitudinal vortex generators*. International Journal of Heat and Mass Transfer, 2010. **53**(15–16): p. 3023-3029.
 29. Habchi, C., et al., *Enhancing heat transfer in vortex generator-type multifunctional heat exchangers*. Applied Thermal Engineering, 2012. **38**(0): p. 14-25.
 30. Al-Damook, A., et al., *An experimental and computational investigation of thermal air flows through perforated pin heat sinks*. Applied Thermal Engineering, (0).
 31. Kai-Shing, Y., et al., *On the Heat Transfer Characteristics of Heat Sinks: With and Without Vortex Generators*. Components and Packaging Technologies, IEEE Transactions on, 2010. **33**(2): p. 391-397.
 32. Leu, J.-S., Y.-H. Wu, and J.-Y. Jang, *Heat transfer and fluid flow analysis in plate-fin and tube heat exchangers with a pair of block shape vortex generators*. International Journal of Heat and Mass Transfer, 2004. **47**(19–20): p. 4327-4338.
 33. Wu, J.M. and W.Q. Tao, *Effect of longitudinal vortex generator on heat transfer in rectangular channels*. Applied Thermal Engineering, 2012. **37**(0): p. 67-72.
 34. Khoshvaght-Aliabadi, M., S. Zangouei, and F. Hormozi, *Performance of a plate-fin heat exchanger with vortex-generator channels: 3D-CFD simulation and experimental validation*. International Journal of Thermal Sciences, 2015. **88**(0): p. 180-192.
 35. Li, J., et al., *Numerical study on a slit fin-and-tube heat exchanger with longitudinal vortex generators*. International Journal of Heat and Mass Transfer, 2011. **54**(9–10): p. 1743-1751.
 36. Chomdee, S. and T. Kiatsiriroat, *Enhancement of air cooling in staggered array of electronic modules by integrating delta winglet vortex generators*. International Communications in Heat and Mass Transfer, 2006. **33**(5): p. 618-626.
 37. Liu, C., et al., *Experimental investigations on liquid flow and heat transfer in rectangular microchannel with longitudinal vortex generators*. International Journal of Heat and Mass Transfer, 2011. **54**(13–14): p. 3069-3080.
 38. Ma, J., et al., *Experimental investigations on single-phase heat transfer enhancement with longitudinal vortices in narrow rectangular channel*. Nuclear Engineering and Design, 2010. **240**(1): p. 92-102.
 39. Aris, M.S., I. Owen, and C.J. Sutcliffe, *The development of active vortex generators from shape memory alloys for the convective cooling of heated surfaces*. International Journal of Heat and Mass Transfer, 2011. **54**(15–16): p. 3566-3574.

References

40. Mudawar, I., *Assessment of high-heat-flux thermal management schemes*. Components and Packaging Technologies, IEEE Transactions on, 2001. **24**(2): p. 122-141.
41. Yeh, L., *Review of heat transfer technologies in electronic equipment*. Journal of electronic packaging, 1995. **117**(4): p. 333-339.
42. Simons, R.E., *Direct liquid immersion cooling for high power density microelectronics*. Electronics Cooling, 1996. **2**: p. 24-29.
43. Chen, C., et al., *A study on fluid flow and heat transfer in rectangular microchannels with various longitudinal vortex generators*. International Journal of Heat and Mass Transfer, 2014. **69**: p. 203-214.
44. Tong, X.C., *Development and Application of Advanced Thermal Management Materials*, in *Advanced Materials for Thermal Management of Electronic Packaging*. 2011, Springer. p. 527-593.
45. Chol, S., *Enhancing thermal conductivity of fluids with nanoparticles*. ASME-Publications-Fed, 1995. **231**: p. 99-106.
46. Xie, H., et al. *Influencing factors for thermal conductivity enhancement of nanofluids*. in *ASME 2009 Second International Conference on Micro/Nanoscale Heat and Mass Transfer*. 2009. American Society of Mechanical Engineers.
47. Trisaksri, V. and S. Wongwises, *Critical review of heat transfer characteristics of nanofluids*. Renewable and Sustainable Energy Reviews, 2007. **11**(3): p. 512-523.
48. Yu, W., et al., *Review and Comparison of Nanofluid Thermal Conductivity and Heat Transfer Enhancements*. Heat Transfer Engineering, 2008. **29**(5): p. 432-460.
49. Palm, S.J., G. Roy, and C.T. Nguyen, *Heat transfer enhancement with the use of nanofluids in radial flow cooling systems considering temperature-dependent properties*. Applied Thermal Engineering, 2006. **26**(17-18): p. 2209-2218.
50. Myers, T.G., H. Ribera, and V. Cregan, *Does mathematics contribute to the nanofluid debate?* International Journal of Heat and Mass Transfer, 2017. **111**(Supplement C): p. 279-288.
51. Wen, D. and Y. Ding, *Formulation of nanofluids for natural convective heat transfer applications*. International Journal of Heat and Fluid Flow, 2005. **26**(6): p. 855-864.
52. Choi, S.U.S., et al., *Anomalous thermal conductivity enhancement in nanotube suspensions*. Applied Physics Letters, 2001. **79**(14): p. 2252-2254.
53. Lo, C.H. and T.T. Tsung, *Low-therm-temperature effect on the stability of CuO nanofluid*. Rev. Adv. Mater. Sci, 2005. **10**: p. 64-68.
54. Daungthongsuk, W. and S. Wongwises, *A critical review of convective heat transfer of nanofluids*. Renewable and Sustainable Energy Reviews, 2007. **11**(5): p. 797-817.

References

55. Al-Asadi, M.T., et al., *Heat Transfer Enhancements Using Traditional Fluids and Nanofluids in Pipes with Different Orientations: A Review*. Journal of Nanofluids, 2017. **6**(6): p. 987-1007.
56. Das, S.K., et al., *Nanofluids: science and technology*. 2008: Wiley-Interscience.
57. Knight, R.W., J.S. Goodling, and D.J. Hall, *Optimal Thermal Design of Forced Convection Heat Sinks-Analytical*. Journal of Electronic Packaging, 1991. **113**(3): p. 313-321.
58. Knight, R.W., J.S. Goodling, and B.E. Gross. *Optimal thermal design of air cooled forced convection finned heat sinks-experimental verification*. in *Thermal Phenomena in Electronic Systems, 1992. I-THERM III, InterSociety Conference on*. 1992.
59. Teertstra, P., M.M. Yovanovich, and J.R. Culham, *Analytical forced convection modeling of plate fin heat sinks*. Journal of Electronics Manufacturing, 2000. **10**(04): p. 253-261.
60. Copeland, D. *Optimization of parallel plate heatsinks for forced convection*. in *Semiconductor Thermal Measurement and Management Symposium, 2000. Sixteenth Annual IEEE*. 2000.
61. Sparrow, E.M., J.W. Ramsey, and C.A.C. Altemani, *Experiments on In-line Pin Fin Arrays and Performance Comparisons with Staggered Arrays*. Journal of Heat Transfer, 1980. **102**(1): p. 44-50.
62. Al-Asadi, M.T., A. Al-damook, and M.C.T. Wilson, *Assessment of vortex generator shapes and pin fin perforations for enhancing water-based heat sink performance*. International Communications in Heat and Mass Transfer, 2018. **91**: p. 1-10.
63. Al-Asadi, M.T., F.S. Alkasmoul, and M.C.T. Wilson, *Benefits of spanwise gaps in cylindrical vortex generators for conjugate heat transfer enhancement in micro-channels*. Applied Thermal Engineering, 2017.
64. Zhou, F. and I. Catton, *Numerical Evaluation of Flow and Heat Transfer in Plate-Pin Fin Heat Sinks with Various Pin Cross-Sections*. Numerical Heat Transfer, Part A: Applications, 2011. **60**(2): p. 107-128.
65. Jacobs, E.N., *Tests of six symmetrical airfoils in the variable density wind tunnel*. 1931.
66. Jacobs, E.N., K.E. Ward, and R.M. Pinkerton, *The characteristics of 78 related airfoil sections from tests in the variable-density wind tunnel*. 1933.
67. Kherbeet, A.S., et al., *Heat transfer and fluid flow over microscale backward and forward facing step: A review*. International Communications in Heat and Mass Transfer, 2016. **76**: p. 237-244.
68. Al-asadi, M.T., et al., *Numerical study of assisting and opposing mixed convective nanofluid flows in an inclined circular pipe*. International Communications in Heat and Mass Transfer, 2017. **85**: p. 81-91.
69. Kherbeet, A.S., et al., *Mixed convection nanofluid flow over microscale forward-facing step — Effect of inclination and step heights*.

References

- International Communications in Heat and Mass Transfer, 2016. **78**: p. 145-154.
70. Depaiwa, N., T. Chompookham, and P. Promvong. *Thermal enhancement in a solar air heater channel using rectangular winglet vortex generators*. in *Energy and Sustainable Development: Issues and Strategies (ESD), 2010 Proceedings of the International Conference on*. 2010.
71. R. Vasudevan, V.E.G.B., *Winglet-type vortex generators for plate-fin heat exchangers using triangular fins*. Numerical Heat Transfer, Part A: Applications, 2000. **38**(5): p. 533-555.
72. Nagarani, N., et al., *Review of utilization of extended surfaces in heat transfer problems*. Renewable and Sustainable Energy Reviews, 2014. **29**: p. 604-613.
73. Johnson, T. and P. Joubert, *The influence of vortex generators on the drag and heat transfer from a circular cylinder normal to an airstream*. Journal of Heat Transfer, 1969. **91**(1): p. 91-99.
74. Safaei, M.R., et al., *Mathematical Modeling for Nanofluids Simulation: A Review of the Latest Works*, in *Modeling and Simulation in Engineering Sciences*, N.S. Akbar and O.A. Beg, Editors. 2016, InTech: Rijeka. p. Ch. 09.
75. Koşar, A., *Effect of substrate thickness and material on heat transfer in microchannel heat sinks*. International Journal of Thermal Sciences, 2010. **49**(4): p. 635-642.
76. Abed, W.M., et al., *Numerical and experimental investigation of heat transfer and fluid flow characteristics in a micro-scale serpentine channel*. International Journal of Heat and Mass Transfer, 2015. **88**: p. 790-802.
77. Choi, S.U.S. and J.A. Eastman, *Enhancing thermal conductivity of fluids with nanoparticles*. 1995. Medium: ED; Size: 8 p.
78. Shkarah, A.J., et al., *A 3D numerical study of heat transfer in a single-phase micro-channel heat sink using graphene, aluminum and silicon as substrates*. International Communications in Heat and Mass Transfer, 2013. **48**(0): p. 108-115.
79. Lee, P.-S. and S.V. Garimella, *Thermally developing flow and heat transfer in rectangular microchannels of different aspect ratios*. International Journal of Heat and Mass Transfer, 2006. **49**(17–18): p. 3060-3067.
80. Mansoor, M.M., K.-C. Wong, and M. Siddique, *Numerical investigation of fluid flow and heat transfer under high heat flux using rectangular micro-channels*. International Communications in Heat and Mass Transfer, 2012. **39**(2): p. 291-297.
81. Lee, P.-S., S.V. Garimella, and D. Liu, *Investigation of heat transfer in rectangular microchannels*. International Journal of Heat and Mass Transfer, 2005. **48**(9): p. 1688-1704.

References

82. Deng, D., et al., *Experimental investigations on flow boiling performance of reentrant and rectangular microchannels – A comparative study*. International Journal of Heat and Mass Transfer, 2015. **82**(0): p. 435-446.
83. Balaj, M., E. Roohi, and H. Akhlaghi, *Effects of shear work on non-equilibrium heat transfer characteristics of rarefied gas flows through micro/nanochannels*. International Journal of Heat and Mass Transfer, 2015. **83**(0): p. 69-74.
84. Xia, G.D., et al., *Effects of different geometric structures on fluid flow and heat transfer performance in microchannel heat sinks*. International Journal of Heat and Mass Transfer, 2015. **80**(0): p. 439-447.
85. Ghasemian, M., et al., *Heat transfer characteristics of Fe₃O₄ ferrofluid flowing in a mini channel under constant and alternating magnetic fields*. Journal of Magnetism and Magnetic Materials, 2015. **381**(0): p. 158-167.
86. Pongsoi, P., S. Pikulkajorn, and S. Wongwises, *Heat transfer and flow characteristics of spiral fin-and-tube heat exchangers: A review*. International Journal of Heat and Mass Transfer, 2014. **79**(0): p. 417-431.
87. Pan, M., et al., *Optimal design of complex manifold geometries for uniform flow distribution between microchannels*. Chemical Engineering Journal, 2008. **137**(2): p. 339-346.
88. Gamrat, G., M. Favre-Marinet, and D. Asendrych, *Conduction and entrance effects on laminar liquid flow and heat transfer in rectangular microchannels*. International Journal of Heat and Mass Transfer, 2005. **48**(14): p. 2943-2954.
89. Qu, W. and I. Mudawar, *Experimental and numerical study of pressure drop and heat transfer in a single-phase micro-channel heat sink*. International Journal of Heat and Mass Transfer, 2002. **45**(12): p. 2549-2565.
90. Hsu, L.-C., et al., *An experimental study of inclination on the boiling heat transfer characteristics of a micro-channel heat sink using HFE-7100*. International Communications in Heat and Mass Transfer, 2015. **62**(0): p. 13-17.
91. Suwankamnerd, P. and S. Wongwises, *An experimental study of two-phase air–water flow and heat transfer characteristics of segmented flow in a microchannel*. Experimental Thermal and Fluid Science, 2015. **62**(0): p. 29-39.
92. Mirmanto, M., *Heat transfer coefficient calculated using a linear pressure gradient assumption and measurement for flow boiling in microchannels*. International Journal of Heat and Mass Transfer, 2014. **79**(0): p. 269-278.
93. Konishi, C., et al., *Flow boiling in microgravity: Part 1 – Interfacial behavior and experimental heat transfer results*. International Journal of Heat and Mass Transfer, 2015. **81**(0): p. 705-720.

References

94. Gan, Y., J. Xu, and Y. Yan, *An experimental study of two-phase pressure drop of acetone in triangular silicon micro-channels*. Applied Thermal Engineering, 2015. **80**(0): p. 76-86.
95. Fang, X., Z. Zhou, and H. Wang, *Heat transfer correlation for saturated flow boiling of water*. Applied Thermal Engineering, 2015. **76**(0): p. 147-156.
96. Shojaeian, M. and A. Koşar, *Pool boiling and flow boiling on micro- and nanostructured surfaces*. Experimental Thermal and Fluid Science, 2015. **63**(0): p. 45-73.
97. Asadi, M., G. Xie, and B. Sunden, *A review of heat transfer and pressure drop characteristics of single and two-phase microchannels*. International Journal of Heat and Mass Transfer, 2014. **79**(0): p. 34-53.
98. ofScience, W., *Growth of Publications* 2017.
99. Guo, J., M. Xu, and L. Cheng, *Numerical investigations of curved square channel from the viewpoint of field synergy principle*. International Journal of Heat and Mass Transfer, 2011. **54**(17–18): p. 4148-4151.
100. Chu, J.-C., J.-T. Teng, and R. Greif, *Experimental and numerical study on the flow characteristics in curved rectangular microchannels*. Applied Thermal Engineering, 2010. **30**(13): p. 1558-1566.
101. Dehghan, M., et al., *Enhancing heat transfer in microchannel heat sinks using converging flow passages*. Energy Conversion and Management, 2015. **92**(0): p. 244-250.
102. Mirzaee, H., et al., *HEAT TRANSFER ENHANCEMENT IN MICROCHANNELS USING AN ELASTIC VORTEX GENERATOR*. 2012. **19**(3): p. 199-211.
103. Liu, J., G. Xie, and T.W. Simon, *Turbulent flow and heat transfer enhancement in rectangular channels with novel cylindrical grooves*. International Journal of Heat and Mass Transfer, 2015. **81**(0): p. 563-577.
104. Bi, C., G.H. Tang, and W.Q. Tao, *Heat transfer enhancement in mini-channel heat sinks with dimples and cylindrical grooves*. Applied Thermal Engineering, 2013. **55**(1): p. 121-132.
105. Zhai, Y.L., et al., *Exergy analysis and performance evaluation of flow and heat transfer in different micro heat sinks with complex structure*. International Journal of Heat and Mass Transfer, 2015. **84**(0): p. 293-303.
106. Knupp, D.C., R.M. Cotta, and C.P. Naveira-Cotta, *Fluid flow and conjugated heat transfer in arbitrarily shaped channels via single domain formulation and integral transforms*. International Journal of Heat and Mass Transfer, 2015. **82**(0): p. 479-489.
107. Henze, M. and J. von Wolfersdorf, *Influence of approach flow conditions on heat transfer behind vortex generators*. International Journal of Heat and Mass Transfer, 2011. **54**(1–3): p. 279-287.

References

108. Dai, Z., D.F. Fletcher, and B.S. Haynes, *Impact of tortuous geometry on laminar flow heat transfer in microchannels*. International Journal of Heat and Mass Transfer, 2015. **83**(0): p. 382-398.
109. Karathanassis, I.K., et al., *Experimental and numerical evaluation of an elongated plate-fin heat sink with three sections of stepwise varying channel width*. International Journal of Heat and Mass Transfer, 2015. **84**(0): p. 16-34.
110. Kundu, B. and P.K. Das, *Performance and optimum design analysis of convective fin arrays attached to flat and curved primary surfaces*. International Journal of Refrigeration, 2009. **32**(3): p. 430-443.
111. Hong, F.J., et al., *Conjugate heat transfer in fractal-shaped microchannel network heat sink for integrated microelectronic cooling application*. International Journal of Heat and Mass Transfer, 2007. **50**(25): p. 4986-4998.
112. Torii, K., K.M. Kwak, and K. Nishino, *Heat transfer enhancement accompanying pressure-loss reduction with winglet-type vortex generators for fin-tube heat exchangers*. International Journal of Heat and Mass Transfer, 2002. **45**(18): p. 3795-3801.
113. Zhang, Y.H., et al., *The effects of span position of winglet vortex generator on local heat/mass transfer over a three-row flat tube bank fin*. Heat and Mass Transfer, 2004. **40**(11): p. 881-891.
114. Wang, C.-C., et al., *Flow visualization of annular and delta winlet vortex generators in fin-and-tube heat exchanger application*. International Journal of Heat and Mass Transfer, 2002. **45**(18): p. 3803-3815.
115. Ahmed, S., W. Mohammed, and J. Laith, *Numerical investigation into velocity and temperature fields over smooth and rough ducts for several types of turbulators*. Journal of Engineering Technology, 2007. **25**(10): p. 1110-1128.
116. Gorji-Bandpy, M., S. Soleimani, and F. Hossein-Nejad, *Pressure and Heat Transfer in Staggered Arrangement Circular Tubes with Airfoil Vortex Generator*. International Energy Journal, 2008. **9**(3).
117. Wang, J. and Y. Zhao, *Heat and fluid flow characteristics of a rectangular channel with a small diameter circular cylinder as vortex generator*. International Journal of Thermal Sciences, 2015. **92**: p. 1-13.
118. Chai, L., G.D. Xia, and H.S. Wang, *Numerical study of laminar flow and heat transfer in microchannel heat sink with offset ribs on sidewalls*. Applied Thermal Engineering, 2016. **92**: p. 32-41.
119. Chai, L., G.D. Xia, and H.S. Wang, *Parametric study on thermal and hydraulic characteristics of laminar flow in microchannel heat sink with fan-shaped ribs on sidewalls – Part 1: Heat transfer*. International Journal of Heat and Mass Transfer, 2016. **97**: p. 1069-1080.
120. Chai, L., G.D. Xia, and H.S. Wang, *Parametric study on thermal and hydraulic characteristics of laminar flow in microchannel heat sink with fan-shaped ribs on sidewalls – Part 2: Pressure drop*. International Journal of Heat and Mass Transfer, 2016. **97**: p. 1081-1090.

References

121. Chai, L., G.D. Xia, and H.S. Wang, *Parametric study on thermal and hydraulic characteristics of laminar flow in microchannel heat sink with fan-shaped ribs on sidewalls – Part 3: Performance evaluation*. International Journal of Heat and Mass Transfer, 2016. **97**: p. 1091-1101.
122. Li, Y.F., et al., *Characteristics of laminar flow and heat transfer in microchannel heat sink with triangular cavities and rectangular ribs*. International Journal of Heat and Mass Transfer, 2016. **98**: p. 17-28.
123. Behnampour, A., et al., *Analysis of heat transfer and nanofluid fluid flow in microchannels with trapezoidal, rectangular and triangular shaped ribs*. Physica E: Low-dimensional Systems and Nanostructures, 2017. **91**: p. 15-31.
124. Jama, M., et al., *Critical Review on Nanofluids: Preparation, Characterization, and Applications*. Journal of Nanomaterials, 2016. **2016**: p. 22.
125. Li, Y., et al., *A review on development of nanofluid preparation and characterization*. Powder Technology, 2009. **196**(2): p. 89-101.
126. Kakaç, S. and A. Pramuanjaroenkij, *Single-phase and two-phase treatments of convective heat transfer enhancement with nanofluids – A state-of-the-art review*. International Journal of Thermal Sciences, 2016. **100**: p. 75-97.
127. Azmi, W.H., et al., *Heat transfer augmentation of ethylene glycol: water nanofluids and applications — A review*. International Communications in Heat and Mass Transfer, 2016. **75**: p. 13-23.
128. Eastman, J.A., et al., *Enhanced Thermal Conductivity through the Development of Nanofluids*. MRS Proceedings, 1996. **457**.
129. Lee, S., et al., *Measuring Thermal Conductivity of Fluids Containing Oxide Nanoparticles*. Journal of Heat Transfer, 1999. **121**(2): p. 280-289.
130. Choi, S.U.S. and J.A. Eastman, *Enhanced heat transfer using nanofluids*. 2001, ; Argonne National Laboratory (ANL), Argonne, IL. p. Medium: ED.
131. Zhu, H.-t., Y.-s. Lin, and Y.-s. Yin, *A novel one-step chemical method for preparation of copper nanofluids*. Journal of Colloid and Interface Science, 2004. **277**(1): p. 100-103.
132. Gleiter, H., *Nanocrystalline Materials*, in *Advanced Structural and Functional Materials: Proceedings of an International Seminar Organized by Deutsche Forschungsanstalt für Luft- und Raumfahrt (DLR), Köln, June 1991*, W.G.J. Bunk, Editor. 1991, Springer Berlin Heidelberg: Berlin, Heidelberg. p. 1-37.
133. Ashley, S., *Small-scale structure yields big property payoffs*. Mechanical Engineering, 1994. **116**(2): p. 52.
134. Bowles, R.S., et al., *Generation of molecular clusters of controlled size*. Surface Science, 1981. **106**(1): p. 117-124.

References

135. Iijima, S., *Helical microtubules of graphitic carbon*. *nature*, 1991. **354**(6348): p. 56-58.
136. Scott, C.D., et al., *Growth mechanisms for single-wall carbon nanotubes in a laser-ablation process*. *Applied Physics A*, 2001. **72**(5): p. 573-580.
137. Hernadi, K., *Catalytic synthesis of multiwall carbon nanotubes from methylacetylene*. *Chemical Physics Letters*, 2002. **363**(1–2): p. 169-174.
138. Yatsuya, S., et al., *Preparation of extremely fine particles by vacuum evaporation onto a running oil substrate*. *Journal of Crystal Growth*, 1978. **45**: p. 490-494.
139. Thompson, L. and R. DiMelfi, *JA Eastman, US Choi, S. Lil, G. Soyozl, 4*. 1998.
140. Mohammed, H.A., et al., *Heat transfer and fluid flow characteristics in microchannels heat exchanger using nanofluids: A review*. *Renewable and Sustainable Energy Reviews*. **15**(3): p. 1502-1512.
141. Rayleigh, L., *On the influence of obstacles arranged in rectangular order upon the properties of a medium*. *Phil. Mag*, 1892. **34**(481-502): p. 205.
142. Fricke, H., *A mathematical treatment of the electric conductivity and capacity of disperse systems I. The electric conductivity of a suspension of homogeneous spheroids*. *Physical Review*, 1924. **24**(5): p. 575.
143. Fricke, H., *The Maxwell-Wagner dispersion in a suspension of ellipsoids*. *The Journal of Physical Chemistry*, 1953. **57**(9): p. 934-937.
144. Böttcher, C., *The dielectric constant of crystalline powders*. *Recueil des Travaux Chimiques des Pays-Bas*, 1945. **64**(2): p. 47-51.
145. Landauer, R., *The electrical resistance of binary metallic mixtures*. *Journal of Applied Physics*, 1952. **23**(7): p. 779-784.
146. Jeffrey, D., *Conduction through a random suspension of spheres*. *Proceedings of the Royal Society of London. A. Mathematical and Physical Sciences*, 1973. **335**(1602): p. 355.
147. Davis, R., *The effective thermal conductivity of a composite material with spherical inclusions*. *International Journal of Thermophysics*, 1986. **7**(3): p. 609-620.
148. Nan, C.W., et al., *Effective thermal conductivity of particulate composites with interfacial thermal resistance*. *Journal of Applied Physics*, 1997. **81**: p. 6692.
149. Lu, S.Y. and J.L. Song, *Effective conductivity of composites with spherical inclusions: Effect of coating and detachment*. *Journal of Applied Physics*, 1996. **79**(2): p. 609-618.
150. Benveniste, Y., *Effective thermal conductivity of composites with a thermal contact resistance between the constituents: Nondilute case*. *Journal of applied physics*, 1987. **61**(8): p. 2840-2843.

References

151. Hasselman, D. and L.F. Johnson, *Effective thermal conductivity of composites with interfacial thermal barrier resistance*. Journal of Composite Materials, 1987. **21**(6): p. 508.
152. Abed, A.M., et al., *Enhance heat transfer in the channel with V-shaped wavy lower plate using liquid nanofluids*. Case Studies in Thermal Engineering, 2015. **5**(0): p. 13-23.
153. Al-Asadi, M.T., F.S. Alkasmoul, and M.C.T. Wilson, *Heat transfer enhancement in a micro-channel cooling system using cylindrical vortex generators*. International Communications in Heat and Mass Transfer, 2016. **74**: p. 40-47.
154. Wang, X., X. Xu, and S.U. S. Choi, *Thermal Conductivity of Nanoparticle - Fluid Mixture*. Journal of Thermophysics and Heat Transfer, 1999. **13**(4): p. 474-480.
155. Das, S.K., et al., *Temperature Dependence of Thermal Conductivity Enhancement for Nanofluids*. Journal of Heat Transfer, 2003. **125**(4): p. 567-574.
156. Xie, H., et al., *Thermal conductivity enhancement of suspensions containing nanosized alumina particles*. Journal of Applied Physics, 2002. **91**(7): p. 4568-4572.
157. Li, C.H. and G.P. Peterson, *Experimental investigation of temperature and volume fraction variations on the effective thermal conductivity of nanoparticle suspensions (nanofluids)*. Journal of Applied Physics, 2006. **99**(8): p. 084314.
158. Wen, D. and Y. Ding, *Experimental investigation into convective heat transfer of nanofluids at the entrance region under laminar flow conditions*. International Journal of Heat and Mass Transfer, 2004. **47**(24): p. 5181-5188.
159. Yoo, D.-H., K.S. Hong, and H.-S. Yang, *Study of thermal conductivity of nanofluids for the application of heat transfer fluids*. Thermochemica Acta, 2007. **455**(1–2): p. 66-69.
160. Zhang, X., H. Gu, and M. Fujii, *Experimental Study on the Effective Thermal Conductivity and Thermal Diffusivity of Nanofluids*. International Journal of Thermophysics, 2006. **27**(2): p. 569-580.
161. Kim, S.J., et al., *Surface wettability change during pool boiling of nanofluids and its effect on critical heat flux*. International Journal of Heat and Mass Transfer, 2007. **50**(19–20): p. 4105-4116.
162. Li, C.H. and G. Peterson, *The effect of particle size on the effective thermal conductivity of Al₂O₃-water nanofluids*. Journal of Applied Physics, 2007. **101**(4): p. 44312-44312.
163. Beck, M.P., et al., *The effect of particle size on the thermal conductivity of alumina nanofluids*. Journal of Nanoparticle Research, 2009. **11**(5): p. 1129-1136.
164. Mintsa, H.A., et al., *New temperature dependent thermal conductivity data for water-based nanofluids*. International Journal of Thermal Sciences, 2009. **48**(2): p. 363-371.

References

165. Jwo, C.-S., T.-P. Teng, and H. Chang, *A simple model to estimate thermal conductivity of fluid with acicular nanoparticles*. Journal of Alloys and Compounds, 2007. **434–435**: p. 569-571.
166. Murshed, S.M.S., K.C. Leong, and C. Yang, *Enhanced thermal conductivity of TiO₂—water based nanofluids*. International Journal of Thermal Sciences, 2005. **44**(4): p. 367-373.
167. Wen, D. and Y. Ding, *Natural convective heat transfer of suspensions of titanium dioxide nanoparticles (nanofluids)*. IEEE Transactions on Nanotechnology, 2006. **5**(3): p. 220-227.
168. He, Y., et al., *Heat transfer and flow behaviour of aqueous suspensions of TiO₂ nanoparticles (nanofluids) flowing upward through a vertical pipe*. International Journal of Heat and Mass Transfer, 2007. **50**(11–12): p. 2272-2281.
169. Turgut, A., et al., *Thermal Conductivity and Viscosity Measurements of Water-Based TiO₂ Nanofluids*. International Journal of Thermophysics, 2009. **30**(4): p. 1213-1226.
170. Zhu, H., et al., *Effects of nanoparticle clustering and alignment on thermal conductivities of Fe₃O₄ aqueous nanofluids*. Applied Physics Letters, 2006. **89**(2): p. 023123.
171. Hwang, Y.J., et al., *Investigation on characteristics of thermal conductivity enhancement of nanofluids*. Current Applied Physics, 2006. **6**(6): p. 1068-1071.
172. Eastman, J.A., et al., *Anomalously increased effective thermal conductivities of ethylene glycol-based nanofluids containing copper nanoparticles*. Applied Physics Letters, 2001. **78**(6): p. 718-720.
173. Xuan, Y. and Q. Li, *Heat transfer enhancement of nanofluids*. International Journal of Heat and Fluid Flow, 2000. **21**(1): p. 58-64.
174. Liu, M.-S., et al., *Enhancement of thermal conductivity with Cu for nanofluids using chemical reduction method*. International Journal of Heat and Mass Transfer, 2006. **49**(17–18): p. 3028-3033.
175. Hong, T.-K., H.-S. Yang, and C.J. Choi, *Study of the enhanced thermal conductivity of Fe nanofluids*. Journal of Applied Physics, 2005. **97**(6): p. 064311.
176. Hong, K.S., T.-K. Hong, and H.-S. Yang, *Thermal conductivity of Fe nanofluids depending on the cluster size of nanoparticles*. Applied Physics Letters, 2006. **88**(3): p. 031901.
177. Patel, H.E., et al., *Thermal conductivities of naked and monolayer protected metal nanoparticle based nanofluids: Manifestation of anomalous enhancement and chemical effects*. Applied Physics Letters, 2003. **83**(14): p. 2931-2933.
178. Putnam, S.A., et al., *Thermal conductivity of nanoparticle suspensions*. Journal of Applied Physics, 2006. **99**(8): p. 084308.
179. Zeinali Heris, S., M. Nasr Esfahany, and S.G. Etemad, *Experimental investigation of convective heat transfer of Al₂O₃/water nanofluid in*

References

- circular tube*. International Journal of Heat and Fluid Flow, 2007. **28**(2): p. 203-210.
180. Pak, B.C. and Y.I. Cho, *HYDRODYNAMIC AND HEAT TRANSFER STUDY OF DISPERSED FLUIDS WITH SUBMICRON METALLIC OXIDE PARTICLES*. Experimental Heat Transfer, 1998. **11**(2): p. 151-170.
181. Hwang, K.S., S.P. Jang, and S.U.S. Choi, *Flow and convective heat transfer characteristics of water-based Al₂O₃ nanofluids in fully developed laminar flow regime*. International Journal of Heat and Mass Transfer, 2009. **52**(1-2): p. 193-199.
182. Zeinali Heris, S., S.G. Etemad, and M. Nasr Esfahany, *Experimental investigation of oxide nanofluids laminar flow convective heat transfer*. International Communications in Heat and Mass Transfer, 2006. **33**(4): p. 529-535.
183. Maxwell, J.C., *A treatise on electricity and magnetism*. Vol. 1. 1892: Clarendon.
184. Bruggeman, D., *Calculation of various physics constants in heterogenous substances I Dielectricity constants and conductivity of mixed bodies from isotropic substances*. Ann. Phys, 1935. **24**(7): p. 636-664.
185. Hasselman, D.P.H. and L.F. Johnson, *Effective Thermal Conductivity of Composites with Interfacial Thermal Barrier Resistance*. Journal of Composite Materials, 1987. **21**(6): p. 508-515.
186. Yu, W. and S.U.S. Choi, *The Role of Interfacial Layers in the Enhanced Thermal Conductivity of Nanofluids: A Renovated Maxwell Model*. Journal of Nanoparticle Research, 2003. **5**(1): p. 167-171.
187. Xie, H., M. Fujii, and X. Zhang, *Effect of interfacial nanolayer on the effective thermal conductivity of nanoparticle-fluid mixture*. International Journal of Heat and Mass Transfer, 2005. **48**(14): p. 2926-2932.
188. Shima, P., J. Philip, and B. Raj, *Role of microconvection induced by Brownian motion of nanoparticles in the enhanced thermal conductivity of stable nanofluids*. Applied Physics Letters, 2009. **94**(22): p. 223101-223101-3.
189. Vadasz, P., *Nanofluid Suspensions and Bi-composite Media as Derivatives of Interface Heat Transfer Modeling in Porous Media*. Emerging topics in heat and mass transfer in porous media: from bioengineering and microelectronics to nanotechnology, 2008: p. 283.
190. Prasher, R., P.E. Phelan, and P. Bhattacharya, *Effect of Aggregation Kinetics on the Thermal Conductivity of Nanoscale Colloidal Solutions (Nanofluid)*. Nano Letters, 2006. **6**(7): p. 1529-1534.
191. Nie, C., W.H. Marlow, and Y.A. Hassan, *Discussion of proposed mechanisms of thermal conductivity enhancement in nanofluids*. International Journal of Heat and Mass Transfer, 2008. **51**(5-6): p. 1342-1348.

References

192. Ghasemi, B. and S.M. Aminossadati, *Brownian motion of nanoparticles in a triangular enclosure with natural convection*. International Journal of Thermal Sciences, 2010. **49**(6): p. 931-940.
193. Xuan, Y. and W. Roetzel, *Conceptions for heat transfer correlation of nanofluids*. International Journal of Heat and Mass Transfer, 2000. **43**(19): p. 3701-3707.
194. Patel, H.E., T. Sundararajan, and S.K. Das, *An experimental investigation into the thermal conductivity enhancement in oxide and metallic nanofluids*. Journal of Nanoparticle Research, 2010. **12**(3): p. 1015-1031.
195. Tillman, P. and J.M. Hill, *Modelling the Thermal Conductivity of Nanofluids*, in *IUTAM Symposium on Mechanical Behavior and Micro-Mechanics of Nanostructured Materials: Proceedings of the IUTAM Symposium held in Beijing, China, June 27–30, 2005*, Y.L. Bai, Q.S. Zheng, and Y.G. Wei, Editors. 2007, Springer Netherlands: Dordrecht. p. 105-118.
196. Xie, H., et al., *Dependence of the thermal conductivity of nanoparticle-fluid mixture on the base fluid*. Journal of Materials Science Letters, 2002. **21**(19): p. 1469-1471.
197. Godson, L., et al., *Enhancement of heat transfer using nanofluids—An overview*. Renewable and Sustainable Energy Reviews, 2010. **14**(2): p. 629-641.
198. Sharma, P., et al., *Enhancement of thermal conductivity of ethylene glycol based silver nanofluids*. Powder Technology, 2011. **208**(1): p. 7-19.
199. Madhusree, K. and T.K. Dey, *Thermal conductivity and viscosity of Al₂O₃ nanofluid based on car engine coolant*. Journal of Physics D: Applied Physics, 2010. **43**(31): p. 315501.
200. Corcione, M., *Heat transfer features of buoyancy-driven nanofluids inside rectangular enclosures differentially heated at the sidewalls*. International Journal of Thermal Sciences, 2010. **49**(9): p. 1536-1546.
201. Al-aswadi, A.A., et al., *Laminar forced convection flow over a backward facing step using nanofluids*. International Communications in Heat and Mass Transfer, 2010. **37**(8): p. 950-957.
202. Guo, S.-Z., et al., *Nanofluids Containing γ -Fe₂O₃ Nanoparticles and Their Heat Transfer Enhancements*. Nanoscale Research Letters, 2010. **5**(7): p. 1222.
203. Mohammed, H.A., et al., *Convective heat transfer and fluid flow study over a step using nanofluids: A review*. Renewable and Sustainable Energy Reviews, 2011. **15**(6): p. 2921-2939.
204. Yulong, D., et al., *Relationship between the thermal conductivity and shear viscosity of nanofluids*. Physica Scripta, 2010. **2010**(T139): p. 014078.
205. Kumar, N. and S.S. Sonawane, *Experimental study of thermal conductivity and convective heat transfer enhancement using CuO and*

References

- TiO₂ nanoparticles*. International Communications in Heat and Mass Transfer, 2016. **76**: p. 98-107.
206. Buongiorno, J., et al., *A benchmark study on the thermal conductivity of nanofluids*. Journal of Applied Physics, 2009. **106**(9): p. 094312.
207. Bigdeli, M.B., et al., *A review on the heat and mass transfer phenomena in nanofluid coolants with special focus on automotive applications*. Renewable and Sustainable Energy Reviews, 2016. **60**: p. 1615-1633.
208. Das, S.K., et al., *Nanofluids: science and technology*. 2007: John Wiley & Sons.
209. Krajnik, P., F. Pusavec, and A. Rashid, *Nanofluids: Properties, Applications and Sustainability Aspects in Materials Processing Technologies*, in *Advances in Sustainable Manufacturing: Proceedings of the 8th Global Conference on Sustainable Manufacturing*, G. Seliger, M.K.M. Khraisheh, and I.S. Jawahir, Editors. 2011, Springer Berlin Heidelberg: Berlin, Heidelberg. p. 107-113.
210. Colla, L., et al., *Characterization and Simulation of the Heat Transfer Behaviour of Water-Based ZnO Nanofluids*. Journal of Nanoscience and Nanotechnology, 2015. **15**(5): p. 3599-3609.
211. Ahammed, N., et al., *Measurement of thermal conductivity of graphene–water nanofluid at below and above ambient temperatures*. International Communications in Heat and Mass Transfer, 2016. **70**: p. 66-74.
212. Kherbeet, A.S., H.A. Mohammed, and B.H. Salman, *The effect of nanofluids flow on mixed convection heat transfer over microscale backward-facing step*. International Journal of Heat and Mass Transfer, 2012. **55**(21–22): p. 5870-5881.
213. Kherbeet, A.S., et al., *Experimental and numerical study of nanofluid flow and heat transfer over microscale backward-facing step*. International Journal of Heat and Mass Transfer, 2014. **79**: p. 858-867.
214. Salman, B.H., H.A. Mohammed, and A.S. Kherbeet, *Numerical and experimental investigation of heat transfer enhancement in a microtube using nanofluids*. International Communications in Heat and Mass Transfer, 2014. **59**: p. 88-100.
215. Haridas, D., N.S. Rajput, and A. Srivastava, *Interferometric study of heat transfer characteristics of Al₂O₃ and SiO₂-based dilute nanofluids under simultaneously developing flow regime in compact channels*. International Journal of Heat and Mass Transfer, 2015. **88**: p. 713-727.
216. Tarighaleslami, A.H., et al., *Heat Transfer Enhancement for site level indirect heat recovery systems using nanofluids as the intermediate fluid*. Applied Thermal Engineering, 2016. **105**: p. 923-930.
217. Shahrul, I.M., et al., *Experimental investigation on Al₂O₃–W, SiO₂–W and ZnO–W nanofluids and their application in a shell and tube heat exchanger*. International Journal of Heat and Mass Transfer, 2016. **97**: p. 547-558.

References

218. Chon, C.H., et al., *Empirical correlation finding the role of temperature and particle size for nanofluid (AlO) thermal conductivity enhancement*. Applied Physics Letters, 2005. **87**: p. 153107.
219. Das, S.K., et al., *Temperature dependence of thermal conductivity enhancement for nanofluids*. Journal of Heat Transfer, 2003. **125**: p. 567.
220. Li, C.H. and G. Peterson, *Experimental investigation of temperature and volume fraction variations on the effective thermal conductivity of nanoparticle suspensions (nanofluids)*. Journal of Applied Physics, 2006. **99**: p. 084314.
221. Koblinski, P., R. Prasher, and J. Eapen, *Thermal conductance of nanofluids: is the controversy over?* Journal of Nanoparticle Research, 2008. **10**(7): p. 1089-1097.
222. Behrangzade, A. and M.M. Heyhat, *The effect of using nano-silver dispersed water based nanofluid as a passive method for energy efficiency enhancement in a plate heat exchanger*. Applied Thermal Engineering, 2016. **102**: p. 311-317.
223. Salehi, J.M., M.M. Heyhat, and A. Rajabpour, *Enhancement of thermal conductivity of silver nanofluid synthesized by a one-step method with the effect of polyvinylpyrrolidone on thermal behavior*. Applied Physics Letters, 2013. **102**(23): p. 231907.
224. Özerinç, S., S. Kakaç, and A.G. Yazıcıoğlu, *Enhanced thermal conductivity of nanofluids: a state-of-the-art review*. Microfluidics and Nanofluidics, 2010. **8**(2): p. 145-170.
225. Lin, C.-Y., J.-C. Wang, and T.-C. Chen, *Analysis of suspension and heat transfer characteristics of Al₂O₃ nanofluids prepared through ultrasonic vibration*. Applied Energy, 2011. **88**(12): p. 4527-4533.
226. Colangelo, G., et al., *Results of experimental investigations on the heat conductivity of nanofluids based on diathermic oil for high temperature applications*. Applied Energy, 2012. **97**: p. 828-833.
227. Gupta, M., et al., *A comprehensive review of experimental investigations of forced convective heat transfer characteristics for various nanofluids*. International Journal of Mechanical and Materials Engineering, 2014. **9**(1): p. 1-21.
228. Heyhat, M.M., et al., *Experimental investigation of laminar convective heat transfer and pressure drop of water-based Al₂O₃ nanofluids in fully developed flow regime*. Experimental Thermal and Fluid Science, 2013. **44**: p. 483-489.
229. Heyhat, M.M., et al., *Experimental investigation of turbulent flow and convective heat transfer characteristics of alumina water nanofluids in fully developed flow regime*. International Communications in Heat and Mass Transfer, 2012. **39**(8): p. 1272-1278.
230. Ahmed, H.E., M.I. Ahmed, and M.Z. Yusoff, *Heat transfer enhancement in a triangular duct using compound nanofluids and turbulators*. Applied Thermal Engineering, 2015. **91**: p. 191-201.

References

231. Koo, J. and C. Kleinstreuer, *A new thermal conductivity model for nanofluids*. Journal of Nanoparticle Research, 2004. **6**(6): p. 577-588.
232. Vajjha, R.S. and D.K. Das, *Experimental determination of thermal conductivity of three nanofluids and development of new correlations*. International Journal of Heat and Mass Transfer, 2009. **52**(21–22): p. 4675-4682.
233. Kherbeet, A.S., et al., *Experimental study of nanofluid flow and heat transfer over microscale backward- and forward-facing steps*. Experimental Thermal and Fluid Science, 2015. **65**: p. 13-21.
234. Vajjha, R.S., D.K. Das, and D.P. Kulkarni, *Development of new correlations for convective heat transfer and friction factor in turbulent regime for nanofluids*. International Journal of Heat and Mass Transfer, 2010. **53**(21–22): p. 4607-4618.
235. Haddad, Z., et al., *A review on natural convective heat transfer of nanofluids*. Renewable and Sustainable Energy Reviews, 2012. **16**(7): p. 5363-5378.
236. Haghighi, E.B., et al., *Combined effect of physical properties and convective heat transfer coefficient of nanofluids on their cooling efficiency*. International Communications in Heat and Mass Transfer, 2015. **68**: p. 32-42.
237. Alkasmoul, F.S., *Characterisation of the Properties and Performance of Nanofluid Coolants with Analysis of Their Feasibility for Datacentre Cooling*. 2015, University of Leeds.
238. Alkasmoul, F.S., et al., *A practical evaluation of the performance of Al₂O₃-water, TiO₂-water and CuO-water nanofluids for convective cooling*. International Journal of Heat and Mass Transfer, 2018. **126**, Part A: p. 639-651.
239. Xia, G.D., et al., *The characteristics of convective heat transfer in microchannel heat sinks using Al₂O₃ and TiO₂ nanofluids*. International Communications in Heat and Mass Transfer, 2016. **76**: p. 256-264.
240. Hussien, A.A., M.Z. Abdullah, and M.d.A. Al-Nimr, *Single-phase heat transfer enhancement in micro/minichannels using nanofluids: Theory and applications*. Applied Energy, 2016. **164**: p. 733-755.
241. Rosa, P., T.G. Karayiannis, and M.W. Collins, *Single-phase heat transfer in microchannels: The importance of scaling effects*. Applied Thermal Engineering, 2009. **29**(17–18): p. 3447-3468.
242. Kandlikar, S.G., *History, Advances, and Challenges in Liquid Flow and Flow Boiling Heat Transfer in Microchannels: A Critical Review*. Journal of Heat Transfer, 2012. **134**(3): p. 034001-034001.
243. Mohammed Adham, A., N. Mohd-Ghazali, and R. Ahmad, *Thermal and hydrodynamic analysis of microchannel heat sinks: A review*. Renewable and Sustainable Energy Reviews, 2013. **21**: p. 614-622.
244. Al-Asadi, M.T., and M.C.T. Wilson, *Evaluation of nanofluid performance with vortex generators for enhanced micro-channel heat*

References

- transfer*. Eleven International Conference on Thermal Engineering: Theory and Applications February 25-28, 2018, Doha, Qatar, 2018.
245. Webb, R.L., *Performance evaluation criteria for use of enhanced heat transfer surfaces in heat exchanger design*. International Journal of Heat and Mass Transfer, 1981. **24**(4): p. 715-726.
246. Zhang, J., et al., *Thermal-hydraulic performance of multiport microchannel flat tube with a sawtooth fin structure*. International Journal of Thermal Sciences, 2014. **84**: p. 175-183.
247. Shetab Bushehri, M.R., H. Ramin, and M.R. Salimpour, *A new coupling method for slip-flow and conjugate heat transfer in a parallel plate micro heat sink*. International Journal of Thermal Sciences, 2015. **89**(0): p. 174-184.
248. Chen, Q. and J. Srebric, *A Procedure for Verification, Validation, and Reporting of Indoor Environment CFD Analyses*. HVAC&R Research, 2002. **8**(2): p. 201-216.
249. Venturino, M. and P. Rubini, *Coupled fluid flow and heat transfer analysis of steel reheat furnaces*. Leuckel et al, 1995: p. 8.
250. Baukal Jr, C.E., V. Gershtein, and X.J. Li, *Computational fluid dynamics in industrial combustion*. 2000: CRC press.
251. Versteeg, H.K. and W. Malalasekera, *An introduction to computational fluid dynamics: the finite volume method*. 2007: Pearson Education.
252. Lewis, R.W., P. Nithiarasu, and K.N. Seetharamu, *Fundamentals of the finite element method for heat and fluid flow*. 2004: John Wiley & Sons.
253. Zhu, J., *The finite element method: its basis and fundamentals*. 2013: Elsevier.
254. Tu, J., G.H. Yeoh, and C. Liu, *Computational fluid dynamics: a practical approach*. 2012: Butterworth-Heinemann.
255. Lewis, R.W., P. Nithiarasu, and K.N. Seetharamu, *Front Matter*. 2004: Wiley Online Library.
256. Patankar, S., *Numerical heat transfer and fluid flow*. 1980: CRC Press.
257. Romero-Méndez, R., et al., *Effect of fin spacing on convection in a plate fin and tube heat exchanger*. International Journal of Heat and Mass Transfer, 2000. **43**(1): p. 39-51.
258. Chuan, L., et al., *Fluid flow and heat transfer in microchannel heat sink based on porous fin design concept*. International Communications in Heat and Mass Transfer, 2015. **65**(Supplement C): p. 52-57.
259. Abdollahi, A. and M. Shams, *Optimization of shape and angle of attack of winglet vortex generator in a rectangular channel for heat transfer enhancement*. Applied Thermal Engineering, 2015. **81**(0): p. 376-387.
260. Kawano, K., et al., *Micro channel heat exchanger for cooling electrical equipment*. ASME Heat Transfer Div Publ Htd, 1998. **361**: p. 173-180.

References

261. Qu, W. and I. Mudawar, *Analysis of three-dimensional heat transfer in micro-channel heat sinks*. International Journal of Heat and Mass Transfer, 2002. **45**(19): p. 3973-3985.
262. Ahmed, H.E., M.I. Ahmed, and M.Z. Yusoff, *Heat Transfer Enhancement in a Triangular Duct using Compound Nanofluids and Turbulators*. Applied Thermal Engineering.
263. Al-Damook, A., et al., *An experimental and computational investigation of thermal air flows through perforated pin heat sinks*. Applied Thermal Engineering, 2015. **89**: p. 365-376.
264. Promvonge, P., S. Sripattanapipat, and S. Kwankaomeng, *Laminar periodic flow and heat transfer in square channel with 45° inline baffles on two opposite walls*. International Journal of Thermal Sciences, 2010. **49**(6): p. 963-975.
265. Yu, X., et al., *Development of a plate-pin fin heat sink and its performance comparisons with a plate fin heat sink*. Applied Thermal Engineering, 2005. **25**(2–3): p. 173-182.
266. Gurrum, S.P., et al., *Thermal issues in next-generation integrated circuits*. Device and Materials Reliability, IEEE Transactions on, 2004. **4**(4): p. 709-714.
267. Yuan, W., et al., *Numerical simulation of the thermal hydraulic performance of a plate pin fin heat sink*. Applied Thermal Engineering, 2012. **48**(0): p. 81-88.
268. Bassi, A. and S. De Marchi, *A Scilab radial basis function toolbox*. 2012, Master's thesis, University of Padova, 2012. 1, 4, 4.1, 4.1.
269. Khatir, Z., et al., *Dropwise condensation heat transfer process optimisation on superhydrophobic surfaces using a multi-disciplinary approach*. Applied Thermal Engineering, 2016. **106**: p. 1337-1344.
270. Khatir, Z., et al., *Numerical study of coupled fluid–structure interaction for combustion system*. International Journal for Numerical Methods in Fluids, 2008. **56**(8): p. 1343-1349.
271. Fonseca, C.M. and P.J. Fleming. *Genetic Algorithms for Multiobjective Optimization: Formulation Discussion and Generalization*. in *Icga*. 1993.
272. Deb, K., et al., *A Fast Elitist Non-dominated Sorting Genetic Algorithm for Multi-objective Optimization: NSGA-II*, in *Parallel Problem Solving from Nature PPSN VI: 6th International Conference Paris, France, September 18–20, 2000 Proceedings*, M. Schoenauer, et al., Editors. 2000, Springer Berlin Heidelberg: Berlin, Heidelberg. p. 849-858.